

Air Force Institute of Technology

AFIT Scholar

Theses and Dissertations

Student Graduate Works

1-1997

Spectroscopic and Kinetic Studies of Bismuth Dimers

Robert Eugene Frankin

Follow this and additional works at: <https://scholar.afit.edu/etd>



Part of the [Plasma and Beam Physics Commons](#)

Recommended Citation

Frankin, Robert Eugene, "Spectroscopic and Kinetic Studies of Bismuth Dimers" (1997). *Theses and Dissertations*. 5673.

<https://scholar.afit.edu/etd/5673>

This Dissertation is brought to you for free and open access by the Student Graduate Works at AFIT Scholar. It has been accepted for inclusion in Theses and Dissertations by an authorized administrator of AFIT Scholar. For more information, please contact richard.mansfield@afit.edu.



19970403 054

SPECTROSCOPIC AND KINETIC STUDIES
OF BISMUTH DIMERS

DISSERTATION

Robert Eugene Franklin
Captain, USAF

AFIT/DS/ENP/97-04

DISTRIBUTION STATEMENT A
Approved for public release
Distribution Unlimited

DTIC QUALITY INSPECTED

DEPARTMENT OF THE AIR FORCE
AIR UNIVERSITY
AIR FORCE INSTITUTE OF TECHNOLOGY

Wright-Patterson Air Force Base, Ohio

REPORT DOCUMENTATION PAGE

Form Approved
OMB No. 0704-0188

Public reporting burden for this collection of information is estimated to average 1 hour per response, including the time for reviewing instructions, searching existing data sources, gathering and maintaining the data needed, and completing and reviewing the collection of information. Send comments regarding this burden estimate or any other aspect of this collection of information, including suggestions for reducing this burden, to Washington Headquarters Services, Directorate for Information Operations and Reports, 1215 Jefferson Davis Highway, Suite 1204, Arlington, VA 22202-4302, and to the Office of Management and Budget, Paperwork Reduction Project (0704-0188), Washington, DC 20503.

1. AGENCY USE ONLY (Leave blank)	2. REPORT DATE February 1997	3. REPORT TYPE AND DATES COVERED Doctoral Dissertation	
4. TITLE AND SUBTITLE Spectroscopic and Kinetic Studies of Bismuth Dimers		5. FUNDING NUMBERS	
6. AUTHOR(S) Robert E. Franklin, Capt, USAF		8. PERFORMING ORGANIZATION REPORT NUMBER AFIT/DS/ENP/97-04	
7. PERFORMING ORGANIZATION NAME(S) AND ADDRESS(ES) Air Force Institute of Technology, WPAFB OH 45433-6583		10. SPONSORING / MONITORING AGENCY REPORT NUMBER	
9. SPONSORING / MONITORING AGENCY NAME(S) AND ADDRESS(ES) AFOSR/NC Bolling AFB Washington D.C. 20332-6448 Attn. Dr. Michael Berman		11. SUPPLEMENTARY NOTES	
12a. DISTRIBUTION / AVAILABILITY STATEMENT Approved for public release; distribution unlimited		12b. DISTRIBUTION CODE A	
13. ABSTRACT (Maximum 200 words) The spectroscopy of high rotational levels ($J \leq 211$) in $\text{Bi}_2 X(0_g^+)$ and $A(0_u^+)$ was investigated for $2 \leq v' \leq 5$ and $0 \leq v'' \leq 4$ by observing total fluorescence from laser excitation. Dunham coefficients were derived that fit all observed rotational lines to within 0.01 cm^{-1} . Franck-Condon factors were calculated and experimentally verified for transitions originating from the initially populated levels $0 \leq v' \leq 5$. Vibrational energy transfer upon collision with rare gas collision partners was investigated for the low-lying vibrational levels of the A-state using spectrally resolved, continuous wave laser induced fluorescence. Vibrational transfer was adequately modeled by Landau-Teller scaling of the $\Delta v = -1$ vibrational transfer rates with fundamental rate coefficients ranging from $k_v = 5.29 \times 10^{-12} \text{ cm}^3/\text{molec-sec}$ for collisions with helium to $2.38 \times 10^{-12} \text{ cm}^3/\text{molec-sec}$ for krypton. Electronic quenching and multi-quantum transfer rates were approximately an order of magnitude slower than single quantum transfer rates. State-to-state rotational energy transfer was studied for $\text{Bi}_2(A)$ collisions with helium, neon and argon after laser excitation of $J' = 171, 202, 231$. Rotational energy transfer from the parent state occurred at gas kinetic rates and was adequately modeled by the energy based statistical power gap law. Total rotational removal from the parent state varied from $k_J = 8.87 \times 10^{-10} \text{ cm}^3/\text{molec-sec}$ for collisions with helium to $2.84 \times 10^{-10} \text{ cm}^3/\text{molec-sec}$ for argon. The relative rotational transfer efficiencies displayed a linear dependence on the square root of the collision pair reduced mass.			
14. SUBJECT TERMS Bismuth, Diatomic Bismuth, Spectroscopy, Kinetics, Vibrational Energy Transfer, Rotational Energy Transfer			15. NUMBER OF PAGES 199
17. SECURITY CLASSIFICATION OF REPORT Unclassified			16. PRICE CODE
18. SECURITY CLASSIFICATION OF THIS PAGE Unclassified	19. SECURITY CLASSIFICATION OF ABSTRACT Unclassified	20. LIMITATION OF ABSTRACT UL	

AFIT/DS/ENP/97-04

SPECTROSCOPIC AND KINETIC STUDY OF BISMUTH DIMERS

DISSERTATION

Robert Eugene Franklin
Captain, USAF

AFIT/DS/ENP/97-04

Approved for public release; distribution unlimited

AFIT/DS/ENP/97-04

SPECTROSCOPIC AND KINETIC STUDY OF BISMUTH
DIMERS

DISSERTATION

Presented to the Faculty of the School of Engineering
of the Air Force Institute of Technology

Air University

In Partial Fulfillment of the
Requirements for the Degree of
Doctor of Philosophy

Robert Eugene Franklin, B.S., M.S.
Captain, USAF

February, 1997

Approved for public release; distribution unlimited

SPECTROSCOPIC AND KINETIC STUDIES

OF BISMUTH DIMERS

Robert E. Franklin, B.S., M.S.
Captain, USAF

Approved:

[Redacted Signature]

Maj. Glen P. Perram (Chairman)

19 February 1997
Date

[Redacted Signature]

Dr. William M. Brown (Dean's Representative)

24 Feb 1997
Date

[Redacted Signature]

Lt. Col. W. Jerry Bowman

19 Feb 97
Date

[Redacted Signature]

Dr. Won B. Roh

19 Feb 97
Date

[Redacted Signature]

Lt. Col. Paul J. Wolf

19 FEB 97
Date

Accepted:

[Redacted Signature]

Robert A. Calico, Jr.
Dean, Graduate School of Engineering

Preface

This study of the spectroscopy and kinetics of diatomic bismuth has been both interesting and rewarding. The chance to work independently in the laboratory has opened my eyes aspects of the scientific world that most certainly cannot be found in the classroom environment. However, this research would never have been completed without the help of numerous people. The first person I'd like to thank is my advisor, Maj Glen Perram. He not only had the confidence to allow me to proceed with the topic of this research, but he also proved to be an invaluable source of both experimental and theoretical knowledge. His door was always open and his encouragement was always appreciated. Next, I'd like to thank Lt Col Paul Wolf for helping with some of the early experimental setup as well as providing me with additional insight into the relevant physics of the processes being studied. Numerous other people assisted with actual work in the laboratory. Most notably were Maj Jack McCrae and Capt Monte Turner - the two doctoral students with labs next door to mine. Their knowledge of laboratory equipment and techniques proved invaluable in obtaining the necessary data. Additionally, Mr. Jim Reynolds, laboratory technician, was of considerable help during the build-up phase of the experiment by helping me to obtain the needed laboratory equipment. I especially thank my God for the ability and endurance He gave me to make it through this project. Finally, I need to thank my wife [REDACTED] and my son [REDACTED]. My son was born during this research project and his smiling face was always a joy to come to after a long day in the lab. As for my wife, were it not for her love, encouragement and patience over these past long months, this work would never have been successful.

Robert Eugene Franklin

Table of Contents

	Page
Preface	iii
List of Figures	viii
List of Tables	xiii
List of Symbols	xv
Abstract	xviii
I. Introduction	1-1
1.1 Motivation	1-1
1.2 Bismuth	1-4
1.2.1 Motivation to Study Bi ₂	1-4
1.2.2 Current Knowledge of Bi ₂	1-6
1.3 Problem Statement	1-8
1.4 Organization	1-9
II. Background Theory	2-1
2.1 Molecular Theory	2-1
2.1.1 Group V Diatomic Structure	2-1
2.1.2 Hund's Cases	2-1
2.1.3 Spectroscopy of Bi ₂	2-5
2.2 Laser Induced Fluorescence	2-8
2.3 Kinetic Theory	2-12
2.3.1 Energy Transfer Processes	2-12
2.3.2 Master Rate Equation	2-16

	Page
2.3.3	Time-Independent Solution 2-17
2.3.4	Energy Transfer Rates 2-20
III.	Spectroscopy of High J levels in the $\text{Bi}_2 X(0_g^+) \rightarrow A(0_u^+)$ Transition 3-1
3.1	Introduction 3-1
3.2	Experimental Setup 3-2
3.3	Laser Excitation Spectra 3-6
3.4	Experimental Results and Discussion 3-7
3.4.1	Relative Rotational Numbering 3-7
3.4.2	Absolute Rotational Numbering 3-11
3.4.3	Determination of Molecular Constants 3-14
3.5	Franck-Condon Factors 3-27
3.5.1	Experimental Procedures 3-27
3.5.2	Results and Discussion 3-30
IV.	Vibrational Energy Transfer in $\text{Bi}_2 A(0_u^+)$ 4-1
4.1	Introduction 4-1
4.2	Experimental Setup 4-1
4.3	Experimental Procedures 4-1
4.3.1	Data Collection 4-1
4.3.2	Population Ratios 4-5
4.4	V \rightarrow T Transfer with Rare Gas Collision Partners 4-11
4.4.1	Direct Vibrational Transfer 4-11
4.4.2	Rate Matrix Technique 4-16
4.4.3	Helium, Argon, Krypton, Xenon 4-28
4.5	Comparison to SSH Theory 4-29
4.6	Conclusions 4-33

	Page
V. Rotational Energy Transfer in Bi_2 $A(0_u^+)$	5-1
5.1 Introduction	5-1
5.2 Experimental Setup	5-1
5.3 Experimental Procedures	5-2
5.3.1 Data Collection	5-2
5.3.2 Population Ratios	5-5
5.4 R \rightarrow T Transfer with Helium, Neon and Argon Collision Partners	5-9
5.4.1 Direct Rotational Transfer	5-9
5.4.2 Direct Rotational Transfer	5-9
5.4.3 Neon, Argon	5-16
5.5 Rotational Transfer Fitting Laws	5-16
5.6 Discussion of Results	5-20
5.7 Conclusions	5-25
VI. Conclusions	6-1
6.1 Summary of the High J Spectroscopy of Bi_2	6-1
6.2 Summary of Vibrational Energy Transfer Studies	6-2
6.3 Summary of Rotational Energy Transfer Studies	6-3
6.4 Further studies	6-3
Appendix A. Basic Energy Transfer Theories	A-1
A.1 Gas Kinetic Collision Rate	A-1
A.2 Landau-Teller Theory	A-2
A.3 SSH Theory	A-3
A.4 Rate Matrix Solution	A-4
Appendix B. Observed Bi_2 Rotational Lines	B-1

	Page
Appendix C. Spectral Fitting Function for CW LIF Spectra	C-1
C.1 Synthetic Spectra	C-1
C.2 Fitting Function	C-2
Appendix D. Rotational Transfer Fit Parameters	D-1
Appendix E. Error Analysis	E-1
Bibliography	BIB-1
Vita	VITA-1

List of Figures

Figure	Page
2.1. Ground state Group V diatomic electronic configuration	2-2
2.2. Hund's case correlation diagram for Bi ₂	2-4
2.3. Bi ₂ potential energy curves derived from reported spectroscopic constants	2-9
2.4. Simplified representation of laser induced fluorescence from collisionally populated satellite states	2-10
3.1. Block diagram of the experimental apparatus used to observe LIF in Bi ₂	3-3
3.2. Plot of Bi ₂ vapor pressure as a function of temperature.	3-5
3.3. High resolution laser excitation spectra of Bi ₂ X→A showing a typical P-R doublet progression in the $v'' = 4$ to $v' = 0$ vibrational band	3-8
3.4. Doppler limited laser excitation spectrum of the $v'' = 4$ to $v' = 0$ bandhead	3-9
3.5. Residuals of the second difference fits of the $(v'', v') = (4, 0)$ and $(4, 1)$ bands of the Bi ₂ X→A laser excitation spectrum	3-12
3.6. Plot of the second differences of the Bi ₂ 4-0 band versus rotational quantum number. The dashed lines on the graph show that the zero intercept occurs at $J = -1/2$	3-13
3.7. Direct fit of the $v'' = 3$ to $v' = 3$ observed rotational line positions to a single equation in m	3-15
3.8. Residuals of current and previous predicted values of the rotational line position of the $v'' = 4 \rightarrow v' = 0$ band	3-20
3.9. Comparison of Gerber's predicted B_v'' term values with those derived from this research	3-22
3.10. Comparison of all reported B_v'' term values with a least-squares fit to the entire data set	3-23

Figure	Page
3.11. Comparison of Gerber's predicted values for B'_v with all reported B'_v term values	3-24
3.12. Comparison of this study's observed D''_v values to those reported by Effantin. The solid line is a least-squares fit to this study's observed values.	3-26
3.13. Spectrally resolved emission from the initially populated level Bi_2 (A) $v' = 3$	3-31
3.14. Bi_2 potential energy curves derived from the final set of spectroscopic constants presented in this research	3-32
3.15. Comparison of experimentally derived Franck-Condon factors with those calculated from an RKR based fitting routine for the initially populated $v' = 2$ level.	3-36
3.16. Comparison of experimentally derived Franck-Condon factors with those calculated from an RKR based fitting routine for the initially populated $v' = 5$ level.	3-37
4.1. Spectrally resolved fluorescence profile after initially populating $v'=3$ with 4.758 torr of neon buffer gas. Identifiable bands are labeled (v',v'')	4-4
4.2. Comparison of a spectrally resolved fluorescence profile after initially populating $v'=3$ with 4.758 torr of neon buffer gas with the results of a fitted spectral simulation. Open circles are the data points while the line running through them is the numerical fit.	4-9
4.3. Comparison of the $\Delta v = -1$ population ratios after initially populating $v' = 3$ with a least-squares fit to the direct transfer equation. Neon is the collision partner.	4-12
4.4. Comparison of the $\Delta v = -2$ population ratios after initially populating $v' = 3$ with a least-squares fit to the direct transfer equation. Neon is the collision partner.	4-13
4.5. Plot of the $\Delta v = -3$ population ratios after initially populating $v' = 3$. Neon is the collision partner.	4-14

Figure	Page
4.6. Comparison of the $\Delta v = +1$ population ratios after initially populating $v' = 3$ with a least-squares fit to the direct transfer equation. Neon is the collision partner.	4-15
4.7. Comparison of the $\Delta v = -1$ population ratios after initially populating $v' = 3$ with the predicted ratio from the rate matrix calculation	4-19
4.8. Comparison of the $\Delta v = -2$ population ratios after initially populating $v' = 3$ with the predicted ratio from the rate matrix calculation	4-20
4.9. Comparison of the $\Delta v = -3$ population ratios after initially populating $v' = 3$ with the predicted ratio from the rate matrix calculation	4-21
4.10. Comparison of the $\Delta v = +1$ population ratios after initially populating $v' = 3$ with the predicted ratio from the rate matrix calculation	4-22
4.11. Plot of the $\Delta v = -1$ vibrational transfer rates versus the vibrational quantum number, v' . The straight line represent a linear regression of this data and indicates a fundamental transfer rate of $k_v(1, 0) = (4.84 \pm 0.87) \times 10^{-12}$ cm ³ /molec-sec	4-24
4.12. Rotational temperature of $v'' = 1$ at a mix pressure of 1.2 torr of nitrogen buffer gas. Data comes from laser excitation of the $v'' = 1$ to $v' = 4$ transition	4-27
4.13. Vibrational transfer probabilities ($\Delta v = -1$) for Bi ₂ , Br ₂ , BrCl and IF with rare gas collision partners as a function of the cube root of the reduced mass.	4-32
4.14. Interaction lengths as a function of collision pair reduced mass for Bi ₂ , Br ₂ , BrCl and IF.	4-34
5.1. Spectrally resolved Bi ₂ (A→X) laser-induced fluorescence from the $v' = 1 \rightarrow v'' = 5$ band in the presence of 753 mtorr of helium buffer gas. The parent rotational state is $J' = 231$	5-3

Figure	Page
5.2. Spectrally resolved Bi_2 ($A \rightarrow X$) laser-induced fluorescence from the $v' = 1 \rightarrow v'' = 5$ band in the presence of 855 mtorr of helium buffer gas. The parent rotational state is $J' = 171$	5-4
5.3. Comparison of neon calibration line as recorded on the optical multi-channel analyzer with a spectral fitting function. The entrance slit width is $5\mu\text{m}$ and the resolution is 0.32 cm^{-1}	5-7
5.4. Comparison of spectrally resolved Bi_2 fluorescence in the presence of 855 mtorr of helium buffer gas with a spectral fit to the data. The parent state of this rotational spectra was Bi_2 ($A, v' = 1, J' = 171$).	5-8
5.5. Plot of the population of the satellite $J' = 165$ rotational level relative to the parent state ($J' = 171$) for collisions with helium buffer. The solid line running through the plot is a least-squares fit to the data using the direct transfer equation.	5-10
5.6. Observed rotational energy transfer rate coefficients as a function of change in rotational energy transfer for Bi_2 ($B, v'_0 = 1, J'_0 = 171$) collisions with helium. A fit to both the statistical power gap law and the exponential gap law is shown.	5-13
5.7. Observed rotational energy transfer rate coefficients as a function of change in rotational energy transfer for Bi_2 ($B, v'_0 = 1, J'_0 = 201$) collisions with helium. A fit to the SPG scaling law is also shown.	5-14
5.8. Observed rotational energy transfer rate coefficients as a function of change in rotational energy transfer for Bi_2 ($B, v'_0 = 1, J'_0 = 231$) collisions with helium. A fit to the SPG scaling law is also shown.	5-15
5.9. Observed rotational energy transfer rate coefficients as a function of change in rotational energy transfer for Bi_2 ($B, v'_0 = 1, J'_0 = 201$) collisions with neon. A fit to the SPG scaling law is also shown.	5-17
5.10. Observed rotational energy transfer rate coefficients as a function of change in rotational energy transfer for Bi_2 ($B, v'_0 = 1, J'_0 = 201$) collisions with argon. A fit to the SPG scaling law is also shown.	5-18
5.11. Observed rotational energy transfer rate coefficients as a function of change in rotational energy transfer for Bi_2 ($B, v'_0 = 1, J'_0 = 201$) collisions with helium, neon and argon.	5-22

Figure	Page
5.12. Plot of the rotational transfer efficiencies vs the product $\mu^{1/2}b$ for different collision partners after pumping $v' = 1, J' = 210$	5-24
C.1. Comparison of vibrational band “stick spectrum” with the synthetic CW LIF spectrum	C-3
C.2. Comparison of synthetic CW LIF spectrum with a spectral fitting function. The arrow on the graph indicates the relative position of the next vibrational bandhead.	C-5
C.3. Scaling of the spectral fitting function c parameter with temperature. The solid line is a least-squares parametric fit	C-7

List of Tables

Table	Page
2.1. Spectroscopic constants for the X(0_g^+) and A(0_u^+) states of Bi ₂	2-7
3.1. Observed Bi ₂ band origins for the X→ A Transitions	3-14
3.2. Vibrational constants for the X and A states of Bi ₂ (cm ⁻¹)	3-17
3.3. Rotational term values for the observed Bi ₂ X states (cm ⁻¹)	3-18
3.4. Rotational term values for the observed Bi ₂ A states (cm ⁻¹)	3-18
3.5. Rotational constants for the X and A states of Bi ₂ derived from this work compared with previously reported values (cm ⁻¹)	3-19
3.6. Final rotational constants for the X and A states of Bi ₂ derived from a merged fit of reported Bi ₂ term values with (cm ⁻¹)	3-25
3.7. Excitation wavelengths for Franck-Condon factor studies	3-28
3.8. Predicted and observed Franck-Condon factors for the Bi ₂ (A→X) transition. The observed value is on the bottom.	3-33
4.1. Excitation wavelengths, rovibrational assignments and range of spectral observation used in vibrational transfer studies.	4-2
4.2. Fit parameters obtained from the direct transfer equation for Bi ₂ (A) vibrational transfer population ratios as a function of neon buffer gas pressure. Listed errors are the fit standard error for that parameter.	4-17
4.3. $\Delta v = -1$ vibrational transfer rate coefficients (k_v), upper bound electronic quenching rate ($k_q \times 10^{-12}$ cm ³ /molec-sec), translational temperature, and multi-quantum fraction number (f) for Bi ₂ collisions with Neon buffer as determined from a rate matrix solution. For comparison purposes, the $\Delta v = -1$ transfer coefficient from the direct transfer equation is also listed.	4-18
4.4. Comparison of rate matrix temperatures with rotational temperatures for Bi ₂ collisions with neon buffer gas.	4-25

Table	Page
4.5. Fundamental vibrational transfer rate coefficients and $\Delta v = -1$ rate coefficients (10^{-12} cm ³ /molec-sec) for Bi ₂ (A) collisions with the rare gases	4-29
5.1. Comparison of the gas kinetic collision rate coefficient at 300 K with the total rotational transfer rate as predicted by summing all calculated state-to-state rotational transfer rates.	5-12
5.2. Fit parameters to the statistical power gap law	5-20
A.1. Gas Kinetic Collision Parameters for Bi ₂	A-2
B.1. Observed rotational line positions for $v'' = 2 \rightarrow v' = 2$	B-2
B.2. Observed rotational line positions for $v'' = 3 \rightarrow v' = 0$	B-3
B.3. Observed rotational line positions for $v'' = 3 \rightarrow v' = 1$	B-5
B.4. Observed rotational line positions for $v'' = 3 \rightarrow v' = 3$	B-6
B.5. Observed rotational line positions for $v'' = 3 \rightarrow v' = 4$	B-8
B.6. Observed rotational line positions for $v'' = 4 \rightarrow v' = 0$	B-9
B.7. Observed rotational line positions for $v'' = 4 \rightarrow v' = 1$	B-11
B.8. Observed rotational line positions for $v'' = 4 \rightarrow v' = 2$	B-13
B.9. Observed rotational line positions for $v'' = 5 \rightarrow v' = 1$	B-15
D.1. Fit parameters and rotational transfer coefficients for Bi ₂ (A, $v'_0 = 1, J'_0 = 171$) collisions with Helium.	D-2
D.2. Fit parameters and rotational transfer coefficients for Bi ₂ (A, $v'_0 = 1, J'_0 = 171$) collisions with Helium.	D-4
D.3. Fit parameters and rotational transfer coefficients for Bi ₂ (A, $v'_0 = 1, J'_0 = 231$) collisions with Helium.	D-6
D.4. Fit parameters and rotational transfer coefficients for Bi ₂ (A, $v'_0 = 1, J'_0 = 201$) collisions with Neon.	D-7
D.5. Fit parameters and rotational transfer coefficients for Bi ₂ (A, $v'_0 = 1, J'_0 = 201$) collisions with Argon.	D-9

List of Symbols

v', J'	Vibrational and rotational quantum numbers for electronically excited molecules
v'', J''	Vibrational and rotational quantum numbers for ground state molecules
ω_e	Vibrational frequency term for a diatomic molecule
$\omega_e \chi_e / \omega_e$	Ratio describing the degree of harmonic behavior present in a diatomic molecule (anharmonicity factor)
μ	Collision pair reduced mass
k	Boltzmann's constant
ω_e / kT	Vibrational energy spacing with respect to the average thermal energy T
$X(0_g^+)$	Molecular term symbol for the ground state of Bi_2
$A(0_u^+)$	Molecular term symbol for the electronically excited A state of Bi_2
$E(v, J)$	Energy of rovibrational energy level
T_e	Electronic energy of a rovibrational energy level
G_v	Vibrational energy of a rovibrational energy level
$F_v(J)$	Rotational energy of a rovibrational energy level
B_v	Rotational energy of a rigid rotor
B_e, α_e	Rotational constants used to define B_v
D_v	Centrifugal distortion correction to the rotational energy term
D_e, β_e	Rotational constants used to define D_v
I_f	Fluorescence intensity

I_{vw}^{obs}	Fluorescence intensity observed on the transition from state v to state w
ν_{vw}	Frequency of the v to w transition
q_{vw}	Franck-Condon factor for states v and w
R_e	Electric dipole moment
S_J	Rotational linestrength factor
$D(\nu_{vw})$	Detector response function
$N(v)$	Number of molecules in state v
τ_r	Collisionless radiative lifetime from an excited electronic state
M	Buffer gas collision partner
k_q, k_q^M	Total collisional quenching rate coefficient for collisions with collision partner M
k_{vJ}	Rovibrational transfer rate coefficient
$k_v(v_i \rightarrow v_f)$	State-to-state vibrational transfer rate coefficient for transfer from state v_i to state v_f
$\Gamma(v')$	Collisionless removal rate from state v'
$K_v(v')$	Total collisional removal rate from state v'
a, b, c	Numerical fitting parameters
$k_J(J_i \rightarrow J_f)$	State-to-state rotational transfer rate coefficient for transfer from state J_i to state J_f
A	Exponential gap law parametric fit parameter
χ	Exponential gap law scaling parameter

B	Statistical power gap law parametric fit parameter
γ	Statistical power gap law scaling parameter
$f(J)$	Rotational distribution function
$\rho(\Delta E, T)$	Density of state ratio (≈ 1)
$P(J)$	Label for a P-branch rotational transition
$R(J)$	Label for an R-branch rotational transition
m	Label for the rotational quantum number in a single band fit equation
$F(a, b, c, \lambda_{v'w}, \lambda)$	Spectral fitting function predicting the spectral output of a thermalized vibrational band
α, β, ξ	Rotational temperature fitting parameters
A_g	Intensity of a Gaussian fitting function
R	Resolution parameter for a symmetric peak function
$G(A_g, \lambda_0, R, \lambda)$	Gaussian peak function
f	Multi-quantum fraction percentage
$\sigma_v(10)$	Thermally averaged fundamental vibrational transfer cross section
σ_g	Thermally averaged gas kinetic cross section
$P_{10}, P(10)$	Fundamental probability of transfer from $v' = 1$ to $v' = 0$; experimentally equivalent to $\sigma_v(10)/\sigma_g$
L	Characteristic interaction length between collision partners
v_g	Mean relative velocity between collision partners
$I_{GL}(\lambda)$	Spectral output of the Gauss-Lorentzian peak function

Abstract

The spectroscopy of high rotational levels in $\text{Bi}_2 \text{X}(0_g^+)$ and $\text{A}(0_u^+)$ was investigated for $2 \leq v'' \leq 5$ and $0 \leq v' \leq 4$ by observing total fluorescence from laser excitation with a scanning, continuous wave, narrow linewidth ring laser. Rotational levels with $J \leq 211$ were accessed. Dunham coefficients were derived that fit all observed rotational lines to within 0.01 cm^{-1} . From these coefficients, Franck-Condon factors were calculated that accurately reflect a set of experimentally determined Franck-Condon factors originating from the initially populated levels $0 \leq v' \leq 5$.

Vibrational energy transfer in the low-lying vibrational levels ($v' \leq 4$) of the $\text{A}(0_u^+)$ state of Bi_2 was investigated using spectrally resolved, continuous wave laser induced fluorescence. Spectrally resolved emissions from collisionally populated $\text{Bi}_2(\text{A})$ vibrational levels were observed for rare gas collision partners. Vibrational transfer promoted rapid thermalization of the excited A state molecules. Landau-Teller scaling of vibrational transfer rates was found to be an acceptable model for the scaling of transfer rates with vibrational quantum number. Fundamental transfer rate coefficients ranged from $k_v(1, 0) = 5.29 \pm 0.73 \times 10^{-12} \text{ cm}^3/\text{molec-sec}$ for helium to $k_v(1, 0) = 2.38 \pm 0.36 \times 10^{-12} \text{ cm}^3/\text{molec-sec}$ for krypton. Electronic quenching and multi-quantum transfer rates were found to be approximately an order of magnitude slower than the corresponding single quantum transfer rates.

Rotational energy transfer in high rotational levels of the A state of Bi_2 was also investigated by spectrally resolved, continuous wave laser induced fluorescence. Spectrally resolved emissions from collisionally populated $\text{Bi}_2(\text{A})$ rotational levels were observed for collisions with helium, neon and argon after laser excitation of $J' = 171, 201, 231$. Rotational energy transfer was the most efficient kinetic process in $\text{Bi}_2(\text{A})$ and is adequately modeled by the energy based statistical power gap law. Total rotational removal rates from the initially prepared state range from

8.87×10^{-10} cm³/molec-sec for collisions with helium to 2.84×10^{-10} cm³/molec-sec for collisions with argon. The relative rotational transfer efficiencies displayed a linear dependence on the square root of the collision pair reduce mass.

SPECTROSCOPIC AND KINETIC STUDY OF BISMUTH DIMERS

I. Introduction

1.1 Motivation

Since the early 1970's, the United States Air Force has maintained a continued interest in the development of a large scale chemical laser for missions such as strategic defense against ballistic attack, anti-satellite weapons and theater missile defense (TMD) (1). Chemical lasers are an ideal choice for these missions due to their large output power and very high beam quality. An early example of this type of system is the HF laser that was first demonstrated in 1970 (2). Another example is the Chemical Oxygen Iodine Laser (COIL) that has undergone continued research and development at the Air Force Phillips Laboratory since the mid-1970's (3, 4). This system has been chosen as the laser weapon for the first operational Air Force TMD system. This program intends to mate a high-power COIL device to a Boeing 747 airframe for use as theater defense against ballistic missile attack by destroying these weapons in the boost phase. COIL has the shortest wavelength ($1.315 \mu\text{m}$) of any high power chemical laser system currently developed (5).

A chemically pumped electronic transition laser uses an exothermic chemical reaction to provide the energy needed to populate the upper electronic laser level. This can be accomplished either through direct excitation of the lasant species, such as in the HF laser, or via collision with a metastable intermediate, as in COIL. In diatomic or polyatomic molecules, the excited state population induced by the chemical reaction will invariably be produced in a highly non-thermal distribution over many possible rovibrational levels. Therefore, a good lasant molecule should

thermalize rapidly without losing electronic excitation. This will allow for a much larger population inversion as the molecules thermalize in the excited electronic state.

With the multitude of potential uses envisioned for chemical lasers, there is an obvious need to find how to best improve these systems. From a weapons viewpoint there are several compelling reasons why a move to a visible chemical laser is desirable. Laser output power, beam divergence, beam jitter and optical quality of the beam are just a few of the many parameters that affect the ability of a laser weapon to damage a distant target (5). Beam divergence during propagation directly affects the amount of output laser power that is delivered to the target. The area of a Gaussian beam diverges as the square of the emitted laser wavelength, thus a major increase in brightness/intensity can be realized for a laser that emits at a visible wavelength. For example, a BiF(A-X) laser operating on a blue wavelength would realize a 30-40 fold increase in on-target intensity as compared to an HF laser with an equivalent output power (5) assuming that problems with beam jitter and atmospheric turbulence can be solved. Thus, visible chemical lasers can possibly provide a strong enhancement in on-target intensity.

Space based applications would also benefit from a visible chemical laser. Chemical lasers contain their own energy source and thus reduce the amount of weight needed in orbit, thus directly reducing the cost. The electronic transitions involved in visible chemical lasers has the potential for greater mass efficiency and nozzle flux power than the current generation of chemical lasers (5). Laser output energies per mass of input reactants on the order of 1MJ/kg are possible with a visible system. These high mass efficiencies are beneficial as it is the cost of lifting reagents to orbit that would dominate the overall expense on a space based chemical laser system (5). To these ends, considerable Air Force effort has been expended on the search for a scalable visible chemical laser (6).

A great deal of research has been accomplished on the diatomic halogens and interhalogens as potential lasants for a visible chemical laser (7, 8, 9, 10, 11). The

strong visible absorption and emission characteristics of these molecules make them ideal candidates from which to begin a search. In order to properly evaluate the potential of using these species as lasing molecules their spectroscopic, kinetic and chemical properties must be understood. Spectroscopic information allows for the calculation of potential energy curves for the various electronic states. From these curves informed judgments are made about properties of the system such as Franck-Condon factors, wavelength tunability and lifetimes.

As was alluded to earlier, a good lasing molecule must thermalize rapidly in the excited electronic state to help create a large population inversion. Thus, a thorough knowledge of energy transfer rates and mechanisms is critical to the selection of a suitable lasing species. To this end, quantum-resolved energy transfer among small molecules in the gas phase has been a significant area of chemical physics research, both theoretical and experimental, for the past several decades (6). A large number of these energy transfer studies have focused on vibrational energy transfer in diatomic molecules. This extensive database allows the opportunity to examine the effects of vibrational frequency, ω_e , reduced mass of the collision pair, μ , and anharmonicity, $\omega_e\chi_e/\omega_e$ on vibration-to-translation (V-T) energy transfer rates (12). Vibrational frequency appears to play a critical role in the vibrational transfer process. Studies accomplished on the diatomic halogens and interhalogens have found the probability for V-T transfer increasing by almost two orders of magnitude as ω_e/kT ranges from 2.0 for IF to 0.63 for Br₂. Plots of vibrational transfer probability as a function of reduced mass of the collision pair further indicate the importance of vibrational frequency in the V-T process. These plots show an inverse relationship between reduced mass and transfer probability for $\omega_e/kT \gg 1$ and the opposite trend for $\omega_e/kT < 1$. In BrCl ($\omega_e/kT \approx 1$) there is no discernible trend either positive or negative (12).

A more interesting observation from reported vibrational energy transfer studies is the apparent importance of anharmonicity in determining the probability of

multi-quantum transfer during a single collision event. Perram reported $\Delta v = -2$ vibrational transfer rates approximately 40% of $\Delta v = -1$ rates for rare gas collisions with BrCl (13). This is in contrast to the 10% multi-quantum fraction reported by Holmberg for rare gas collisions with Br₂ (12). As was already noted, $\omega_e/kT \approx 0.63$ for Br₂ and 1.0 for BrCl. Thus, collisions with bromine have a greater excess of energy with respect to vibrational frequency than similar collisions with BrCl. However, Br₂ has an anharmonicity ≈ 0.01 , while the anharmonicity of BrCl ≈ 0.02 . Thus, it appears that harmonic oscillator selection rules are an important consideration when the electronic state of interest displays harmonic behavior.

Compared to the wealth of data available on vibrational energy transfer, rotational energy transfer (R-T) is still in its infancy. As a matter of fact, there are currently no analytically derivable rotational transfer theories. Current scaling laws and results are unclear as to the importance of either energy or angular momentum change in the R-T process. If these basic relationships can be established, then suitable theories may be developed. To this end, R-T transfer data needs to be gathered and suitable relationships need to be found for the various system parameters.

1.2 Bismuth

1.2.1 Motivation to Study Bi₂. NF(*a*¹Δ) has been proposed as the metastable intermediate for a visible chemical laser (6). This molecule is favored due to its high electronic energy content (1.4 eV), low self-annihilation rate in comparison with other (N₂) triplet metastables and the availability of two efficient pumping reactions which can be used for its chemical generation (14). Benard demonstrated weak lasing at 470 nm by using NF(*a*¹Δ) to electronically excite BiF(A) (14). This work used trimethylbismuthine (Bi(CH₃)₃) (TMB) as the source for the bismuth atom in the BiF dimers. A conclusion of his research was that the unreacted TMB was rapidly quenching the excited BiF molecules and thus a more suitable source of bismuth donors was needed to allow for a larger gain coefficient (14). Herbelin showed that

an order of magnitude improvement in BiF(A) concentration was achievable for a given $NF(a^1\Delta)$ concentration if metallic bismuth was used in the previous chemical reaction as opposed to TMB (15). Approximately equal densities of Bi and Bi₂ are present in the vapor formed as metallic bismuth is heated past its vaporization point (16). Bi₃ and Bi₄ are also formed but are present only in negligible amounts. As the Bi atom is the donor for the generated BiF, the Bi₂ is an unnecessary constituent in the reaction (15). Since bismuth dimer kinetics are poorly understood, a detailed study of energy transfer in Bi₂ would assist in the development of this laser system.

An optically pumped diatomic bismuth laser was first demonstrated in 1978 (17). Continued development of this system through the early 1980's achieved lasing on approximately 150 different rovibrational transitions with photon conversion efficiencies approaching 20% (18). This system lased at wavelengths between 590 and 790 nm and thus also deserves consideration as a potential lasing molecule for a visible chemical laser. As in the case of the BiF laser, a better understanding of bismuth dimer kinetics would allow for a more complete analysis of this laser system.

From a purely scientific viewpoint, there are certain physical properties of Bi₂ that make it an excellent subject for the study of collisional energy transfer. First, Bi₂ has extremely strong absorption and emission characteristics in the visible. In addition, Bi₂ forms the heaviest known stable diatomic molecule. Thus, a study of this species allows the exploration of the extremes of mass influence on collisional energy transfer. Because of the large mass, Bi₂ has very small energy spacing. During a collision event there is a large excess of translational energy present with respect to what is needed to accomplish a single quantum transfer ($\omega_e/kT = 0.62$ @ T=300 K). From the previous discussion on vibrational energy transfer, this small energy spacing indicates there is probably some sort of positive relationship between collision pair reduced mass and probability of vibrational transfer for rare gas collisions with Bi₂. Furthermore, Bi₂ has an anharmonicity of $\omega_e\chi_e/\omega_e = 0.002$. If previous trends

in the diatomic halogens hold, multi-quantum fractions are probably relatively small for collisional processes involving bismuth dimers.

A study of rotational energy transfer in $\text{Bi}_2(\text{A})$ provides another unique scientific opportunity. The large mass of the Bi_2 dimer corresponds to a large value for the molecular moment of inertia with a resulting extremely small value for the rotational energy terms ($B'_v \approx 0.02 \text{ cm}^{-1}$). The maximum in the rotational distribution occurs at $J \approx 75$ which is much higher than in other lighter diatomics. Thus, very high J levels are accessible that have relatively low rotational energy. As discussed earlier, energy based scaling laws have been found that accurately model rotational energy transfer in other diatomics. The combination of large angular momentum with low rotational energy will thus provide an extreme test of the validity of energy based scaling laws.

1.2.2 Current Knowledge of Bi_2 . The $\text{A}(0_u^+)-\text{X}(0_g^+)$ system of Bi_2 has been the most studied system using absorption, emission, laser induced fluorescence (LIF), laser excitation and polarization spectroscopies. The bands of this system exhibit simple P and R branch structure, with the small vibrational and rotational spacings causing this spectra to be very dense. Fortunately, there is only one isotope of bismuth.

LIF and absorption techniques are the two most widely used spectroscopic methods to study the X and A states of bismuth. The most comprehensive spectroscopic study of the Bi_2 X-state involved laser induced fluorescence from the $\text{B}'(0_g^+)$ state located which is located approximately 7000 cm^{-1} below the A state. In this study, Effantin, et al. observed rotational structure of the vibrational levels $7 \leq v'' \leq 45$ with a Fourier transform spectrometer and the levels $10 \leq v'' \leq 105$ with a grating spectrograph (19). The range of rotational levels observed was not reported. Ehret and Gerber used polarization spectroscopy to study the A state vibrational manifold, $0 \leq v' \leq 57$, in 1984 (20). This study focused only on the

determination of accurate values of the vibrational bandheads. Rotational constants for $J \leq 65$ in the Bi_2 X and A states were reported by Gerber, et al. (21). Together, these three studies provide the best set of reported molecular constants for the A-X system of Bi_2 .

The only other investigations conducted on the A state of Bi_2 are lifetime studies conducted by Blondeau, et al. (22) and Ehret and Gerber (23). Blondeau used LIF to find lifetimes of various A state vibrational levels between 5 and 40. He observed lifetimes between 50 ns and 1 μs . and noted a strong decrease in observed lifetime near $v' = 23$. This decrease continued to $v' = 27$. He found another strong decrease in lifetime near $v' = 35$. Associated with both these decreases in lifetime was a decrease in the fluorescence signal. Blondeau interpreted these decreases as being a predissociative phenomenon. Ehret and Gerber attempted to improve on this work in the earlier study (23). They made measurements at significantly lower buffer gas pressures which greatly improved the quality of their data. This was important as multiple collisions were becoming an important consideration at foreign gas pressures above 1 torr. As in the Blondeau study, Ehret and Gerber noted the dramatic decrease in lifetime for $v' > 27$. Their conclusion was that the A state was strongly predissociated above this level.

In their work, Ehret and Gerber used argon as a buffer gas. This allowed them to calculate rotational quenching cross sections of the $\text{Bi}_2\text{-Ar}$ collision pair for the different vibrational levels they observed. For the most part, they found $\sigma (\text{Bi}_2^*\text{-Ar}) \approx 60 \times 10^{-16} \text{ cm}^2$ (23).

These two lifetime studies comprise the entire breadth of reported radiative and collisional studies conducted on $\text{Bi}_2(\text{A})$. As can readily be seen, there is much to be learned about this diatomic system. The major obstacle to overcome in a study of the A state is to build a system in which appreciable quantities of Bi_2 can be contained. As indicated in the previous discussion, predissociation does not affect the low lying rovibrational levels of the A state. Therefore, if these states can be

individually populated, the effects of collisional energy transfer can be studied using spectroscopic techniques that have already been developed.

1.3 Problem Statement

Continuous Wave (CW) laser excitation and LIF techniques were used in this research to investigate fundamental spectroscopic properties and collisional dynamics of molecular bismuth. This work was divided into three separate, yet related experimental phases. First, spectroscopic investigations were undertaken to characterize the low lying vibrational levels of both the $X(0_g^+)$ and $A(0_u^+)$ states of Bi_2 by laser excitation techniques. This characterization included the observation of very high rotational states ($J \leq 211$). Spectroscopic constants for these states were calculated and compared to those of previous investigations. Along with these spectroscopic studies, experimental Franck-Condon factors were observed for $0 \leq v' \leq 5$. These values were compared to Franck-Condon factors calculated from an RKR fitted potential. The second phase involved state-to-state vibrational energy transfer within the low lying vibrational manifold ($1 \leq v' \leq 4$) of the Bi_2 A-state using steady-state spectrally resolved laser induced fluorescence. Vibrational energy transfer rates were determined from this data for rare gas collision partners using rate matrix techniques. These results were compared to both previous studies done on the halogens and interhalogens and also to the SSH theory. The third and last phase of the research used the same techniques as used in the second phase, albeit with greater resolution on the resolved fluorescence, to study state-to-state rotational energy transfer within the Bi_2 A-state. Rotational transfer rates were determined after pumping $J' = 201$ for collisions with He, Ne, and Ar and for pumping $J' = 171$ and 231 for collisions with He. These transfer rates were fit to the statistical power gap law.

1.4 Organization

Chapter II will first present a review of molecular theory as it pertains to bismuth, followed by a synopsis of laser induced fluorescence techniques and kinetic energy transfer theory as it applies to both vibrational and rotational energy transfer. Chapter III will discuss the experiment and results of the spectroscopic study of the Bi_2 A-X system as well as the results of the experimentally determined Franck-Condon factors. Chapter IV will discuss the same topics for the vibrational energy transfer study while Chapter V will discuss rotational energy transfer. Chapter VI will present the overall conclusions of this research as well as discuss future research possibilities on the Bi_2 A state.

II. Background Theory

This chapter reviews current spectroscopic and kinetic theories relevant to this research on molecular bismuth (Bi_2). A summary of the various types of data obtained will also be presented. Additional theories relevant to each phase of the data will be presented in the appropriate chapters.

2.1 Molecular Theory

2.1.1 Group V Diatomic Structure. Group V atoms have an outer shell electronic configuration of Znp^3 where $n = 2, 3, 4, 5$ and 6 for $Z = \text{N, P, As, Sb}$ and Bi . This configuration results in the spin-orbit split term symbols $^4S_{3/2}, ^2D_{3/2}, ^2D_{5/2}, ^2P_{1/2}$ and $^2P_{3/2}$, with the $^4S_{3/2}$ term having the lowest energy according to Hund's rules. One method for determining the molecular orbital configuration for Bi_2 is to describe the the orbitals as a linear combination of atomic orbitals. This is termed the "MO-LCAO" approximation (24). According to this approximation, two $^4S_{3/2}$ atoms combine to form σ_g, π_u, π_g and σ_u molecular orbitals. The molecular term symbols arise from the possible permutations of the six valence electrons within these four orbitals. The ground electronic state, shown graphically in Figure 2.1 occurs when the valence electrons occupy the six lowest energy positions within these orbitals. This state is denoted $(\sigma_g)^2 (\pi_u)^4 (\pi_g)^0 (\sigma_u)^0$ or 2400. As with all diatomics with outer shells consisting of only closed orbitals, the ground state of Bi_2 is designated $X^1\Sigma_g^+$. Excited electronic configurations arise from the promotion of one or more electrons to a higher lying level, such as 2310, 2220 or 2301.

2.1.2 Hund's Cases. Hund has investigated several limiting cases of angular momentum coupling, known as Hund's cases (a)–(e), and found them to adequately describe the majority of molecules (24, 25). Cases (a) and (c) apply to the Group V diatomics. In Hund's case (a), it is assumed the interaction between the nuclear rotation and the electronic motion is very weak. Furthermore, the electronic mo-

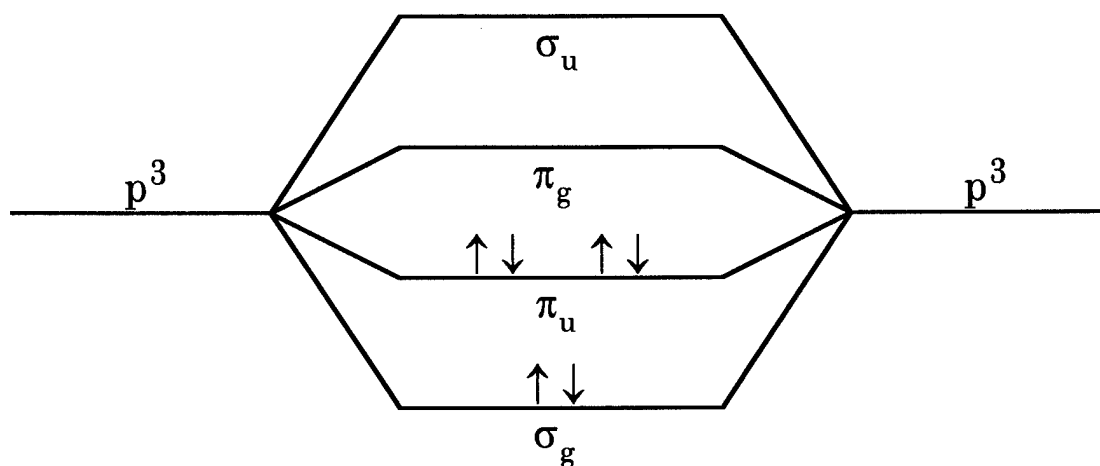


Figure 2.1 Ground state Group V diatomic electronic configuration

tion is coupled very strongly to the internuclear axis. The projection of the angular momentum, L , on the internuclear axis is designated Λ and the projection of the electronic spin, S , is designated Σ . These two values combine to give the electronic angular momentum, $\Omega = \Lambda + \Sigma$. The molecular angular rotation N , which is perpendicular to the internuclear axis is then coupled to Ω to give the total angular momentum of the molecule, $J = \Omega + N$, where $N = 0, 1, 2 \dots$. This coupling case yields the molecular term symbols $^1\Sigma_g^+$ for the 2400 configuration, $^{1,3}\Delta_u$ and $^{1,3}\Sigma_u$ for 2310, $^{1,3}\Pi_g$ for 2301 and $^{1,3,5}(\Gamma, \Delta, \Sigma)_g$ for the 2220 configuration. For the 2310 case, the weak spin-orbit interaction then splits the $^3\Delta$ state into $^3\Delta(3)$, $^3\Delta(2)$ and $^3\Delta(1)$ states according to the total electronic angular momentum Ω . The $^3\Sigma$ state is split into $^3\Sigma^+$ and $^3\Sigma^-$ states because of reflection symmetry with each of these states being split into (1) and (0) states due to the total electronic angular momentum. Finally, the $^1\Sigma$ state is split into (+/-) components. Thus, the 2310 configuration gives 10 separate spin-orbit split states. By similar arguments, the 2301 and 2220 states will give large numbers of spin-orbit split states.

For heavy diatomic molecules, Hund's case (c) has been found to be a more suitable approximation. In this scheme, the spin-orbit coupling is so strong that Λ and Σ are not defined. Instead, L and S couple to form J_a , the total electronic angular momentum. J_a couples to the internuclear axis giving a resultant projection Ω . The electronic angular momentum and the nuclear angular momentum, N , then combine to give the total angular momentum J . This type of coupling results in a manifold of levels appearing as several distinct electronic states, rather than as a splitting of rotational levels in a single state and is commonly referred to as jj-coupling (24). According to Mulliken, the addition of two $^4S_{3/2}$ states yield $(3u, 2u, 2g, 1u, 1g, 1u, 0g^+, 0u^-, 0g^+, 0u^-)$ states, while a $^4S_{3/2}$ and a $^2D_{3/2}$ yield $(3u, 3g, 2u, 2u, 2g, 2g, 1u, 1u, 1g, 1g, 0g^+, 0u^+, 0g^-, 0u^-)$ (26). A summary of the states and the correlation between case(a) and case (c) coupling as they apply to Bi_2 is presented in Figure 2.2.

These coupling cases are idealized examples that provide adequate descriptions for most diatomic molecules. In reality, no molecule is either purely case (a) or (c). Molecules merely tend to exhibit more of one character than the other.

Through theoretical and experimental work, Bi_2 is found to exhibit behavior more indicative of case (c). The second column on the left of Figure 2.2 shows the relative theoretical energy separation of the different jj-coupled states, with the next column spaced according to the observed value of T_e for each particular state as reported by Das, et al. (27). The close agreement between theoretical predictions assuming jj-coupling and observed experimental data is readily apparent. The case (a) coupled electronic states on the right side of Figure 2.2 are depicted according to the ordering of energy levels as predicted by Hund (24), although the relative energy spacings are not to scale. The multiple crossings of symmetry needed to correlate case (a) electronic states with the experimentally observed ordering of those states indicates case (a) coupling is not an accurate representation of the energy levels of

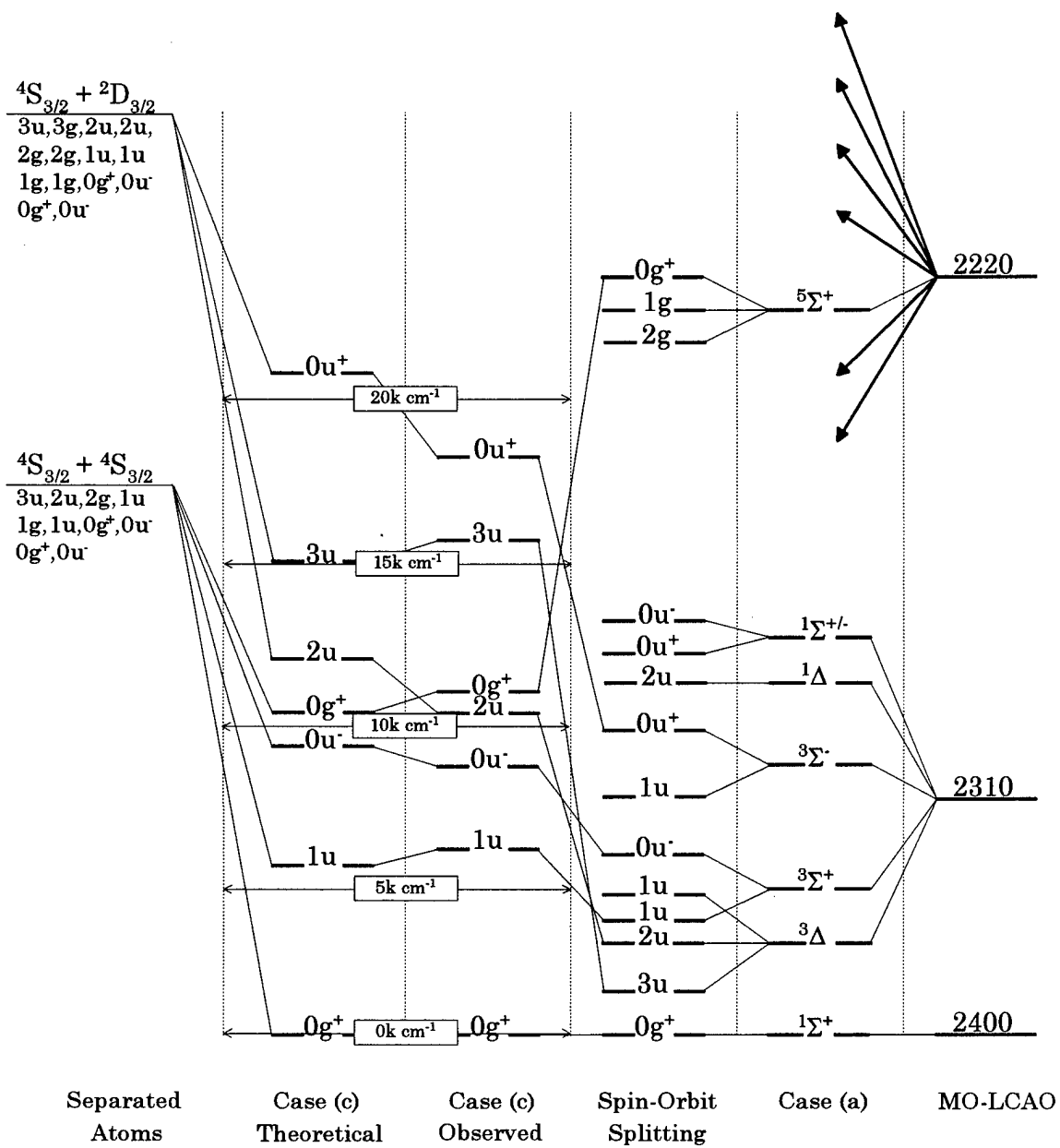


Figure 2.2 Hund's case correlation diagram for Bi_2

Bi₂. This correlation between the case (a) and case (c) schemes is reflective of the theoretical calculations made by Das (27).

As stated previously, the actual coupling of the angular momentum appears to exhibit a tendency towards case (c) coupling. Lifetime data illustrates this effect. According to case (c) coupling, this transition is A(0_u⁺)→X(0_g⁺). This transition is strongly allowed by electric dipole electronic selection rules. However, in case (a) coupling, this transition is A(3⁻Σ_u⁻)→X(1⁺Σ_g⁺), a forbidden transition due to the change in multiplicity. Results of lifetime studies on the A-state reported values between 50–600 ns (23). These lifetimes are indicative of strongly allowed transitions. The 600 ns lifetime is for the *v*' = 1 level. The reduced lifetimes of the higher vibrational levels is apparently due to predissociation.

2.1.3 Spectroscopy of Bi₂. In diatomic molecules, the energy of any specific rovibrational energy level is defined by the equation

$$E(v, J) = T_e + G_v + F_v(J) \quad (2.1)$$

where T_e is the electronic energy of the state of interest, $G(v)$ is the vibrational energy and $F_v(J)$ is the rotational energy. The vibrational energy can be expressed as

$$G(v) = \omega_e(v + 1/2) - \omega_e\chi_e(v + 1/2)^2 + \omega_e y_e(v + 1/2)^3 + \dots \quad (2.2)$$

where v is the vibrational quantum number, ω_e is the vibrational energy of a harmonic oscillator, $\omega_e\chi_e$ is the anharmonicity factor and any higher order terms are further corrections for the anharmonic nature of the potential energy curve. The rotational energy can be expanded as

$$F_v(J) = B_v J(J + 1) - D_v J^2(J + 1)^2 + \dots \quad (2.3)$$

where J is the rotational quantum number, B_v is the rotational energy of a rigid rotor and D_v is a centrifugal distortion correction due to the vibrational nature of the rotor. The v subscripts on the rotational terms indicates there is a vibration level dependence. B_v can be further expanded as

$$B_v = B_e - \alpha_e(v + 1/2) + \dots \quad (2.4)$$

and D_v can be expressed as

$$D_v = D_e + \beta_e(v + 1/2) + \dots \quad (2.5)$$

The first reported analysis of the X→A transition was the absorption measurements made by Almy and Sparks in 1933 (28). In their work, they reported spectroscopic constants for $v'' \leq 55$ in the ground state and $v' \leq 59$ in the A state. They were unable to perform any rotational analysis on the system due to lack of resolution. Further vibrational studies of this system were not accomplished until the laser photoluminescence work of Gerber, et al. in 1975 (29, 30). They reported improved vibrational constants for both the ground and A states of Bi₂, however, their work falls short of observing all bound vibrational levels in either state. This work attempted to fit spectroscopic constants by fitting Franck-Condon factors to spectrally resolved emissions out of $v' = 17 - 20$. They did not report either their numerically or experimentally derived Franck-Condon factors. The most extensive set of constants reported for the Bi₂ ground state comes from the work of Effantin, et al. (19). In this LIF study, Effantin observed the ground state vibrational levels $0 \leq v'' \leq 105$ after excitation with different lines off argon and krypton lasers. The Dunham coefficients he reported were derived mainly from low resolution spectroscopy done on the B'(0_g⁺) → X(0_g⁺) transition. These constants are reported in Table 2.1. A drawback to these constants stems from the low resolution of the data from which they were derived. In addition to these molecular constants, Effantin

Table 2.1 Spectroscopic constants for the X(0_g⁺) and A(0_u⁺) states of Bi₂

	X(0 _g ⁺) (19)	A(0 _u ⁺) (20, 21)
T_e	0.0	17740.7 ± 0.1
ω_e	173.0625 ± 0.0091	132.4030 ± 0.015
$\omega_e \chi_e$	0.37589 ± 0.00096	0.31227 ± 0.001
$\omega_e y_e$	$-(8.11 \pm 0.47) \times 10^{-04}$	$-(1.8 \pm 0.2) \times 10^{-04}$
$\omega_e z_{e1}$	$(1.61 \pm 0.12) \times 10^{-05}$	$(2.3 \pm 0.2) \times 10^{-06}$
$\omega_e z_{e2}$	$-(5.07 \pm 0.17) \times 10^{-07}$	
$\omega_e z_{e3}$	$(5.42 \pm 0.11) \times 10^{-09}$	
$\omega_e z_{e4}$	$-(1.83 \pm 0.33) \times 10^{-11}$	
B_e	$(2.2802 \pm 0.004) \times 10^{-03}$	$(1.9739 \pm 0.004) \times 10^{-03}$
α_e	$(4.160 \pm 0.1) \times 10^{-05}$	$(5.34 \pm 0.01) \times 10^{-05}$
γ_e	$-(4.2 \pm 0.3) \times 10^{-07}$	$-(1.55 \pm 0.4) \times 10^{-07}$
D_e	$(1.68 \pm 0.15) \times 10^{-09}$	$(1.77 \pm ?) \times 10^{-09}$
β_e	$(1.06 \pm 0.45) \times 10^{-11}$	$(8.9 \pm 0.4) \times 10^{-12}$

also reported vibrational and rotational term values for the levels $7 \leq v'' \leq 45$ derived from grating spectrograph measurements done on A→X transitions. He made no effort to individually fit this data to a Dunham expansion but did state that this data was incorporated into his other, more global fit. Curiously, even though this work involved the A state, Effantin did not report any A state terms or constants. Furthermore, he never reported the range of J values observed. These issues will be revisited when comparing Effantin's results with the spectroscopy performed in this research. Still, this study represents the best currently available data on the X state of Bi₂.

The most extensive work on the A state comes from two different sources. The first of these was the polarization labeling spectroscopy performed by Ehret and Gerber (20). They selectively excited $0 \leq v' \leq 57$ and derived very accurate vibrational constants for the Bi₂ A state. These constants, along with those reported in the work by Effantin, adequately describe the vibrational spectrum of the A-X band system and are listed in Table 2.1. The only reported A state rotational

constants come from laser excitation spectroscopy performed by Gerber, et al. (21). This work is ambiguous to the range of J values observed as the journal article specifically states that the research was limited to $J < 65$, but also states that D_v terms were determined from $J \leq 270$. This analysis was supposedly discussed in another journal article that was "to be published." Extensive literature searches have been unable to locate this data. Additionally, for the A-X transition, this rotational study is the most internally consistent set of reported constants in that it is the only rotational study to list both upper and lower state rotational constants. These A-state rotational constants are reported in Table 2.1.

Figure 2.3 presents a graphical representation of the Bi_2 X and A electronic states. This plot was derived from RKR turning points calculated from the spectroscopic constants presented in Table 2.1. A few features of these potential curves are worth noting. The potential well of the A-state displays very little anharmonic behavior. This is an important feature when considering selection rules for energy transfer events within this electronic state. The near coincidence of the internuclear separation for the zero-point energy of each curve shows that transitions out of the lowest v'' levels will have large Franck-Condon factors for transitions to low-lying v' levels. Finally, the numbered vibrational levels on each potential curve attest to both the small vibrational spacing present in Bi_2 and the very strongly bound nature of the system.

2.2 Laser Induced Fluorescence

Laser induced fluorescence (LIF) is a technique where a very narrow linewidth laser source is used to selectively excite, or "pump", a specific quantum level in a species being studied. For diatomic molecules, the narrow pulsed or CW laser source allows the pumping of a specific quantum state v', J' . Collisional energy transfer either with self or buffer gases can then redistribute the initial parent population among other quantum states such as $J'+1$ and $J'-1$ or $v'+1$ and $v'-1$. This manifold

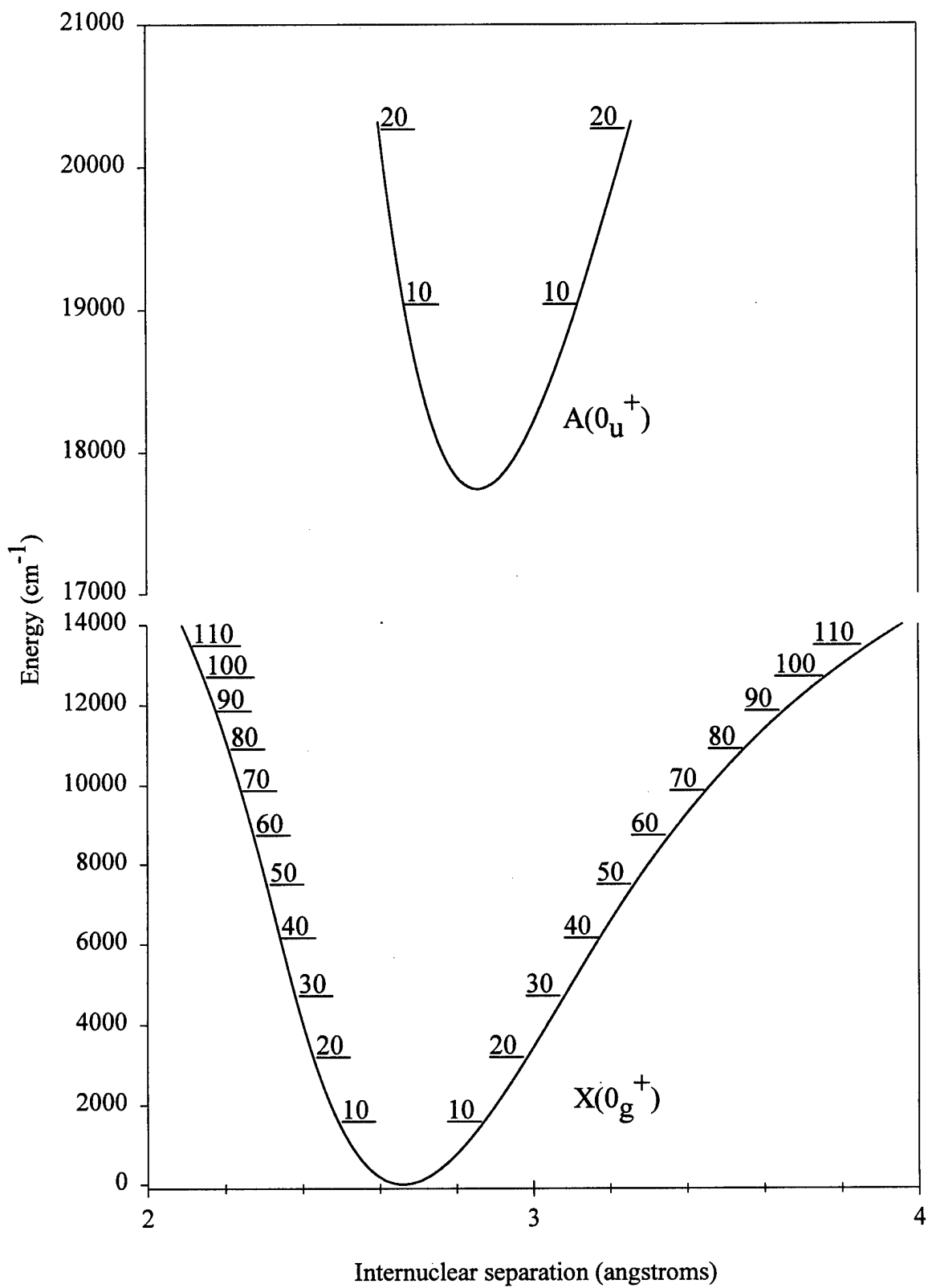


Figure 2.3 Bi_2 potential energy curves derived from reported spectroscopic constants

of levels can then relax back to the ground state due to collisional, collisionless and radiative processes, the last of these at wavelengths characteristic of the specific excited molecular quantum state (7). Figure 2.4 gives a simplified representation of this process where the initially pumped state is v' and the collisionally populated states are $v' + 1$ and $v' - 1$. Note that the satellite states typically have lower fluorescence intensity than the parent state.

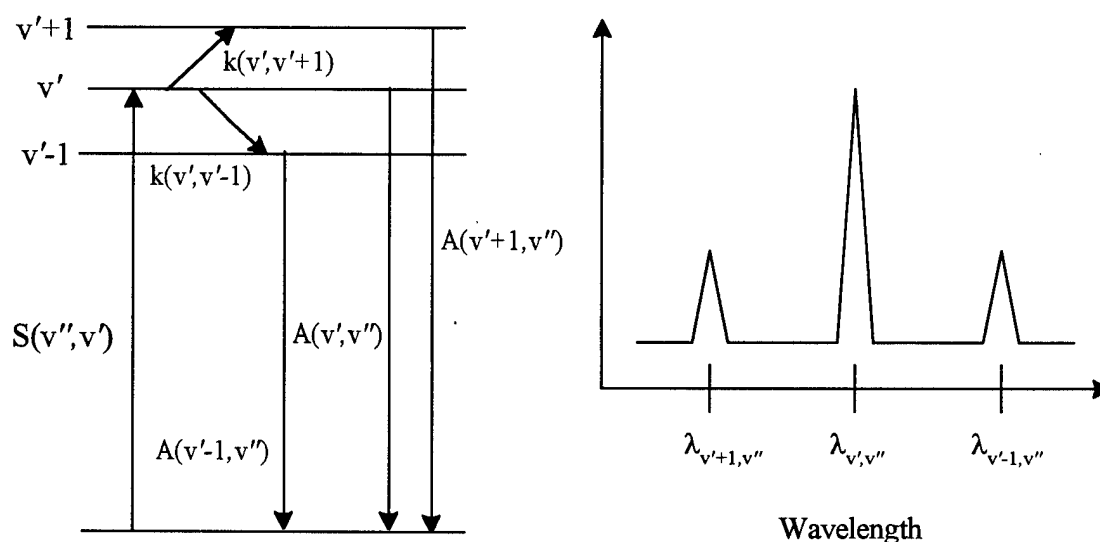


Figure 2.4 Simplified representation of laser induced fluorescence from collisionally populated satellite states

The fluorescence intensity of a given transition is directly proportional to the number density of the excited state, N_v (7),

$$I_f = \sum_{v,w} I_{vw}^{obs} = \sum_{vw} (64\pi^4/3) c \nu_{vw}^4 q_{vw} |R_e|^2 (S_J/(2J+1)) D(\nu_{vw}) N_v \quad (2.6)$$

where

I_{vw}^{obs} = observed emission intensity from state v to state w

ν_{vw} = transition frequency from state v to state w

$q_{vw} = |\langle v|w \rangle|^2 =$ Franck-Condon factor for states v, w

$|R_e| =$ electric dipole moment

$S_J =$ rotational linestrength factor

$D(\nu_{vw}) =$ detection system wavelength dependence.

This equation shows the fluorescence intensity to be directly proportional to the number density in the excited state. Continuous wave LIF experiments generate time-independent excited state populations. Collisional energy transfer rates between parent and satellite states can be derived from relative intensity measurements. Pulsed LIF, because of its ability to generate pure excited rovibrational levels on the order of 5-10 nsec, allow the temporal evolution of states to be monitored. This is done through the monitoring of either unresolved or spectrally resolved emissions.

The fluorescence intensity of a single rovibrational transition is also directly proportional to the Franck-Condon factor of that transition. Simply put, the Franck-Condon factor is the squared overlap integral of the vibrational wavefunctions of the two states involved in the transition being observed. There are several ways to go about determining the value of this parameter. If the potential curve of the electronic states are known, the wavefunctions associated with the upper and lower state can be computed. Once the wavefunctions are known, their overlap can be calculated numerically. Obviously, this method is only as accurate as the knowledge of the potential curves. In the absence of being able to accurately compute these parameters, they can also be determined experimentally. This is possible because of the normalization:

$$\sum_w q_{vw} = 1 \quad (2.7)$$

where v is the initial state and w is the final state. Note that this relation is a summation over all final states w originating from the same initial state v . As can be seen from Equation 2.6, if the detector response function is properly characterized,

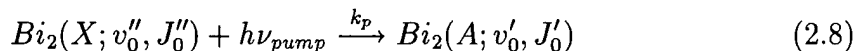
a comparison of relative intensities of all transitions originating from the same initial state allows the determination of absolute Franck-Condon factors.

2.3 Kinetic Theory

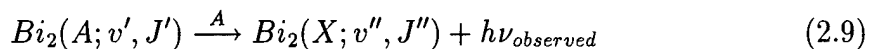
A major goal of the current work is to experimentally investigate collisional energy processes within the low lying vibrational levels ($0 \leq v' \leq 4$) of the $\text{Bi}_2 \text{ A}(0_u^+)$ electronic state using CW LIF techniques. The energy transfer processes involved included state-to-state vibrational transfer among low v' levels and state-to-state rotational transfer among high J' levels. To properly interpret the results of the LIF experiments, a thorough understanding of the relevant kinetic processes that affect observable quantities within the system is needed. The following section will discuss the radiative, collisionless and collisional energy transfer processes as they pertain to the $\text{Bi}_2 \text{ A}(0_u^+)$ state. The time independent master rate equation (MRE) that describes both vibrational and rotational energy transfer will be discussed as well as the development of a rate matrix to be used in extracting data as necessary.

2.3.1 Energy Transfer Processes. This section describes the fundamental energy transfer processes that take place in the A state of diatomic bismuth. They can be described mathematically as follows:

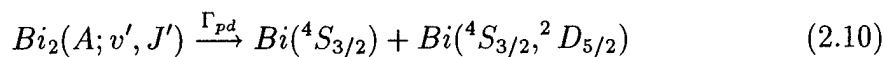
Optical excitation;



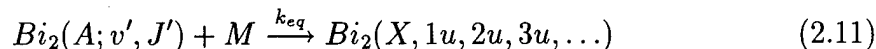
Spontaneous emission;



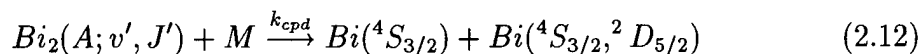
Spontaneous predissociation;



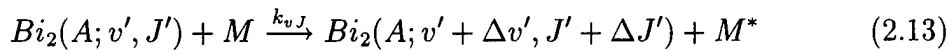
Electronic quenching;



Collisional predissociation;



Rovibrational transfer (V,R→T);



In the above equations, "M" denotes an atomic or molecular collision partner while "M*" denotes an electronically, vibrationally, rotationally or translationally excited collision partner.

Optical excitation, Equation 2.8, is a mechanism which couples the incident laser photon energy to the $Bi_2(X)$ molecules, thereby perturbing the system. The specific $Bi_2(A; v'_0, J'_0)$ state initially populated is referred to as the parent state. The pump rate k_p is given by the expression

$$k_p = (B_{01} I_0 / c) \int_0^\infty a(\nu) g_p(\nu) d\nu \quad (2.14)$$

where

B_{01} = Einstein coefficient for stimulated emission

I_0 = incident pump laser intensity

c = speed of light

$a(\nu)$ = absorption transition lineshape function

$g_p(\nu)$ = pump laser lineshape function

To insure selective pumping of a single rovibrational level, the pump laser linewidth, $\Delta\nu_p$, must be smaller than the spacing between successive rovibrational transitions. Ideally, the laser linewidth needs to be smaller than the absorption transition laser linewidth, $\Delta\nu_a$. If this is the case, the only problem with selectively pumping a single rovibrational level occurs when multiple rotational transitions overlap each other. For Bi_2 , this could happen in two ways. First, the large mass of Bi_2 results in a relatively small rotational spacing. Thus, many rotational levels overlap near the vibrational bandhead. Second, the extremely dense spectrum of Bi_2 often produces overlap of rotational transitions involving different vibrational bands.

Spontaneous emission, Equation 2.9, accounts for the radiative decay from the excited level. These transitions can be to any lower state level. The radiative lifetime from some specific v', J' is proportional to the sum of the Einstein A coefficients from v' to all v'' . It can be expressed as

$$1/\tau_r = \sum_{v'', J''} A(v', J' \rightarrow v'', J'') \quad (2.15)$$

The spontaneous emission rate from a state is directly proportional to the population in that state. This fact allows the use of optical means to monitor the populations of both parent and satellite levels.

In spontaneous predissociation, Equation 2.10, a non-radiative process results in the loss of an excited state molecule without the benefit of an emitted photon. This process occurs due to the overlapping of a bound electronic state with the dissociation continuum belonging to another electronic state (25). The transition takes place without any appreciable alteration of the particle's position or momentum. The end result is a subsequent shortening of the excited state lifetime. As was pointed out

earlier, predissociation appears to play a major role in the A state lifetimes of Bi_2 above $v' \approx 23$ (22, 23). Predissociation appears to dominate over rotational transfer for $v' \geq 26$ (23).

Collisional predissociation and electronic quenching are collisional processes that reduce excited state populations without the emission of a photon from the electronic transition of interest. Pure electronic quenching transfers population directly from $\text{Bi}_2(\text{A})$ to a lower Bi_2 electronic state, $\text{Bi}_2(\text{X}, 1\text{u}, 2\text{u}, 3\text{u}, \dots)$. Collisional predissociation occurs in two ways. In the first, the collision event directly causes the dissociation of the molecule. In the second, population is collisionally transferred to a repulsive state. Since spontaneous predissociation does not occur until $v' \geq 23$ in the Bi_2 A state, its effects should play no role in this study as energy transfer is only being examined for the low-lying vibrational levels ($v' \leq 4$) of the A state. Both of these collisional processes, electronic quenching and collisional predissociation, can be linked together to give a total quenching rate defined by

$$k_q = k_{eq} + k_{cpd} \quad (2.16)$$

which can depend on v' and J' . Clearly, this quenching rate also depends on the collision partner present. No electronic quenching rates have been reported for Bi_2 collisions with any collision partners.

Rovibrational energy transfer is accounted for by Equation 2.13. This is a collisional process that causes a redistribution of the A-state population. Vibrational energy transfer (V-T) occurs whenever $\Delta v \neq 0$, irregardless of any change in J . This change in v can be positive or negative. Pure rotational transfer (R-T) occurs whenever $\Delta v = 0$ and $\Delta J \neq 0$. For molecular buffer gases, vibrational (V-V) energy transfer to the buffer gas is also possible. Thus, the total, nonquenching energy transfer rate out of a specific (v, J) level is proportional to the population in that level and must include all vibrational and rotational transfer rates for all

available collision partners. If multiple collision conditions exist, the possibility of repopulation of the initial (v, J) level must be considered.

In this study, rovibrational energy transfer occurs because the excited electronic state is produced in a highly non-Boltzmann, or non-thermal, population distribution. Rovibrational transfer is the processes that “thermalizes” the distribution within the excited state. This energy transfer rate can take the form of either vibration to translational (V-T) or rotation to translational (R-T) energy transfer to any buffer gas. If a molecular buffer gas is used, the possibility of vibration to vibration (V-V) transfer exists. For ease of notation, the rovibrational energy transfer rate coefficient will be written as k_{vJ} .

2.3.2 Master Rate Equation. Using the terms from the previous section, a master rate equation (MRE) describing the time evolution of a specific (v, J) level can be written as

$$\begin{aligned}
 dN(A; v, J)/dt = & \\
 & S\delta_{vv_0}\delta_{JJ_0} - \Gamma_0(v, J)N(A; v, J) \\
 & - \sum_M k_q^M(v, J)MN(A; v, J), \\
 & - \sum_M \sum_{\Delta v} \sum_{\Delta J} k_{vJ}^M(v \rightarrow v + \Delta v, J \rightarrow J + \Delta J)MN(A; v, J) \\
 & + \sum_M \sum_{\Delta v} \sum_{\Delta J} k_{vJ}^M(v + \Delta v \rightarrow v, J + \Delta J \rightarrow J)MN(A; v + \Delta v, J + \Delta J)
 \end{aligned} \tag{2.17}$$

where $N(A; v, J)$ is the population in the rovibrational level of interest and the terms on the right hand side denote optical pumping, collisionless removal, total quenching, collisional removal and multi-collision repopulation of the observed state. The term k_v^M is the rovibrational energy transfer rate coefficient for collisions with buffer gas M . The summation over M in Equation 2.17 allows for energy transfer collisions with multiple buffer gas species. The last term in Equation 2.17 allows for the repopulation of the initial state through collisional energy transfer. This

equation can be written more concisely using the notation from Perram (9) with the following definitions:

$p = (A; v, J)$, label for the observed rovibrational level

$p_0 = (A; v_0, J_0)$, label for the parent rovibrational level

$q = (v + \Delta v, J + \Delta J)$, label for the indexed rovibrational level

$w_{pq} = \sum_M k_{vJ}^M(q \rightarrow p)M$, the collisional transfer rate constant

$R_{pq} = w_{pq} - \delta_{pq}(\sum_l w_{lp} + \Gamma_0(p) + \sum_M k_q^M(p)M)$, the energy transfer rate matrix.

δ_{pq} = Kronecker delta function.

Applying these definitions to Equation 2.17, the MRE can be written in tensor notation as

$$dN_p/dt = S\delta_{pp_0} + R_{pq}N_q \quad (2.18)$$

where repeated indices denote a summation. In this form, the state-to-state transfer rates are the off-diagonal elements of the rate matrix. In order to determine these rates, solutions to the MRE must be developed. As pointed out by Holmberg (7), a strongly coupled n -level system may have as many as $n^2 - n$ allowed transitions but only n observable states. Numerical methods can be used to solve for the elements of the transition matrix, R_{pq} , by simultaneously fitting n spectrally resolved emission traces. The problem arises in that these calculations are computationally laborious, and there is no guarantee of uniqueness of fit. To solve this dilemma, reasonable approximations to these parameters are developed.

2.3.3 Time-Independent Solution. Two simplifying conditions can be forced on the MRE to ease the task of finding the state-to-state transfer rates. The first simplification is to make the partial pressure of the Bi_2 small in comparison to the total cell pressure when observing the spectrally resolved emissions. This ensures that virtually all collisions involving Bi_2 take place between a bismuth molecule and a buffer gas collision partner. Second, only one buffer gas will be allowed in the cell

at any given time. These two preconditions effectively remove the summation over M in Equation 2.17.

Vibrational energy transfer can be treated separately from rotational energy transfer with the following simplification

$$k_v(v \rightarrow v + \Delta v) = \sum_{\Delta J} k_{vJ}(v \rightarrow v + \Delta v, J \rightarrow J + \Delta J) \quad (2.19)$$

which simply states that vibrational energy transfer rates equal the sum of all rovibrational transfer rates that have the appropriate change in v regardless of the change in J . With this approximation, the population in a satellite vibrational level can be expressed as

$$\begin{aligned} dN(v')/dt = & k_v(v'_0 \rightarrow v')[M]N(v'_0) \\ & -(\Gamma(v') + K_v(v')[M])N(v') \\ & + \sum_i k_v(v'_i \rightarrow v')[M]N(v'_i) \end{aligned} \quad (2.20)$$

where $K_v(v')$ is the summation of all energy transfer rates from v' to any other level. The observed satellite state v' is principally populated by single collisions from the initially populated state v'_0 . The first term in Equation 2.21 represents this process. The second term represents removal processes from the observed state while the summation accounts for the possibility of multiple collisions that populate the observed state. In steady state, this equation can be rearranged to yield

$$\frac{N(v')}{N(v'_0)} = \quad (2.21)$$

$$\frac{k_v(v'_0 \rightarrow v')[M]/\Gamma(v')}{1 + K_v(v')[M]/\Gamma(v') - \sum_i k_v(v'_i \rightarrow v')\{N(v'_i)/N(v')\}[M]/\Gamma(v')}$$

where the third term in the denominator again accounts for multiple collisions. At higher pressures, the observed vibrational state can be populated by vibrational

transfer from levels other than the parent state. These processes are accounted for by the summation. However, at low pressures where secondary collisions are not significant, the summation is small compared to the first two terms. Assuming that this term is linearly proportional to $[M]$, then Equation 2.21 can be simplified to the nonlinear form

$$\frac{N(v')}{N(v'_0)} = \frac{a[M]}{1 + b[M]} \quad (2.22)$$

where $[M]$ is the bath gas pressure, $b[M]$ accounts for various secondary collisions and $a[M]$ accounts for direct transfer into the observed vibrational level from the parent state. Population ratios can be plotted versus bath gas pressure. A least-squares fit to the data using Equation 2.22 will provide values for a and b . From a , the desired vibrational rate constant can be found through the expression

$$k_v(v'_0 \rightarrow v') = a\Gamma(v')p \quad (2.23)$$

where p is a constant required to convert units of pressure to population density ($p = 2.8289 \times 10^{-17}$ cm³-torr/molec). As pointed out by Massman (31), this equation is valid only if the summation in Equation 2.21 is independent of bath gas pressure. If it is not, and if the summation has a quadratic dependence on bath gas pressure, the nonlinear equation would be

$$\frac{N(v')}{N(v'_0)} = \frac{a[M]}{1 + b[M] + c[M]^2} \quad (2.24)$$

This same course of analysis can be followed for the case of rotational transfer by substituting J for v in Equation 2.21. This result stems from limiting the summations over Δv in Equation 2.17 to the specific case of $\Delta v = 0$.

2.3.4 Energy Transfer Rates.

2.3.4.1 *Vibrational Energy Transfer.* Holmberg noted that Br₂(B) ($\omega_e/kT \approx 0.6$) exhibited very limited amounts of multi-quantum vibrational transfer during collisions with rare gas collision partners (12). Most of the population he observed in states with $|\Delta v > 1|$ was due to multiple collisions with the buffer gas. This is equivalent to saying the summation in the denominator of Equation 2.21 has become large with respect to the other terms in the denominator. Thus, the approximations leading to Equation 2.21 have broken down. This necessitates the use of the rate matrix shown in Equation 2.18 to properly define the vibrational transfer rates. The rate matrix contains $n^2 - n$ independent elements for a system with only n observable states. Previous vibrational transfer studies have shown that the number of independent elements in the rate matrix can be greatly reduced by assuming certain relationships between the various vibrational transfer rates (9, 32, 7). The foundation of these relationships lies in the development of the Landau-Teller (L-T) (33) and Schwartz, Slawsky and Herzfeld (SSH) (34) theories. These two theories are more fully developed in Appendix A. These assumptions appear to be fairly rigorous in their application and are summarized below.

1. Detailed balance is used for inverse transfer rates

$$k_v(v-1 \rightarrow v) = k_v(v \rightarrow v-1) \exp(-\Delta E_{v,v-1}/kT) \quad (2.25)$$

2. Landau-Teller scaling of V→T transfer rates applies

$$k_v(v \rightarrow v-1) = v k_v(1 \rightarrow 0) \quad (2.26)$$

3. Multi-quantum rates are a constant fraction of their parent $v' \rightarrow v' - 1$ rate

$$k_v(v \rightarrow v-2) = f k_v(v \rightarrow v-1) \quad (2.27)$$

4. Electronic quenching rates are independent of vibrational level

$$k_q = \text{constant} \quad (2.28)$$

5. Collisionless lifetimes are independent of vibrational level

$$\Gamma(v') = \text{constant} \quad (2.29)$$

In some instances, Equation 2.26 needs to be modified to include a power scaling of the vibrational quantum number used to define the $\Delta v = -1$ transfer rates:

$$k_v(v \rightarrow v - 1) = v^\eta k_v(1 \rightarrow 0) \quad (2.30)$$

where η is the scaling parameter of the vibrational quantum number.

2.3.4.2 Rotational Energy Transfer. Rotational energy transfer is typically more rapid than vibrational transfer and appreciable populations appear in satellite levels at relatively low pressures before secondary collisions become significant. This greatly simplifies the analysis of rotational energy transfer because the assumption that the summation in the denominator of Equation 2.21 is small compared to the rest of the denominator is usually valid (35). Thus, when solving for the rate constant from Equation 2.22, it is reasonable to assume the a coefficient is proportional to the direct transfer rate between the parent and satellite state. Fortunately, these transfer rates are not entirely independent of one another. In most cases, they can be related through a small number of empirically determined parameters with the help of scaling laws. These laws relate the rotational energy transfer probabilities on rotational quantum number J' . Two commonly used scaling laws are the exponential gap law (EGL) (36),

$$k_J(J'_0 \rightarrow J') = Af(J')\exp(-\chi|\Delta E/B_v|)\rho(\Delta E, T) \quad (2.31)$$

and the statistical gap law (SPG) (37, 38),

$$k_J(J'_0 \rightarrow J') = Bf(J')|\Delta E/B_v|^{-\gamma}\rho(\Delta E, T) \quad (2.32)$$

where $\rho(\Delta E, T)$ is the ratio of final to initial densities of translational states at temperature T and $f(J')$ is a statistical factor. ΔE is simply the difference in energy between the two rotational states. For Bi_2 , the change in rotational energy is small compared to the average translational energy, which implies $\rho(\Delta E, T) \sim 1$. If $M_{J'}$ is completely randomized in the collision, then $f(J') = 2J' + 1$. One of the goals of this research is to test the validity of these two models on Bi_2 .

III. Spectroscopy of High J levels in the $\text{Bi}_2 \text{X}(0_g^+) \rightarrow \text{A}(0_u^+)$

Transition

3.1 Introduction

The $\text{A} \rightarrow \text{X}$ electronic transition is the most studied spectroscopic system in the bismuth dimer. Spectroscopic constants for the vibrational levels in both the X and A states have been reported (19, 20, 21). Unfortunately, reported studies of the $\text{A} \rightarrow \text{X}$ system have not made any systematic attempts to characterize the behavior of the high J rotational levels. The few studies completed for high rotational levels merely report rotational constants on a level by level basis (39, 40). The only reported Dunham coefficients were calculated after observing rotational levels with $J \leq 65$ (21). Because of the large mass of the bismuth dimer, the rotational spacing, like the vibrational spacing, is small relative to most other diatomics. The rotational maximum in a thermal distribution of bismuth dimers at 300 K occurs near $J \approx 75$. Thus, there should be appreciable population of bismuth dimers in high J levels. The lack of reported data on these levels indicates the need for further studies.

This spectroscopic study was undertaken to determine whether or not previously reported spectroscopic constants accurately reflect the high rotational level behavior of the X and A states of Bi_2 . This information is crucial if one is to know which rovibrational level is being selectively excited in the energy transfer studies proposed. Laser excitation spectroscopy is used to selectively excite low-lying v' rotational manifolds of the $\text{Bi}_2 \text{A}(0_u^+)$ state from low-lying rovibrational levels of the $\text{Bi}_2 \text{X}(0_g^+)$ state. Rotational assignments have been made and spectroscopic constants have been calculated. These are compared with the reported data.

As an extension of the spectroscopic work, experimental measurements of A state Franck-Condon factors from $v' \leq 5$ were also accomplished. The need to gather this data comes about for several reasons. First, there are no Franck-Condon factors reported in the available literature. Gerber, et al. reported good experi-

mental agreement with Franck-Condon factors calculated from an RKR potential for $v' = 17, 19, 20, 21$ (29). However, he did not report the numerical values of these factors. More importantly, these factors numerically represent the transition probability between the upper and lower state involved in the transition. This is a critical piece of information if one is to accurately calculate population ratios from spectrally resolved fluorescence. Finally, the numerical calculation of Franck-Condon factors requires a detailed knowledge of the potential energy curves in the vicinity of the vibration levels of interest. Thus, agreement between experimental and theoretical Franck-Condon factors provides a robust check of the spectroscopic constants used to generate the potential energy curves.

3.2 Experimental Setup

A block diagram of the setup is shown in Figure 3.1. The fluorescence cell was a 6-way stainless steel cross, 3.8 cm diameter. Three of the horizontal arms of the cross were 20 cm long, as measured from the center of the cross with quartz windows mounted on their ends. The fourth arm had an additional 12.5 cm of length added to it in the form of a stainless steel "T". The bottom of this "T" was used to connect the test cell to a vacuum pump. The bottom arm of the cross was 16 cm tall and had a 4-wire copper feed-through, capable of loads up to 1000 amps per wire, located on its end. The top arm of the cross was similar to the 20 cm long horizontal arms with the only difference being that a stainless steel blank was located on its end instead of a quartz window. Two of the horizontal arms as well as the lower arm had 1 cm thick flanges installed between the arm and the endpiece. This flange had two radially drilled 1/8 in NPT holes in it. These ports allowed for the attachment of pressure sensors or the input of buffer gases. All flanges on the system consisted of conflat type fittings.

The cell was evacuated with a Varian Model 15 vacuum pump that was capable of an ultimate pressure of ≈ 5 mtorr. When very low pressures were necessary, as in

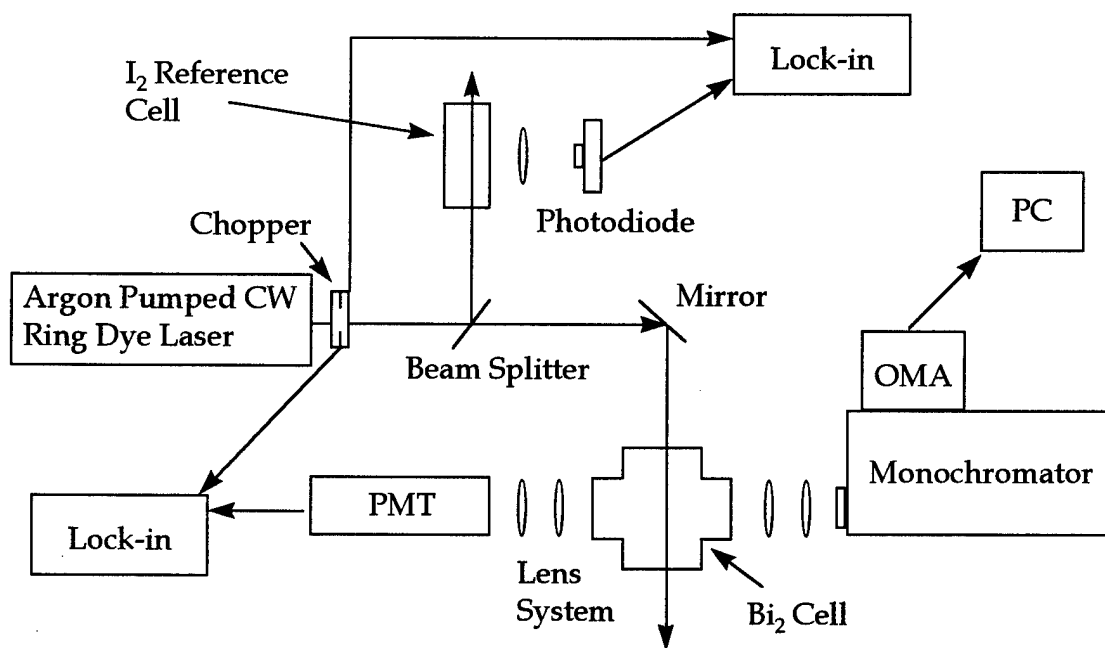


Figure 3.1 Block diagram of the experimental apparatus used to observe LIF in Bi_2

the calibration of the pressure sensors, A Varian model VH-4 diffusion pump with an attached liquid nitrogen trap was used when very low pressures were necessary, as in the calibration of the pressure sensors. This diffusion pump produced an ultimate pressure of ≈ 0.008 mtorr. Cell pressure was monitored on the horizontal axis of the cell with an MKS model 390-HA 10 Torr capacitance manometer and an MKS model 122A 100 Torr capacitance manometer. The cell leak rate was approximately 2-3 mtorr/hour in a static condition and 1-2 mtorr/minute when the cell was at operating temperature. This larger leak rate stems from the extreme heating of the lower flange on the 6-way cross.

Spectroscopic studies were conducted with approximately 1 Torr of nitrogen added to the cell. The buffer gas allowed larger concentrations of bismuth to be transported to the center of the 6-way cross. Gaseous bismuth was created by heating a small sample of granular bismuth (Mallinckrodt, 99.8%) above its vaporization point. Bismuth was baked in a 1 cm tall by 1 cm diameter aluminum oxide crucible.

This crucible was placed inside an appropriately sized tungsten basket whose ends were connected to two of the of the copper leads from the 4-wire feed-through. Power to the basket was supplied by a Lakeshore model 647 power supply. Typically, approximately 110 watts of power were supplied to the basket to create appreciable levels of Bi_2 . This large amount of power was necessary due to the thermal properties of metallic bismuth. Bismuth has a melting point of 544 K, and as can be seen in Figure 3.2, its vapor pressure does not reach 1 mtorr until a temperature of approximately 900 K is attained (16).

Laser excitation was provided by a Coherent model 899-29 Autoscan continuous wave ring dye laser pumped by a Spectra-Physics model 2080 Argon ion laser operating single wavelength at 514.5 nm. Rhodamine 590 Chloride dye (Exciton) was used to excite various Bi_2 (A) rovibrational levels. Continuous output power of the pump laser was 6.9 watts while the ring laser output power varied from 300 to 900 mwatts. The dye laser linewidth was < 100 MHz. The output of the dye laser was first directed through a chopper operating at 380 Hz and then a beam splitter before being directed down the longer horizontal axis of the test cell.

Side fluorescence emissions (LIF) were detected at a right angle to the laser excitation source through the quartz windows located along the shorter horizontal axis of the test cell. For the spectroscopic work, a two-lens system was used to collect the emissions from the Bi_2 sample. The first was a 2 inch diameter, 25 cm focal length lens placed approximately one focal length from the center of the fluorescence line. The second was a 2 inch diameter, 17.5 cm focal length lens that focused the collected light into the entrance aperture of an RCA C31034 Photomultiplier Tube (PMT). A variable diaphragm and a Corian 600 nm long pass interference filter was placed in between the last lens and the PMT. The filter and the diaphragm were used to minimize collection of scattered light into the PMT. The PMT output was directed into a Stanford Research model 850 lock-in amplifier that received its reference signal from the optical chopper. The integration time of the lock-in was 100 msec. A 386-

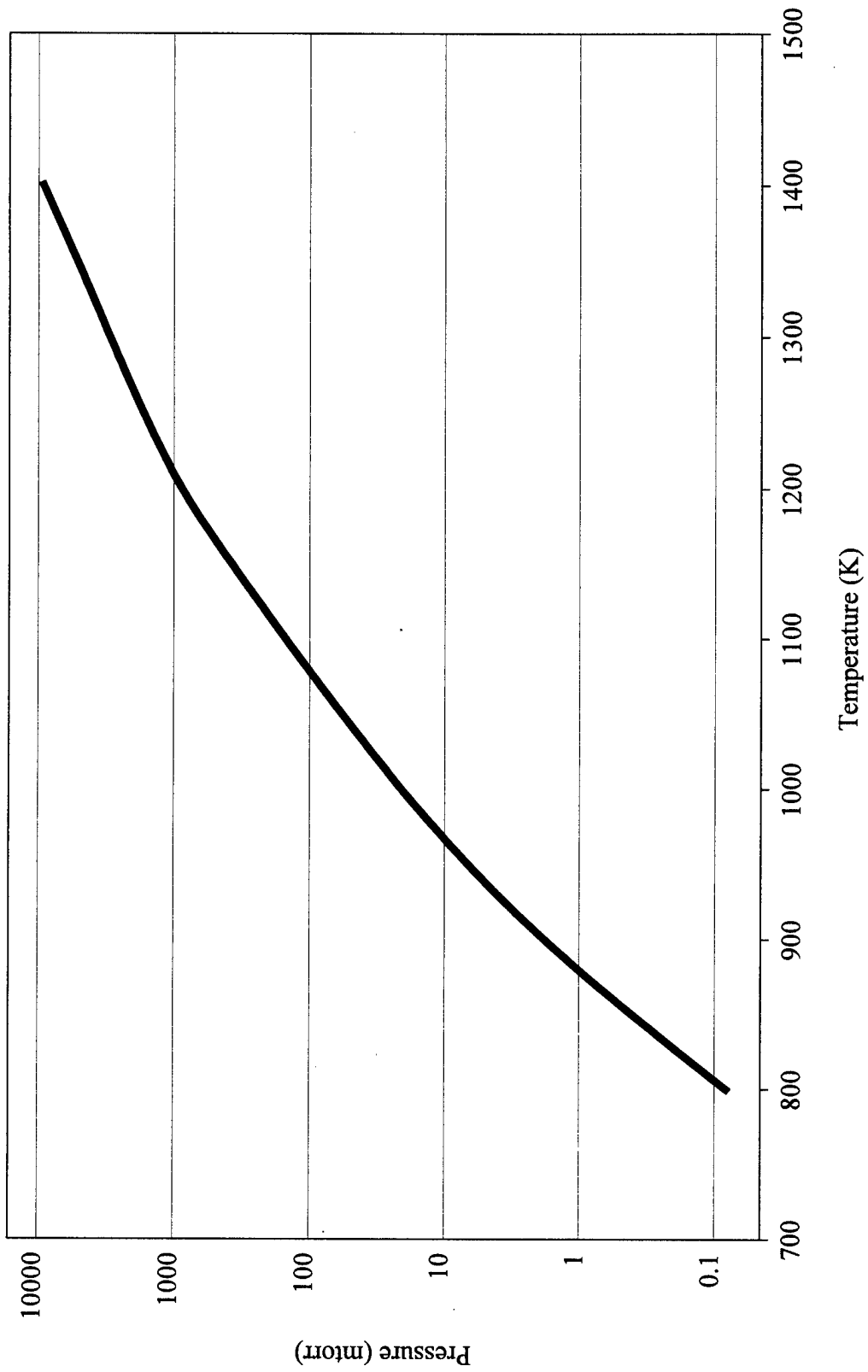


Figure 3.2 Plot of Bi₂ vapor pressure as a function of temperature.

based personal computer was then used to correlate the integrated signal from the lock-in amplifier with scan wavelength of the ring laser. The ring laser was set up to collect data over a 210 GHz scan range at a scan rate of 0.5 GHz/sec. Data was collected at 50 MHz intervals.

To verify the accuracy of the wavemeter on the ring laser, a beam was directed through a test cell containing a small sample of I_2 . The fluorescence line of this cell was focused onto a Hamamatsu type S2281 silicon photodiode with a 2 inch diameter 15 cm lens. From here, the output of the photodiode was treated identically to the output from the PMT except that it was read into a different channel on the Autoscan computer. This allowed the known line positions from the from the I_2 to be correlated with the observed lines from the Bi_2 .

3.3 Laser Excitation Spectra

Laser excitation spectra were gathered identically for all vibrational bands analyzed. The method will be briefly described here along with the methodology for assigning the spectrum described in the next section. After the crucible was allowed to heat to operating temperature, approximately 1 Torr of research grade nitrogen was added to the test chamber. A wavelength near the region of interest was tuned on the ring laser and the ring laser was scanned over a 30 GHz range. The output from the PMT was fed into the lock-in and the signal was analyzed after the scan was finished. The laser was tuned to the wavelength of the strongest feature in this spectrum and after this wavelength was established, the position of the PMT was optimized for data collection. From here, data collection was a simple matter of scanning the laser in the 210 GHz segments described in the previous section. Data was collected on the following bands: 2-2, 3-0, 3-1, 3-3, 3-4, 4-0, 4-1, 4-2, 5-1.

3.4 Experimental Results and Discussion

The excited rovibrational transitions are observed via detection of total fluorescence as the laser was scanned over a 210 GHz scan range. A scan depicting the P-R doublet structure of the $v'' = 4 \rightarrow v' = 0$ band is shown in Figure 3.3. This figure depicts a 3 cm^{-1} section of the collected 7 cm^{-1} spectrum. Successive scans were fitted to previous ones by overlapping at least three rotational features from the previous scan. The wavelength of individual rotational lines was assigned by overlaying a simultaneously collected I_2 spectrum on top of the bismuth spectrum. The wavelengths as read out by the ring laser system's wavemeter were compared to those of the iodine spectrum as listed in Gerstenkorn's iodine atlas after first converting the atlas readings from vacuum wavenumbers (41). The iodine wavenumbers were corrected for the 0.0056 cm^{-1} deviation that exists in their reported values (42). Any offset in the wavemeter readings was then corrected. Using these procedures, the absolute wavenumber position of the rotational lines is estimated at 0.007 cm^{-1} , the manufacturer's stated accuracy of the wavemeter.

As shown in Figure 3.4, direct assignment of the rotational lines in the vicinity of the bandhead is precluded due to the small rotational spacing relative to the doppler broadening of the transitions. However, at higher J , as seen in Figure 3.3, the P-R doublet structure that is characteristic of a homonuclear diatomic is readily apparent. This, along with the fact that there is only one abundant isotope of bismuth, makes the tracking of P-R progressions relatively simple.

3.4.1 Relative Rotational Numbering. Before proceeding with an explanation of how the relative rotational numbering was accomplished, an explanation of P and R lines is warranted. For the $\text{Bi}_2(\text{A-X})$ transitions, optical selection rules dictate that $\Delta J = \pm 1$ for the $\text{X} \rightarrow \text{A}$ electronic transition (25). A P line can be defined by the equation

$$P(J) = \nu_0 + F'_v(J - 1) - F''_v(J) \quad (3.1)$$

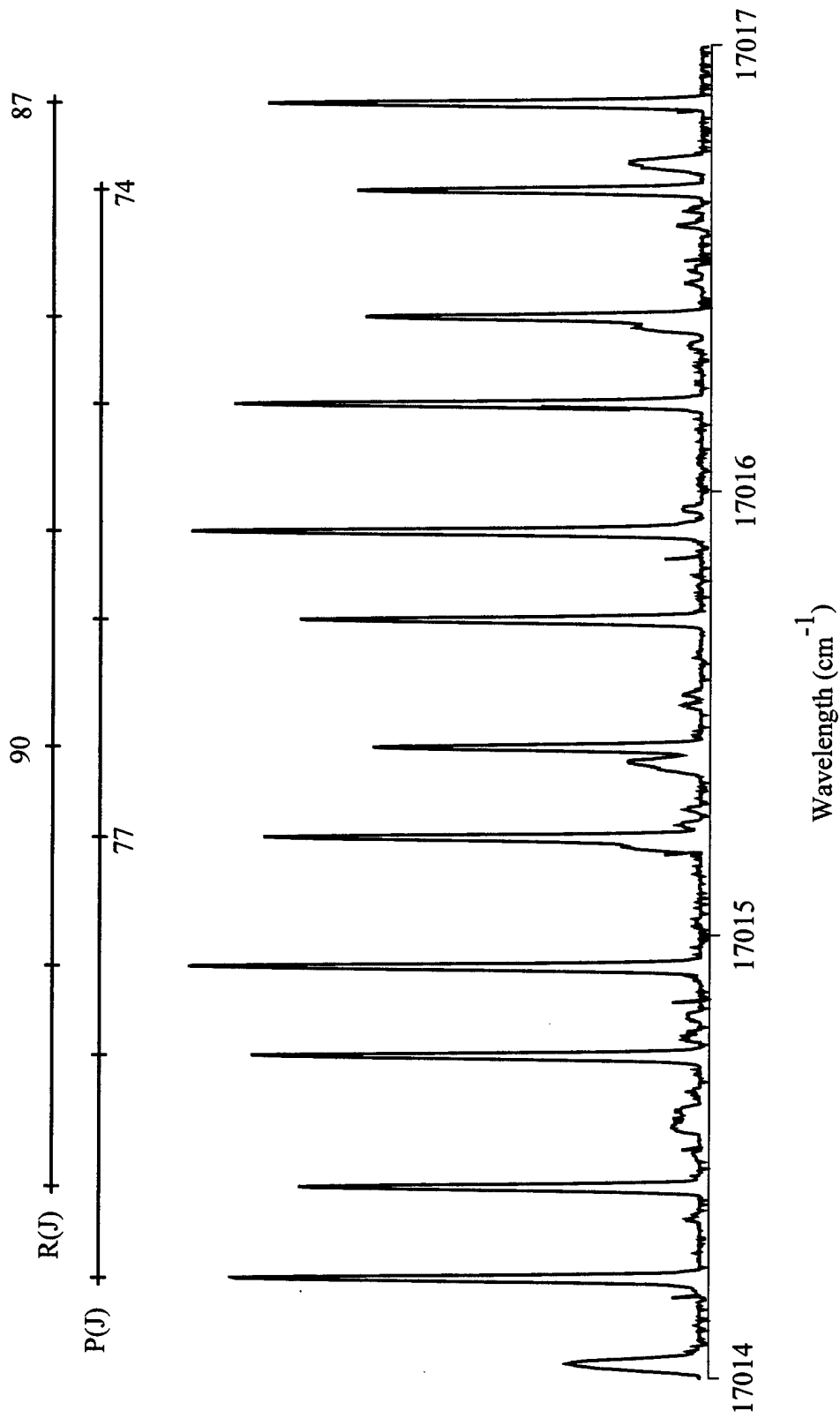


Figure 3.3 High resolution laser excitation spectra of $\text{Bi}_2(X \rightarrow A)$ showing a typical P-R doublet progression in the $v''=4$ to $v'=0$ vibrational band

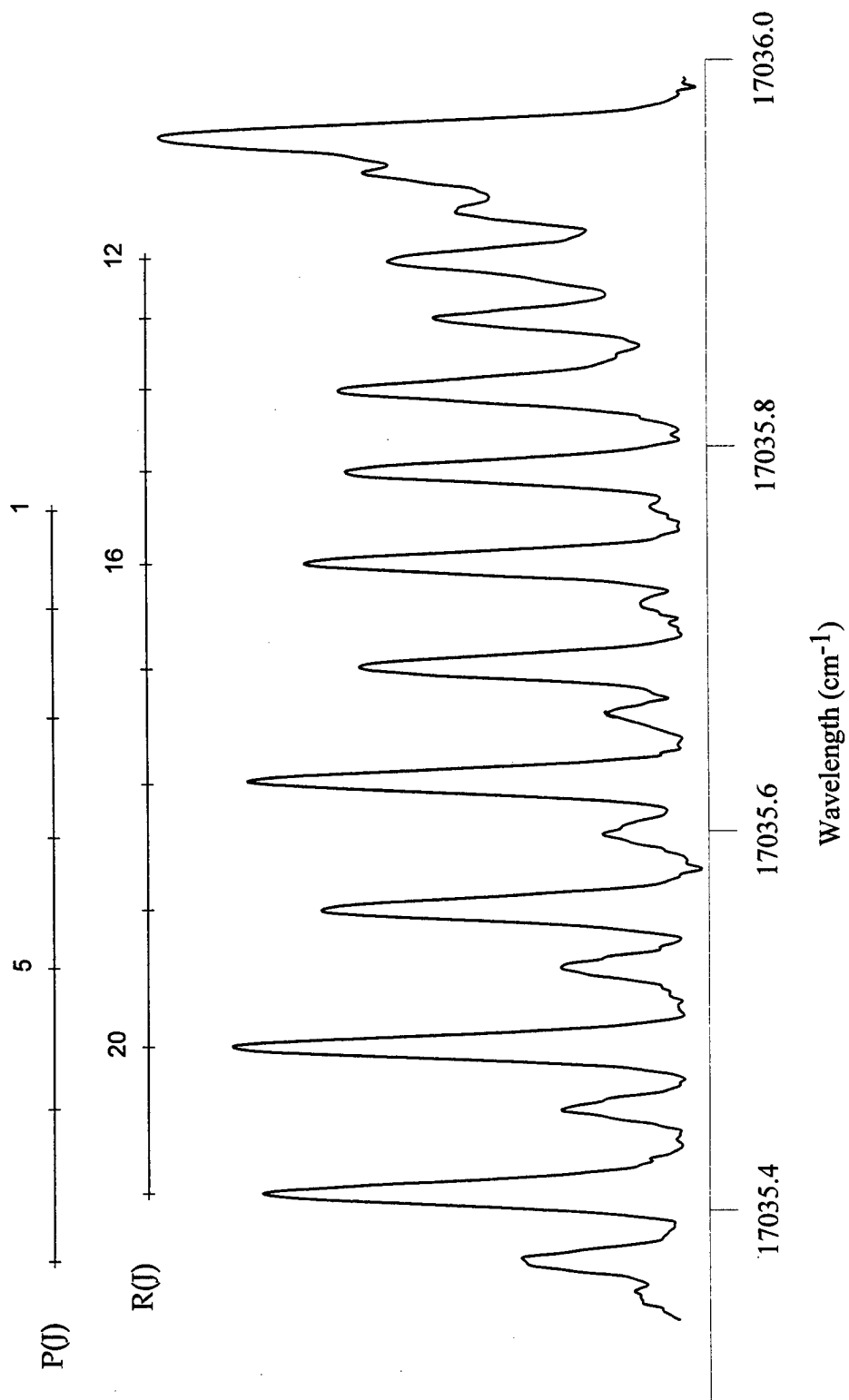


Figure 3.4 Doppler limited laser excitation spectrum of the $v'' = 4 \rightarrow v' = 0$ bandhead

where ν_0 is the vibrational band origin and $F_v(J)$ is the rotational energy of the either the upper or lower state. This equation shows that for a P line the rotational quantum number changes by $J' - J'' = -1$ and also that the transition is labeled by the rotational quantum number of the lower state. Similarly, an R line is defined by

$$R(J) = \nu_0 + F'_v(J + 1) - F''_v(J) \quad (3.2)$$

which expresses that the R line rotational quantum changes by $J' - J'' = +1$ with respect to the upper state.

For $\text{Bi}_2(\text{A-X})$ transitions, there is for every line in the P branch a corresponding line in the R branch with the same upper state. The wavenumber difference of these two lines is equal to the separation, $\Delta_2 F''(J)$, between alternating lower-state rotational levels (25). For example, the difference between $P(5)$ and $R(3)$ (both having $J = 4$ in the upper state) is equal to the separation of the rotation levels $J = 3$ and $J = 5$ in the lower state. Thus

$$R(J - 1) - P(J + 1) = F''_v(J + 1) - F''_v(J - 1) = \Delta_2 F''(J) \quad (3.3)$$

Similarly, the difference between the wavenumbers of two lines with a common lower state is equal to the separation of alternating upper state rotational levels (25):

$$R(J) - P(J) = F'_v(J + 1) - F'_v(J - 1) = \Delta_2 F'(J) \quad (3.4)$$

These last two equations show that either one of these combination differences can be expressed by the same relation, namely:

$$\Delta_2 F(J) = F_v(J + 1) - F_v(J - 1) \quad (3.5)$$

where v is either either the upper or lower state vibrational quantum number and $F_v(J)$ is the rotational energy associated with a specific rovibrational level defined

by the equation

$$F_v(J) = B_v J(J+1) - D_v J^2(J+1)^2 + \dots \quad (3.6)$$

Thus, the use of two different vibrational bands, with either the upper or lower level in common, should provide identical sets of differences, within some experimental error bound, when the correct relative numbering of the rotational levels is established within each particular band. This methodology was used on all vibrational bands observed and the relative numbering of the rotational levels was established. Figure 3.5 shows the residuals between second difference fits of the 4-0 and 4-1 bands once the correct relative numbering is established. Notice that the residuals are located within $\pm 0.007 \text{ cm}^{-1}$, the estimated accuracy of the rotational line measurements.

3.4.2 Absolute Rotational Numbering. Once the correct relative numbering has been determined, a different criteria can be used to establish the absolute numbering. The method employed in the last section is inadequate to provide this information since its validity is independent of the absolute numbering. However, if one is to take a closer look at the second difference equation, the issue of absolute numbering can be solved relatively easily. If the expressions for $F_v(J)$ are substituted into Equation 3.5, one obtains the expression

$$\Delta_2 F(J) = (4B_v - 6D_v)(J + \frac{1}{2}) - 8D_v(J + \frac{1}{2})^3 \quad (3.7)$$

By plotting $\Delta_2 F(J)$ against J , a curve is established. According to Equation 3.7, this curve should have a zero intercept at $J = -1/2$. If this is not the case, the correct absolute numbering can be found by shifting the abscissa until the correct intercept is established. Figure 3.6 depicts the second difference plot of the 4-0 band against the correct absolute numbering. Note that the plot does indeed have a zero intercept of $J = -1/2$. This methodology was employed on all vibrational bands observed to determine the correct rotational numbering. All bands achieved a zero intercept at $J = -0.5 \pm 0.1$.

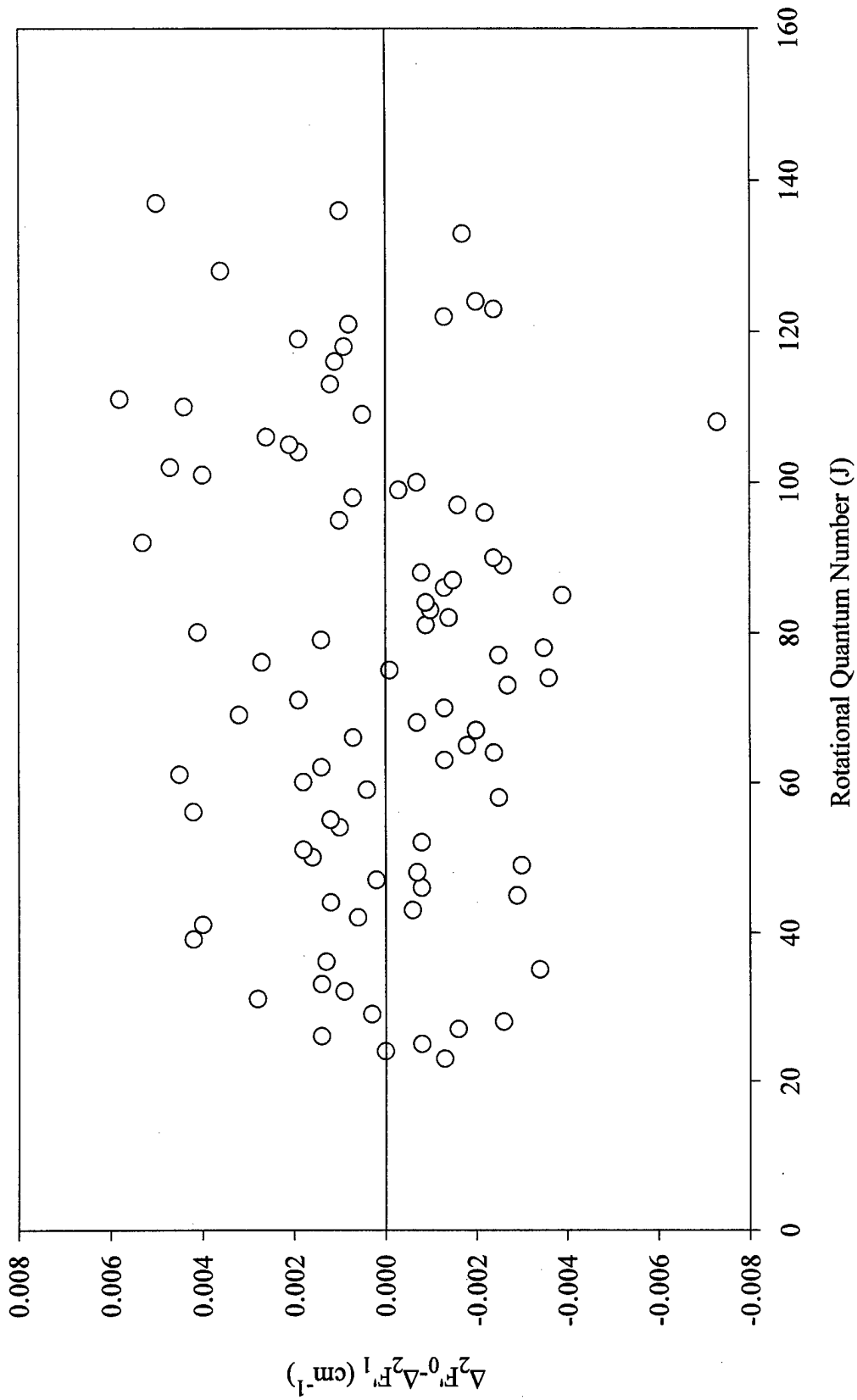


Figure 3.5 Residuals of the second difference fits of the $(v'', v') = (4, 0)$ and $(4, 1)$ bands of the $\text{Bi}_2(X \rightarrow A)$ laser excitation spectrum.

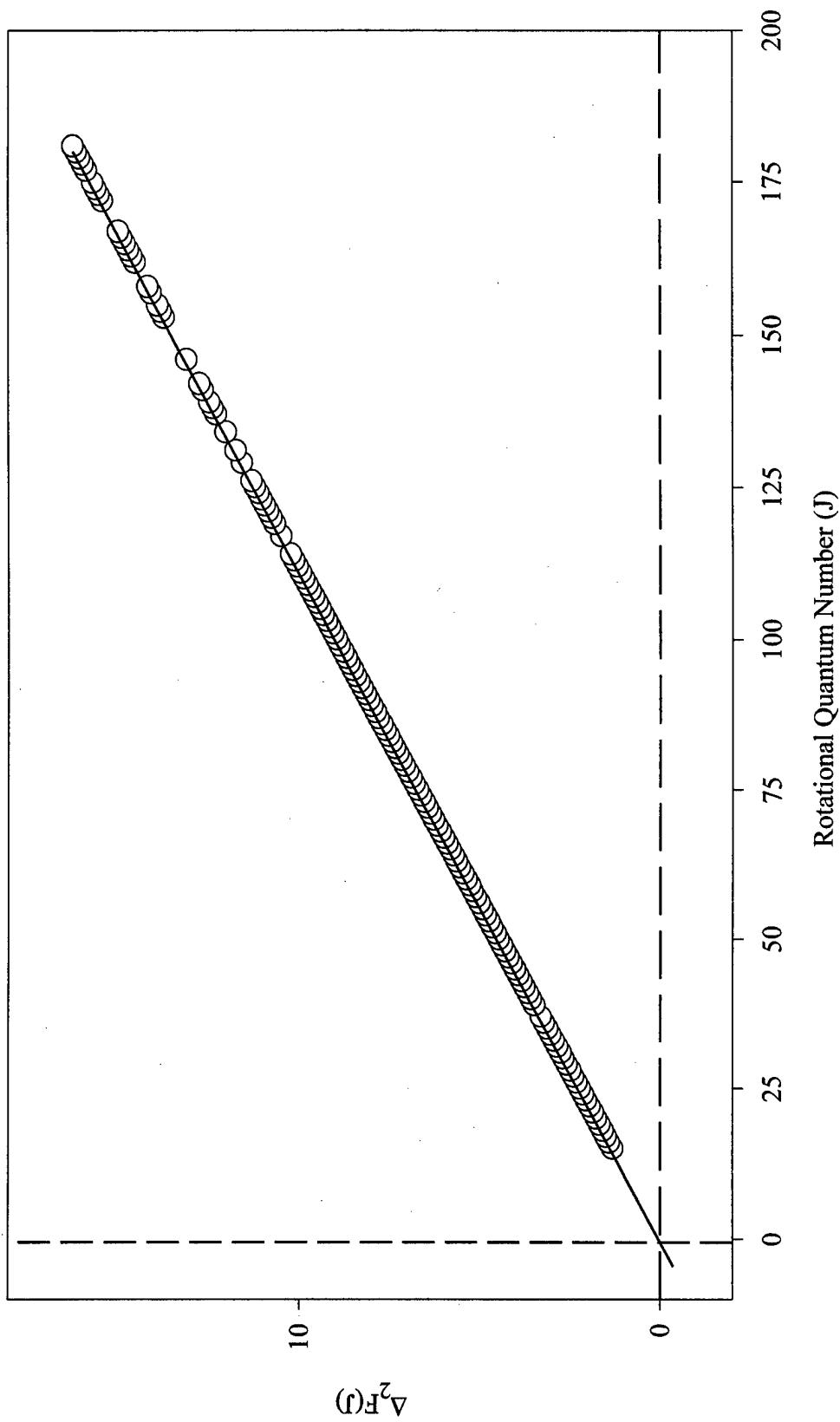


Figure 3.6 Plot of the second differences of the Bi_2 4-0 band versus rotational quantum number. The open circles are the data points and the solid line is the least-squares fit to a cubic polynomial in J . The dashed lines on the graph show that the zero intercept occurs at $J = -1/2$.

Table 3.1 Observed Bi₂ band origins for the X→ A Transitions

ν_0 Observed (cm ⁻¹)	ν_0 Predicted (19, 20) (cm ⁻¹)	Residual (cm ⁻¹)	Vibrational Assignment (v'', v')
17639.483	17639.460	0.023	(2,2)
17205.814	17205.742	0.059	(3,0)
17337.574	17337.521	0.053	(3,1)
17599.233	17599.199	0.034	(3,3)
17729.138	17729.097	0.041	(3,4)
17035.813	17035.722	0.091	(4,0)
17167.575	17167.501	0.074	(4,1)
17298.716	17298.654	0.062	(4,2)
16998.341	16998.252	0.089	(5,1)

3.4.3 *Determination of Molecular Constants.* With the absolute numbering of the vibrational bands established, attention is now focused on determining the spectroscopic constants. A single equation can be used to express all the rotational constants within a given vibrational band. This equation is

$$\begin{aligned} \nu = & \nu_0 + (B_{v'} + B_{v''})m + (B_{v'} - B_{v''} - D_{v'} + D_{v''})m^2 \\ & - 2(D_{v'} + D_{v''})m^3 - (D_{v'} - D_{v''})m^4 \end{aligned} \quad (3.8)$$

where ν_0 is the band origin ($J = 0$) and m is an integral number representing the rotational quantum number of the transition. For an R line, $m = J + 1$, and for a P line, $m = -J$. An example of this equation applied to the 3-3 band is shown in Figure 3.7. The major piece of information garnered from this fit is the values of the vibrational band origins which are listed in Table 3.1. For comparison purposes, band origin positions were calculated using the molecular constants reported by Effantin (19) and Gerber (20). Differences between the experimentally determined bandhead positions and the calculated values as well as the assignment of each bandhead are included in Table 3.7.

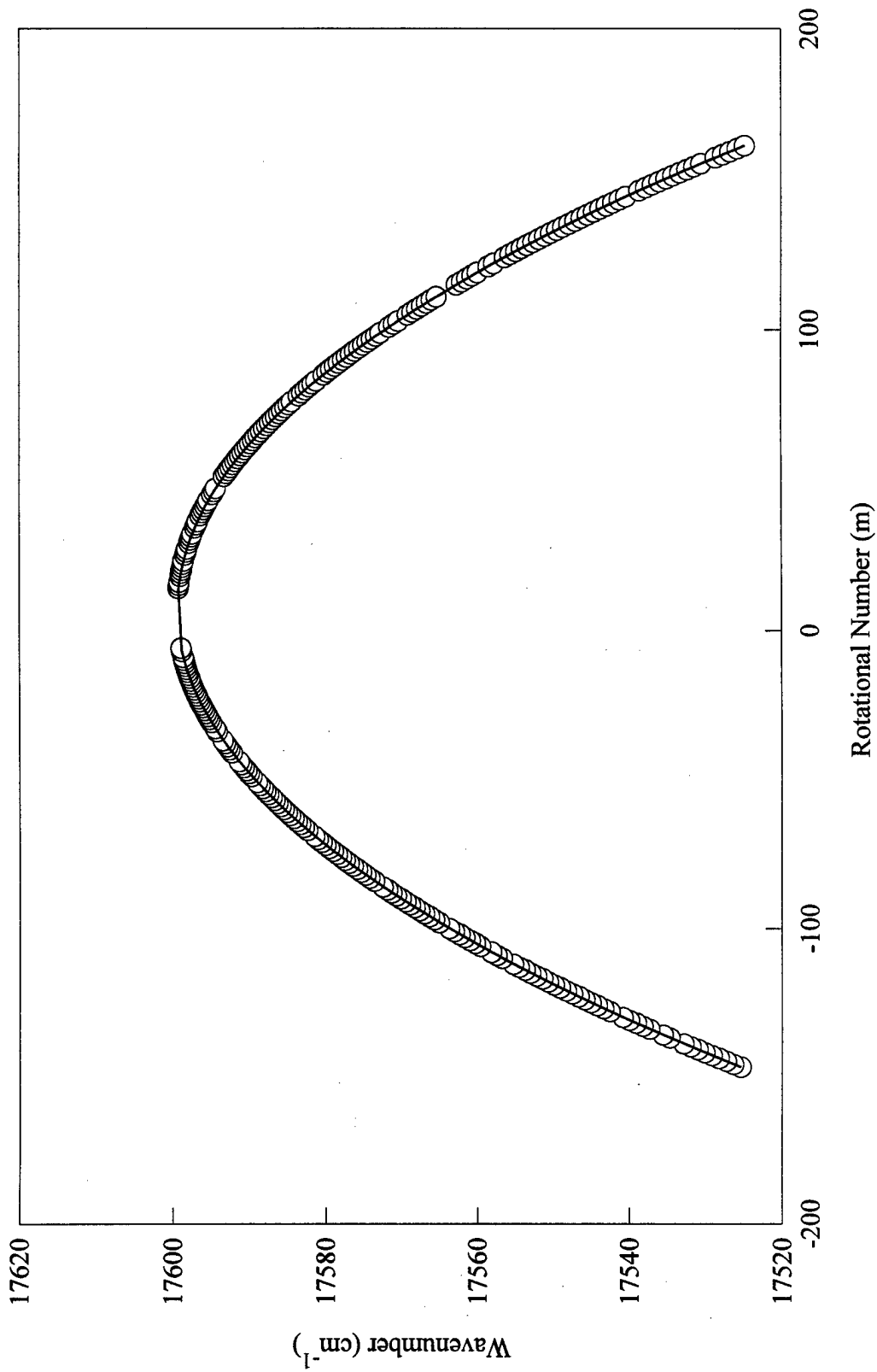


Figure 3.7 Direct fit of the the $\text{Bi}_2 \text{X} (v'' = 3) \rightarrow \text{A} (v' = 3)$ observed rotational line positions to a single equation in m .

Vibrational constants were calculated from the bandhead assignments in Table 3.1 using a non-linear least squares fitting routine implemented with Table-Curve 3-D software (Jandell Scientific). The fit equation, derived from the rotationless band origins, was

$$\Delta E_{vib} = T_e(A) + G_v(A) - G_v(X) \quad (3.9)$$

where the electronic energy of the ground state is assumed to be zero and G_v is the vibrational energy of the respective state. This equation can be expanded as

$$\begin{aligned} \Delta E_{vib} = & T_e + \omega'_e(v' + 1/2) - \omega_e \chi'_e(v' + 1/2)^2 \\ & - \omega''_e(v'' + 1/2) + \omega_e \chi''_e(v'' + 1/2)^2 \end{aligned} \quad (3.10)$$

where the specific term values are as defined in Chapter II. The standard deviation of this fit was 0.001 cm^{-1} and the vibrational constants derived are reported in Table 3.2 along with the ground state constants reported by Effantin (19) and the A state constants reported by Ehret (20). The vibrational constants reported in Table 3.2 contain enough digits to reproduce the band origins listed in Table 3.1. The reported errors are the fit standard error as generated by Table-Curve 3-D's nonlinear least-squares fitting algorithm.

Because of the large number of terms used in the two reported studies, it is difficult to make a comparison between the two different sets of data. The reason for the discrepancy in the number of terms stems from the amount of data analyzed. The Effantin study was an attempt to simultaneously fit X state energy levels of $0 \leq v'' \leq 105$ (19). Thus, it is reasonable that a large number of fit parameters might be necessary. However, this study was only able to define band origins to about $\pm 0.05 \text{ cm}^{-1}$. Over the range of vibrational levels studied in this experiment, $2 \leq v'' \leq 5$, the largest difference between this study's derived values of T_v and those predicted using Effantin's reported constants is 0.06 cm^{-1} .

Table 3.2 Vibrational constants for the X and A states of Bi₂ (cm⁻¹)

	Current Work	Literature
X(0g ⁺)		
ω_e	173.0697 ± 0.0059	173.0625 ± 0.0091
$\omega_e\chi_e$	0.38369 ± 0.00073	0.37589 ± 0.00096
$\omega_e y_e$		-(8.11 ± 0.47) × 10 ⁻⁰⁴
$\omega_e z_{e1}$		(1.61 ± 0.12) × 10 ⁻⁰⁵
$\omega_e z_{e2}$		-(5.07 ± 0.17) × 10 ⁻⁰⁷
$\omega_e z_{e3}$		(5.42 ± 0.11) × 10 ⁻⁰⁹
$\omega_e z_{e4}$		-(1.83 ± 0.33) × 10 ⁻¹¹
A(0u ⁺)		
T_e	17740.739 ± 0.012	17740.7 ± 0.1
ω_e	132.3807 ± 0.0019	132.4030 ± 0.015
$\omega_e\chi_e$	0.30997 ± 0.00038	0.31227 ± 0.001
$\omega_e y_e$		-(1.8 ± 0.2) × 10 ⁻⁰⁴
$\omega_e z_e$		(2.3 ± 0.2) × 10 ⁻⁰⁶

Similarly, the Gerber study observed A state vibrational energy levels of $0 \leq v' \leq 57$ with a resolution of 0.1 cm⁻¹. The largest difference in the predicted energy levels for the A state 0.02 cm⁻¹.

With the vibrational bandhead locations determined, attention is now shifted to the determination of the rotational parameters of the Dunham expansion. A FORTRAN program was written to accomplish a global least squares fit to all observed rotational transitions. The inputs to this program were the vibrational term values and the rotational line positions as well as their corresponding rotational numbering (J). The output of this program was the global least-squares fitted rotational term values associated with each vibrational level, both upper and lower, observed in this study. These rotational term values, along with the vibrational term values from Table 3.1 provide a standard deviation of 0.0068 cm⁻¹ for all observed rotational transitions. The rotational term values for the ground state are listed in Table 3.3 while the term values for the A state are listed in Table 3.4. As a reminder, these rotational terms are designated B_v , the rotational energy of a rigid rotor, and D_v , the centrifugal distortion correction to the rigid rotor. All terms in Tables 3.3 and

Table 3.3 Rotational term values for the observed Bi₂ X states (cm⁻¹)

v''	B_v''	$D_v'' \times 10^{-9}$
2	0.022674	1.610
3	0.022622	1.635
4	0.022569	1.659
5	0.022516	1.683

Table 3.4 Rotational term values for the observed Bi₂ A states (cm⁻¹)

v'	B_v'	$D_v' \times 10^{-9}$
0	0.019643	1.753
1	0.019592	1.761
2	0.019541	1.769
3	0.019489	1.776
4	0.019438	1.784

3.4 are given in terms of their full estimated accuracy. The FORTRAN computer program did not estimate error bounds. However, a global least-squares second difference fit using Equation 3.7 was accomplished for each upper and lower vibrational level using TableCurve. The reported term values in Tables 3.3 and 3.4 reflect the same number of significant digits as predicted from these global second difference fits.

The rotational terms values were then fit to the rotational Dunham expansion, namely

$$B_v = B_e - \alpha_e(v + \frac{1}{2}) + \dots \quad (3.11)$$

and

$$D_v = D_e + \beta_e(v + \frac{1}{2}) \dots \quad (3.12)$$

The rotational constants derived from these fits are listed in Table 3.5 and compared with previously reported constants (21). Error bounds are fit standard errors as calculated by TableCurve software. Ultimately, the goal is to come up with a set of terms that will accurately reproduce the observed data. Figure 3.8 focuses on the

Table 3.5 Rotational constants for the X and A states of Bi₂ derived from this work compared with previously reported values (cm⁻¹)

	Current Work	Literature (21)
X(0g ⁺)		
B_e''	$2.280605 \times 10^{-3} \pm 7.2 \times 10^{-7}$	$2.2802 \times 10^{-3} \pm 4.0 \times 10^{-6}$
α_e''	$(5.270 \pm 0.017) \times 10^{-05}$	$(4.160 \pm 0.1) \times 10^{-05}$
γ_e''		$-(4.2 \pm 0.3) \times 10^{-07}$
D_e''	$(1.550 \pm 0.009) \times 10^{-09}$	$(1.68 \pm 0.15) \times 10^{-09}$
β_e''	$(2.42 \pm 0.22) \times 10^{-11}$	$(1.06 \pm 0.45) \times 10^{-11}$
A(0u ⁺)		
B_e'	$1.966885 \times 10^{-3} \pm 2.9 \times 10^{-7}$	$1.9739 \times 10^{-3} \pm 4.0 \times 10^{-6}$
α_e'	$(5.130 \pm 0.01) \times 10^{-05}$	$(5.34 \pm 0.01) \times 10^{-05}$
γ_e'		$-(1.55 \pm 0.4) \times 10^{-07}$
D_e'	$(1.7489 \pm 0.004) \times 10^{-09}$	$(1.77 \pm ?) \times 10^{-09}$
β_e'	$(7.8 \pm 1.5) \times 10^{-12}$	$(8.9 \pm 0.4) \times 10^{-12}$

$v'' = 4 \rightarrow v' = 0$ vibrational band and compares this study's residuals ($\nu_{observed} - \nu_{predicted}$) with residuals derived from the spectroscopic constants reported in Table 3.5. Gerber's rotational constants were picked as a comparison for this data as they exhibited the smallest set of residuals for the observed transitions. As is readily apparent, previously reported constants are unable to accurately model the high rotational levels of the Bi₂ X→A transition. As a matter of fact, they do a poor job at even low rotational levels. Gerber reported the resolution of his rotational data as $< 0.001 \text{ cm}^{-1}$, so this poor performance is surprising. It needs to be noted that Gerber states his data was not consistent with high resolution spectroscopy of Bi₂(A-X) performed by Aslund (39).

The poor performance exhibited in Figure 3.8 stems from the inability of earlier work to adequately predict accurate rotational term values. This fact will become self evident in the next several paragraphs. Figure 3.9 is a plot of the X(0_g⁺) B_v terms determined in this research compared to the values for these terms predicted by Gerber's rotational constants (29). There is poor agreement for these two sets

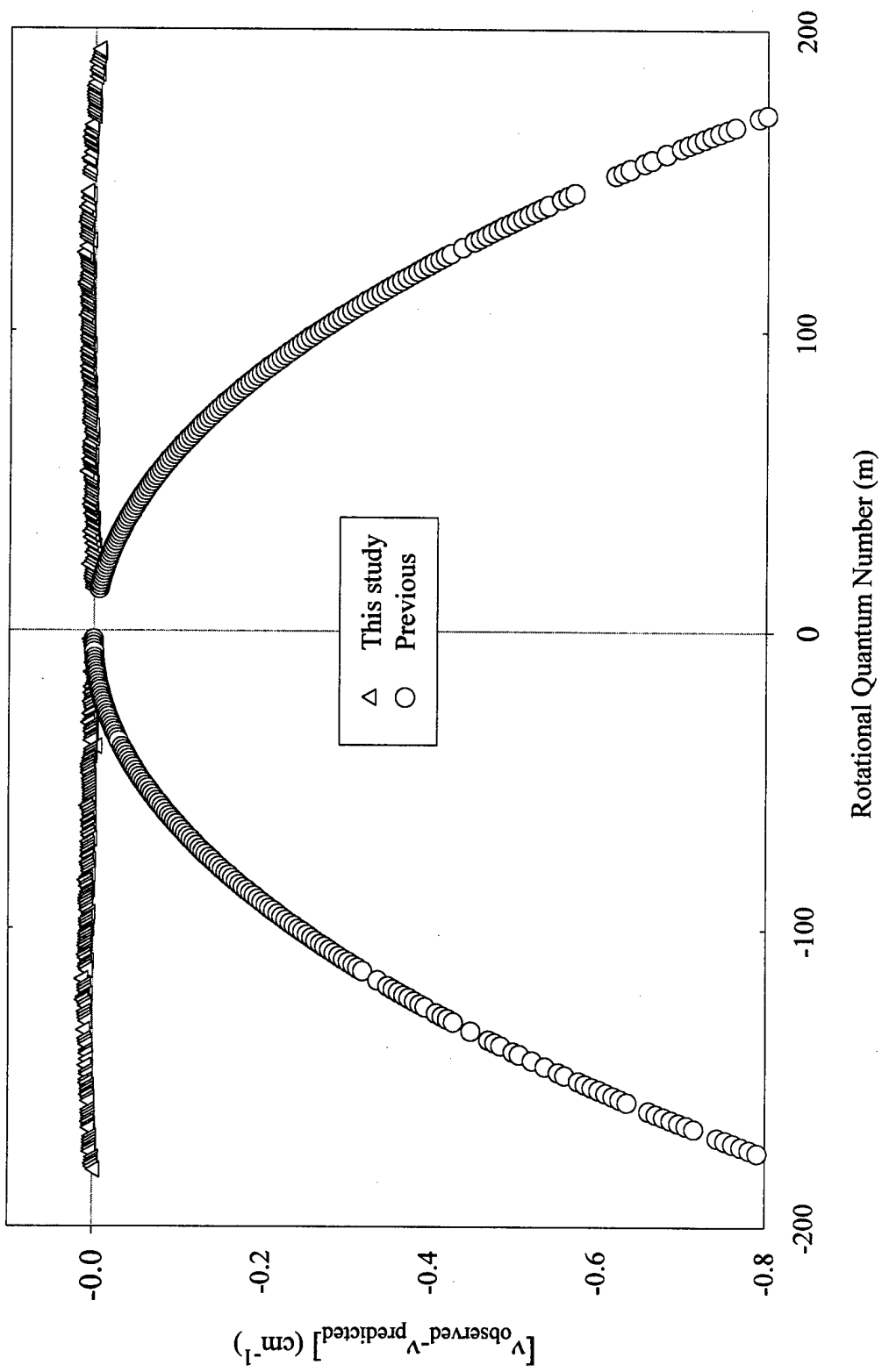


Figure 3.8 Residuals of the current and previous predicted values of the rotational line positions of the $v'' = 4 \rightarrow v' = 0$ vibrational band.

of data. In an effort to understand this difference, other rotational studies of the X state need to be examined. As was pointed out in Section 2.1.3, Effantin reported a set of rotational term values for the levels $7 \leq v'' \leq 45$ derived from A→X emissions. He also reported a set of rotational constants derived from an incorporation of this work and observed B' →X emissions. The actual term values derived in this second study are not reported. Other rotational term values for the X state are reported by Fabre ($v'' = 0$) and Aslund ($v'' = 5, 6$). The B_v'' term values reported in these three studies were merged with the values derived in this research, and a least-squares fit using the rotational Dunham equation (Equation 3.11) was accomplished. The result was a set of data easily represented by Equation 3.11 as is shown in Figure 3.10. Thus, it is reasonable to assume that the B_v'' values derived in this work accurately model the rotational behavior of low vibrational levels in the $\text{Bi}_2 \text{X}(0_g^+)$ state. To this end, an improved set of rotational constants for B_v'' is reported in Table 3.6. These constants were derived from the least squares fit to all reported B_v'' term values.

A similar picture emerges when the B_v' terms are examined. Figure 3.11 depicts values of B_v' predicted from Gerber's constants with terms derived from three different sources: 1) this work ($0 \leq v' \leq 4$); 2) Aslund ($v' = 8, 9, 11$) (39); 3) Fabre ($v' = 0, 1$) (40). Not surprisingly, Gerber's predictions are too large. This is due to his ground state value overpredicting the values for B_v'' which causes a need for additional offset in the B_v' term of the rotational expansion. The good agreement of term values reported from the other three sources indicates that the best set of rotational constants can be derived from using these three studies. The constants derived from a least-squares fit to these rotational term values are reported in Table 3.6. It needs to be pointed out Gerber did not report the term values he used in deriving his rotational constants.

In order to determine the best set of values for D_v'' , the values derived in this research were compared to the term values as reported by Effantin. This comparison is shown graphically in Figure 3.12. A least-squares fit to the entire data set did

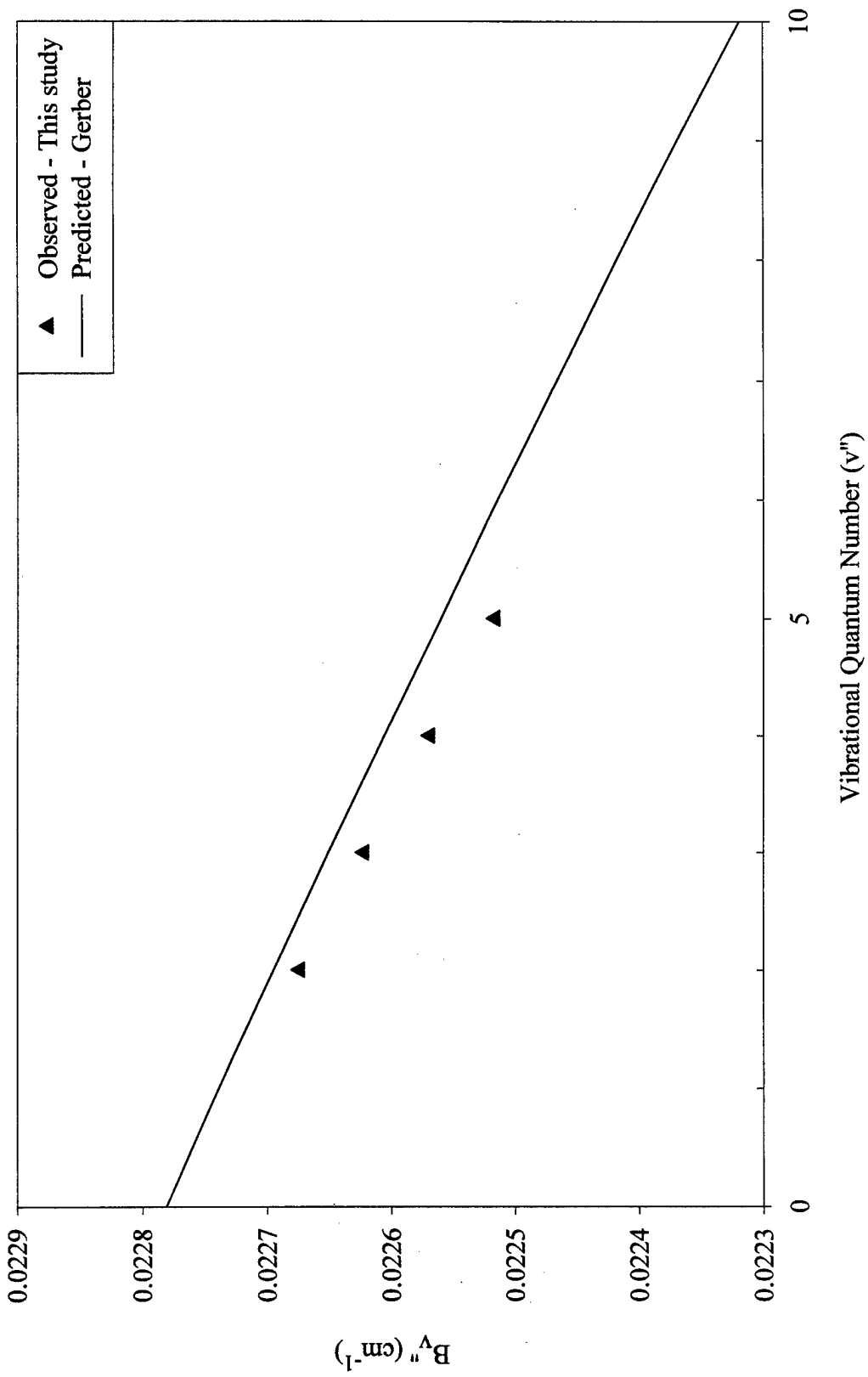


Figure 3.9 Comparison of Gerber's predicted Bv'' term values with those derived from this research

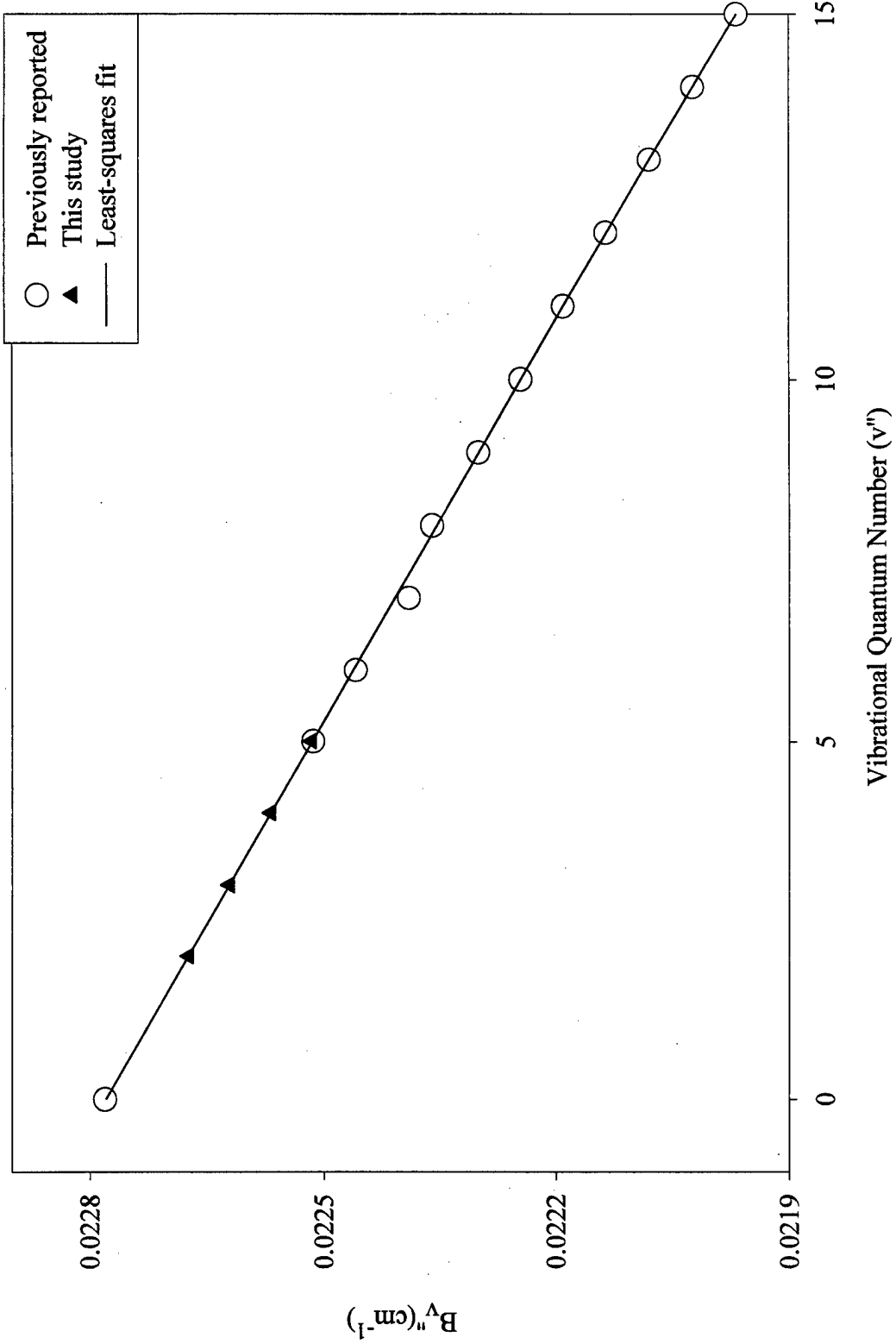


Figure 3.10 Comparison of all reported B_v'' term values with a least-squares fit to the entire data set

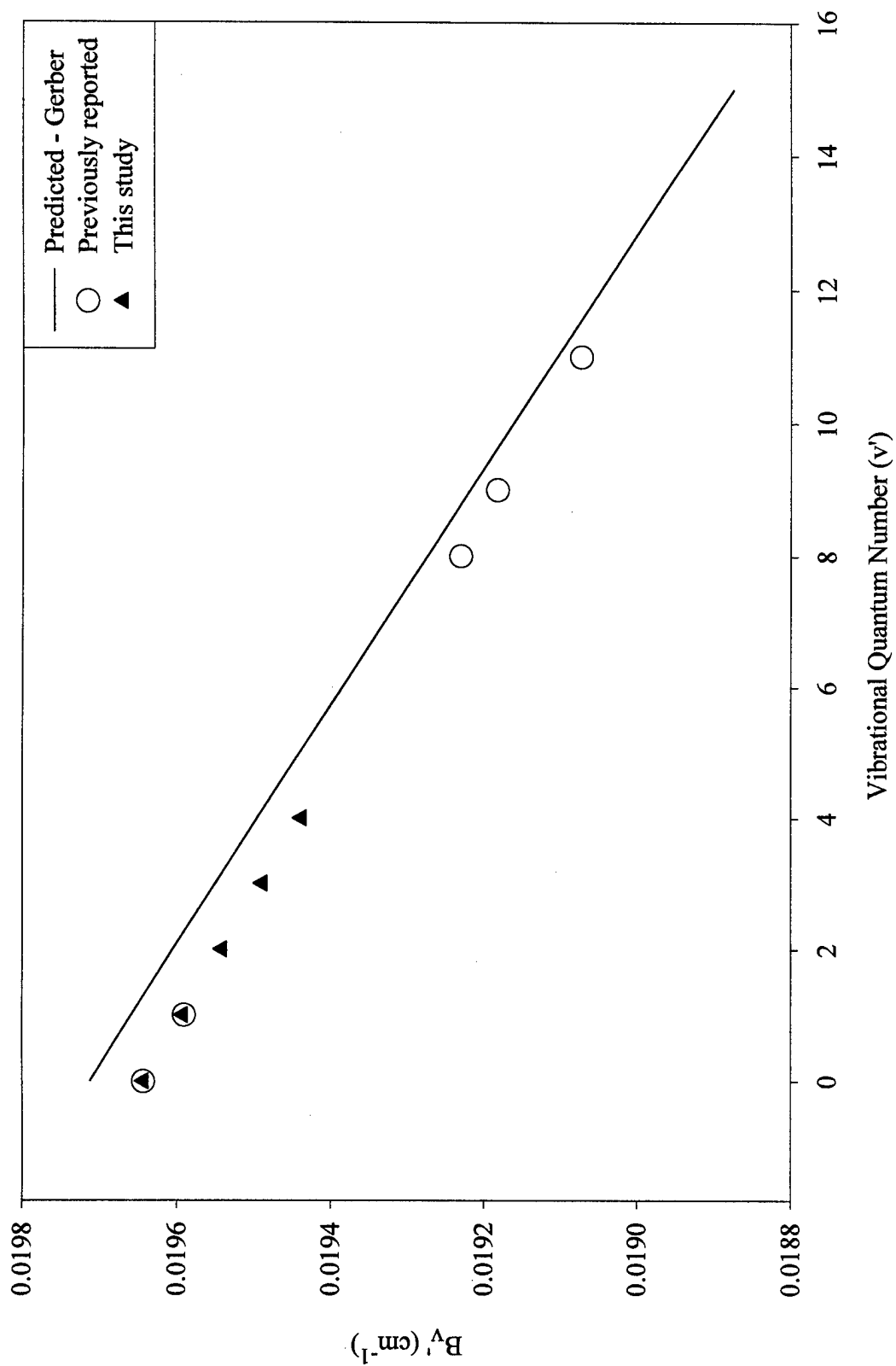


Figure 3.11 Comparison of Gerber's predicted values for $B_{v'}'$ with all reported $B_{v'}'$ term values

Table 3.6 Final rotational constants for the X and A states of Bi₂ derived from a merged fit of reported Bi₂ term values with (cm⁻¹)

	X(0 _g ⁺)	A(0 _u ⁺)
B_e	$0.02280598 \pm 4.8 \times 10^{-7}$	$0.0196677 \pm 1.1 \times 10^{-6}$
α_e	$(5.2264 \pm 0.0089) \times 10^{-5}$	$(5.048 \pm 0.055) \times 10^{-5}$
γ_{e1}	$-(1.009 \pm 0.045) \times 10^{-7}$	$-(1.04 \pm 0.47) \times 10^{-7}$
γ_{e2}	$-(1.347 \pm 0.066) \times 10^{-9}$	
D_e	$(1.550 \pm 0.009) \times 10^{-9}$	$(1.7489 \pm 0.004) \times 10^{-9}$
β_e	$(2.42 \pm 0.22) \times 10^{-11}$	$(7.8 \pm 1.5) \times 10^{-12}$

not provide an adequate fit to the values derived in this research. Similarly, as is graphically depicted, a fit to the term values derived in this work did not accurately model the term values reported by Effantin. A probable cause for this discrepancy lies in the range of rotational levels observed. This study observed J as high as 211. Effantin does not report the range of J values used in his calculations. Therefore, for lack of further clarification, the least-squares fit to the D''_v term values derived in this research is believed to be the best set of rotational constants to model that parameter. This same analysis is unnecessary for the A state, as there are no other reported term values to use in a global least squares fit. Aslund's reported values for D'_v have too much error associated with them to consider them reliable. Fabre's values are not reported consistently within the journal article, and it is difficult to determine what is actually reported as the actual term value. Thus, Table 3.6 gives the same values reported in Table 3.5. It is believed, Table 3.6 represents the best set of rotational constants currently available for the Bi₂ X(0_g⁺) and A(0_u⁺) states. The error bounds associated with these terms are the errors bounds as calculated by TableCurve's nonlinear least-squares fitting routine. These rotational constants have a fit standard deviation of 0.01 cm⁻¹ for all observed rotational transitions.

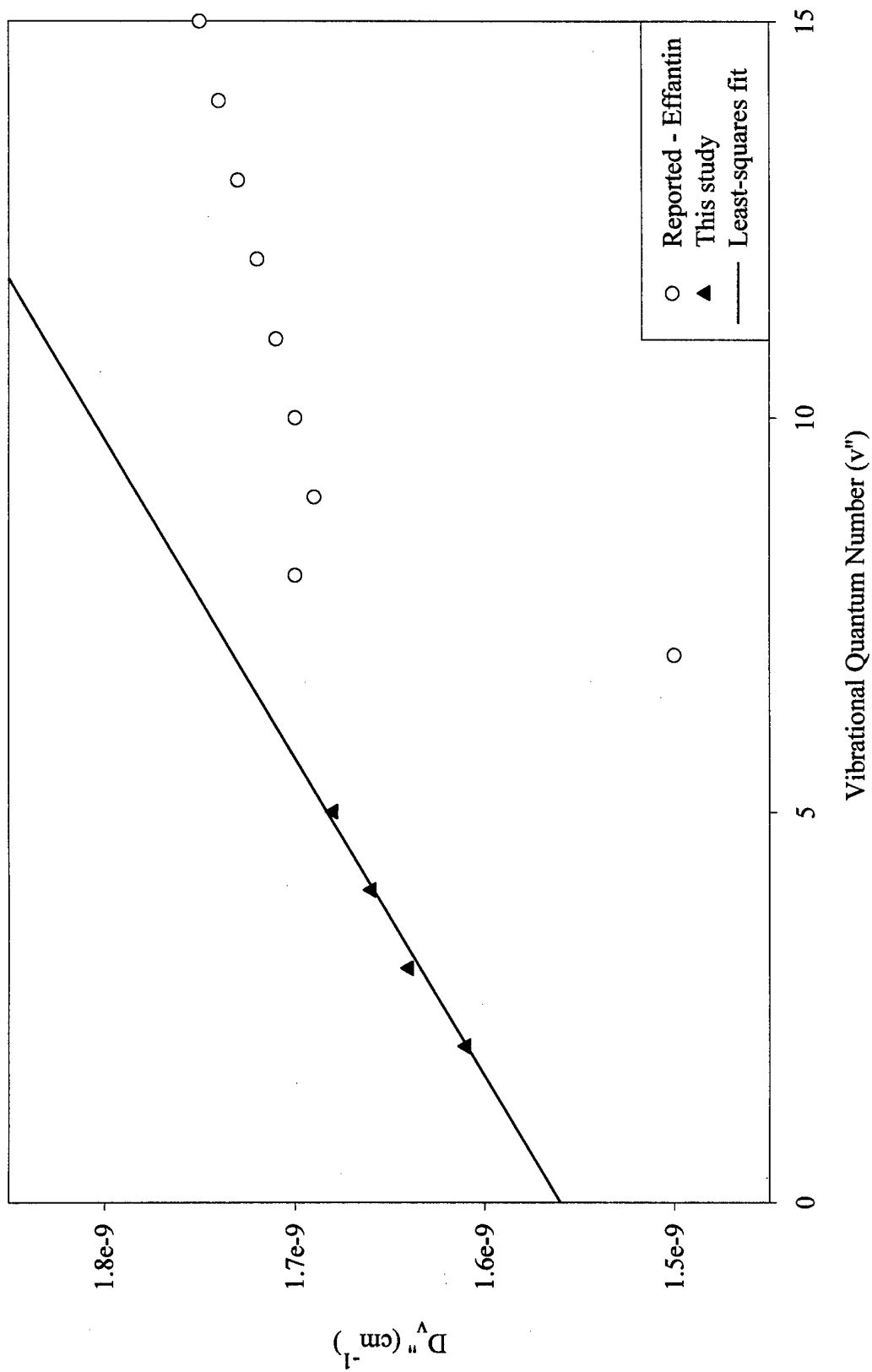


Figure 3.12 Comparison of this study's observed D_v'' values to those reported by Effantoin. The solid line is a least-squares fit to this study's observed values.

3.5 Franck-Condon Factors

As stated earlier in this chapter, accurate Franck-Condon (F-C) factors are a necessary to interpret the energy transfer studies. To this end a systematic approach was used to find the "best" set of factors to use for emission from the Bi_2 A state vibration levels $v' \leq 5$. The same procedure was used for each different vibration band studied. This section will discuss those procedures as well as compare the results with F-C factors numerically derived from the use of RKR potentials using both previously reported molecular constants and those derived in the last section. The calculation of Franck-Condon factors should provide a robust check on the derived spectroscopic constants since F-C factors are strongly dependent on the shape of the potential describing the electronic state.

3.5.1 Experimental Procedures. The experimental setup is the same basic design as shown in Figure 3.1. The differences are as follows: (a) The chopper, beam splitter and iodine reference were removed; (b) The emission from the Bi_2 cell was spectrally resolved through a McPherson model 218 0.3 m monochromator which contained a 1200 groove/mm grating blazed at 5000 angstroms; (c) The entrance slit of the monochromator was set to $\approx 30\mu\text{m}$ and the exit slit was removed so that a Princeton-Instruments model 1024 S/RB 1024 pixel optical multichannel analyzer (OMA) could be used to record the spectra. The pixel spacing on the OMA is $25\mu\text{m}$ and resolution of the monochromator was $\approx 1.5\text{ \AA}$. The dispersion of the monochromator allowed for the simultaneous collection of approximately 45 nm of spectrum on the OMA. Spectra were recored on computer disks for later processing.

Bi_2 was produced in an analogous manner to the previous discussion. A single rovibrational level in the $A(0_u^+)$ state was excited by tuning the ring laser to a spectrally isolated rotational transition. The ability to spectrally isolate a single rovibrational transition is clearly illustrated in Figure 3.3. Table 3.7 lists the wavelengths and band assignments used to selectively pump the different A state

Table 3.7 Excitation wavelengths for Franck-Condon factor studies

Transition $v'' \rightarrow v'$	Wavelength cm^{-1}
3 \rightarrow 0	17196.500
4 \rightarrow 0	17020.776
3 \rightarrow 1	17309.819
5 \rightarrow 1	16988.448
2 \rightarrow 2	17600.577
4 \rightarrow 2	17277.969
3 \rightarrow 3	17588.337
4 \rightarrow 3	17420.110
5 \rightarrow 4	17389.527
6 \rightarrow 4	17212.170
5 \rightarrow 5	17505.328
6 \rightarrow 5	17340.230

vibrational levels. There are two pump lines for each upper state because emission back to the initial X-state vibrational level was dominated by noise from the excitation wavelength. The second lower pump level was needed to determine the intensity of transitions from the prepared A state back to the first lower pump level. A major difference in the experimental procedure from the previous discussion was that the buffer gas pressure was kept less than 150 mtorr. This was to minimize the effect of vibrational energy transfer taking place within the excited bismuth molecules. As will be shown later, vibrational transfer would have induced great difficulties in interpreting the data. The range of transitions from the prepared upper state spanned a greater spectral range than could be collected on a single data run with the OMA. To solve this problem, multiple data runs were pieced together by overlapping at least three major spectral features per run. Since the data was collected under steady-state conditions, this allowed the different data runs to be scaled relative to each other.

The analysis of the resolved spectra is fairly straightforward. An example of the resolved fluorescence after initially populating $v' = 3$ is shown in Figure 3.13.

The strong pair of doublets seen to be extending across the spectrum are the P and R lines from the initially prepared state. In other words, the doublets all have the same upper state. As will be recalled from Chapter 2, for spectrally resolved fluorescence

$$I_{vw}^{obs} = (64\pi^4/3)c\nu_{vw}^4 q_{vw} |R_e|^2 (S_J/(2J+1)) D(\nu_{vw}) N_v \quad (3.13)$$

where v is the upper state and w is the lower state. This equation applies to each one of the P-R doublets seen in Figure 3.13. By comparing the intensities of the different features in the spectrally resolved fluorescence, the F-C factors can be calculated. Equation 3.13 can be rewritten as

$$I_{vw}^{obs} = A\nu_{vw}^4 q_{vw} |R_e|^2 N_v D(\nu_{vw}) N_v \quad (3.14)$$

where A is a constant. In general R_e is very difficult to calculate and for a specific electronic transition is usually approximated by $\overline{R_e}$. This assumes that R_e is a slowly varying function of the internuclear separation (29). For the A→X transition, Ehret has calculated this value to be 1.4 ± 0.4 D (23). He also states that he feels this term is a constant, albeit, with a large error. In this research, A→X is the electronic transition of interest. By assuming the electronic transition moment is a constant, the relative intensity of any two P or R lines can be expressed as

$$\frac{I_{vw}^{obs}}{I_{vu}^{obs}} = \left(\frac{\nu_{vw}}{\nu_{vu}}\right)^4 \left(\frac{q_{vw}}{q_{vu}}\right) \left(\frac{D(\nu_{vw})}{D(\nu_{vu})}\right) \quad (3.15)$$

A rearrangement of Equation 3.15 allows a set of Franck-Condon factors relative to the vu Franck-Condon factor to be expressed as

$$\frac{q_{vw}}{q_{vu}} = \left(\frac{I_{vw}^{obs}}{I_{vu}^{obs}}\right) \left(\frac{\nu_{vw}}{\nu_{vu}}\right)^4 \left(\frac{D(\nu_{vw})}{D(\nu_{vu})}\right) \quad (3.16)$$

When normalization is considered,

$$\sum_w q_{vw} = 1 \quad (3.17)$$

a set of absolute Franck-Condon factors is determined assuming that emission to all lower states w have been observed.

3.5.2 Results and Discussion. Spectrally resolved fluorescence was recorded for the $A(0_u^+)$ vibrational levels $v' \leq 5$ over the entire range of observable transitions. After correcting the recorded data for detector spectral response, the intensity of each P-R doublet feature was given a numerical value based on the formula

$$B = A\lambda^4 \quad (3.18)$$

where A is the numerical count read off the OMA and λ is the wavelength of the transition without units. This equation is a simple restatement of Equation 3.16. The normalized values of B were then equated to the Franck-Condon factors. These factors are recorded as the bottom of the two numbers displayed in each transition in Table 3.8. Having accomplished this, F-C factors were then numerically calculated using an RKR based Franck-Condon computer code obtained from Heaven (43). The code was run once using vibrational constants from Effantin (19) and Ehret (20) and rotational constants from Gerber (21). The Gerber rotational data was selected because it was a single study focused on both states involved in this research. A second run of the computer code was accomplished using the rotational constants derived in the first part of this chapter. This latter data is also recorded in Table 3.8 as the top number for each transition. Figure 3.14 graphically depicts the potential energy curves generated from the RKR program using the spectroscopic constants derived in this research.

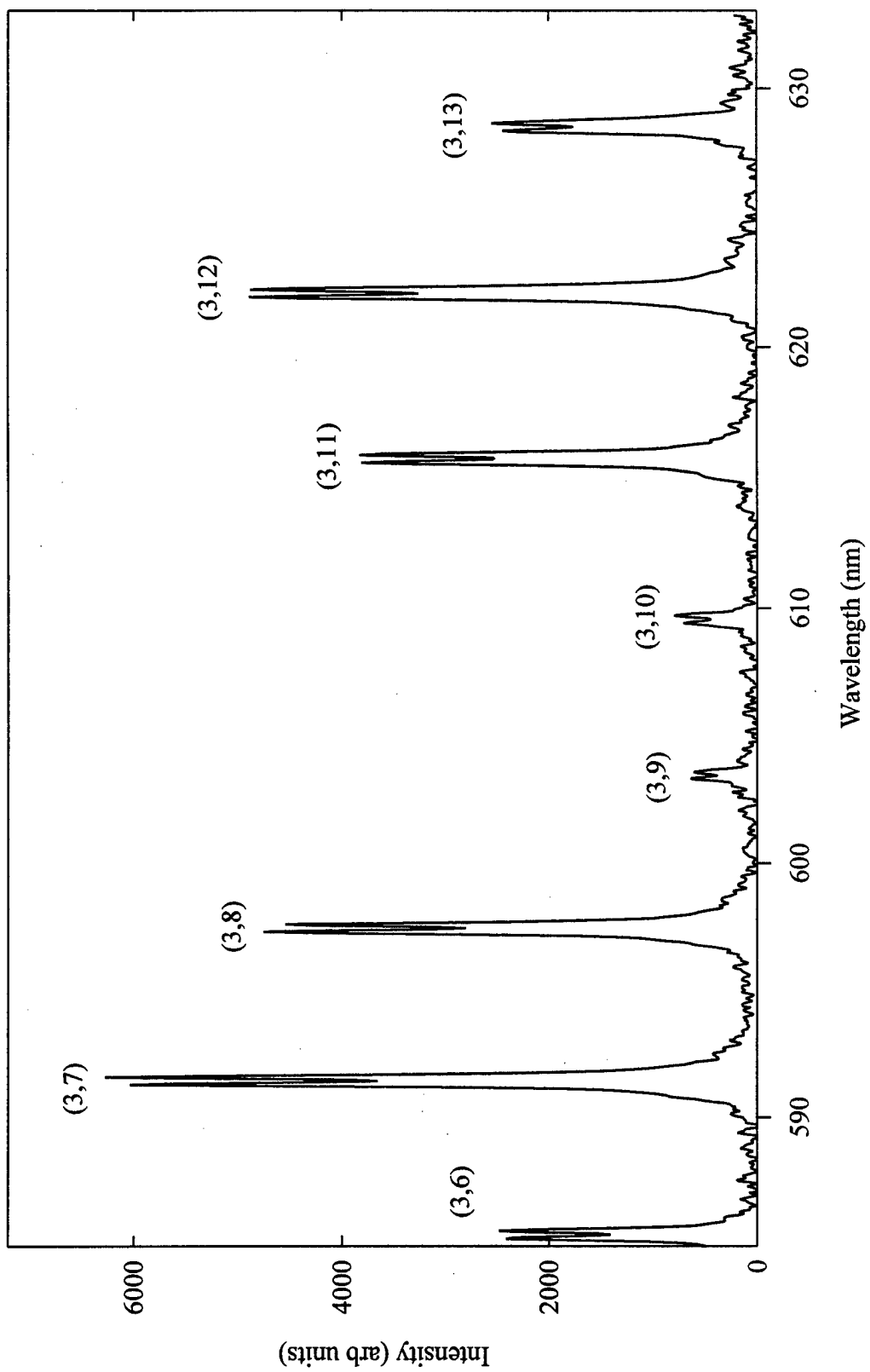


Figure 3.13 Spectrally resolved emission from the initially populated level $\text{Bi}_2(\text{A}) v' = 3$. Numbers on the graph indicate the various transitions (v', v'') .

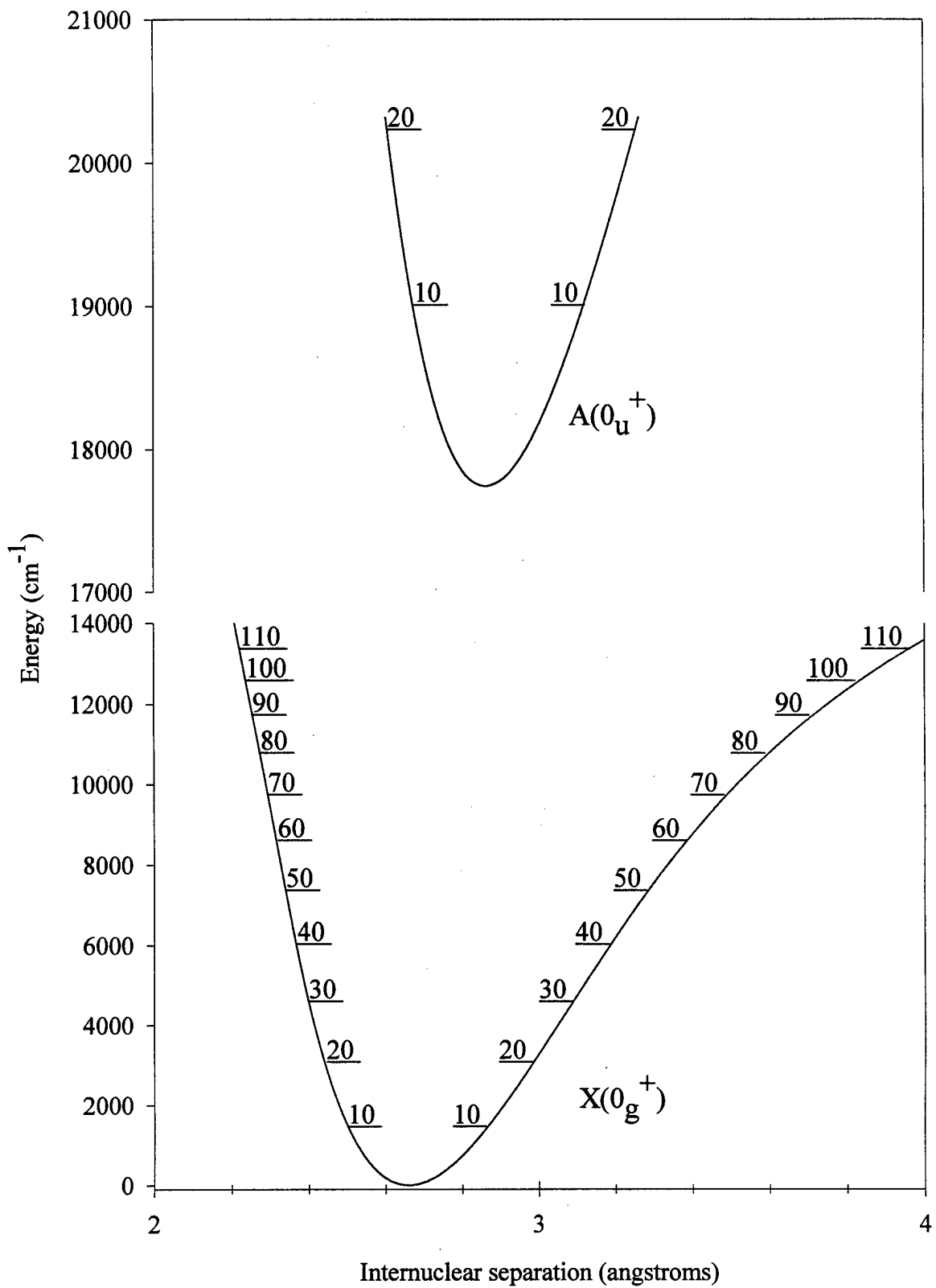


Figure 3.14 Bi_2 potential energy curves derived from the final set of spectroscopic constants presented in Chapter 3.

Table 3.8 Predicted and observed Franck-Condon factors for the Bi_2 ($A \rightarrow X$) transition. The observed value is on the bottom.

v''	v'					
	0	1	2	3	4	5
0	2.471E-05	8.247E-04	9.667E-03	4.854E-02	9.791E-02	4.830E-02
	0.000E-00	2.409E-03	0.000E-00	5.955E-03	9.458E-03	3.265E-02
1	6.458E-04	4.332E-03	1.474E-02	3.376E-02	5.821E-02	7.988E-02
	0.000E-00	7.180E-03	1.666E-02	3.521E-02	5.165E-02	9.731E-02
2	3.564E-03	1.863E-02	4.786E-02	7.914E-02	9.212E-02	7.639E-02
	4.285E-03	2.886E-02	4.975E-02	8.224E-02	8.604E-02	9.611E-02
3	1.269E-02	4.941E-02	8.897E-02	9.301E-02	5.528E-02	1.219E-02
	1.201E-02	5.821E-02	9.243E-02	9.749E-02	4.790E-02	1.550E-02
4	3.279E-02	8.917E-02	9.901E-02	4.696E-02	2.497E-03	1.297E-02
	3.119E-02	1.002E-01	1.056E-01	5.066E-02	8.238E-03	1.532E-02
5	6.550E-02	1.131E-01	5.872E-02	1.600E-03	2.264E-02	5.539E-02
	6.473E-02	1.194E-01	6.333E-02	2.019E-03	1.949E-02	6.104E-02
6	1.053E-01	9.837E-02	8.809E-03	2.127E-02	5.966E-02	2.814E-02
	1.093E-01	1.049E-01	1.165E-02	2.112E-02	6.425E-02	3.159E-02
7	1.399E-01	5.149E-02	6.720E-03	6.250E-02	3.106E-02	7.742E-04
	1.433E-01	5.556E-02	6.564E-03	6.298E-02	3.231E-02	0.000E-00
8	1.567E-01	8.519E-03	4.925E-02	4.974E-02	1.222E-05	3.804E-02
	1.585E-01	1.062E-02	4.872E-02	5.245E-02	0.000E-00	3.945E-02
9	1.503E-01	3.610E-03	7.673E-02	7.039E-03	3.115E-02	4.348E-02
	1.485E-01	4.048E-03	7.880E-02	7.789E-03	2.753E-02	4.670E-02
10	1.247E-01	3.892E-02	5.400E-02	8.872E-03	5.594E-02	4.327E-03
	1.221E-01	3.857E-02	5.659E-02	9.203E-03	5.229E-02	4.557E-03
11	9.028E-02	8.657E-02	1.203E-02	5.102E-02	2.362E-02	1.508E-02
	8.971E-02	8.319E-02	1.316E-02	5.139E-02	2.545E-02	1.464E-02
12	5.750E-02	1.156E-01	2.189E-03	6.557E-02	2.828E-04	5.032E-02
	5.121E-02	1.059E-01	2.024E-03	6.559E-02	0.000E-00	4.918E-02

v''	v'					
	0	1	2	3	4	5
13	3.238E-02 3.432E-02	1.139E-01 1.039E-01	3.615E-02 3.603E-02	3.238E-02 3.214E-03	3.163E-02 2.899E-02	3.107E-02 2.897E-02
14	1.620E-02 1.632E-02	8.978E-02 7.799E-02	8.265E-02 8.320E-02	1.249E-03 0.000E-00	6.198E-02 5.813E-02	2.928E-04 0.000E-00
15	7.226E-03 1.442E-02	5.892E-02 4.950E-02	1.070E-01 1.024E-01	1.496E-02 1.666E-02	4.159E-02 4.130E-02	2.339E-02 2.340E-02
16	2.882E-03 0.000E-00	3.295E-02 2.941E-02	9.949E-02 9.638E-02	6.035E-02 6.153E-02	5.150E-03 0.000E-00	5.775E-02 5.559E-02
17	1.030E-03 0.000E-00	1.594E-02 1.371E-02	7.276E-02 6.807E-02	9.629E-02 9.795E-02	7.972E-03 1.456E-02	4.305E-02 3.858E-02
18	3.305E-04 0.000E-00	6.738E-03 6.526E-03	4.375E-02 4.053E-02	9.992E-02 9.686E-02	5.005E-02 5.699E-02	6.329E-03 5.119E-03
19	9.528E-05 0.000E-00	2.506E-03 0.000E-00	2.220E-02 2.046E-02	7.785E-02 7.415E-02	8.977E-02 1.045E-01	6.857E-03 9.580E-03
20	2.471E-05 0.000E-00	8.247E-04 0.000E-00	9.667E-03 7.691E-03	4.854E-02 4.567E-02	9.791E-02 1.129E-01	4.830E-02 4.647E-02
21	5.763E-06 0.000E-00	2.409E-04 0.000E-00	3.652E-03 0.000E-00	2.508E-02 2.111E-02	7.786E-02 8.877E-02	8.800E-02 8.943E-02
22	1.209E-06 0.000E-00	6.259E-05 0.000E-00	1.206E-03 0.000E-00	1.096E-02 9.811E-03	4.871E-02 5.200E-02	9.543E-02 8.218E-02
23	2.280E-07 0.000E-00	1.449E-05 0.000E-00	3.499E-04 0.000E-00	4.115E-03 0.000E-00	2.496E-02 2.727E-02	7.463E-02 5.770E-02
24	3.860E-08 0.000E-00	2.992E-06 0.000E-00	8.954E-05 0.000E-00	1.338E-03 0.000E-00	1.072E-02 0.000E-00	4.556E-02 3.433E-02
25	5.857E-09 0.000E-00	5.509E-07 0.000E-00	2.026E-05 0.000E-00	3.792E-04 0.000E-00	3.923E-03 0.000E-00	2.263E-02 1.650E-02
26	7.965E-10 0.000E-00	9.040E-08 0.000E-00	4.058E-06 0.000E-00	9.414E-05 0.000E-00	1.235E-03 0.000E-00	9.376E-03 8.130E-03

There is generally good agreement between the three different methods used to calculate the F-C factors as is shown in Figure 3.15 which is a plot of the F-C factors out of the A state level $v' = 2$. However, there are a few notable features in this figure that need to be specifically pointed out. The first is the behavior of the different methods for transitions to the first Franck-Condon minimum at $v'' = 6, 7$. The Gerber prediction misses the location of the experimental minimum by $\Delta v = 1$ while the current predictions accurately predict the experimental behavior. This is significant in that a small F-C factor comes about from a small value for the overlap of the wavefunctions of the two states involved in the transition. The shape of the potential curve must be known very precisely to properly calculate these wavefunctions. Any deviation of the shape of the potential from its true nature will result in improperly calculated wavefunctions. This in turn leads to improperly calculated F-C factors. For large F-C factors, this is not as significant of a development as a slight miscalculation of the wavefunction will probably still result in a large value of the overlap integral. However, if the overlap is small, improper wavefunctions will probably cause significant error in calculating the correct value of the Franck-Condon due to the wavefunction's deviation from correctly modeling the actual overlap. The trend for the Gerber predictions to incorrectly predict the behavior at the minimums was present for all A state levels ($0 \leq v' \leq 5$) used in this experiment. Another example of this behavior is seen in Figure 3.16 where the behavior at $v'' = 3, 4$ and $v'' = 18, 19$ is correctly modeled by the current work but not by the Gerber predictions.

The second notable feature of the different methods used to obtain the F-C factors lies in the relative behavior of consecutive data points ($v - 1, v, v + 1$). The connected lines on Figures 3.15 and 3.16 help illustrate this point. In Figure 3.15, the relative magnitude of the F-C factor for $v'' = 3, 4$ is mirrored in the experimental work and also in the current calculation. This behavior is not seen with the Gerber predictions. This same trend repeats itself numerous times in the two figures displayed as well as in the other data collected. This is another indication

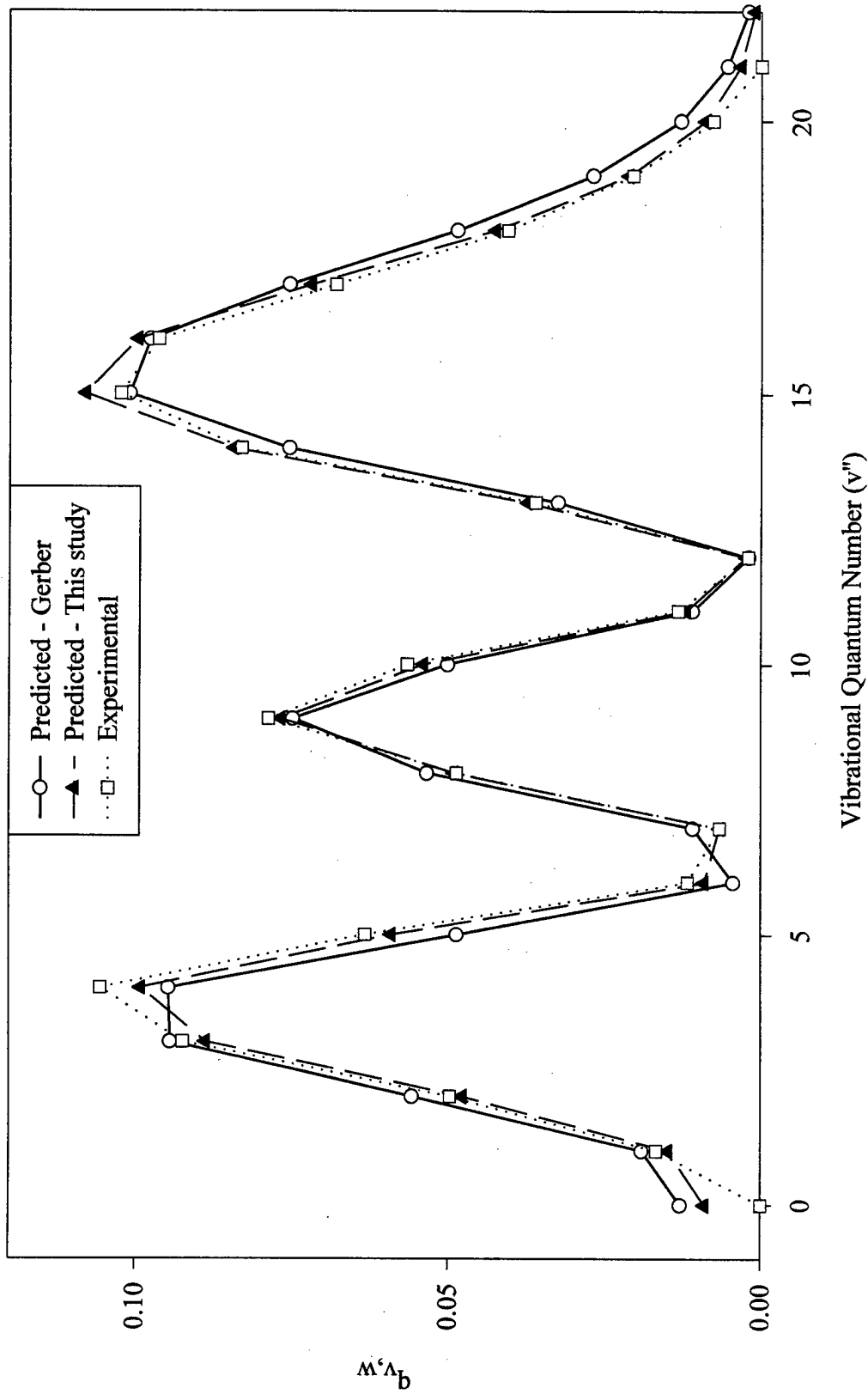


Figure 3.15 Comparison of experimentally derived Franck-Condon factors with those calculated from an RKR based fitting routine for the initially populated $v'=2$ level

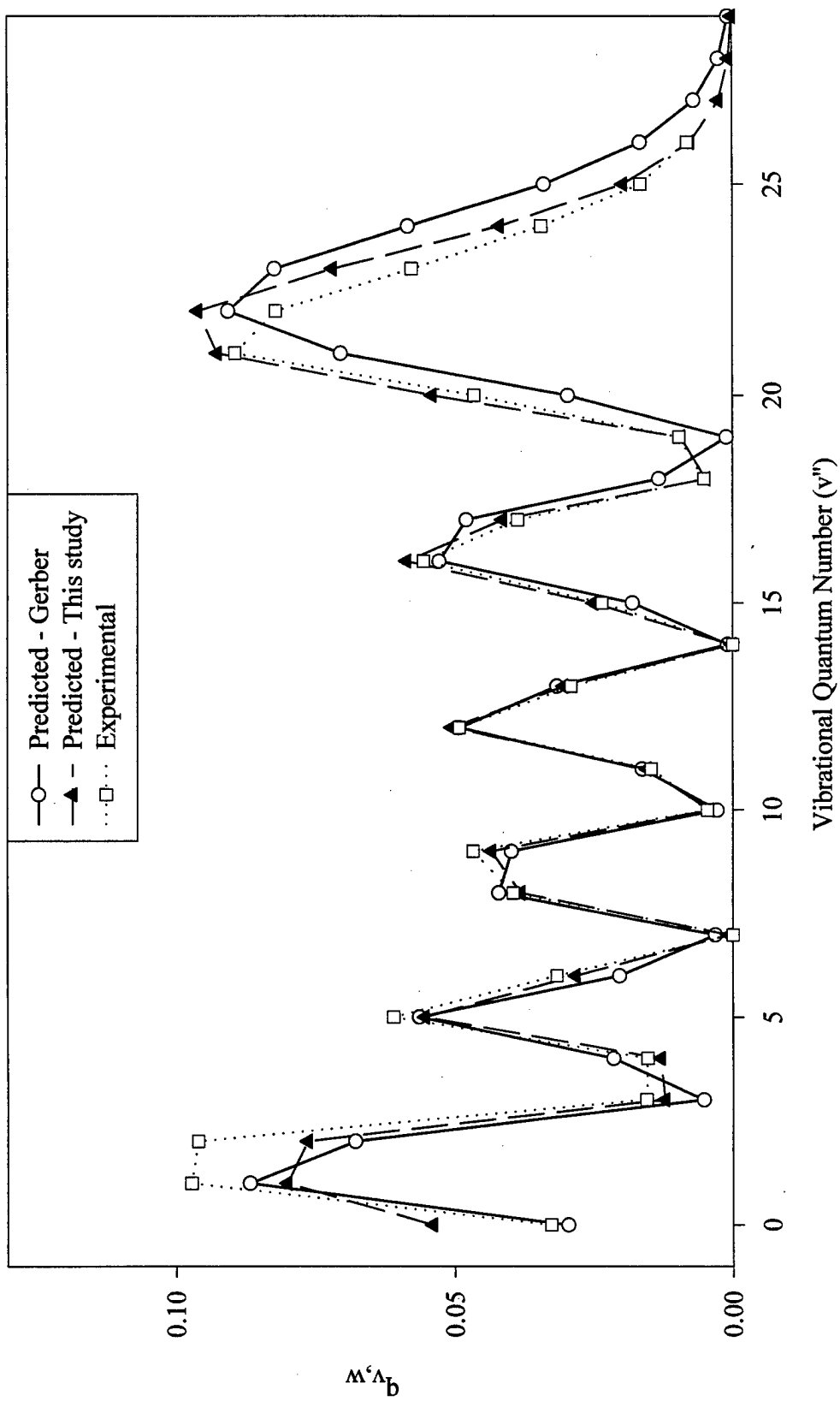


Figure 3.16 Comparison of experimentally derived Franck-Condon factors with those calculated from an RKR based fitting routine for the initially populated $v'=5$ level

that the spectroscopic constants provided in the current work are doing a better job of modeling the potential curves of the X and A states.

The error associated with the experimentally determined Franck-Condon factors is estimated as follows. The initial detector response function was determined with an Oriel quartz calibration lamp. A blackbody source heated to 993 C was then used to obtain a spectral response on the OMA. After correcting this blackbody spectrum with the detector response function as determined from the quartz lamp, it was then compared to the predicted spectral response of a blackbody emission. There was an approximate $\pm 10\%$ deviation between the experimental and theoretical blackbody response curves as referenced off the center pixel of the OMA. Since both calibration sources were of known spectral response, it is estimated that this deviation of $\pm 10\%$ is the error associated with the experimentally determined Franck-Condon factors. However, as seen in Figures 3.15 and 3.16, the experimental Franck-Condon factors appear to have slight variation with vibrational quantum number of the X-state in that the experimental values appear to be too large at low quantum numbers and too low at the higher levels. The range of variation between experimental and theoretical Franck-Condon factors was $\leq 20\%$ in all cases. This is well within the error bound Ehret reported on his value of the electronic transition moment (23). The variation between the experimental and theoretical factors may indicate the electronic transition moment is not constant. Unfortunately, the data derived in this experiment does not allow for either confirming or denying this supposition. Even with this discrepancy, the results of the Franck-Condon studies indicate the spectroscopic constants reported in this study represent an improvement in the understanding of the Bi_2 X and A states.

IV. Vibrational Energy Transfer in Bi_2 $A(O_u^+)$

4.1 Introduction

Collisional energy transfer in the diatomic halogens and interhalogens has been extensively studied. Vibrational-to-translational, $V \rightarrow T$, energy transfer studies have been carried out on IF(B) (11), BrF(B) (8), BrCl(B) (9) and $\text{Br}_2(\text{B})$ (7, 10) in an effort to determine the feasibility of using these species as the lasing molecule in a chemically pumped laser. Additionally, studies have also been conducted on $\text{I}_2(\text{B})$ (44). The breadth of molecules covered in these studies comprises one of the most complete databases for $V \rightarrow T$ transfer of any particular group of molecules. By comparing the observed vibrational transfer rates, much insight can be gained into the various theoretical energy transfer models such as the SSH and Landau-Teller theories described earlier in this paper. In this work, $V \rightarrow T$ energy transfer studies have been conducted on the low lying vibrational levels of the Bi_2 (A) state. This chapter discusses state-to-state vibrational energy transfer in Bi_2 (A) with five different collision partners: He, Ne, Ar, Kr and Xe.

4.2 Experimental Setup

The experimental setup for the vibrational transfer experiments was identical to the setup used for the determination of the Franck-Condon factors described in the previous chapter. For the vibrational energy transfer studies, 0.1-12.0 torr of buffer gas was added to the cell. The buffer gases used were helium, neon, argon, krypton and xenon. All gases had a purity of 99.996% or higher.

4.3 Experimental Procedures

4.3.1 Data Collection. In this study, vibrational energy transfer within the Bi_2 (A) state was examined after laser excitation of single rovibrational levels via the following vibrational transitions: $(v'', v') = (3,1)$, $(4,2)$, $(3,3)$, and $(3,4)$. These

Table 4.1 Excitation wavelengths, rovibrational assignments and range of spectral observation used in vibrational transfer studies.

Vibrational Band v'', v'	Rotational Assignment	Wavelength cm^{-1}	Spectral Range nm
3,1	P(105)	17299.732	580-629
4,2	R(89)	17277.969	580-629
3,3	R(88)	17578.156	582-631
6,4	?	17202.402	582-631

X state levels were selected due to their reasonably large Franck-Condon factors to their appropriately pumped A state level and the fact that they had transitions accessible by the Rhodamine 590 chloride. Table 4.1 lists the wavelengths along with their rovibrational assignment used to pump the different A state vibrational levels. The exact rovibrational assignment of the $v'' = 6$ to $v' = 4$ transition is unknown as spectroscopy was not accomplished on this vibrational band. However, spectrally resolved emission confirmed this wavelength did indeed pump the $v' = 4$ vibrational level. These are the same wavelengths used in the Franck-Condon studies to prepare the pure (v', J') states. A rotational line with $J \approx 90$ was selected in all cases for the pump transition. At higher rotational numbers, the resulting P-R doublet emission from the parent rotational level overlapped the $\Delta v = +1$ bandhead and made its location and magnitude unresolvable. At lower rotational quantum numbers, the identification of the parent bandhead became ambiguous. The spectral range observed in emission was chosen so as to have the Franck-Condon factor of the pumped level be very small for at least one vibrational band observed. This was done to ensure the ability to unambiguously identify at least one $\Delta v = +1$ vibrational bandhead. This became an important factor in obtaining an accurate numerical fit to the data as will be explained in the next section. Table 4.1 also lists the spectral observation range for each initially prepared parent state.

A spectrally resolved emission profile showing the effects of vibrational energy transfer after pumping $v' = 3$ is depicted in Figure 4.1. This spectra is in stark contrast to Figure 3.13 which shows little, if any, vibrational transfer at low buffer gas pressures. Identifiable vibrational bands in Figure 4.1 are labeled (v', v'') . A few notable features of this figure need to be pointed out. The only clearly discernible P-R doublet is located in the (3,8) band. This structure is not visible in the other two bands originating from $v' = 3$ because the Franck-Condon factors for these two transitions are almost an order of magnitude less than that for the (3,8) band. A close inspection of the (3,9) band reveals the peaks of the P-R doublet. The bandhead of the (4,10) band is clearly discernible but the (4,9) bandhead cannot be visually located. This demonstrates the need for having a small Franck-Condon factor from the pump level to at least one observed band as it allows for locating a $\Delta v = +1$ transition. A significant degree of R-T relaxation is demonstrated in the satellite bands as they all exhibit near thermal band shapes. Perram noted that during vibrational transfer in BrCl(B), there was little, if any, rotational memory from the parent vibrational level (13). As demonstrated by the spectrally resolved fluorescence, the same effect is present in Bi₂. This explains why there is no P-R doublet structure from the satellite levels. Finally, this figure demonstrates a significant amount of V-T transfer as satellite band are observed from $\Delta v = +1, -1, -2, -3$.

The resolution of the vibrational transfer spectra in Figure 4.1 can be estimated as follows. The excitation line for this spectra selectively pumps ($v' = 3, J' = 89$) in the excited state. The prominent P-R doublet feature consists of an R(88) and a P(90) transition. Using the rotational spectroscopic constants derived in Chapter III, these two lines should have a separation of 2.82 Å for the observed (3,8) band. This compares very favorably to the 2.90 Å spacing as read off the OMA data. There are six pixels peak-to-peak in the P-R doublet. An absolute minimum of four pixels peak-to-peak is needed to identify two separate transitions. As recorded on the OMA, this would correspond to a minimum resolution of approximately 2.0 Å. This

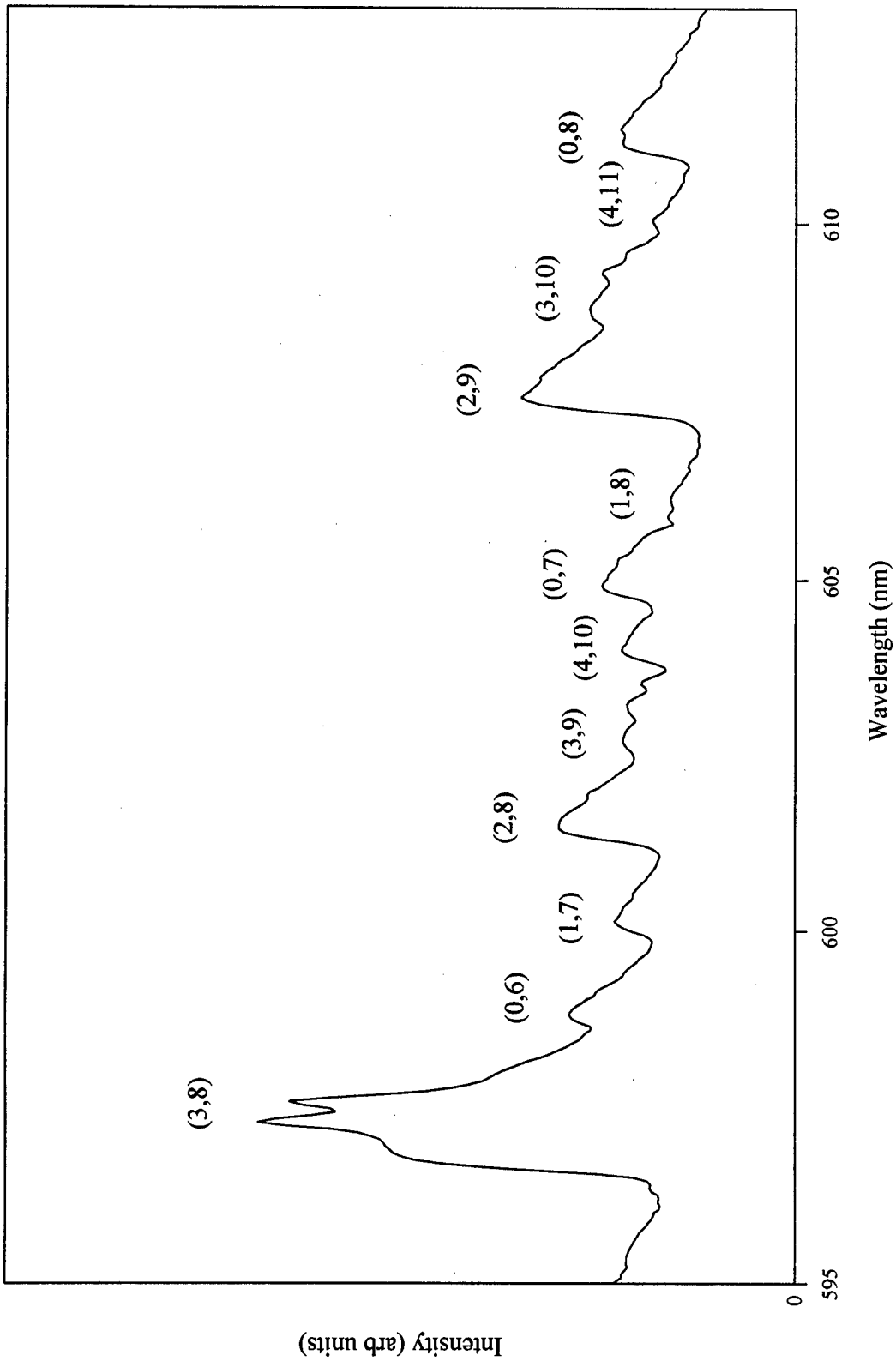


Figure 4.1 Spectrally resolved fluorescence profile after initially populating $v'=3$ with 4.758 torr of neon buffer gas. Identifiable bands are labeled (v', v'').

resolution is too large to individually resolve any rovibrational emissions originating from any state other than the initially pumped rovibrational level.

Spectrally resolved fluorescence profiles were recorded for a variety of buffer gas pressures for each buffer gas species and pumped v' level. Data collection per spectral profile ranged from 1-4 minutes. Longer collection times were needed for the extremes of the buffer gas pressures used. At the low pressure end, this was because there was less bismuth transported to the interaction area of the bismuth cell, thus there was less signal. At higher pressures, quenching of the A state reduced the signal. These data runs consisted of multiple shorter collection runs to equal the total time stated. The length of a single data run was limited to a length of time that did not saturate the count buffers on the OMA. Background subtraction was relatively easily accomplished. A background trace was acquired prior to each data run after tuning the laser approximately 0.03 cm^{-1} off the selected rovibrational resonance line to an area where no spectral transitions existed. This trace was then subtracted from each fluorescence profile prior to processing. This method provided consistent subtraction of the background noise.

4.3.2 Population Ratios. In order to utilize the equations developed in Chapter II to find the vibrational energy transfer rates, the population ratio of daughter to parent state must be found. A spectrally resolved fluorescence profile provides the information necessary to accomplish this task. Fluorescence intensity is directly proportional to the population of the upper transition level. Thus, once the intensity of a vibrational band is properly scaled for the Franck-Condon factor, the intensity will necessarily define the population of that particular band. As already indicated, there is little, if any, rotational memory during a vibrational energy transfer event. This causes the satellite vibrational bands to be thermalized with respect to rotational quantum number. Furthermore, collisions are also taking place that cause rotational energy transfer within the parent vibrational level resulting in emission from the parent vibrational state occurring over a multitude of rotational

levels. In order to find the population of a particular vibrational band, there are numerous transitions to consider.

The task of measuring each and every one of these individual rotational transitions, particularly with the given resolution would be virtually impossible. An effective alternative is to equate the population of a vibrational band to the area under its curve on a spectrally resolved fluorescence profile. If the relative areas between daughter and parent states can be found, the population ratios are then known. Unfortunately, this task is not as easy as it sounds. As is seen in Figure 4.1 there is considerable overlap between vibrational bands with different upper levels. During the rotational studies to be discussed later in this paper, rotational levels as high as $J = 260$ were accessed through rotational energy transfer. This level of J occurs approximately 200 cm^{-1} from the vibrational bandhead. The vibrational spacing in the A state is $\approx 130 \text{ cm}^{-1}$ and for $v' \leq 5$ a new vibrational bandhead occurs approximately every 35 cm^{-1} with the $v' = 5$ bandhead being located between those of $v' = 0$ and $v' = 1$. The considerable overlap of successive vibrational bands requires great care in deconvolving the spectrally resolved fluorescence.

To this end, a mathematical equation has been found that predicts convolved emissions from a vibrational level under finite resolution. This equation is

$$I_v(\lambda) = \frac{ab}{c-b} [\exp(-b(\lambda - \lambda_{v'w})) - \exp(-c(\lambda - \lambda_{v'w}))] = F(a, b, c, \lambda_{v'w}, \lambda) \quad (4.1)$$

where a is the intensity of the vibrational band, b and c are exponential scaling factors that determine the band behavior on either side of the vibrational bandhead and $\lambda_{v'w}$ is the wavelength of the bandhead. This equation was found by generating a synthetic spectrum of a rotationally thermalized vibrational band and then allowing TableCurve (Jandell Scientific) to search its library of reference functions for a functional form that accurately modeled this synthetic spectrum. A thorough development of this equation is presented in Appendix C. Equation 4.1 represents

the general features of a single vibrational band quite well. It rises rapidly at the bandhead and falls off smoothly to the long wavelength side of the bandhead. The rotational temperature of the vibrational band affects the intensity of the emission to the long wavelength side of the bandhead. Similarly, the c parameter scales the rate of fall off of Equation 4.1 to the long wavelength side of $\lambda_{v'w}$. The relationship between the rotational temperature and the c parameter can be expressed by the following relation

$$c = \alpha + \beta T^{-\xi} \quad (4.2)$$

where T is the rotational temperature (K) of the vibrational band and α , β and ξ are empirically generated fit parameters dependent on the resolution used to generate the synthetic spectrum. A more thorough development of this equation, as well as the justification for using it is presented in Appendix C. Equation 4.2 is highly dependent on the resolution parameter used to generate the synthetic spectrum. Any deviations between actual system resolution and the resolution parameter of the synthetic spectrum will cause some error in this calculation. Thus, Equation 4.2 should be used for qualitative comparisons only.

Equation 4.1 models the behavior of every vibrational band in the spectrally resolved fluorescence except the parent state which needs the addition of two Gaussian functions to account for the P-R doublet emission from the initially populated parent rotational level. The Gaussian has the functional form

$$I_g(\lambda) = A_g \exp \left[-0.5 \left(\frac{\lambda - \lambda_0}{R} \right)^2 \right] = G(A_g, \lambda_0, R, \lambda) \quad (4.3)$$

where A is the peak value of the function, λ_0 is the center wavelength and R aids in defining the full width at half maximum.

To simulate a resolved fluorescence profile, the spectra as recorded on the OMA is first corrected for the ν^4 dependence of the intensity. Then, one spectral fitting function, scaled by the appropriate Franck-Condon factor, is summed for

each vibrational band in the spectral range of interest. For the parent vibrational band, this fitting function includes the Gaussians needed for the doublet emission. The Franck-Condon scaling allows the same intensity parameter to be used for each function with a common upper level. Assuming that all satellite vibrational bands will have the same basic shape due to the thermalizing effect of vibrational transfer collisions, the b and c parameters for these level are kept invariant with respect to each other. A different pair of these two parameters (b, c) is used in the parent state to allow for a different rotational temperature. Mathematically, this process can be expressed as

$$\begin{aligned}
 I(\lambda) = & \\
 & \sum_{v' \neq v'_0} \sum_w q_{vw} F(a_{v'}, b, c, \lambda_{v'w}, \lambda) \\
 & + \delta_{v', v'_0} \sum_w q_{vw} [F(a_{v'}, b_0, c_0, \lambda_{v'w}, \lambda) + G(A_g, \lambda_P, R, \lambda) + G(A_g, \lambda_R, R, \lambda)]
 \end{aligned} \tag{4.4}$$

where λ_P is the wavelength associated with the parent state P-branch doublet and λ_R is associated with the R-branch. Using this equation as a starting point, a least-squares fit is then performed to find the parameters ($a_{v'}, b, c, b_0, c_0, A$) that best represent the observed spectral profile. Since R is effectively the resolution of the Gaussian functions, it is left as a constant in all fits. Figure 4.2 shows a comparison of spectrally resolved fluorescence after initially populating $v'_0 = 3, J'_0 = 89$ with the least-squares fit to the simulated spectrum. The open circles represent the data as recorded by the OMA while the solid line running through the data is the spectral fit. The agreement is generally good except for the bandhead area of the parent state. This discrepancy is due to the fitting function rising too sharply in the bandhead region. This discrepancy is discussed in Appendix C. Interestingly, the rotational temperature of the satellite bands (c) converged to a constant value at relatively low pressures, while the rotational temperature of the parent state (c_0) showed a continued rise in rotational temperature as more buffer gas was added.

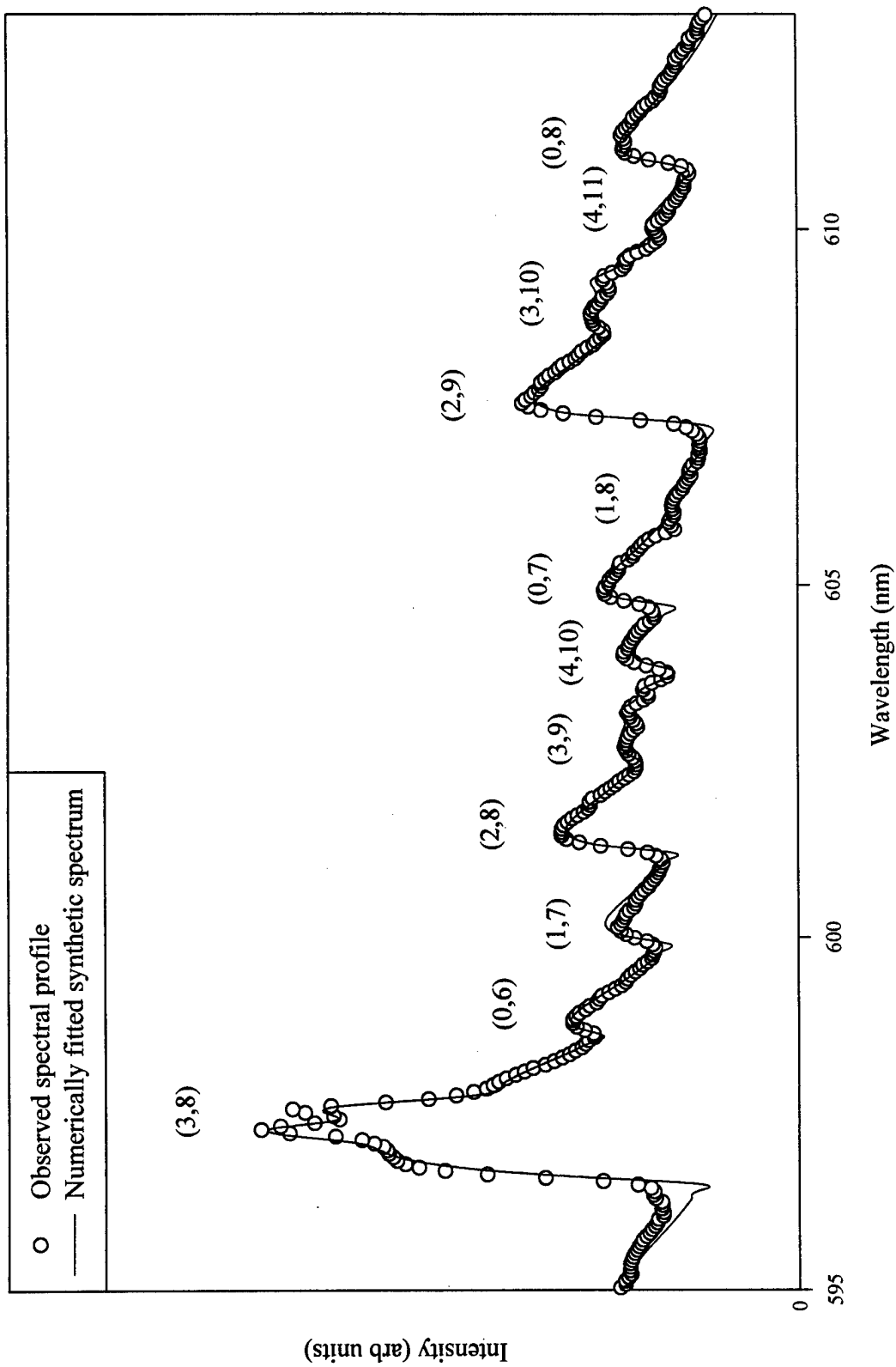


Figure 4.2 Comparison of a spectrally resolved fluorescence profile after initially populating $v'=3$ with 4.758 torr of neon buffer gas with the results of a fitted spectral simulation. Open circles are the data points while the line running through them is the numerical fit.

The relative areas associated with each A state vibrational level is now relatively easy to calculate. According to the TableCurve users manual, the area under the curve generated by Equation 4.1 is given by (45)

$$Area = \frac{a}{c} \quad (4.5)$$

This equation can then be used directly to find the area of each satellite vibrational level. A further consideration is needed for the parent state. As was mentioned earlier, two additional Gaussian functions were needed to account for the large emission from the initially populated rotational level. Thus, the parent state population must take this into account. The area of the parent vibrational level is expressed by

$$Area_p = \frac{a_p}{c_0} + 2Area_{gauss} \quad (4.6)$$

where the p subscript denotes the parameters associated with the parent vibrational level. Population ratios are now a simple matter of comparing the areas found using the different parameters.

A benefit of using this method to deconvolve the spectra is that many vibrational bands can be simultaneously fit at one time. This includes multiple bands from the same parent or satellite state. Thus, there is an internal consistency present in this method that is lacking in previous attempts to analyze data of this type. A common method used in previous studies to attacked this problem is to assume a linear extrapolation of band intensity at high rotational levels from the observed intensity at lower rotational levels. When the extrapolation reached zero, it was assumed there was no further population of interest. The drawback of this method is that generally only a single vibrational band series was analyzed. Thus, it is believed that this method of analysis represents a significant improvement over methods used in previous studies.

4.4 *V→T Transfer with Rare Gas Collision Partners*

Vibrational transfer data was collected for collisions with rare gas collision partners. The rare gases were chosen for several reasons. Atomic species eliminate the need to consider V→V transfer collisions. They are chemically inert which removes the possibility of a chemical reaction. Also, electronic states in rare gases are not energetically accessible. Therefore, the primary difference between the rare gases is nuclear mass, making comparison with the Landau-Teller and SSH theories possible. Finally, this course of action allows for comparison with V→T transfer studies conducted on the halogens and interhalogens. These comparisons will be shown later in this chapter.

Neon was the most extensively studied rare gas in this study. This collision partner was chosen due to the strong Bi₂ signal intensity when neon was used as the bath gas as well as not being located at either the high or low extreme of mass for the rare gases. Vibrationally resolved fluorescence profiles were obtained for the initially pumped levels $0 \leq v' \leq 4$ as a function of Ne pressure. In general, vibrational transfer was observed for $\Delta v = \pm 2$, and for the case of pumping $v' = 3$, vibrational transfer was observed for $\Delta v = -3$. Ne pressures ranged from approximately 0.1-14.0 Torr. Using the spectral fitting techniques described in the last section, population ratios of daughter to parent state were found for each initially pumped v' level over a range of different pressures. Typical sets of population ratios as a function of buffer gas pressure are seen in Figures 4.3 - 4.6. These data sets were observed after initially pumping $v' = 3$. The basis for the error bars in these figure is detailed in Appendix E.

4.4.1 Direct Vibrational Transfer. The simplest mechanism for describing the population present in collisionally populated levels would be to describe the process as a single Δv transfer from the initially prepared state to the satellite state.

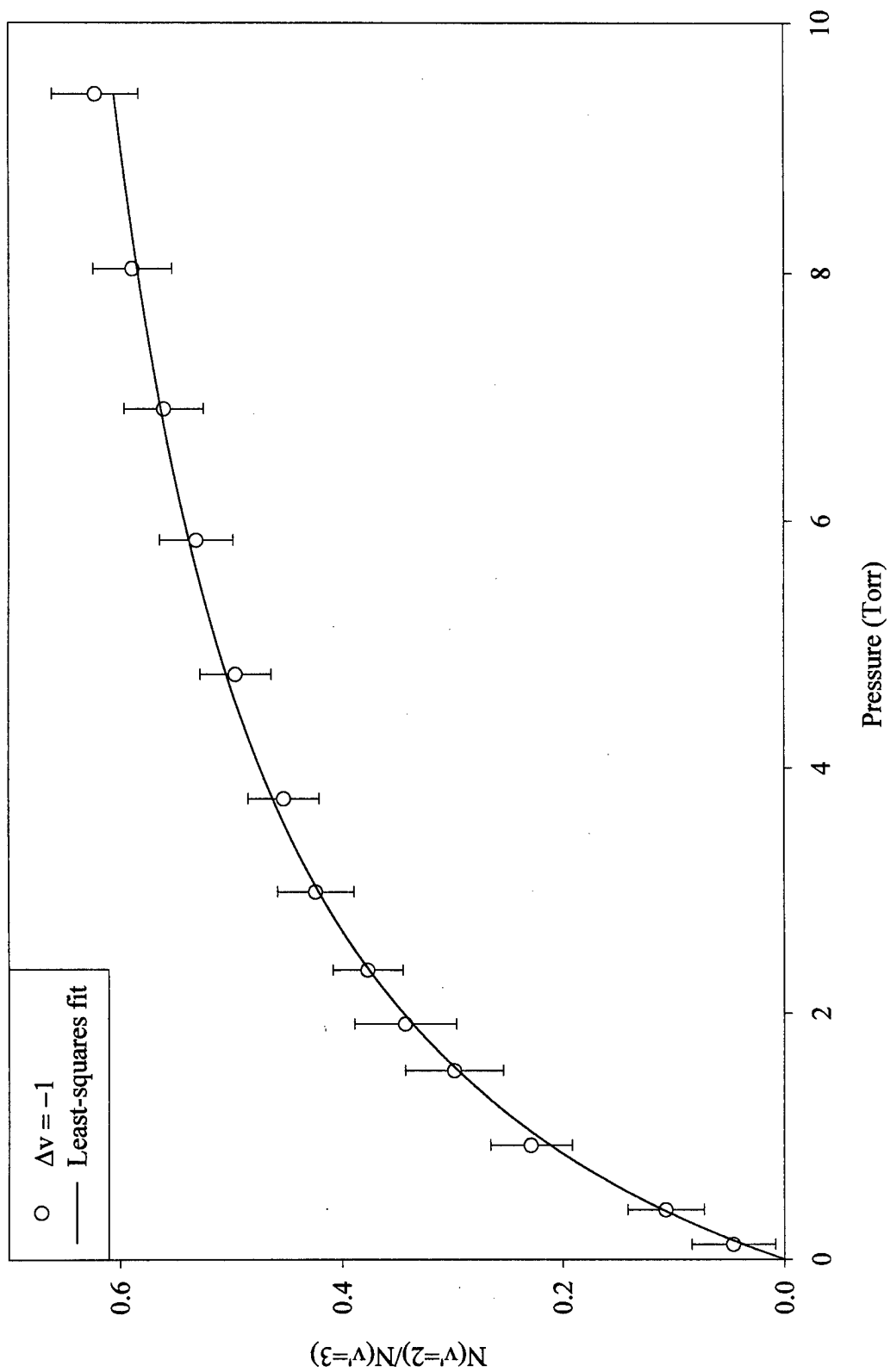


Figure 4.3 Comparison of the $\Delta v = -1$ population ratios after initially populating $v' = 3$ with a least-squares fit to the data. Neon is the collision partner.

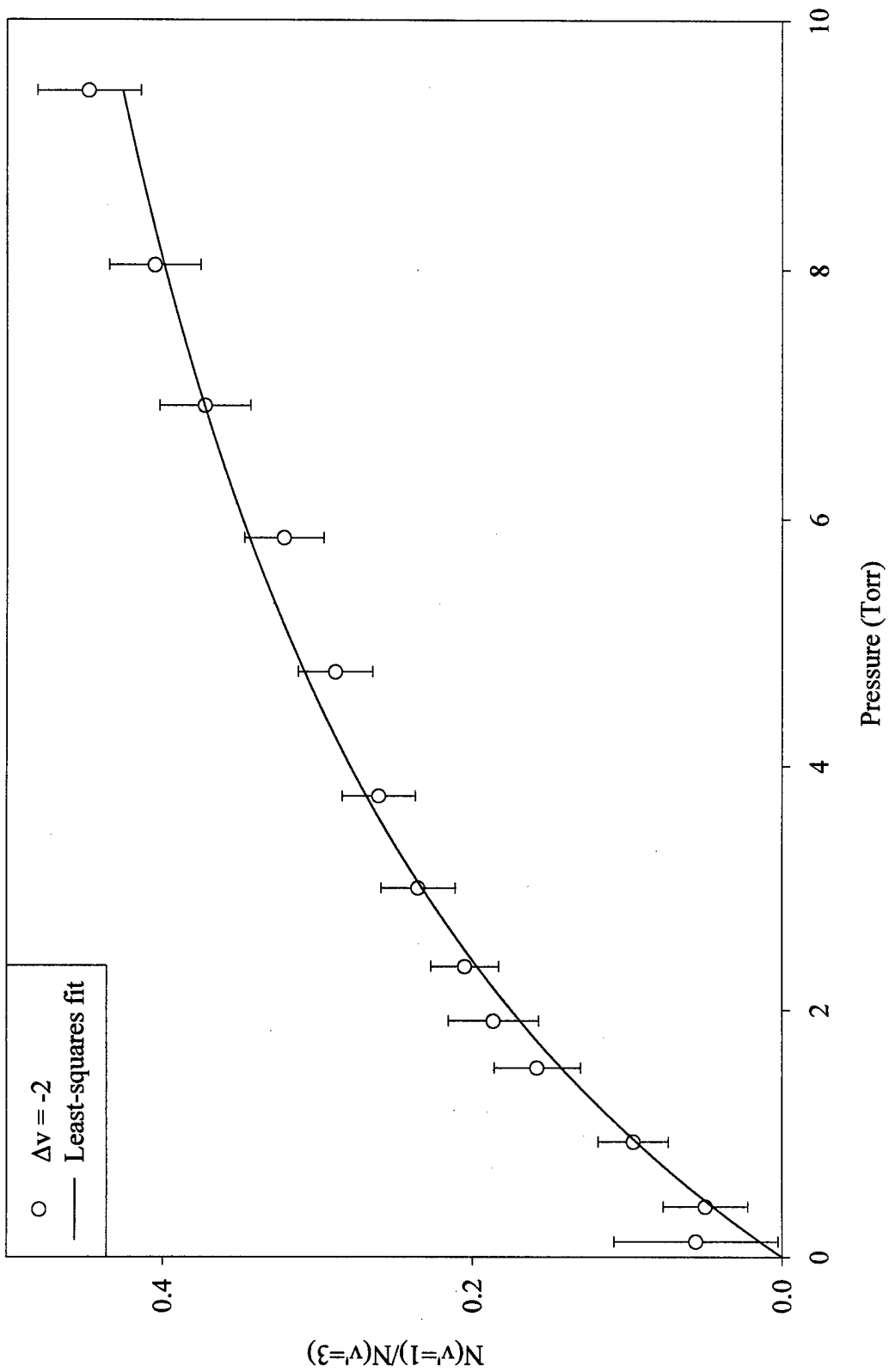


Figure 4.4 Comparison of the $\Delta v = -2$ population ratios after initially populating $v' = 3$ with a least-squares fit to the data. Neon is the collision partner.

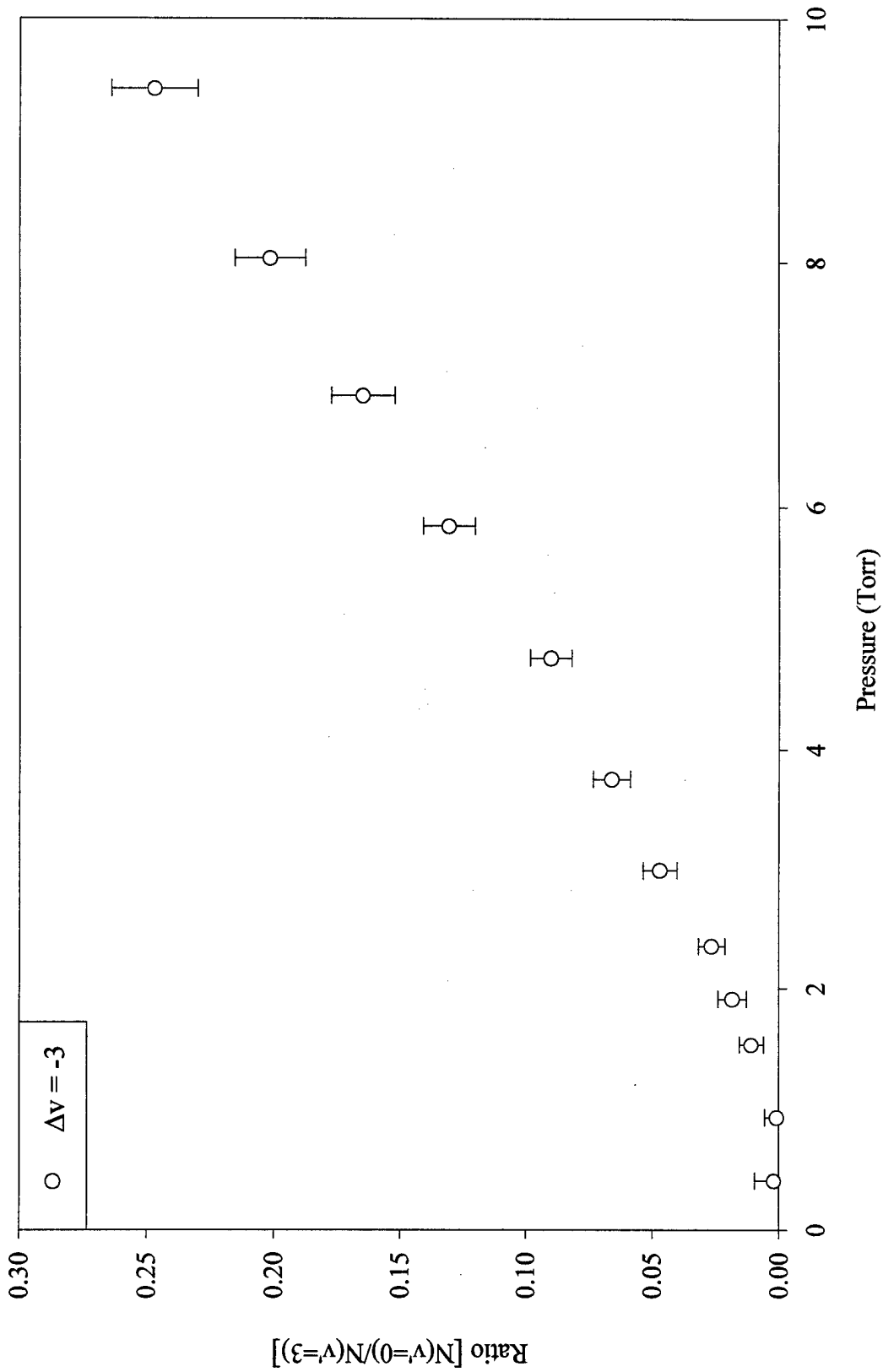


Figure 4.5 Plot of the $\Delta v = -3$ population ratios after initially populating $v' = 3$. Neon is the collision partner.

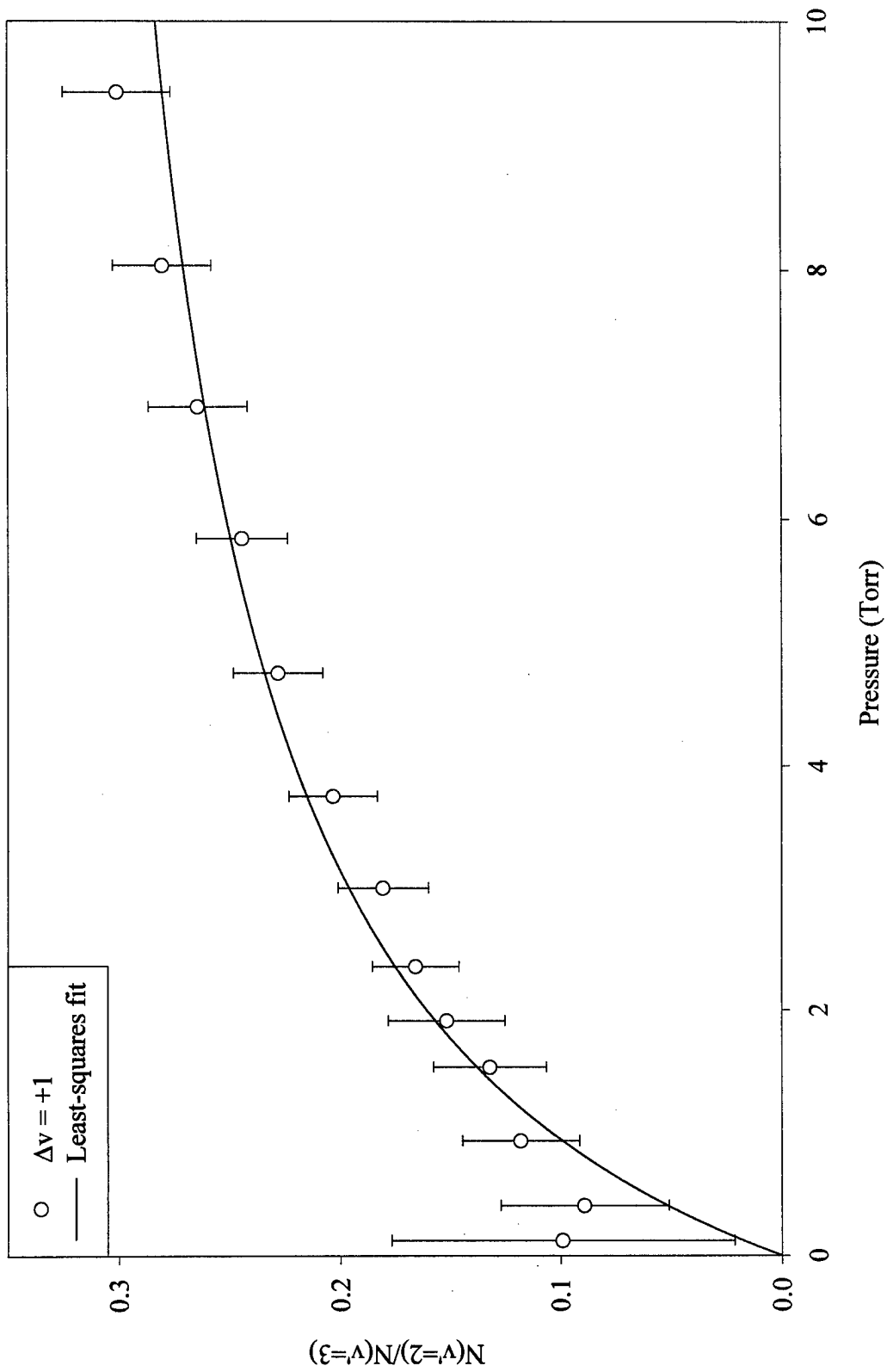


Figure 4.6 Comparison of the $\Delta v = +1$ population ratios after initially populating $v' = 3$ with a least-squares fit to the data. Neon is the collision partner.

This assumption was the basis for the fitting equation

$$\frac{N(v')}{N(v'_0)} = \frac{a[M]}{1 + b[M]} \quad (4.7)$$

developed in Section 2.3.3. As a reminder, $[M]$ is the bath gas pressure $a[M]$ accounts for direct transfer into the observed vibrational level and $b[M]$ accounts for various secondary collisions. The vibrational transfer rate is derived from the relation, $k_v(v'_0 \rightarrow v') = a\Gamma(v')p$. The solid line running through Figures 4.3, 4.4 and 4.6 is the result of this fit being applied to the data at hand. Table 4.2 lists the a and b parameters obtained for all pump-view combinations when using neon as a buffer gas and applying Equation 4.7 to observed population ratios as a function of neon buffer gas pressure. In the current experiments, multiple collision conditions certainly exist. This fact is best demonstrated by Figure 4.5 which could not be fit by Equation 4.7. At very low pressures, there is little, if any population seen in this $\Delta v = -3$ level. Only at higher pressures does the population in this level start to build directly suggesting that multiple collisions are responsible for population of the $v' = 0$ vibrational level. Furthermore, Figure 4.6 shows that transfer up the vibrational ladder is also present, suggesting that repopulation of the parent level from collisionally populated levels ($v' \pm 1 \rightarrow v'$) may also be an important consideration. These factors suggest that direct vibrational transfer from the parent state is an overly simplistic model for the V-T transfer kinetics. Thus, it is probably best to view the “ a ” coefficient as a first guess at the actual transfer coefficient. The method for refining this guess will be discussed in the next section.

4.4.2 Rate Matrix Technique. The rate matrix technique described in Appendix A was used to find the best vibrational transfer coefficients for all sets of spectrally resolved fluorescence profiles. Additionally, this technique provided information on the electronic quenching rate, the multi-quantum vibrational transfer rate ($\Delta v = \pm 2$) and the translational temperature of the collision process. The

Table 4.2 Fit parameters obtained from the direct transfer equation for $\text{Bi}_2(\text{A})$ vibrational transfer population ratios as a function of neon buffer gas pressure. Listed errors are the fit standard error for that parameter.

Parent State v'_0	Satellite State v'	a torr ⁻¹	b torr ⁻¹
1	0	0.1321 ± 0.0020	0.0780 ± 0.0030
	2	0.1240 ± 0.0119	0.3904 ± 0.0554
2	0	0.0447 ± 0.0015	0.0153 ± 0.0046
	1	0.2006 ± 0.0086	0.2347 ± 0.0175
	3	0.1443 ± 0.0087	0.4485 ± 0.0393
	4	0.0368 ± 0.0078	0.3071 ± 0.1035
3	0		
	1	0.1171 ± 0.0081	0.1689 ± 0.0231
	2	0.3158 ± 0.0090	0.4159 ± 0.0176
	4	0.1175 ± 0.0055	0.2983 ± 0.0223
4	3	0.4082 ± 0.0227	0.4627 ± 0.0369
	5	0.1560 ± 0.0115	0.6447 ± 0.0636

following conditions were placed on the various terms of the rate matrix. A single vibrational lifetime of 590 ns was used for all v' levels. This value is the reported lifetime of the ($v' = 1, J' = 10$) rovibrational level (23). All reported rotational state lifetimes in the $v' \leq 5$ vibrational levels are in the approximate range of 500-600 ns. Landau-Teller scaling of the vibrational transfer rates was assumed. This type of scaling has been found to be appropriate even for strongly coupled ($\omega_e/k_B T < 1$) systems (7). Multi-quantum transfer was allowed for $\Delta v = \pm 2$ but not for $\Delta v \geq 3$ with all multi-quantum rates being held at a fixed fractional value of the corresponding $\Delta v = \pm 1$ rate from the same initial v' level. Detailed balance for the inverse rates was assumed. Figures 4.7 - 4.10 show typical predictions of population ratios as a function of buffer gas pressure. These particular figures depict the predictions for the initially pumped level $v' = 3$. As can be seen, there is reasonable reproducibility of the $\Delta v = \pm 1$ population ratios. The ratios predicted for $\Delta v = -2, -3$

Table 4.3 $\Delta v = -1$ vibrational transfer rate coefficients (k_v), upper bound electronic quenching rate ($k_q \times 10^{-12} \text{cm}^3/\text{molec-sec}$), translational temperature, and multi-quantum fraction number (f) for Bi_2 collisions with Neon buffer as determined from a rate matrix solution. For comparison purposes, the $\Delta v = -1$ transfer coefficient from the direct transfer equation is also listed.

v' pump	Direct Transfer $k_v(v' \rightarrow v' - 1)$	Rate Matrix $k_v(v' \rightarrow v' - 1)$	k_q <	Temperature K	f
1	6.34 ± 0.70	6.24	0.92	240	0.16
2	9.62 ± 0.68	9.62	2.93	270	0.10
3	15.14 ± 1.40	14.13	3.33	264	0.12
4	19.57 ± 3.48	19.24	3.28	190	0.05

are not as reasonably reproduced, yet the predicted behavior from the rate matrix technique still provides insight to the population mechanisms of these satellite levels. Table 4.3 lists the important fit parameters used in the rate matrix calculations. The next several paragraphs will discuss the significance of the different columns in Table 4.3. An important point to remember about the rate matrix approach, is that this method predicts an entire set of population ratios based off only four independent parameters. Three of these parameters provide information not readily available from the direct transfer equation. A final paragraph will summarize possible deficiencies present in the rate matrix approach that prevent the $\Delta v = -2, -3$ levels from being predicted any more accurately.

The second and third columns of Table 4.3 show that the $\Delta v = -1$ rates determined from the direct transfer equation were entirely consistent with the same values determined from the rate matrix approach. Since these two terms are of approximately equal value, it is assumed the error bound on the rate matrix $\Delta v = -1$ vibrational transfer rates is equal to the error bound associated with the direct transfer calculations. A plot of the rate matrix determined $\Delta v = -1$ rates as a function of vibrational quantum number, v' , is shown in Figure 4.11. This figure shows $\Delta v = -1$ transfer rates can be described with linear scaling of the vibrational

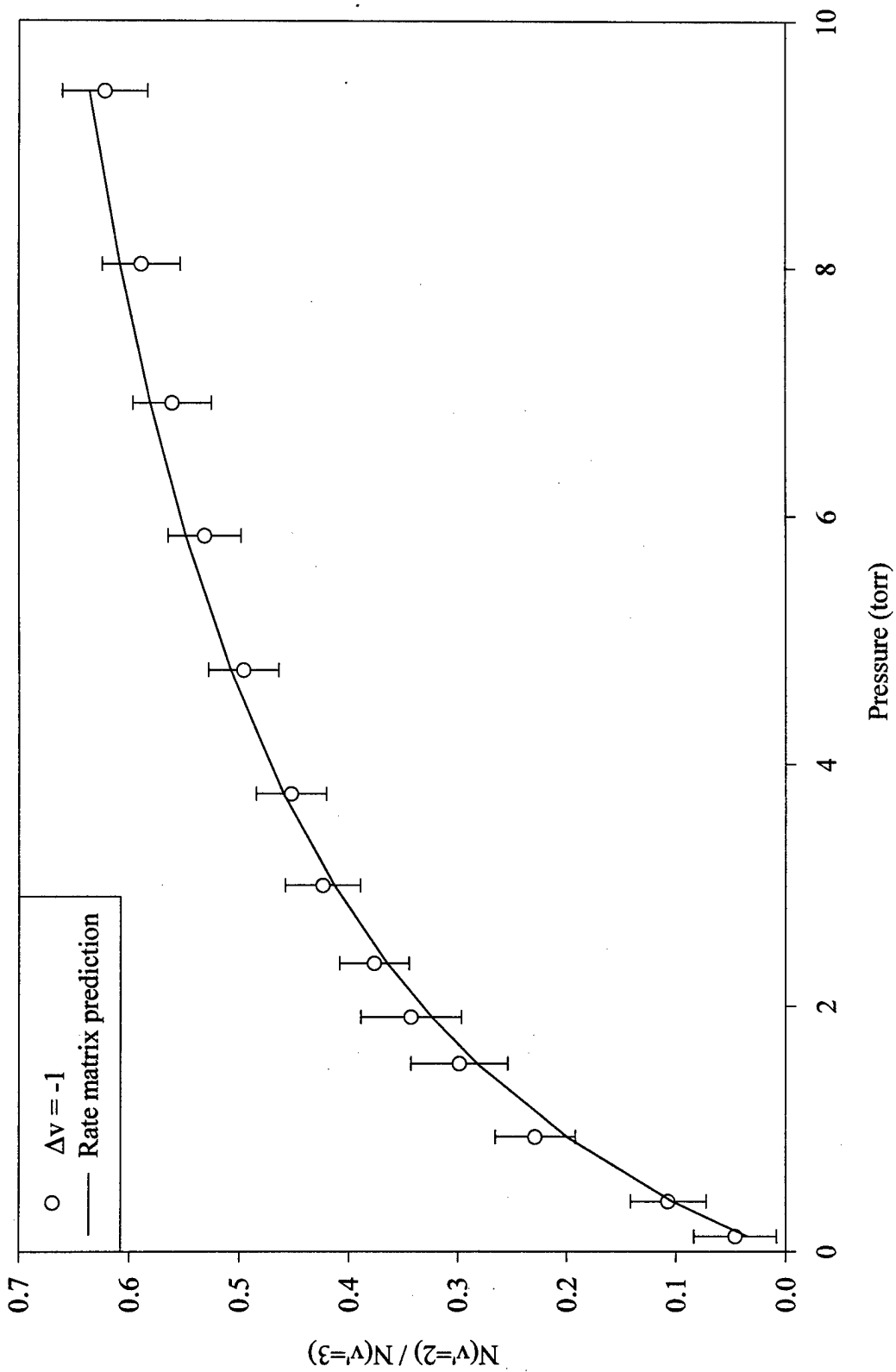


Figure 4.7 Comparison of the $\Delta v = -1$ population ratios after initially populating $v' = 3$ with the predicted ratio from the rate matrix calculations.

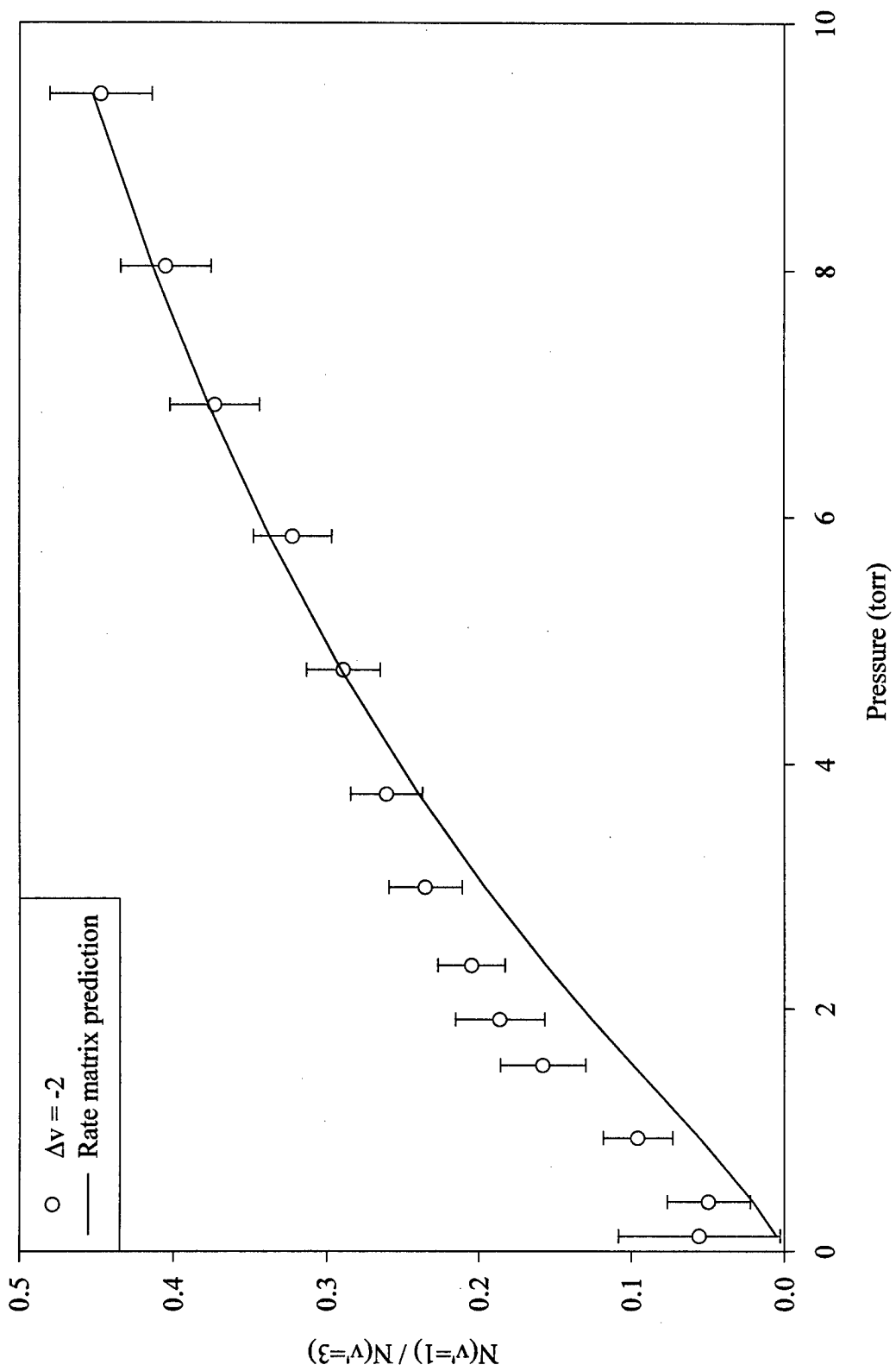


Figure 4.8 Comparison of the $\Delta v = -2$ population ratios after initially populating $v' = 3$ with the predicted ratio from the rate matrix calculations.

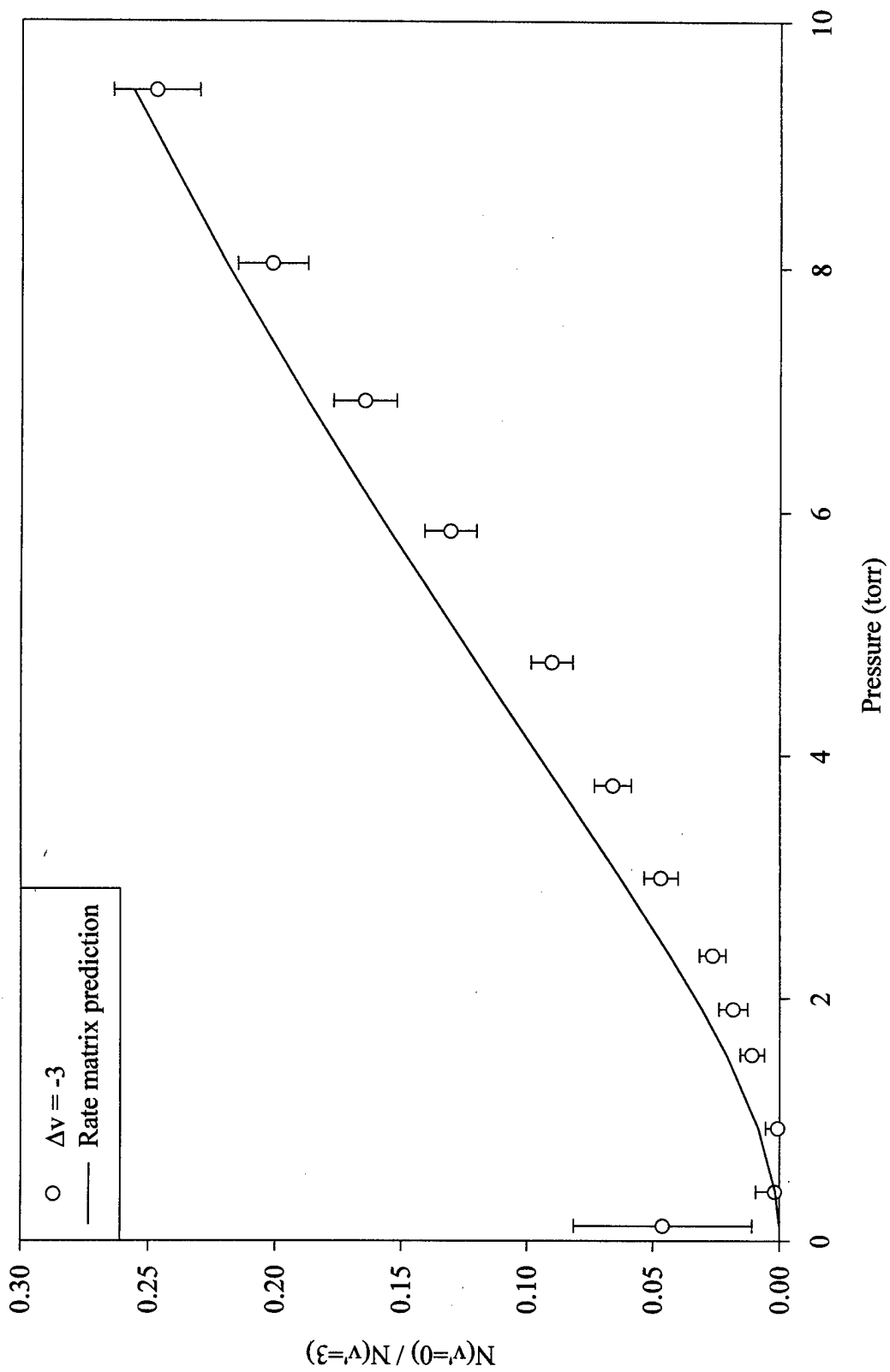


Figure 4.9 Comparison of the $\Delta v = -3$ population ratios after initially populating $v' = 3$ with the predicted ratio from the rate matrix calculations.

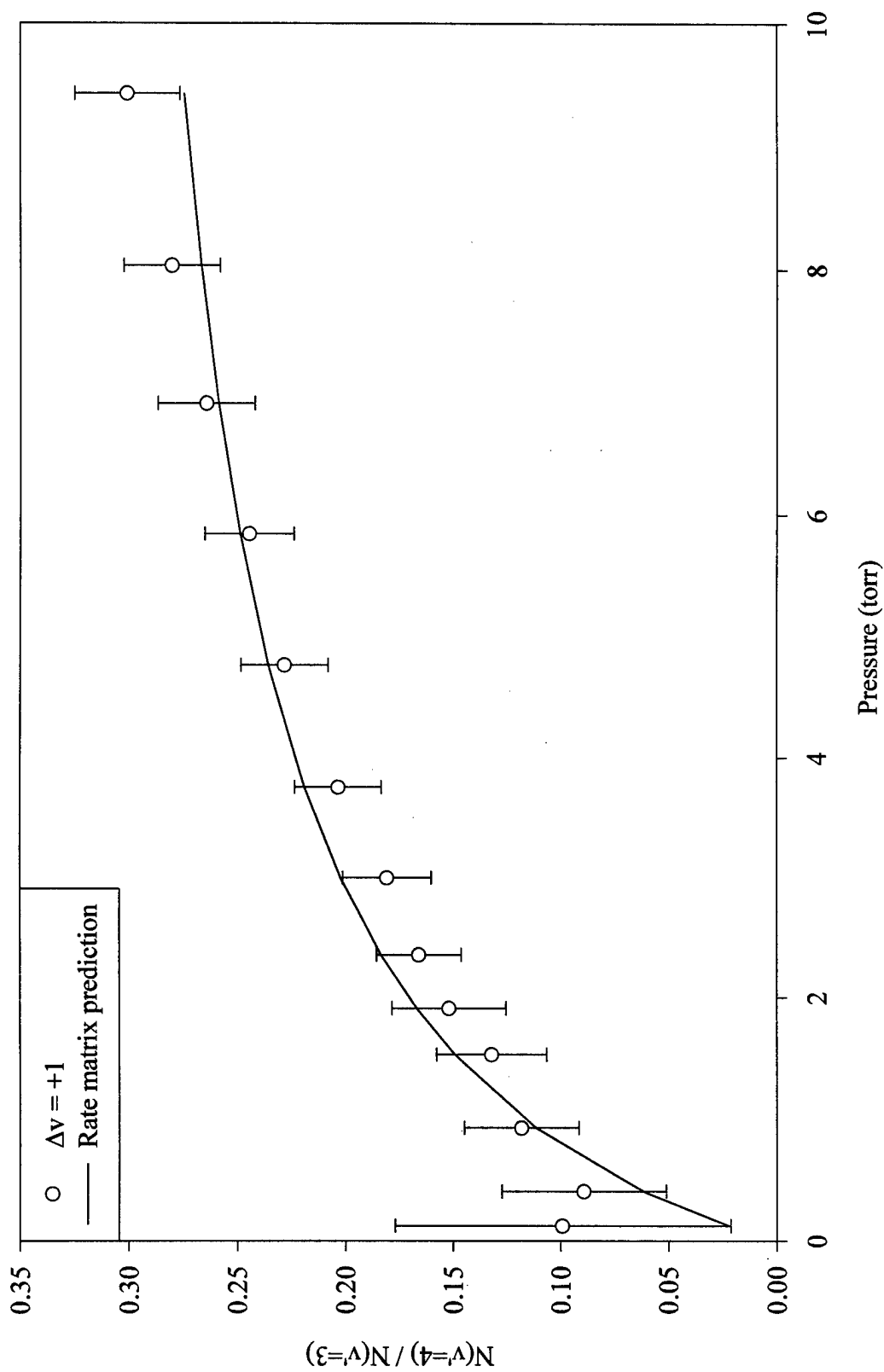


Figure 4.10 Comparison of the $\Delta v = +1$ population ratios after initially populating $v' = 3$ with the predicted ratio from the rate matrix calculations.

quantum number (v'). Thus, for the low v' levels of Bi_2 (A), Landau-Teller scaling is an entirely reasonable assumption. A linear regression of these four data points yields a fundamental vibrational transfer coefficient of $k_v(1,0) = (4.84 \pm 0.87) \times 10^{-12} \text{cm}^{-3}/\text{molec-sec}$. The error bound on these terms are derived from a least-squares fit to the upper and lower limits of the different $\Delta v = -1$ terms. The consistency of the $\Delta v = -1$ terms derived from the two different approaches validates the use of the direct transfer equation for the determination of fundamental transfer rates for Bi_2 collisions with other rare gas collision partners.

The fourth column of Table 4.3 lists an upper bound on the electronic quenching term used in the rate matrix. Larger quench rates than the stated value precluded acceptable fits being calculated with this approach. An assumption was made that this term is independent of vibrational level (v'). From the range of values shown in Table 4.3, this may or may not be a valid assumption. The apparent poor fit of the $\Delta v = -3$ population ratios is another indication that quenching rates might exhibit a vibrational state dependence. A set of pulsed LIF experiments would help to determine this value more accurately. The reported electronic quenching terms provide a first estimate of their actual values.

One truly surprising finding from the rate matrix calculations was that it took a low temperature for detail balance to properly predict the $\Delta v > 0$ transfer rates. For example, a temperature of 190 K was used to fit the $v' = 4$ data. This is despite the fact the Bi_2 was created at temperatures in excess of 800 K. An interesting observation was made when examining the "c" parameter of the spectral fitting function. As was explained in Section 4.3.2, this parameter is the fit function equivalent of the rotational temperature of the vibrational band. The relation between c and T is expressed by Equation 4.2. The spectral fitting function predicted a temperature of (254 ± 49) K for the parent state and (612 ± 103) for the satellite states. Thus, the rotational temperature of the parent state is also very low. Table 4.4 lists the spectral fitting function rotational temperatures for both parent and satellite states

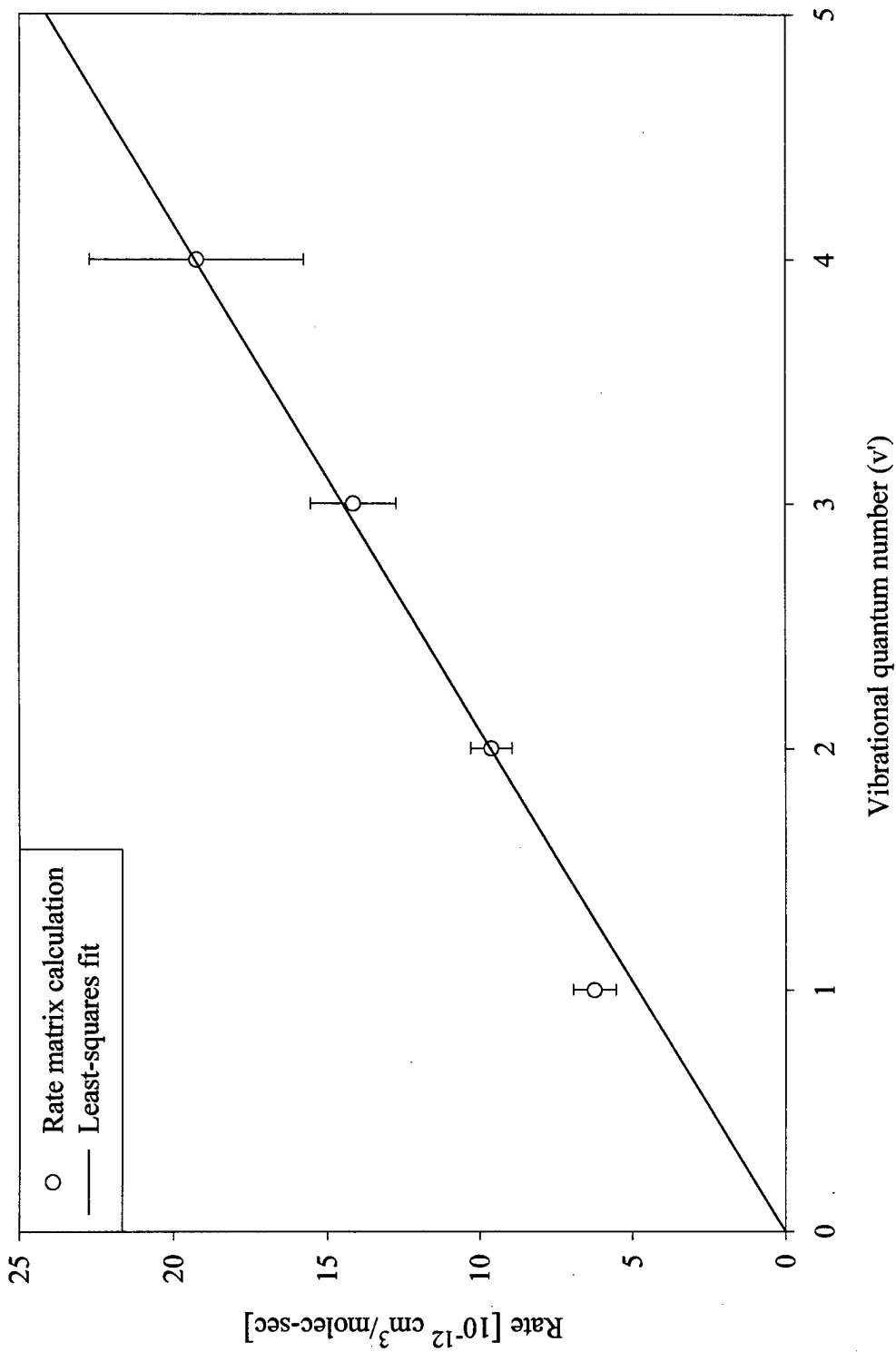


Figure 4.11 Plot of the $\Delta v = -1$ vibrational transfer rates versus the vibrational quantum number, v' . The straight line represents a linear regression of this data and indicates a fundamental transfer rate of $k_{v(1,0)} = (4.84 \pm 0.87) \times 10^{-12} \text{ cm}^3/\text{molec-sec}$

Table 4.4 Comparison of rate matrix temperatures with rotational temperatures for Bi₂ collisions with neon buffer gas.

v'_0	Parent State Temp K	Satellite State Temp K	Rate Matrix Temp K
1	389 ± 90	639 ± 100	240
2	427 ± 111	528 ± 91	270
3	385 ± 102	630 ± 80	264
4	254 ± 49	612 ± 103	190

as well as the predicted temperature from the rate matrix approach for comparison purposes only. As was pointed out earlier, the parametric fit of the "c" parameter to the rotational temperature is strongly dependent on the resolution parameter of the synthetic spectrum accurately matching the instrumental resolution of the monochromator. Thus, this is strictly a qualitative comparison and is not intended to quantify the rotational temperature of the vibrational bands. In all cases, the lower bound of the parent state rotational temperature was approximately equal to the translational temperature predicted from the rate matrix approach.

Another check on the temperature of the Bi₂ was accomplished by examining the laser excitation spectra from Chapter III. The Boltzmann distribution for a thermal population among rotational states, J , is given by (25)

$$N(J)/N_T = (hcB''_v/kT_R)(2J + 1)\exp[-B''_v J(J + 1)hc/kT_R] \quad (4.8)$$

where $N(J)$ is the population in rotational state J , N_T is the total population in state v'' , B''_v is the rotational spectroscopic term value for state v'' and T_R is the rotational temperature. Since fluorescence intensity is proportional to number density, Equation 4.8 yields

$$\ln(I_J/2J + 1) = C - (B''_v hc/kT_R)J(J + 1) \quad (4.9)$$

where C is a constant. This is a linear equation where the slope provides the information to extract the rotational temperature. Figure 4.12 is a plot of $\ln(I_J/2J + 1)$ versus $J(J + 1)$ for the ($v'' = 4 \rightarrow v' = 1$) vibrational band for $J < 58$. The resulting rotational temperature predicted from this plot is 316 ± 29 K. This data is rather noisy as no attempts were made to normalize the laser excitation spectrum for possible fluctuations in laser power. However, this plot still helps illustrate that the Bi_2 is probably at a much cooler temperature in the interaction area of the fluorescence cell than the higher temperatures needed to cause its vaporization. A possible explanation is that as the Bi_2 diffuses into the fluorescence cell, it gives up a considerable amount of energy to the bath gas. Thus, when the Bi_2 reaches the interaction area of the cell, it has cooled considerably, possibly even lower than its melting point. This would account for the low temperatures predicted from detail balance rates and the laser excitation spectra.

The rate matrix calculations found a $|\Delta v| = 2$ transfer rate that was approximately 0.1 of the $|\Delta v| = 1$ rate originating from the same v' level. $|\Delta v| = 3$ rates were found to be insignificant. The predicted population ratios were fairly sensitive to changes in the multi-quantum fraction, f . Even though no error bounds are reported for this term, the multi-quantum fraction probably varies by no more than ± 0.05 . Thus, multi-quantum transfer is not a significant factor in vibrational transfer processes for the Bi_2 (A) state. Due to the small anharmonicity ($\omega_e/kT \approx 0.63$) and vibrational spacing of the Bi_2 A-state, this result indicates anharmonicity and not vibrational frequency dominates the magnitude of multiquantum transfer. This result is in agreement with the findings of Holmberg where he reported a multi-quantum fraction of $\approx 10\%$ for Br_2 collisions ($\omega_e/kT \approx 0.62$) (12) and Perram, who reported a multi-quantum fraction of ≈ 0.4 for BrCl ($\omega_e/kT \approx 0.62$) (13).

As was previously mentioned, the predicted population ratios in the $\Delta v = -2$ and -3 levels is not represented as well as the $\Delta v = \pm 1$ levels. However, their qualitative behavior is reproduced quite well. The rate matrix approach shows that

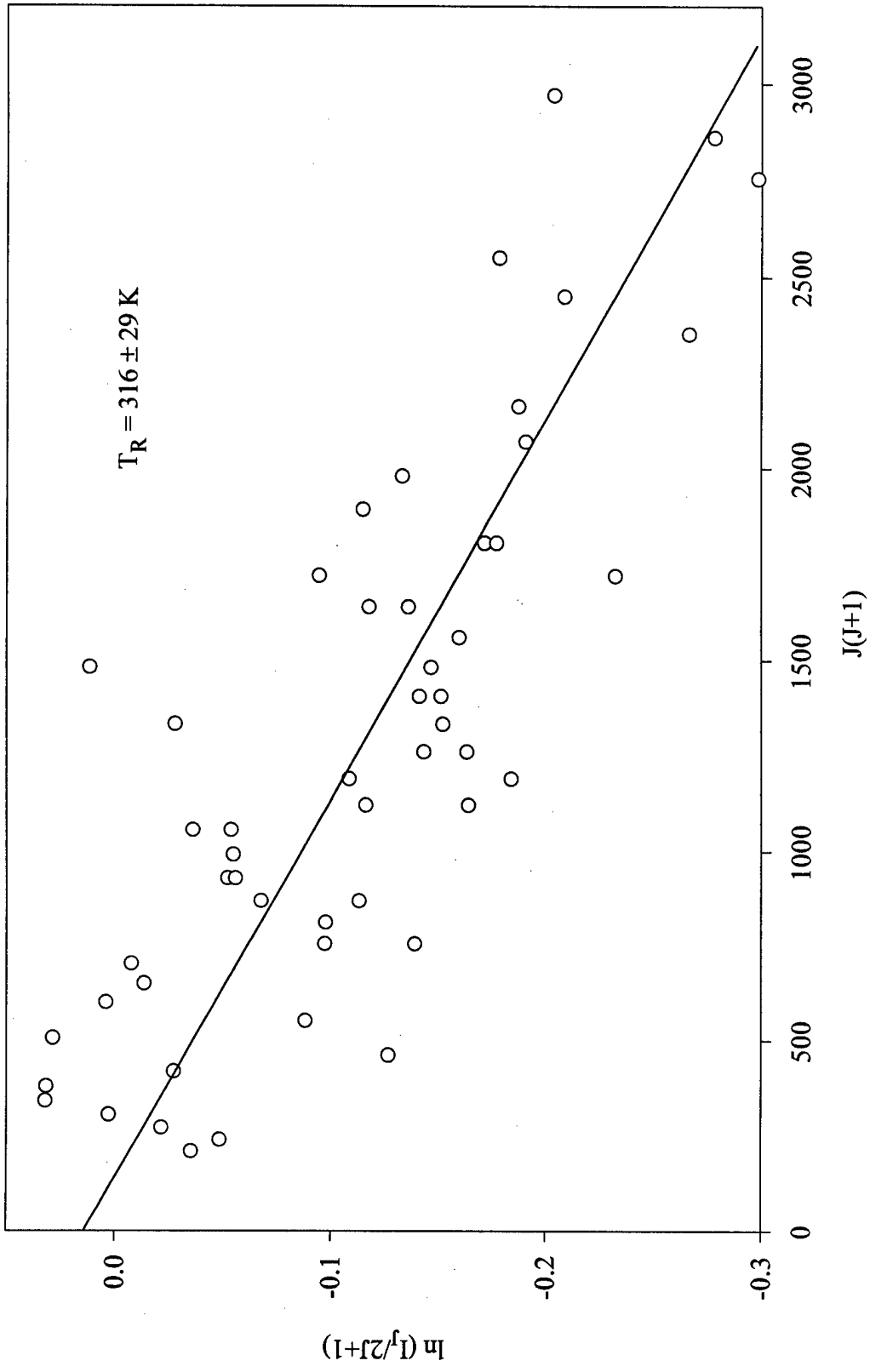


Figure 4.12 Rotational temperature of $v''=1$ at a mix pressure of 1.2 torr of nitrogen buffer gas. Data comes from laser excitation of the $v''=1$ to $v'=4$ transition.

vibrational transfer to $\Delta v = -3$ is most likely the result of cascade transitions from the parent state. Even though the direct transfer approach models the behavior of the $\Delta v = -2$ level well within the reported error bounds, the rate coefficients derived from this approach must be viewed as an upper bound on the actual transfer rate. It is reasonable to assume that population in this satellite state is derived not only from direct transfer from the parent state, but also as the result of multiple collision processes. The errors between the rate matrix predicted population ratios in $\Delta v = -2$ and -3 as opposed to the experimental measurements probably stem from a failure of the assumptions used to define the different elements of the rate matrix. First, a constant multi-quantum fraction was assumed for all $\Delta v = -2$ transfer rates. It is possible this fraction may vary depending on the specific rate matrix element. Second, a constant electronic quenching rate was assumed for all vibrational levels in the A-state. Previous studies on the diatomic halogens have shown that electronic quench rates may have a vibrational level dependence (7). Next, a constant lifetime was assumed for all vibrational levels. The slight variation between experimental and theoretical Franck-Condon factors discussed at the end of Chapter III may indicate a slight variation in the vibrational state lifetimes. Finally, errors in the Franck-Condon factors used to scale the different vibrational bands could lead to incorrectly determined population ratios. However, the spectral fitting technique developed for this research should minimize this error due to its fit over multiple vibrational bands.

4.4.3 Helium, Argon, Krypton, Xenon. As in previous studies (7), the remaining rare gases were studied in less detail. Thus, for helium, krypton and xenon only level $v' = 2$ was pumped while $v' = 3$ was pumped for argon. Table 4.5 lists the fundamental vibrational transfer rate derived from Landau-Teller scaling of the observed $\Delta v = -1$ transfer rate for all buffer gases used in this experiment as well as the calculated $\Delta v = -1$ rate. The error bounds given in the table are derived

Table 4.5 Fundamental vibrational transfer rate coefficients and $\Delta v = -1$ rate coefficients (10^{-12} cm³/molec-sec) for Bi₂ (A) collisions with the rare gases

rare gas	pump level v'	$k_v(1,0)$	$k_v(v, v-1)$	$\sigma_v(1,0)/\sigma_g$
He	2	5.29 ± 0.73	10.57 ± 1.47	0.0075
Ne	1-4	4.84 ± 0.87		0.0142
Ar	3	2.53 ± 0.41	7.60 ± 1.22	0.0089
Kr	2	2.38 ± 0.36	4.77 ± 0.72	0.0112
Xe	2	3.41 ± 0.65	6.81 ± 1.30	0.0175

from a least-squares fit to the upper and lower error bounds on the population ratios derived from the spectral fitting function.

4.5 Comparison to SSH Theory

According to the SSH theory, vibrational transfer probability for collisions between diatomic and monatomic collision partners is dependent on the vibrational spacing of the diatomic, the reduced mass of the collision pair and the interaction length between the two particles. According to Yardley (46) the full form of the SSH theory is

$$P_{10} = M \cdot \left(\frac{\Theta'}{\Theta}\right) \left(\frac{\Theta'}{T}\right)^{1/6} \exp\left[-\frac{3}{2}(\Theta'/T)^{1/3} + (\Theta/2T) + (\varepsilon/k_B T)\right] \quad (4.10)$$

where

P_{10} = Probability of V→T transfer from state 1 to state 0

$$M = \sqrt{\frac{2\pi}{3}} \frac{4A^2BC}{(B+C)(A+B)^2 \cdot \mu}$$

A = mass of collision partner

B, C = masses of the diatomic molecule

μ = reduced mass of collision pair

$$\Theta' = 4\pi^2 L^2 \omega^2 \mu / k_B$$

$$\Theta = \hbar\omega/k_B$$

ε = potential well depth for the collision partners

L = interaction length

If the the exponential term in Equation 4.10 dominates the behavior, the V→T transfer probability should obey the relation

$$\ln(P_{10}) \propto \ln(\sigma_v(1,0)/\sigma_g) = A - B\mu^{1/3} \quad (4.11)$$

This equation says that transfer probability should decrease with increased reduced mass of the collision pair. This probability for Bi₂ collisions with rare gas collision partners is tabulated in Table 4.5. The gas kinetic cross-sections were calculated using atomic radii data from Hirschfelder (47) and Sienko (48) as discussed in Appendix A. These fundamental transfer probabilities are compared to previously reported values for IF(B), BrCl(B) and Br₂(B) in Figure 4.13. This plot shows the fundamental transfer probability plotted as a function of the cube root of the reduced mass of the collision pair. The three comparison cases show three different behaviors of this functional form. IF exhibits the reduced mass dependence as predicted by Equation 4.11. BrCl exhibits a response fairly independent of reduced mass while Br₂ trends in entirely the wrong direction with a positive slope. Bi₂, like BrCl, shows no clear trend in the fundamental transfer rates's dependence on the reduced mass of the collision pair. Surprisingly, the transfer rates calculated for Bi₂ behave similarly to those found for BrCl. As the vibrational spacing of Bi₂ is smaller than that of Br₂, the order of magnitude reduction in vibrational energy transfer rates with respect to Br₂ is a surprising result. It needs to be remembered that bismuth is a Group V atom while bromine is a Group VII atom. Thus it is entirely possible that the different electronic configurations of the two different diatomics is also having an effect on vibrational energy transfer.

From a classical point of view, V-T transfer is most efficient when the duration of the collision is similar to the vibrational period (9). The mean collision time, τ_c can be calculated from

$$\tau_c = L/v_g \quad (4.12)$$

where L is the interaction length and v_g is the mean relative velocity, $v = (8kT/\pi\mu)^{1/2}$. Generally, lower reduced mass results in higher relative velocities between collision partners with a subsequent higher probability of vibrational energy transfer. However, as seen in Figure 4.13, this trend is not apparent. The vibrational transfer probabilities are relatively independent of reduced mass dependence indicating that all collisional partners are equally efficient at inducing vibrational energy transfer.

The SSH theory was developed with time-dependent perturbation theory where interactions are weak and $\Delta v = \pm 1$. In IF ($\omega_e/kT \approx 2$) this approximation is certainly reasonable. However, in BrCl ($\omega_e/kT \approx 1.1$), Br₂ ($\omega_e/kT \approx 1$) and Bi₂ ($\omega_e/kT = 0.63$) this condition is not very well met. Holmberg's analysis of vibrational transfer in Br₂ demonstrated that in strongly coupled systems the simplified form of the SSH theory does not accurately model vibrational energy transfer. As Bi₂ is more strongly coupled than Br₂, it is not surprising that the simplified SSH theory fails here too.

Holmberg noted that the above result possibly indicates that the pre-exponential term in Equation 4.10 plays an important role in determining vibrational energy transfer. Since the interaction length, L , can reasonably be expected to vary with different diatomic-buffer gas combinations, an interesting exercise was to calculate this value for the different collision pairs using the complete SSH equation. According to Yardley (46), accurate values for ε are difficult to obtain. In general, $\varepsilon \ll kT$, thus this exponential can be approximated to unity. Assuming this, values for the interaction length (L) were calculated for the different combinations of diatomic and rare gas species. These results are plotted in Figure 4.14 as a function of collision pair reduced mass. Two observations can be made from this data. First, as

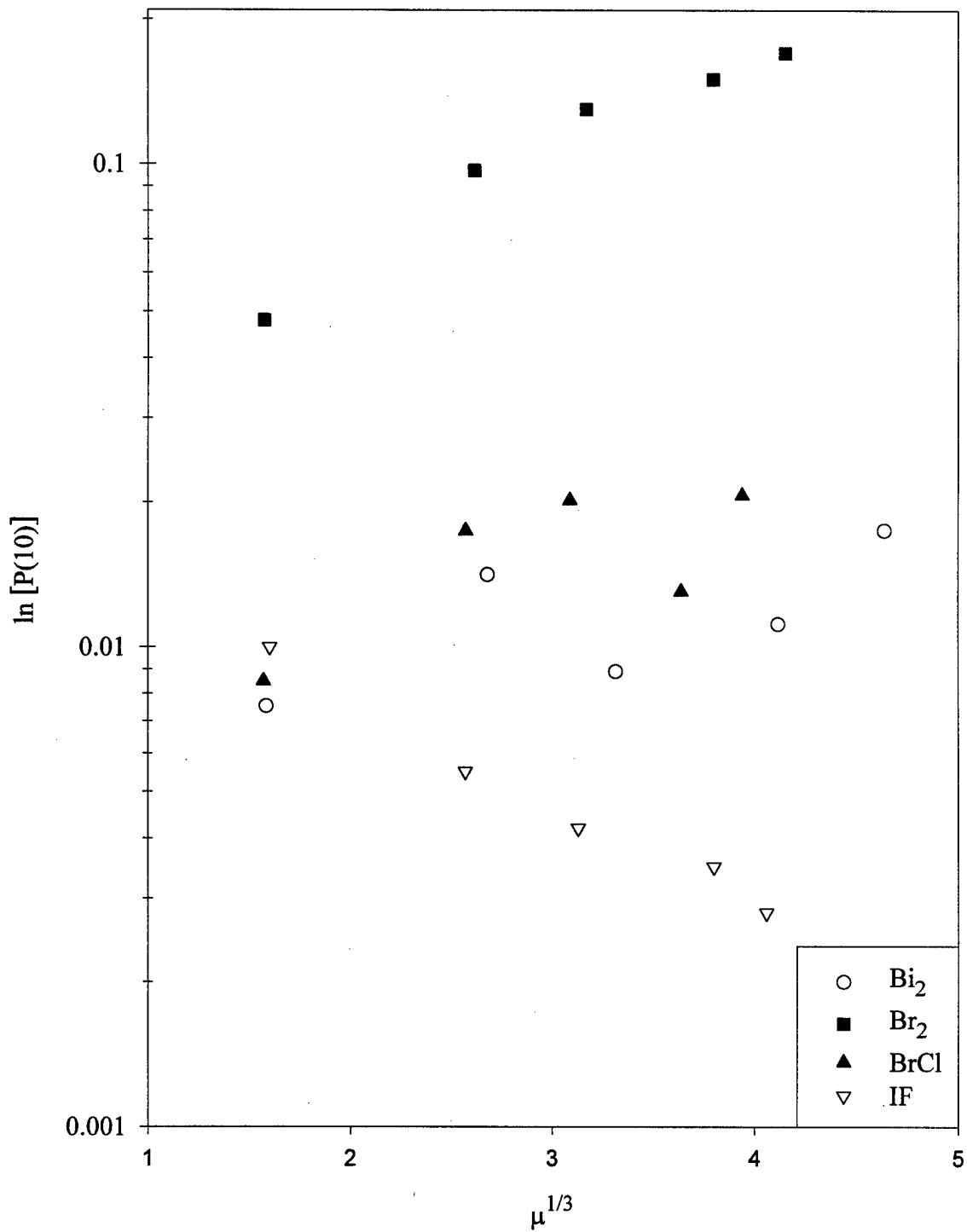


Figure 4.13 Vibrational transfer probabilities ($\Delta v = -1$) for Bi₂, Br₂, BrCl and IF with rare gas collision partners as a function of the cube root of the reduced mass

in the Holmberg study, the values obtained for L are reasonable in all cases. Yardley states that interaction lengths are typically on the order of a few tenths of an angstrom. This statement is consistent with the findings of this research. The second observation is that for each diatomic considered, the interaction length decreased as the mass of the collision partner increased. In the strongly coupled diatomics, this second observation implies that the interaction length decreases as the vibrational transfer probability increases. Interestingly, when comparing the interaction lengths for BrCl and Bi₂, the two species that had very similar fundamental transfer rates for collisions with the rare gases, the Bi₂ length was consistently larger. Considering that Bi₂ is a physically larger molecule than BrCl, this is a reasonable result. As a matter of fact, the Bi₂ interaction lengths were larger than all the other diatomics compared. As Holmberg points out, while the validity of the SSH perturbational approach is questionable for strongly coupled diatomic molecules, the consistent reduced mass trends imply the SSH theory might still be applicable for the class of strongly coupled diatomics. Finally, the earlier failure of the simplified SSH equation points out that the pre-exponential factors are an important part of this theory.

4.6 Conclusions

CW LIF has been used to study vibrational energy transfer for Bi₂ (A) collisions with rare gas collision partners. Rate matrix techniques have been used to provide a more solid understanding of the kinetics involved. Multi-quantum transfer does not occur with great frequency even though the Bi₂ system has very small vibrational energy spacing. From comparisons with previous studies on the diatomic halogens and interhalogens, this trend indicates that anharmonicity is the dominant factor in determining multi-quantum fractions for vibrational transfer. Fundamental vibrational transfer rates have been found that range from 2.38×10^{-12} cm³/molec-sec for collisions with krypton to 5.298×10^{-12} cm³/molec-sec for collisions with helium. The scaling of the various $\Delta v = -1$ transfer rates has been found to be

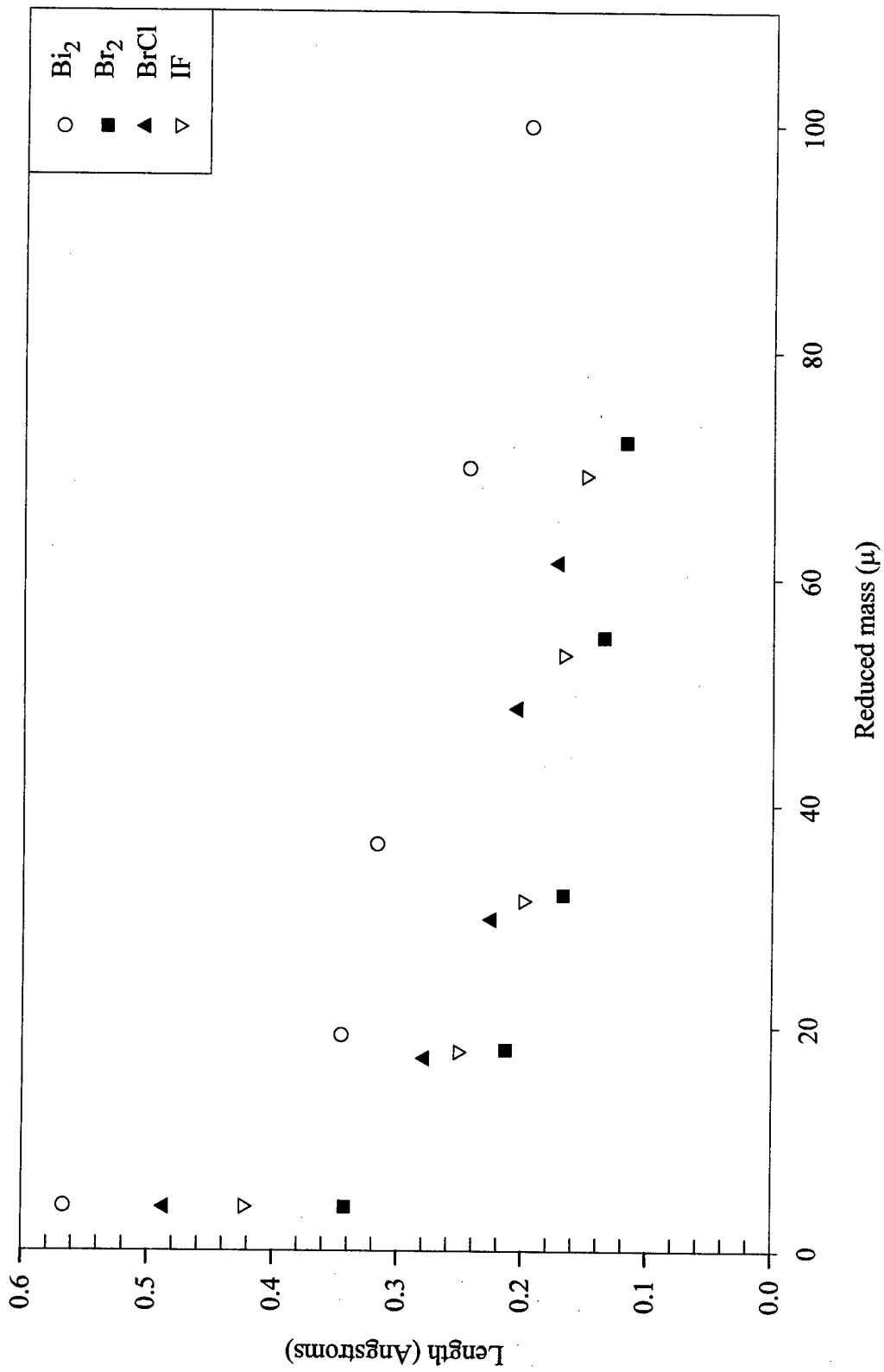


Figure 4.14 Interaction lengths as a function of collision pair reduced mass for Bi_2 , Br_2 , BrCl and IF .

adequately described with the use of Landau-Teller scaling. As in the case of other diatomics with small vibrational spacing, Bi_2 do not display an inverse relationship between vibrational transfer probabilities and increasing reduced mass of the collision pair. No comparisons can be made with previous Bi_2 kinetic studies as this is the first attempt at a detailed study of kinetic processes involving the Bi_2 A state.

V. Rotational Energy Transfer in Bi_2 $A(0_u^+)$

5.1 Introduction

The study of rotational energy transfer in Bi_2 is particularly interesting due to the extremely small rotational spacing between successive rotational levels. As shown in the spectroscopy section of this dissertation, this small spacing allows the accessing of high J rotational levels ($J \geq 200$) with relative ease allowing the determination of rotational transfer rates to a multitude of lower rotational levels without reaching the band origin. Energy transfer between rotation and translation (ΔE_r) can be investigated by comparing the experimentally derived rotational transfer rates with empirical expressions dependent on this E_r . Two common expressions used for this comparison are the exponential gap law (36) and the statistical power gap law (38, 37). In this study on rotational energy transfer in the Bi_2 $A(0_u^+)$ state, state-to-state rotational transfer rates are determined for Bi_2 collisions with helium, neon and argon. These rates are then fit to these two laws.

5.2 Experimental Setup

The experimental setup and procedures for the rotational energy transfer studies were identical to the vibrational transfer experiments with two exceptions. The 0.3 m monochromator was replaced by a 1.3 m monochromator (McPherson model 209) for increased resolution. The monochromator had 1800 groove/mm grating blazed for wavelengths from 350-850 nm. The dispersion of the monochromator was 0.46 nm/mm and allowed for a simultaneous collection of approximately 8.0 nm of spectra on the OMA. Second, pressure in the fluorescence cell was varied over a smaller range (70-1400 mtorr).

5.3 Experimental Procedures

5.3.1 Data Collection. Rotational energy transfer within the Bi_2 $A(0_u^+)$ state was studied after excitation of a single rovibrational level. The ability to accomplish this task was demonstrated in previous chapters of this dissertation. The following laser frequencies were used to excite the respective (v', J') states of Bi_2 : $17256.066 \text{ cm}^{-1}$ for $(v'_0 = 1, J'_0 = 171)$; $17222.215 \text{ cm}^{-1}$ for $(v'_0 = 1, J'_0 = 201)$; and 17185.199 for $(v'_0 = 1, J'_0 = 231)$. Helium was used as a collision partner in conjunction with all three frequencies listed. Neon and Argon were used as a collision partner for only the (1,201) pump transition. Emission spectra were rotationally resolved through a 1.3 m monochromator and recorded with a 1024 channel optical multi-channel analyzer.

Figure 5.1 provides a typical spectrally resolved fluorescence spectrum showing the effects of rotational energy transfer. This data was obtained using 783 mtorr of helium buffer gas. There is a strong P-R emission doublet arising from the single, initially populated state Bi_2 ($A, v'_0 = 1, J'_0 = 231$). The weaker satellite transitions are from nearby collisionally populated rotational states. This spectrum was gathered with the entrance slit at $6 \mu\text{m}$ and a full width at half max (FWHM) of 0.78 cm^{-1} . Note that the peaks of the satellite rotational levels are clearly discernible to $\Delta J = -30$. This was not always the case. As can be seen in Figure 5.2, a spectrum collected for the initially prepared state $(v'_0 = 1, J'_0 = 171)$, at $\Delta J = -30$ the individual rotational peaks are no longer discernible. This is despite the fact the entrance slit was reduced to $4 \mu\text{m}$ with a corresponding reduction in the FWHM to 0.54 cm^{-1} . The manner for dealing with this problem will be discussed in the next section. An interesting observation from Figures 5.1 and 5.2 is that only rotational levels with the same parity as the parent state are observed. A $\Delta J = \text{even}$ collisional selection rule applies because the nuclear spin is not readily altered by collisions. This same behavior was observed by Perram for rotational energy transfer in Br_2 (35) and is explained by Herzberg (25).

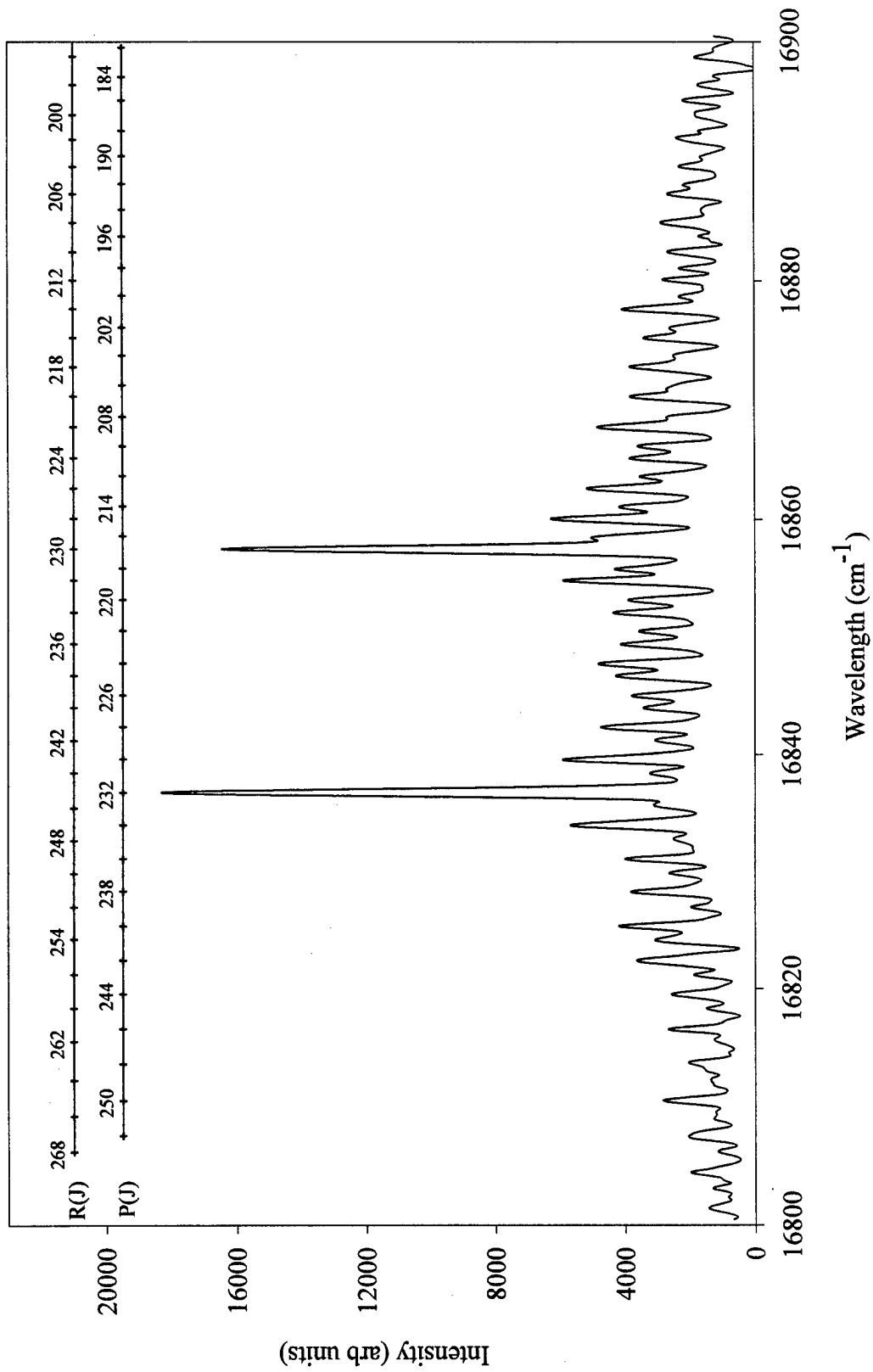


Figure 5.1 Spectrally resolved Bi₂ (A→X) laser-induced fluorescence from the v'=1 to v''=5 band in the presence of 753 mtorr of helium buffer gas. The parent rotational state is J'=231.

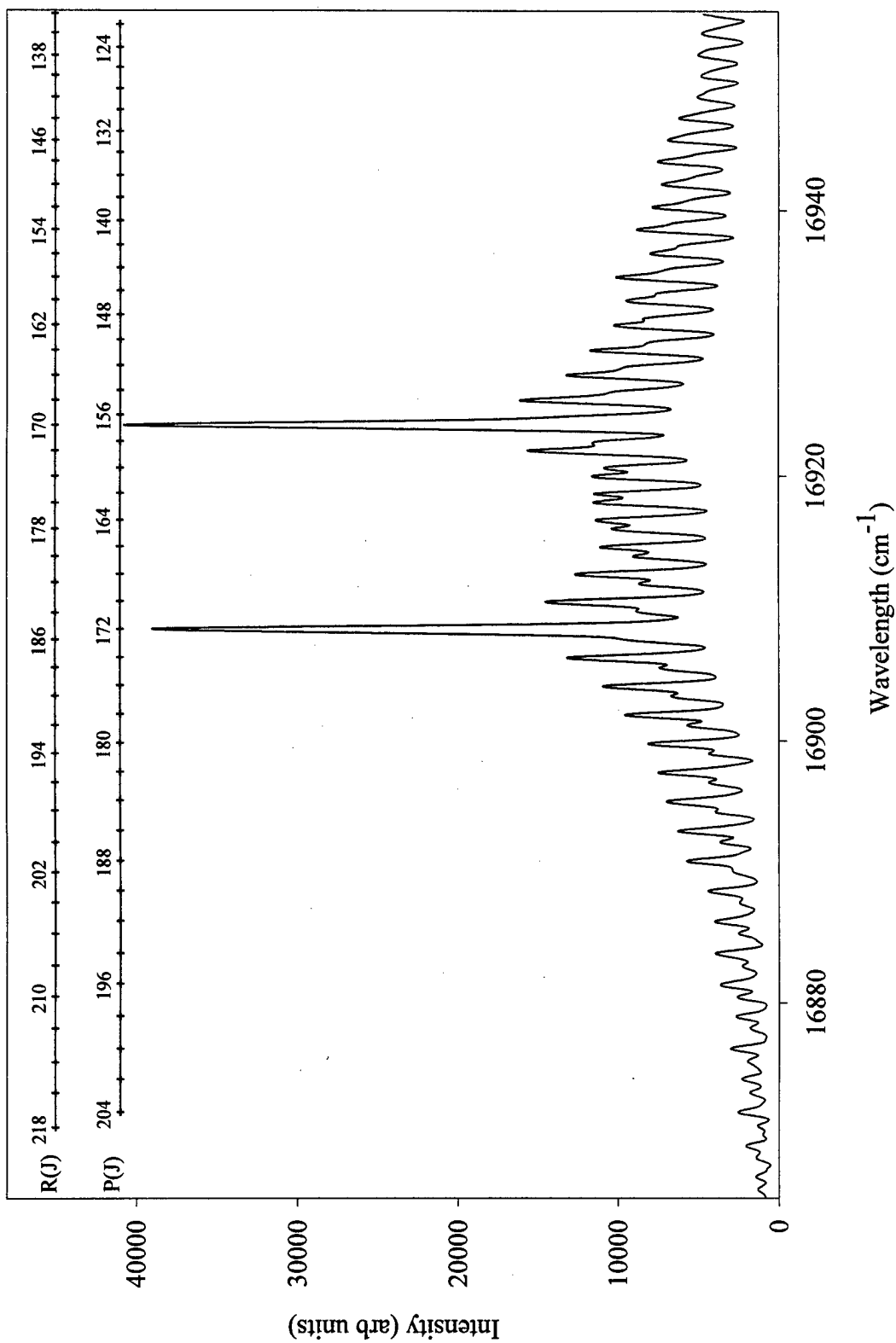


Figure 5.2 Spectrally resolved Bi₂ (A-X) laser-induced fluorescence from the v'=1 to v''=5 band in the presence of 855 mtorr of helium buffer gas. The parent rotational state is J'=171.

The population in the satellite rotational levels is typically quite high. In Figure 5.1 the $|\Delta J| = 2$ levels contain approximately 25% of the parent level population. As will be demonstrated later, state-to-state rotational transfer rates are typically 1-2 orders of magnitude more rapid than either electronic quenching or vibrational transfer thus allowing satellite states to build appreciable population levels at relatively low pressures.

5.3.2 Population Ratios. As in the vibrational transfer study, in order to utilize the equations developed in Chapter II to find the rotational energy transfer rates, the population ratio of daughter to parent state was found. As seen in Figures 5.1 and 5.2 individual rotational transitions were independently resolvable at $J \geq 160$. Below this value, system resolution precluded individual identification of the peaks the P-R doublets. However, there was still enough information in the spectrum to individually assign these transitions. Since the Doppler linewidth of the rotational transitions was 0.02 cm^{-1} (600 MHz), all rotational lines were instrumentally limited to the same linewidth. Assuming no tertiary transition was present under the unresolved P-R doublet, the wavelengths of the two transitions were found by locating the two functions which when summed together represented the unresolved emission doublet. The restriction that these two functions have the same linewidth, as defined by the linewidth of the parent state P-R doublet, made this possible. Thus, the task was simplified to defining the proper functional form of the individual rotational transitions.

Figure 5.3 depicts a single atomic transition of an Oriel neon calibration lamp as recorded on the optical multi-channel analyzer with a $5 \mu\text{m}$ entrance slit on the monochromator. This single transition is thus representative of each and every rotational transition observed in the spectrally resolved fluorescence. If this atomic transition can be mathematically modeled, a spectrally resolved vibrational band can be depicted by summing a series of these modeling functions - one for each rotational transition present in the spectrally resolved fluorescence. The center of the function

must be located at the transition wavelength and each function should have the same full width at half max. Overlaid on Figure 5.3 is a peak fitting function composed of a Gaussian-Lorentzian sum with the functional form

$$I_{GL}(\lambda) = 2a_0 \left[\frac{\kappa\sqrt{\ln 2}}{R\sqrt{\pi}} \exp\left(-4 \ln 2 \left(\frac{\lambda - \lambda_0}{R}\right)^2\right) + \frac{1 - \kappa}{\pi R \left[1 + 4 \left(\frac{\lambda - \lambda_0}{R}\right)^2\right]} \right] \quad (5.1)$$

where λ_0 is the wavelength of the transition, R is a term used in defining the resolution of the function, κ is a parameter which determines the amount of Gaussian or Lorentzian behavior and a_0 is the area under the curve. This functional form was selected from the library of functions in Jandell Scientific's PeakFit software as being most representative of the observed spectral output of a single transition.

Figure 5.4 shows a typical fit to a rotationally resolved emission spectra for the initially prepared ($v' = 1, J' = 171$) state in the presence of 855 mtorr of helium buffer gas. There is good agreement of the fit at both high and low rotational numbers. This fit was achieved by summing Equation 5.1 for each rotational line. The resolution parameter, R , was kept the same for all functions summed. The parameters a_0 and λ_0 were allowed to vary for each rotational transition so that PeakFit could find a best fit to the input spectral profile. No baseline was added to the fit functions. This was deemed unnecessary as checks of the background showed the baseline to be centered about zero. A check on the standard deviation of the peak height associated with each peak function showed this value to be approximately equal to the standard deviation of the background noise. This check was possible because PeakFit allows for either the peak height or the peak area to be an output variable of the fitting functions used. Population ratios of daughter to parent state are now a simple matter of comparing the area parameters associated with the rotational transitions of interest.

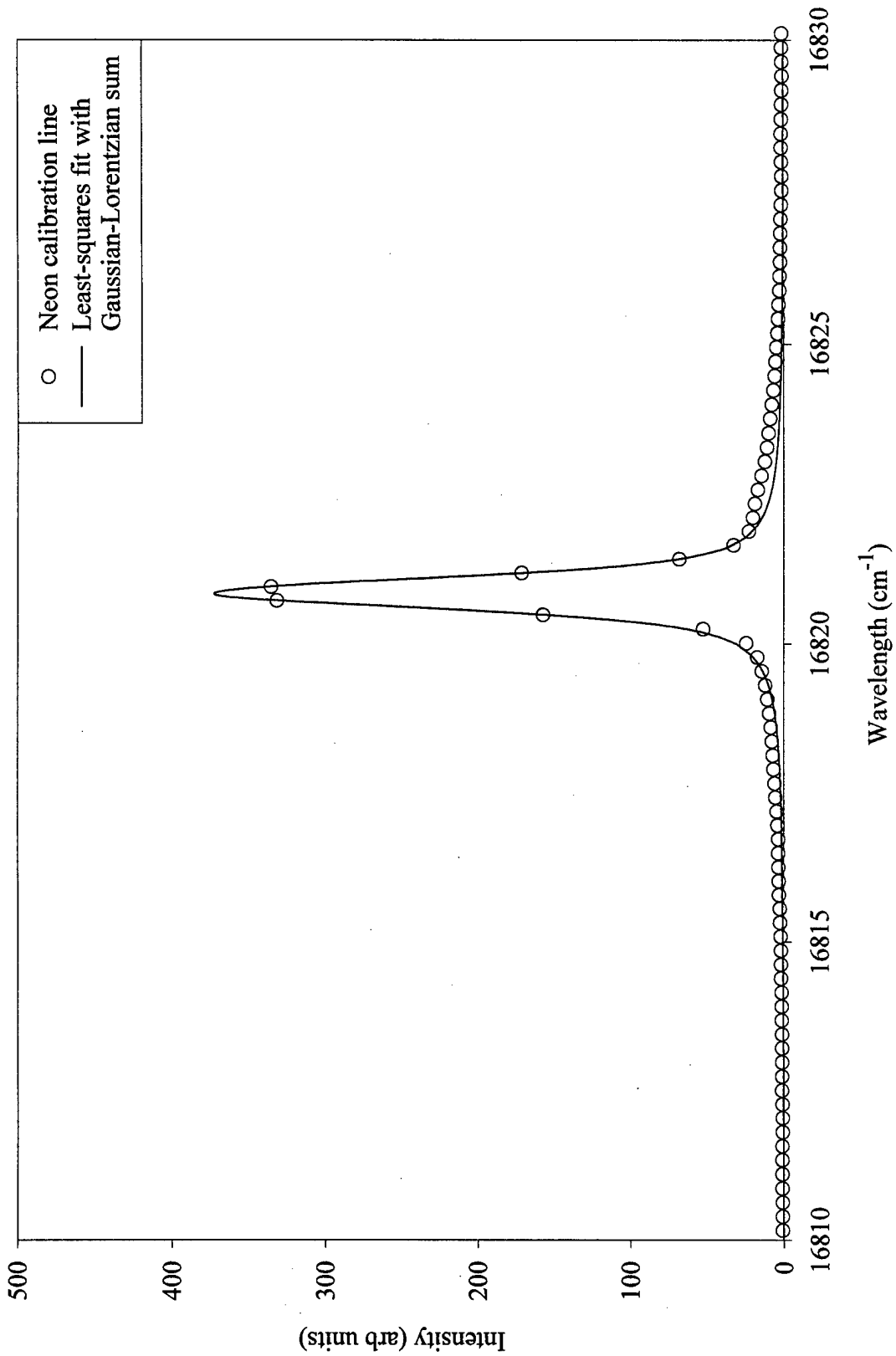


Figure 5.3 Comparison of a neon calibration line as recorded on the optical multi-channel analyzer with a spectral fitting function. The entrance slit width is 5 μm and the resolution is 0.32 cm^{-1} .

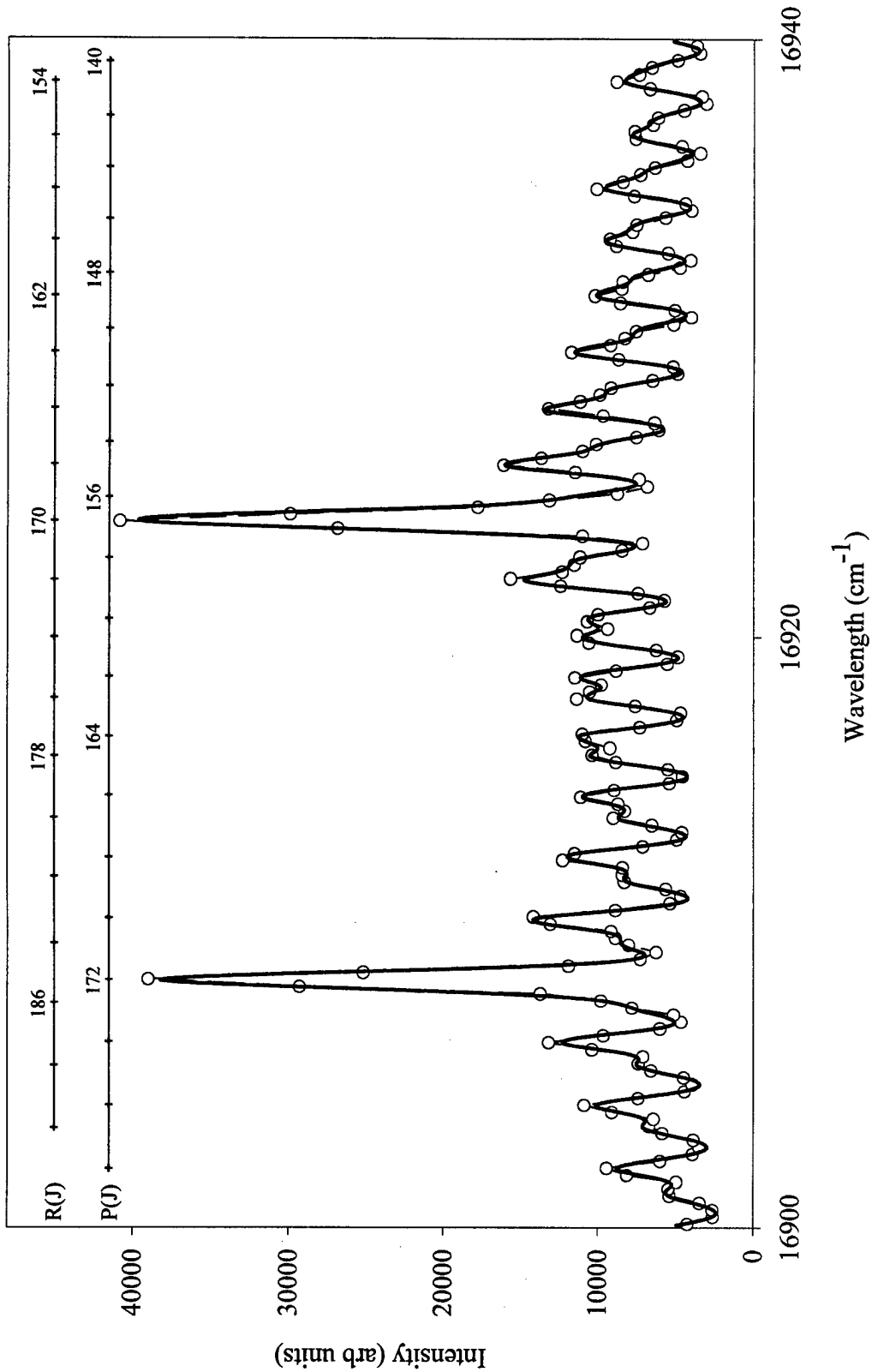


Figure 5.4 Comparison of spectrally resolved Bi_2 fluorescence in the presence of 855 mtorr of helium buffer gas with a spectral fit to the data. The parent state of this rotational spectra is $\text{Bi}_2 (A, v'=1, J'=171)$.

5.4 *R*→*T* Transfer with Helium, Neon and Argon Collision Partners

Rotational transfer data was collected for collisions with helium, neon and argon. The reasons for using these gases are essentially the same as for the case of vibrational energy transfer. Previous studies on Na₂ (37), Br₂ (35) and IF (49) have shown that rotational energy transfer occurs more rapidly with helium than with other rare gas collision partners. This is a direct consequence of the higher gas kinetic collision rate and it allows for more rapid build up of satellite rotational populations at lower pressures.

5.4.1 Direct Rotational Transfer. Helium was the most extensively studied collision partner. Rotationally resolved fluorescence profiles were obtained for the initially pumped levels ($v'_0 = 1, J'_0 = 171, 201, 231$) as a function of helium pressure. Up transfer was observed for $|\Delta J| \leq 44$ in all cases. Down transfer was observed for $|\Delta J| \leq 56$ for the initially pumped $J' = 201$ level and $|\Delta J| \leq 30$ for the other two pump levels. Observed down transfer levels were limited by reduced signal intensity for the initially pumped $J' = 231$ level and the overlapping of the P-R doublet for the case of initially pumping $J' = 171$. Helium pressures ranged from approximately 90-1400 mtorr. Using the spectral fitting technique described in the last section, population ratios of daughter to parent state were found for each initially pumped J' level over a range of different pressures. The population of the satellite rotational level $J' = 165$ relative to that of the parent level $J' = 171$ as a function of helium pressure is depicted in Figure 5.5. Similar data was obtained for all reported rotationally populated levels.

5.4.2 Direct Rotational Transfer. As in the case of vibrational energy transfer, the simplest mechanism for describing the population present in collisionally populated levels would be to describe the process as direct energy transfer from the initially prepared state. As a reminder, the fitting equation developed in Section

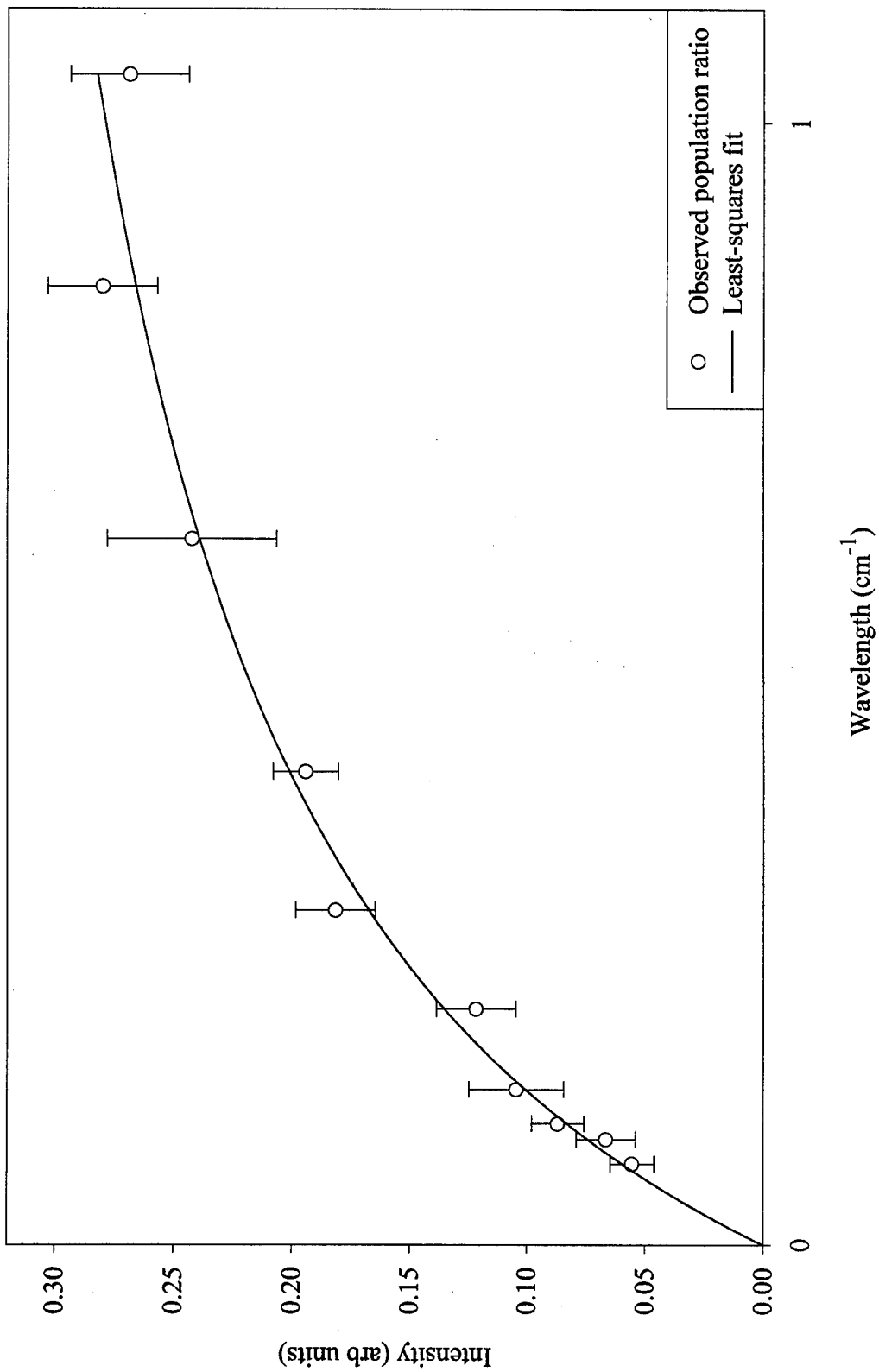


Figure 5.5 Plot of the population of the satellite $J=165$ rotational level relative to the parent state ($J=171$) for collisions with helium buffer. The solid line is a least-squares fit to the data using the direct transfer equation

2.3.3 to model this process can be expressed as

$$\frac{N(J')}{N(J'_0)} = \frac{a[M]}{1 + b[M]} \quad (5.2)$$

where $[M]$ is the buffer gas pressure, a is a fit parameter containing the rate coefficient for direct transfer from the initially prepared state ($k_J(J'_0 \rightarrow J') = a\Gamma(J')$) and b accounts for collisional processes not involved in a single collision event into the observed J' level. At higher pressures, the observed rotational level can be populated by rotational energy transfer from levels other than the parent state. This process is contained in the b parameter. However, for low pressures, population of the observed state through secondary collisions is not as likely to occur (35). Assuming that these secondary collisions, if they do occur, are linearly dependent on buffer gas concentration leads to the functional form expressed in Equation 5.2. This equation has been found to provide accurate rotational energy transfer rates over the range of observed rotational transitions for Na_2 (50) and Br_2 (35). The solid line running through Figure 5.5 is a typical curve fit when Equation 5.2 is applied to the data at hand.

As can be seen in Figure 5.4 there is a fairly strong overlap between the P(172) and R(186) transitions. There is a similar overlap for R(170) and P(156). P(172) and R(170) is the parent state P-R doublet for this particular spectrum. The spectrum between these two transitions consists of 14 separate rotational lines all with varying degrees of spectral overlap. To prevent these transitions (R(172)-R(186) and (P(156)-P(170))) from biasing the data, they were all excluded from the population ratio fits. This did not present a problem since there were two observable transitions visible for each one of these ΔJ levels. Equation 5.2 was then applied to all observed satellite rotational levels for each different initially prepared state and the a parameter was determined. From this parameter, the rotational energy transfer rates were determined by assuming a lifetime of 590 ns. Five hundred and ninety nanoseconds was chosen as the lifetime as it is the only rotational state lifetime given for the $v' = 1$

Table 5.1 Comparison of the gas kinetic collision rate coefficient at 300 K with the total rotational transfer rate as predicted by summing all calculated state-to-state rotational transfer rates.

Collision Partner	J'_0	Gas Kinetic Rate Coefficient ($\text{cm}^3/\text{molec-sec}$)	$\sum_J k_J(J_0 \rightarrow J)$ ($\text{cm}^3/\text{molec-sec}$)
He	171	7.03×10^{-10}	8.87×10^{-10}
	201		7.61×10^{-10}
	231		6.92×10^{-10}
Ne	201	3.41×10^{-10}	6.19×10^{-10}
Ar	201	2.84×10^{-10}	6.38×10^{-10}

level in any reported literature (23). A compilation of the least-squares fitted a and b parameters and their corresponding rotational transfer rates are listed in Appendix D. Figures 5.6 through 5.8 are plots of the observed rotational energy transfer rates plotted as a function of change in rotational energy (ΔE) for the different initially prepared states when using helium as a collision partner. An interesting observation of these plots is the relative symmetry they possess to either side of the parent state.

Additional observations can be made about the specific rotational transfer rates. The $|\Delta J = 2|$ rates are approximately two orders of magnitude greater than the vibrational transfer rates found in the last chapter. Additionally, the low $|\Delta J|$ down transfer rates for a given ΔJ are greater than the up transfer rate. This is not surprising as the rotational maximum in a rotationally thermalized distribution of Bi_2 at 300 K occurs at $J \ll 171$. Finally, when the calculated rotational transfer rates are summed, the result equals approximately one hundred percent of the gas kinetic rate in all cases. This result is tabulated in Table 5.1 and is consistent with a study performed by Ehret and Gerber when they found rotational quenching cross sections approximately equal to collisional cross sections for Bi_2 collisions with argon (23).

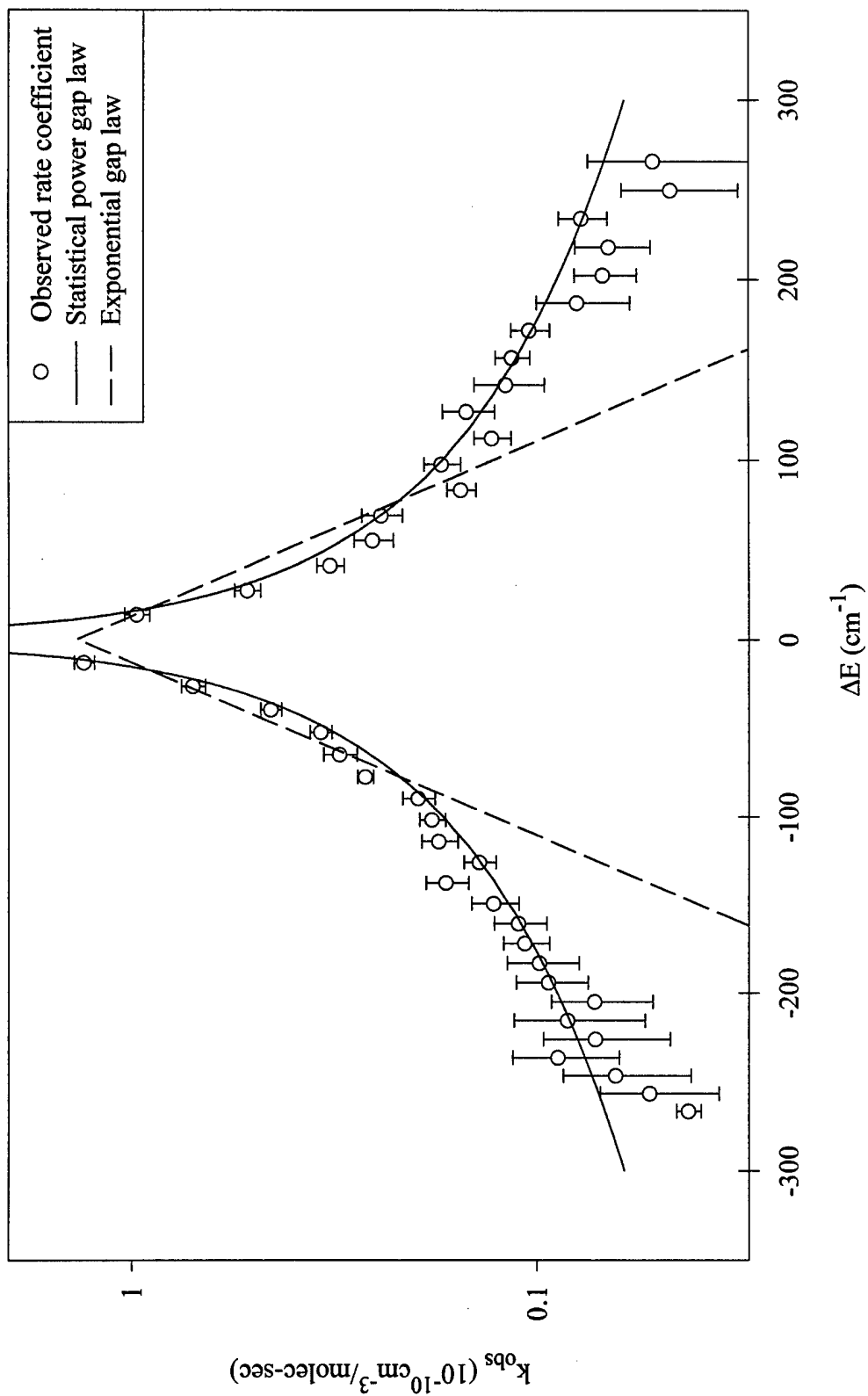


Figure 5.6 Observed rotational energy transfer rate coefficients as a function of change in rotational energy for Bi_2 ($A, v_0=1, J_0=171$) collisions with helium. A fit to both the statistical power gap law and the exponential energy gap law is shown.

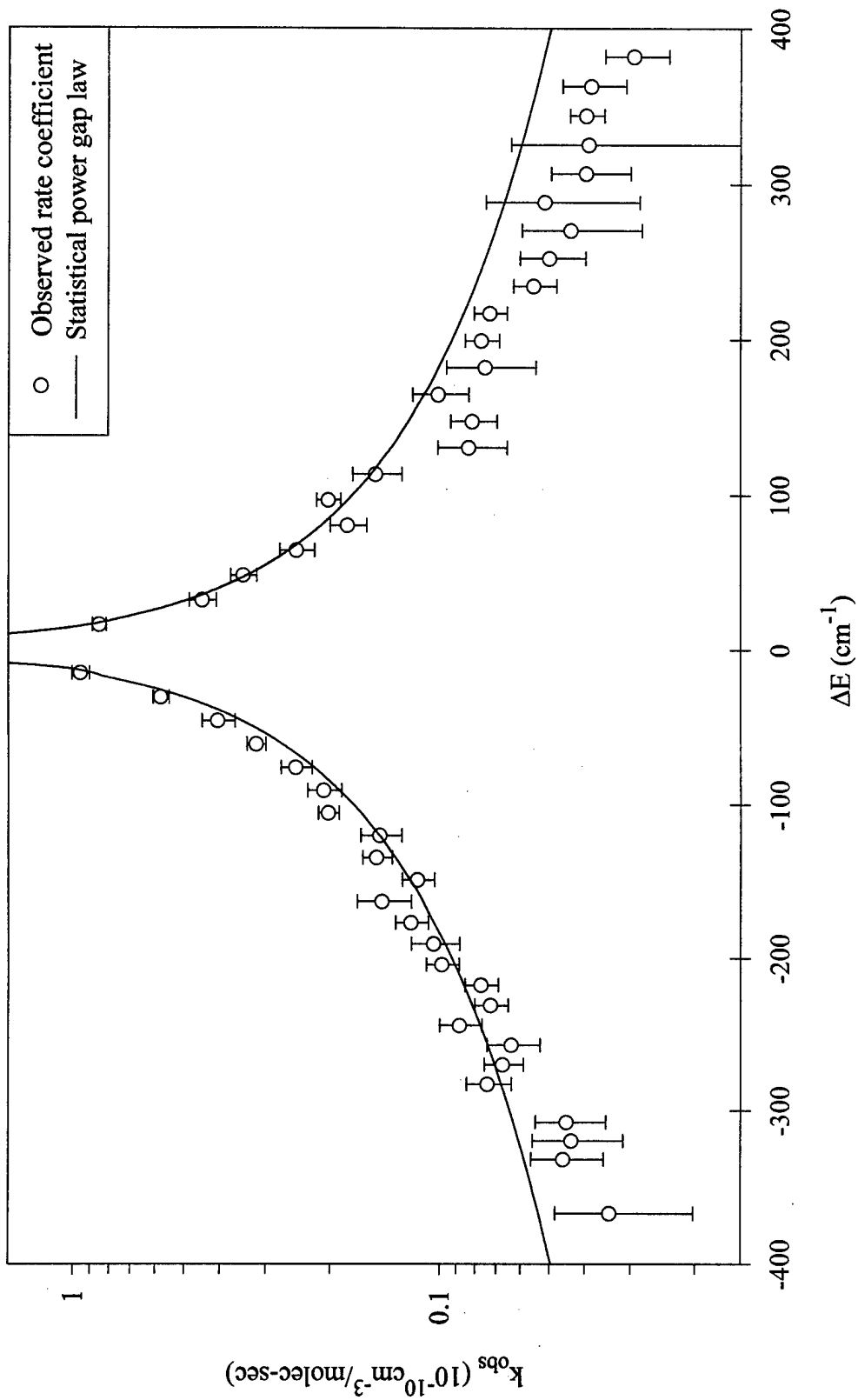


Figure 5.7 Observed rotational energy transfer rate coefficients as a function of change in rotational energy for Bi_2 ($A, v'_0=1, J'_0=201$) collisions with helium. A fit to the statistical power gap law is shown.

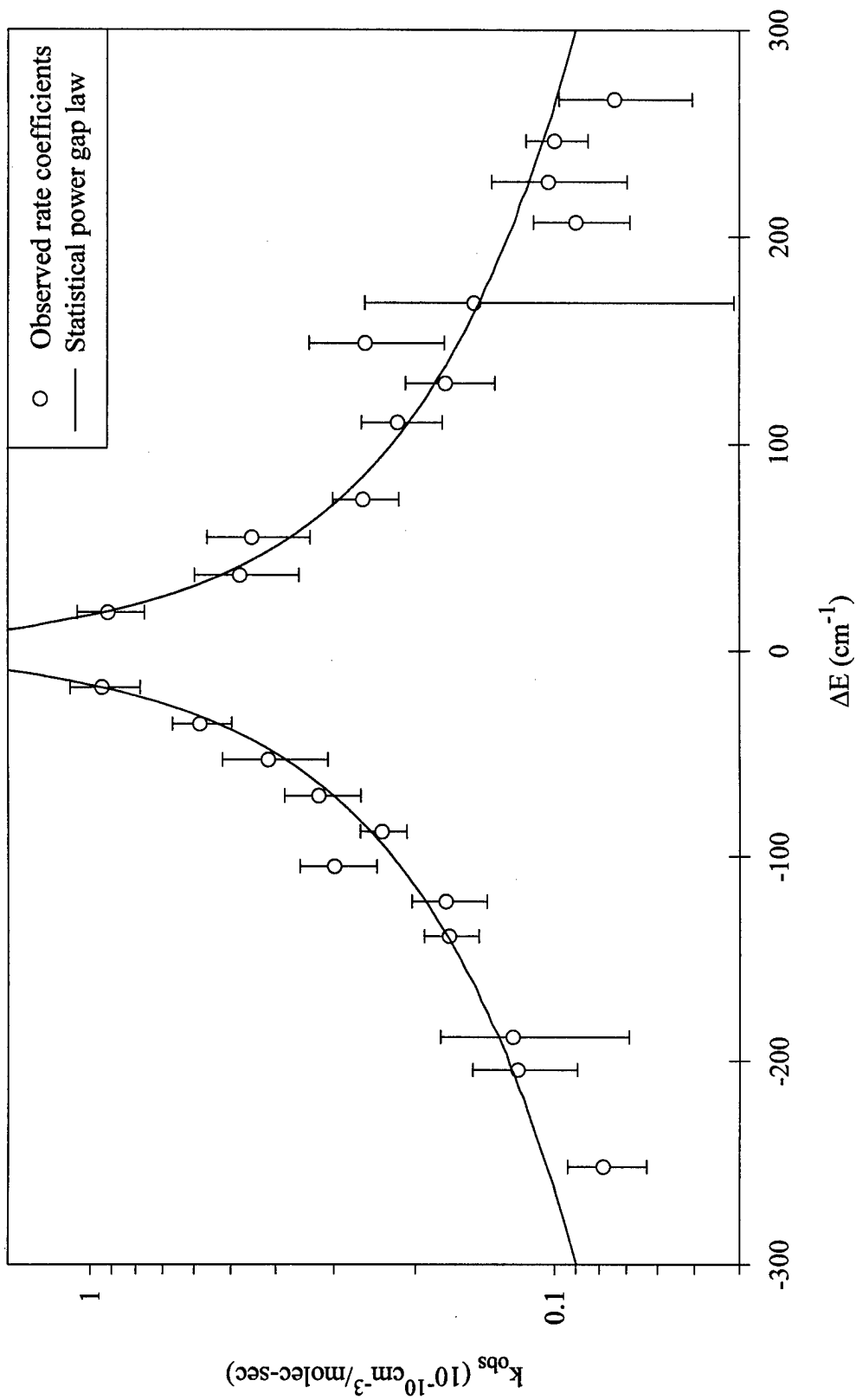


Figure 5.8 Observed rotational energy transfer rate coefficients as a function of change in rotational energy for Bi_2 ($A, v'_0=1, J'_0=231$) collisions with helium. A fit to the statistical power gap law is shown.

5.4.3 Neon, Argon. Neon and Argon were studied in less detail than helium. The primary reason for this was the reduced signal intensity achievable when these gases were used as collision partners. Thus, for neon and argon only level $J' = 201$ was pumped. Figures 5.9 and 5.10 are graphical depictions of the observed rotational transfer rates for these two buffer gases. Once again, the a and b fit parameters from Equation 5.2 as well as the calculated rotational transfer rate coefficient for each observed satellite state are tabulated in Appendix D. As opposed to the data collected for helium, these two sets of rate coefficients are not symmetric about the parent state. Both neon and argon show a flattening of the rotational transfer rates for large negative values of ΔJ . A possible reason for this flattening is that for large negative values of ΔJ secondary collisions are becoming an important consideration. If this were the case, then the a parameter in Equation 5.2 might not necessarily reflect an accurate value for the state-to-state rotational transfer rate. As shown in Table 5.1, the summed rotational transfer coefficients are approximately twice the gas kinetic collision rate for both neon and argon. This is in contrast to the three different helium cases that all summed to within 20% of the gas kinetic rate. However, in regards to the flattening of the rotational transfer rates, a similar behavior for collisions with neon and argon was found by Davis and Holtzclaw in their rotational transfer study of IF(B) (49). IF(B) collisions with helium did not exhibit this behavior. The apparent gas kinetic total rotational transfer rates suggest that the collision event is a brief, highly efficient, impulsive energy transfer.

5.5 Rotational Transfer Fitting Laws

Currently, there are no analytically derived solutions to model rotational energy transfer. To this end empirical fitting laws have been found that accurately model rotational energy transfer in a large number of cases. These fitting laws have their basis in an information-theoretic approach known as surprisal analysis. Simply put, surprisal analysis is a way of comparing what is observed in the lab to what is

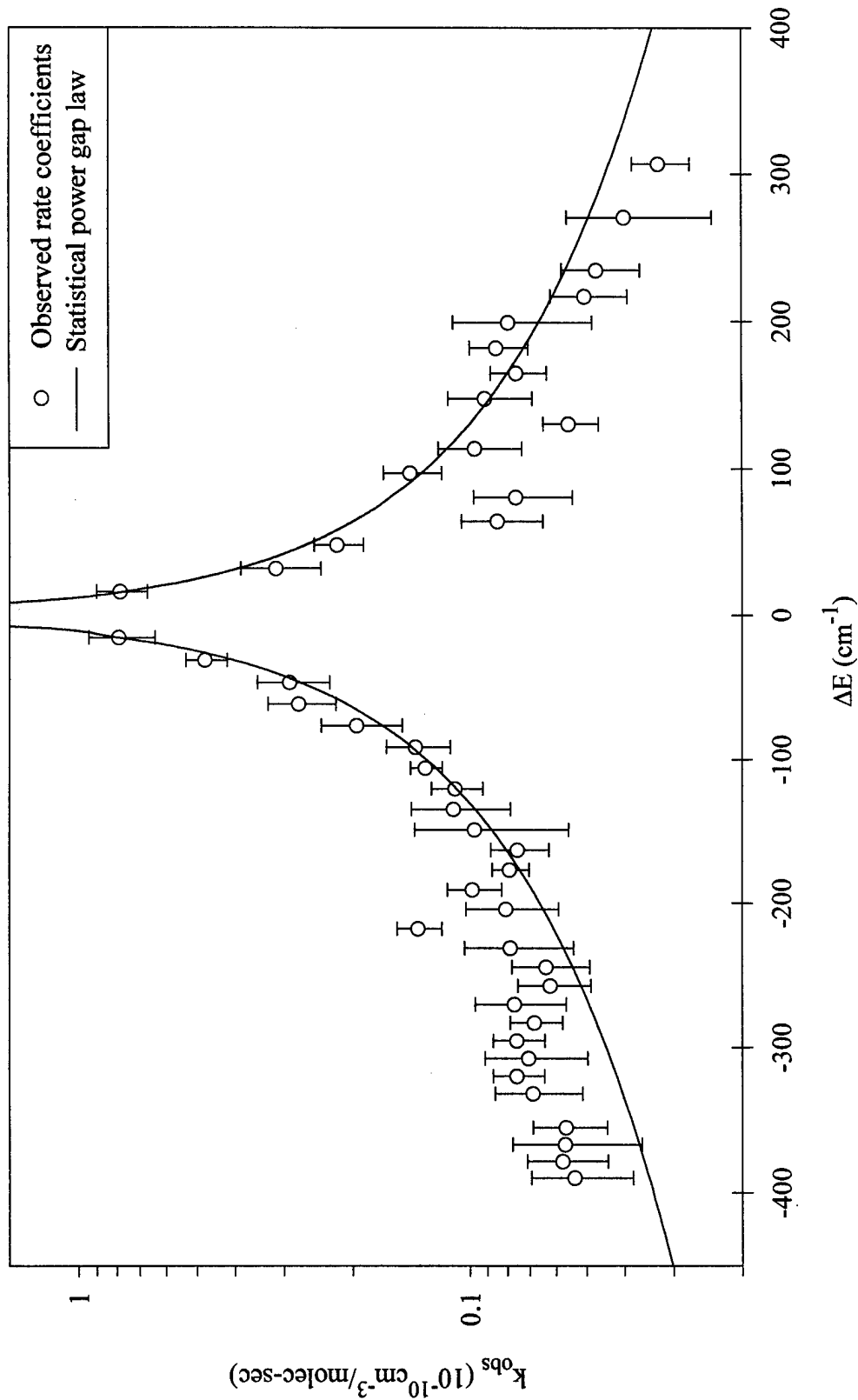


Figure 5.9 Observed rotational energy transfer rate coefficients as a function of change in rotational energy for Bi_2 ($A, v'_0=1, J'_0=201$) collisions with neon. A fit to the statistical power gap law is shown.

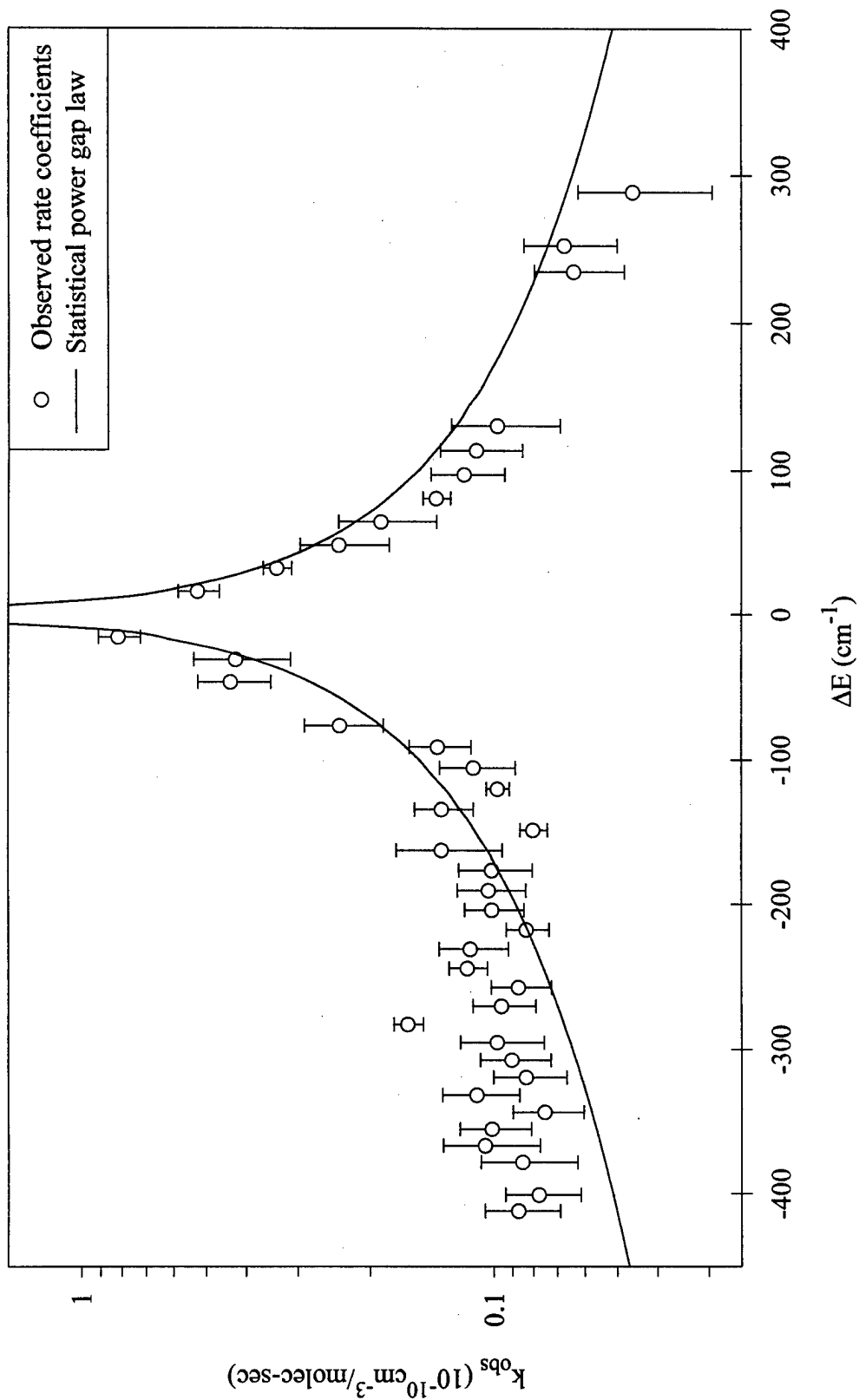


Figure 5.10 Observed rotational energy transfer rate coefficients as a function of change in rotational energy for $\text{Bi}_2 (A, v'_0=1, J'_0=201)$ collisions with argon. A fit to the statistical power gap law is shown.

expected from a Boltzmann-like statistical distribution (51). The surprisal can be expressed as:

$$S \equiv -\ln \left[\frac{k_J(J_0 \rightarrow J_f)}{\rho(\Delta E, T)f(J'_f)} \right] \quad (5.3)$$

where S is the surprisal, $k_{obs}(J_0 \rightarrow J_f)$ is the observed rotational transfer rate from the initially populated level J'_0 to the satellite level J'_f , $\rho(\Delta E, T)$ is a factor comparing the ratio of final to initial densities of states at a temperature T and $f(J'_f)$ is dependent on the final distribution of $M_{J'}$. A useful result of surprisal theory is the expansion of S in powers of $|\Delta E|$:

$$S = -S_0 + c|\Delta E| + c_2|\Delta E|^2 + \dots \quad (5.4)$$

If only the linear term in $|\Delta E|$ is retained, the result is the widely applied exponential gap law:

$$k_{EGL}(J_0 \rightarrow J_f) = Af(J'_f)\exp(-\chi|\Delta E|)\rho(\Delta E, T), \quad (5.5)$$

where A and c are free parameters (37). This relation stems from the assumption that S is a function of ΔE and that the functional form is an exponential. Equation 5.5 has proved adequate in many instances but has been found to fail at low values of $|\Delta E/kT|$ (52, 37). Brunner found that rotational energy transfer in $\text{Na}_2^*\text{-Xe}$ collisions could be better represented by the statistical power gap law:

$$k_{SPG}(J_0 \rightarrow J_f) = Bf(J'_f)|\Delta E/B_v|^{-\gamma}\rho(\Delta E, T), \quad (5.6)$$

where B and γ are free parameters and B_v is the rotational spectroscopic constant of the pumped v' level (53). This equation can be readily derived if the surprisal, S , is expanded in powers of $\ln(|\Delta E|)$, but there is no a priori justification for doing so in the context of rotational energy transfer (37, 24). Even with this lack of analytical development, these two equations are remarkable for their ability to fit large amounts of data with relatively few input parameters.

Table 5.2 Fit parameters to the statistical power gap law

Buffer	(v', J')	B (10^{-8} cm ³ /molec-sec)	γ
He	(1,171)	5.45 ± 1.17	0.944 ± 0.030
He	(1,201)	3.85 ± 0.59	0.902 ± 0.021
He	(1,231)	2.79 ± 0.50	0.834 ± 0.025
Ne	(1,201)	5.00 ± 1.23	0.968 ± 0.034
Ar	(1,201)	1.25 ± 0.50	0.786 ± 0.042

Attempts were made to fit both the exponential gap law and the statistical power gap law to all sets of derived state-to-state rotational transfer rates. If $M_{J'}$ is completely randomized in the collisions, then $f(J') = 2J' + 1$. The other extreme would be for there to be no randomization at all and $f(J') = 1$. These two extremes on $f(J')$ were tested with each fitting law. In all cases, the exponential gap law was unable to provide a satisfactory fit to the data. A representative exponential gap law fit is seen as the dotted line in Figure 5.6. In contrast, the statistical power gap law with $f(J') = 1$ provided a much better fit to the data. The statistical power gap fits are seen as the solid line in Figures 5.6 through 5.10. Table 5.2 lists the resulting statistical power gap law fit parameters obtained in this study. The error bound are the standard errors derived from the least-squares fit to the data.

5.6 Discussion of Results

As can be seen from the plots of the rotational transfer rates, the statistical power gap law does a much better job of fitting the helium transfer data as opposed to either neon or argon. This is the same behavior observed by Brunner et al. in his rotational transfer studies of Na₂ (A). In this study, Brunner found that the statistical power gap law provided better fits to observed data for lower mass collision partners (37). However, the Brunner study only observed rotational energy transfer for $\Delta J \leq 28$. The poor performance of the gap law fit for the neon and argon collision partners used in this study mainly stems from the inability to model the behavior at large negative values of ΔJ . The IF(B) rotational study performed by

Davis is the only other reported rotational energy transfer study to access the same range of ΔJ as the present work. They did not report the results of scaling law fits to their data (49).

An interesting way to look at the performance of the statistical power gap law is seen in Figure 5.11. This plot compares the rotational transfer rates of the three different collision partners when pumping the same parent state ($J' = 201$). The x-axis of this plot is in terms of the natural log of $|\Delta E|$. The functional form of the statistical power gap law predicts a linear correspondence between the two axes on this figure. As can be seen, the helium data is represented quite well by a linear relationship. However, the neon and argon data differ from this result. At $|\Delta E| \approx 300 \text{ cm}^{-1}$, there is a definite departure from linearity. If, as suggested earlier, these high ΔJ are overestimated, this non-linear behavior is an indication of where secondary collisions have assumed an important role with respect to the pressures used to collect the rotational transfer data.

The effective cross section for rotational transfer can be defined as:

$$\sigma_R(i \rightarrow f) = \frac{k_J(i \rightarrow f)}{v_g} \quad (5.7)$$

where $k_R(i \rightarrow f)$ is the rotational transfer rate for direct transfer from state i to state f and v_g is the center-of-mass rms thermal velocity of the $\text{Bi}_2 + \text{M}$ system (49). Table 5.1 presents the total R-T cross section $[\sum_f \sigma_R(i \rightarrow f)]$ for helium, neon and argon. Also listed is the ratio of the total R-T cross section to the effective hard-sphere cross section calculated from atomic data given by Hirschfelder (47). This ratio represents the efficiency of the RT process with respect to the hard-sphere collision cross section.

Classically, the average amount of angular momentum, L , available for exchange in a collision is

$$\mathbf{L} = \mathbf{r} \times \mathbf{P} \quad (5.8)$$

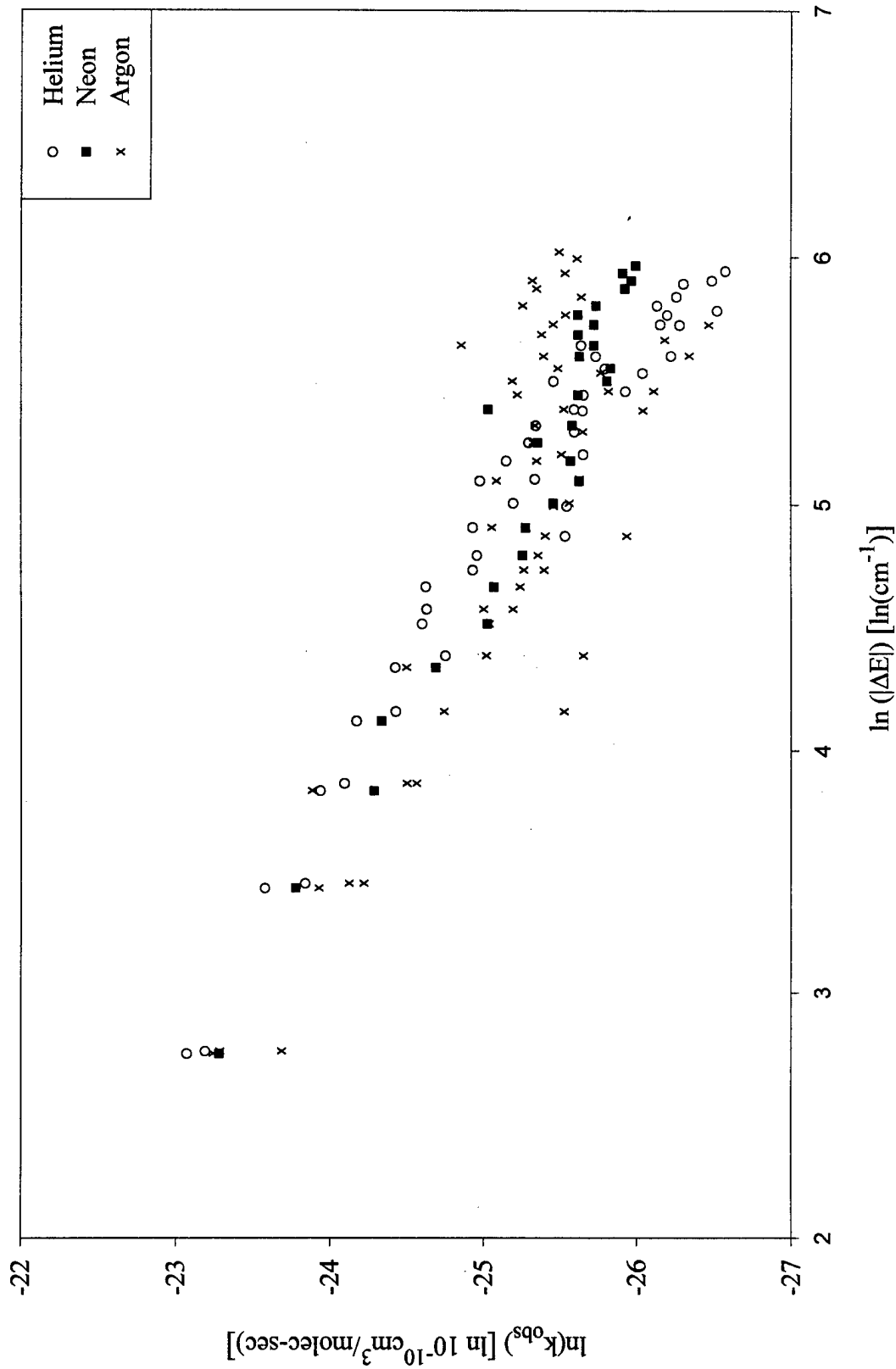


Figure 5.11 Observed rotational energy transfer rate coefficients as a function of change in rotational energy for $\text{Bi}_2(A, v'_0=1, J'_0=201)$ collisions with helium, neon and argon.

In scalar form, this equation can be expressed as

$$L = \mu v_g b = \left(\frac{8kT}{\pi} \right)^{1/2} \mu^{1/2} b \quad (5.9)$$

where v_g is once again the rms thermal velocity, μ is the reduced mass of the collision pair and b is the impact parameter taken to be the sum of the particle radii (49). Figure 5.12 is a plot of the σ_R/σ_g vs $\mu^{1/2}b$ for helium, neon and argon. This plot shows that relative cross sections do increase with the collision reduced mass-impact parameter combination relation as just predicted. For comparison purposes only, Wolf found that the ratio between $(\sigma_R/\sigma_g)_{He}/(\sigma_R/\sigma_g)_{Ne} \approx 0.5$ and this same ratio involving argon was ≈ 0.4 (11). The analogous ratios in this experiment were 0.54 and 0.43 respectively. This result indicates the importance of mass of the collision partner in rotational transfer kinetics. On average, the heavier collision partners bring more orbital angular momentum into the collision which is available for exchange with rotational angular momentum.

As has been shown, the low $|\Delta J|$ rotational energy transfer rates decrease rapidly with rotational energy. The largest change in rotational energy observed in these experiments is for $|\Delta J| \geq 60$. Rotational energy transfer rates were calculated for levels as high as $|\Delta J| = 52$. Higher values were unresolvable due to the overlap of the emission P-R doublets. This is similar to studies on IF(B) where $|\Delta J| = 60$ has also been observed. This is intriguing in light of the fact that the IF(B) rotational constant is approximately ten times larger than the same parameter for the A state of Bi_2 (0.22 vs 0.019 cm^{-1}). In $Br_2(B)$, rotational transfer is not seen for $|\Delta J| > 20$ ($B_v \approx 0.05$ cm^{-1}). In the case of IF, the rotational transfer rates fall off much more slowly than they do for Bi_2 or Br_2 . Bandhead formation is noted at pressures as low as 20 mtorr in IF while pressure of approximately 1200 mtorr were needed for bandhead formation in the present study and bandheads were not seen in Br_2 for pressures as high as several torr (35).

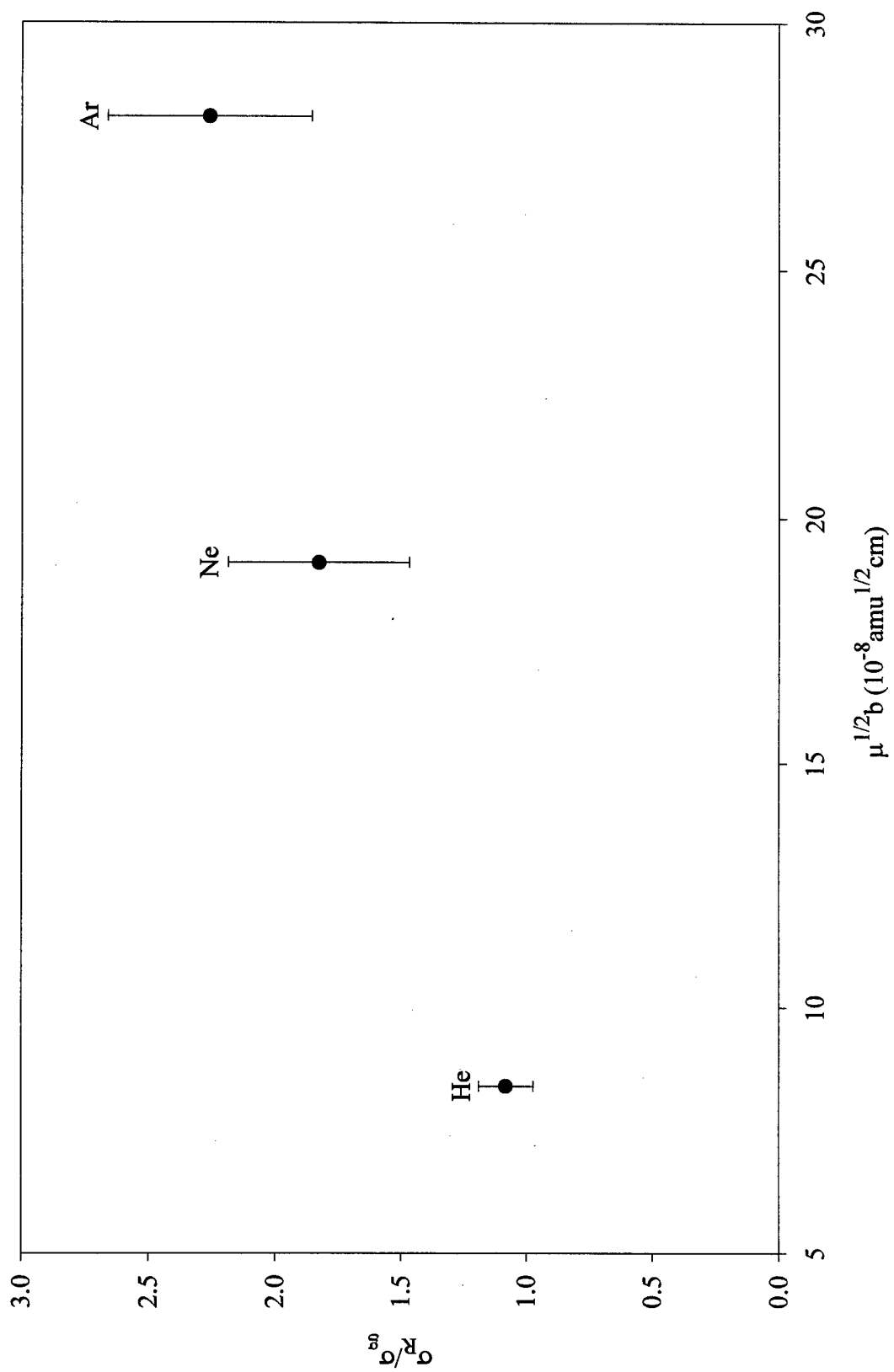


Figure 5.12 Plot of the rotational transfer efficiencies vs the product $\mu^{1/2}b$ for different collision partners after pumping $v=1, J=201$.

5.7 Conclusions

CW LIF has been used to study rotational energy transfer for $\text{Bi}_2(\text{A})$ collisions with helium, neon and argon. State-to-state rotational transfer rates have been determined for rotational states with $|\Delta J| \leq 52$. The scaling of these rates has been found to be adequately described by the statistical power gap law for collisions with helium, and there are indications this law is also adequate to describe the collisions with neon and argon. The total rotational transfer rate out of the parent state occurs at a gas kinetic rate suggesting that rotational energy transfer is a highly efficient energy transfer mechanism. Given the large amount of angular momentum present in the initially prepared parent state, the ability of an energy based rotational fitting law to accurately model the rotational transfer rates indicates that energy change is an important parameter in Bi_2 rotational transfer scaling. As this is the first study to attempt a detailed look at rotational energy transfer in $\text{Bi}_2(\text{A})$, there are no comparisons to be made with previous work.

VI. Conclusions

Three areas of interest were examined in this study of Bi_2 . The spectroscopy of low-lying vibrational levels of both the $X(0_g^+)$ and $A(0_u^+)$ states was investigated using CW laser excitation techniques. Vibrational energy transfer within the A state was studied for Bi_2 collisions with rare gas collision partners using spectrally resolved CW laser induced fluorescence experiments. This vibrational work also led to an upper bound for electronic quenching of the A state by the rare gas atoms. Finally, rotational energy transfer within the A state was studied with the same techniques used in the vibrational study. The main difference in the methodology was the need for higher resolution of the spectrally resolved data.

6.1 Summary of the High J Spectroscopy of Bi_2

The spectroscopy of low vibrational levels within both the ground and A states of Bi_2 was investigated by observing total fluorescence emitted as a result of excitation by a scanning CW ring dye laser. Laser excitation spectra were obtained for pumping out of $v'' = 2 - 5$ to the A state levels $v' = 0 - 4$. Rotational levels as high as $J = 211$ were detected in the Doppler limited spectra. All vibrational bands observed were adequately fit with a two-term rotational expansion. A global least-squares fitting routine was implemented to find the best fit vibrational and rotational term-values that best represented the data. These term values are easily represented with Dunham expansion coefficients that reproduce the observed rotational lines to within 0.007 cm^{-1} . This rotational study represents a significant improvement in the known spectroscopy of high J levels in Bi_2 . These spectroscopic terms were then used to calculate Franck-Condon factors for transitions between the X and A states of Bi_2 . Experimental measurements of these factors showed that the newly derived spectroscopic constants provide a more accurate picture of the potential curves associated with these two electronic states.

6.2 Summary of Vibrational Energy Transfer Studies

Vibrational energy transfer within the low-lying vibrational levels of the $\text{Bi}_2(\text{A})$ state were investigated for rare gas collision partners using spectrally resolved LIF techniques. Vibrationally resolved emissions were observed from $v' = 0 - 5$ after laser excitation of a single rovibrational transition to $v' = 0 - 4$. A rate-matrix technique was implemented to extract state-to-state vibrational transfer coefficients as well as find the upper limit of the electronic quenching term associated with each collision partner. A single fundamental transfer rate was found to adequately describe vibrational transfer rates for $0 \leq v' \leq 4$ for the rare gas collision partners. This rate ranged from $k_v(1, 0) = 5.29 \pm 0.73 \times 10^{-12} \text{ cm}^3/\text{molec-sec}$ for collisions with helium to $k_v(1, 0) = 2.38 \pm 0.36 \times 10^{-12} \text{ cm}^3/\text{molec-sec}$ for collisions with krypton. Landau-Teller scaling of the fundamental transfer rate provides an adequate description of vibrational transfer for the $v' \leq 4$ levels in the $\text{Bi}_2(\text{A})$ state. Even though $\omega_e/kT \approx 0.62$ for this system, multi-quantum effects were found to be negligible with $\Delta v = 2$ rates being approximately 10% of the corresponding $\Delta v = 1$ rates and $\Delta v = 3$ not providing any improvements to the fits. Upper bounds on electronic quenching rates were approximately an order of magnitude less than vibrational transfer rates.

The results of the V \rightarrow T transfer studies were compared to predictions from the SSH theory. The scaling of the transfer rates with reduced mass showed the same basic behavior as BrCl and thus did not reflect the scaling as predicted by the simplified SSH theory. However, calculation of collision pair interaction length, L , using the full SSH equation, did provide reasonable values that decreased with increasing rare gas partner mass. Furthermore, these interaction lengths were of approximately the same size as similar calculations done on the halogens and interhalogens.

6.3 Summary of Rotational Energy Transfer Studies

Rotational energy transfer in the $\text{Bi}_2(\text{A})$ state was studied for collision with helium, neon and argon using spectrally resolved CW LIF. Rotational states with $|\Delta J| \leq 52$ were observed after pumping $v' = 1, J' = 171, 201, 231$. State-to-state rotational transfer rates were calculated from the ratio of daughter to parent state population. The scaling of these rotational transfer rates was well characterized by the statistical power gap scaling law for the case of helium collisions. Neon and argon collisions were also in general agreement with this law, but not as well modeled as the helium case. This indicates that energy change is the important consideration in modeling rotational transfer in $\text{Bi}_2(\text{A})$. A classical model of rotational transfer was used to examine the mass effects in this process. Bi_2 total rotational transfer probabilities scale with reduced mass of the collision pair in a similar manner to IF and I_2 .

6.4 Further studies

There are three main areas that warrant further investigation in Bi_2 collisional processes. All three of these efforts would require the use of pulsed LIF techniques. The first would be a detailed lifetime study on the $\text{Bi}_2(\text{A})$ state. This thrust should focus on two parts. The first being a study of vibrational lifetimes in the $\text{Bi}_2(\text{A})$ state and the next being a detailed study on the dependence of lifetime on rotational level. The next course of action would be a study to find the electronic quenching rates of the $\text{Bi}_2(\text{A})$ state by rare gas collision partners. This study would help reduce the uncertainty of the rate-matrix solution by reducing the number of free parameters in fitting the data. Finally, pulsed LIF would allow for temporally and spectrally resolved data to be collected in one experiment. This could be done either for vibrational or rotational energy transfer. Previous researchers have shown that CW and pulsed experiments are complementary to each other. A great deal of effort has been expended to provide an unambiguous picture of how excited state

populations have been redistributed among the various energy levels of the $\text{Bi}_2(\text{A})$ state. However, as has been pointed out, the absolute values of the reported rate constants is affected by systematic errors present in the system. Pulsed LIF would help reduce these errors by providing real time measurements of time related events.

Appendix A. Basic Energy Transfer Theories

This appendix describes the basic energy transfer processes used in this research. These processes are the gas kinetic collision rate, the Landau-Teller theory and the Schwartz, Slawsky and Herzfeld (SSH) theory. The discussions on the L-T and SSH theories are excerpted from Holmberg (7).

A.1 Gas Kinetic Collision Rate

The usual standard with which to compare the efficiency of various kinetic processes is the gas kinetic collision rate. For collisions between molecule A and collision partner B, both of which are assumed to be hard spheres, the collision rate constant is most simply expressed by the equation

$$k_g = \sigma_g v_{AB} \quad (\text{A.1})$$

where

$$\sigma_g = \text{velocity averaged collision cross section} = \pi(r_A + r_B)^2$$

$$r_A = \text{radius of particle A}$$

$$r_B = \text{radius of particle B}$$

$$v_{AB} = \text{average relative speed of collision partners} = (8k_B T / \pi \mu)^{1/2}$$

$$\mu = \text{reduced mass of the collision pair.}$$

The probability of occurrence for any specific kinetic process can then be expressed in terms of this gas kinetic rate as

$$P = \sigma / \sigma_g \quad (\text{A.2})$$

where P is the probability for the specific process to occur during a collision event and σ is the cross-section for the specific event. Hard sphere cross-sections, reduced

mass, relative particle velocity (300 K) and gas kinetic rate constants for the collision partners used in this research are given in Table A.1. Atomic radii were derived from a (6,12) Lennard-Jones potential from tabulated viscosity data in reference (47). The Bismuth dimer radii was determined by adding half the internuclear separation of the A state to one atomic diameter as reported by Sienko (48).

Table A.1
Gas Kinetic Collision Parameters for Bi₂

Collision Partner	Cross-Section A ²	Reduced Mass (a.u.)	Velocity (cm/sec) @ 300K	Gas Kinetic Rate Constant (cm ³ /molec-sec)
He	48.3	3.96	1.26 x 10 ⁻⁵	7.03 x 10 ⁻¹⁰
Ne	51.8	19.3	5.72 x 10 ⁻⁴	3.41 x 10 ⁻¹⁰
Ar	61.0	36.5	4.16 x 10 ⁻⁴	2.84 x 10 ⁻¹⁰
Kr	62.4	69.8	3.01 x 10 ⁻⁴	2.13 x 10 ⁻¹⁰
Xe	68.7	99.9	2.51 x 10 ⁻⁴	1.95 x 10 ⁻¹⁰

A.2 Landau-Teller Theory

Landau and Teller developed an elementary vibrational energy transfer theory that neglected the long range attractive intermolecular potential. A repulsive limb interaction of the form $V(r) = V_0 \exp(-\alpha \cdot r)$, where $\alpha = 2\pi\nu_0/v$, ν_0 is the oscillator frequency and v is the relative velocity of the collision partners, was used to calculate the probability for vibrational energy transfer from $v' = 1$ to $v' = 0$ using time-dependent perturbation theory. The resulting average probability of vibrational energy transfer per collision is given by Yardley (46) as

$$P_{10} \propto \exp \left\{ -3 \left(2\pi^4 \mu \nu_0^2 / \alpha^2 k_B T \right)^{-1/3} \right\} \quad (\text{A.3})$$

This equation indicates that efficient transfer is favored for small reduced masses, small vibrational spacings, short interaction distances and high temperatures. Matrix elements calculated for vibrational transitions are proportional to those for ra-

diative transitions. Selection rules dictate transitions between adjacent states only ($\Delta v = \pm 1$). Transition probabilities scale by vibrational level as

$$P_{v,v-1} = v \cdot P_{10} \quad (\text{A.4})$$

A.3 SSH Theory

The SSH theory is another widely used vibrational transfer theory proposed by Schwartz, Slawsky and Herzfeld (34). Often used as the basis for evaluating experimentally derived vibrational transfer rates, the SSH theory includes an attractive potential term which was neglected in the L-T theory. Their potential has the form

$$V(r) = V_o \exp(-\alpha \cdot r) - \varepsilon \quad (\text{A.5})$$

The addition of the attractive term ($\varepsilon =$ the potential well depth) causes a slight increase in translational energy just prior to reaching the repulsive potential, thus increasing the vibrational transfer probabilities. The resulting probability for vibrational transfer from $v' = 1$ to $v' = 0$ for the SSH theory is given by Yardley (46) as

$$P_{10} \propto \left(\frac{\Theta'}{\Theta_{SSH}} \right) \left(\frac{\Theta'}{T} \right) \exp \left[-\frac{3}{2}(\Theta'/T)^{1/3} + (\Theta_{SSH}/2T) + (\varepsilon/k_B T) \right] \quad (\text{A.6})$$

where

$$\Theta' = 4\pi^2 L^2 \omega^2 \mu / k_B$$

$$\Theta_{SSH} = \omega_e / k_B$$

$\omega_e =$ vibrational energy spacing

$L =$ interaction length

If the exponential term dominates the probability function above, the logarithm of P_{10} can be rewritten as

$$\ln(P_{10}) = A - B\mu^{1/3}\omega^{2/3} \quad (\text{A.7})$$

where A and B are constants related to the same parameters as Equation A.6. This form of the SSH vibrational transfer probability equation is most often used for examining experimentally determined vibrational transfer rate constants and cross-sections.

A.4 Rate Matrix Solution

This section discusses the methodology for obtaining a numerical solution to a multi-level V→T transfer system. As a reminder, the temporal evolution of any vibrational state can be described by the following equation:

$$\begin{aligned} dN_v/dt = & S\Delta_{vv_0} - \Gamma_0 N(v) \\ & - k_q MN(v) \\ & - \sum_{\Delta v} k_v(v \rightarrow v + \Delta v) MN_v \\ & + \sum_{\Delta v} k_v(v + \Delta v \rightarrow v) MN_v \end{aligned} \quad (\text{A.8})$$

Before proceeding with the solution several assumptions for solving the problem need to be stated. The first is that the electronic quenching rate is independent of vibrational level. Second, the scaling of the $\Delta v = \pm 1$ transfer rates obey the prescription as set forth in the Landau-Teller theory. In other words, $\Delta v = -1$ rates are multiples of the fundamental vibrational transfer rate, $k_v(1, 0)$, and scale as

$$k_{v \rightarrow v-1} = v k_v(1, 0) \quad (\text{A.9})$$

and inverse rates must obey detailed balance -

$$k_{v \rightarrow v+1} = (v + 1) k_v(1, 0) \exp(-\Delta E_{v+1,v}/k_B T) \quad (\text{A.10})$$

Additionally, it is assumed that multi-quantum transfer rates are a constant fraction of the corresponding $\Delta v = -1$ rate originating on the same upper level -

$$k_{v \rightarrow v-2} = f k_{v \rightarrow v-1} \quad (\text{A.11})$$

Once again, detailed balance applies to the reverse multi-quantum rates. There are no $|\Delta v| \geq 3$ rates considered. This allowance for multi-quantum transfer gives this technique more flexibility in modeling more complicated energy transfer systems. Keep in mind that the vibrational energy transfer studies in this experiment indicate that $|\Delta v| \leq 2$ only.

Following the notational convention of Chapter II, and considering there to be a CW illumination of the sample, the rate equation can be rewritten in tensor notation as

$$S \delta_{pp_0} = -R_{pq} N_q \quad (\text{A.12})$$

The conditions set forth earlier in this appendix place additional restrictions on the specific elements within the rate matrix. For instance, $w_{pq} = 0$ for $|p - q| \geq 3$. This accounts for there being no multi-quantum transfer of $\Delta v \geq 3$. The detail balance condition relates elements located symmetrically above and below the diagonal. For a CW experiment, a known initial state is pumped. This is represented by the term S . If the terms in the rate matrix are known, the final steady-state population distribution can be calculated. This distribution is what is observed in a spectrally resolved spectrum. The task of finding the terms in the rate matrix, and thus the vibrational transfer coefficients is simply reduced to finding the correct matrix that will reproduce the observed spectrum. This can be done by inverting the matrix R and then varying the terms until the correct output is predicted.

The following is the form of the rate matrix implemented in MathCad 6.0 software to make predictions of the population ratios. This example is for a 4-level

system. A 7-level matrix was used for the rate matrix calculations in this research. The smaller matrix is shown due to space limitations.

$$R = \begin{pmatrix} -k_q(p) - p \sum_i k(0, i) & k(1, 0)p & 2fk(1, 0)p & 0 \\ k(1, 0)e^{-\Theta}p & -k_q(p) - p \sum_i k(1, i) & 2k(1, 0)p & 0 \\ 2fk(1, 0)e^{-2\Theta}p & 2k(1, 0)e^{-\Theta}p & -k_q(p) - p \sum_i k(2, i) & 3k(1, 0)p \\ 0 & 3fk(1, 0)e^{-2\Theta}p & 3k(1, 0)e^{-\Theta}p & -k_q(p) - p \sum_i k(3, i) \end{pmatrix}$$

where

p = bath gas pressure

$k_q(p) = k_{eq}(p) + \frac{1}{\tau_r}$, the collisionless losses from the state of interest

$k_{eq}(p)$ = electronic quenching rate coefficient

τ_r = radiative lifetime

$k(1, 0)$ = fundamental rate coefficient

f = multi-quantum fraction

$\Theta = \omega_e/kT$, scaling factor for detail balance

As implemented in this research, the best fit to the data was found by varying the following terms to find the least-squared error: $k_{eq}(p)$, $k(1, 0)$, f and T .

Appendix B. Observed Bi_2 Rotational Lines

This appendix contains rotational lines observed in this research along with their spectroscopic assignment. Lines that are missing are not listed due to their overlap with a rotational line from another vibrational band which precluded the unambiguous assignment of that transition. All wavelengths are listed in vacuum wavenumbers.

Table B.1
Observed rotational line positions for $v'' = 2 \rightarrow v' = 2$

J	R(J)	P(J)	J	R(J)	P(J)	J	R(J)	P(J)
105	X	17600.489	143	17580.498	17569.325	181	17543.166	17529.065
106	X	17599.785	144	17579.635	17568.382	182	17542.057	17527.881
107	X	17599.073	145	17578.761	17567.430	183	17540.946	17526.691
108	X	17598.358	146	17577.884	17566.475	184	17539.828	17525.497
109	X	17597.638	147	17576.997	X	185	17538.704	X
110	X	X	148	17576.108	17564.550	186	17537.569	X
111	X	17596.172	149	17575.212	17563.574	187	X	X
112	X	17595.430	150	17574.307	17562.595	188	17535.290	X
113	X	X	151	X	17561.608	189	17534.137	X
114	X	X	152	17572.478	17560.615	190	17532.987	X
115	X	17593.169	153	17571.559	X	191	17531.822	X
116	X	17592.402	154	17570.630	17558.603	192	17530.653	X
117	17600.789	X	155	X	17557.591	193	X	X
118	17600.087	17590.851	156	17568.755	17556.573	194	17528.297	X
119	X	17590.065	157	17567.804	17555.550	195	17527.109	X
120	17598.665	17589.272	158	17566.848	17554.519	196	17525.912	X
121	17597.949	17588.476	159	17565.889	17553.483			
122	X	17587.672	160	X	17552.438			
123	17596.488	17586.857	161	X	17551.390			
124	17595.746	17586.039	162	17562.976	17550.332			
125	17595.002	17585.219	163	17561.992	17549.267			
126	X	17584.388	164	17560.999	17548.200			
127	17593.496	17583.554	165	X	17547.123			
128	17592.727	17582.711	166	17558.997	17546.042			
129	17591.953	X	167	17557.980	17544.954			
130	17591.178	17581.008	168	X	17543.862			
131	17590.394	17580.150	169	X	17542.761			
132	17589.603	17579.281	170	17554.913	X			
133	17588.809	17578.406	171	17553.875	17540.543			
134	17588.005	17577.527	172	17552.833	X			
135	17587.198	17576.644	173	17551.784	17538.294			
136	X	17575.748	174	17550.729	17537.164			
137	17585.560	17574.850	175	17549.669	17536.026			
138	17584.731	17573.944	176	X	17534.876			
139	X	X	177	17547.525	X			
140	17583.057	X	178	17546.443	17532.574			
141	17582.211	17571.191	179	17545.356	X			
142	17581.358	17570.261	180	17544.262	17530.240			

Table B.2
Observed rotational line positions for $v'' = 3 \rightarrow v' = 0$

J	R(J)	P(J)	J	R(J)	P(J)	J	R(J)	P(J)
13	X	17204.753	52	X	17195.560	91	17184.474	17177.298
14	X	17204.631	53	17199.405	17195.205	92	17183.966	17176.708
15	X	17204.504	54	17199.121	17194.842	93	17183.450	17176.116
16	X	17204.367	55	17198.835	17194.474	94	17182.929	17175.514
17	X	17204.227	56	17198.544	X	95	17182.401	17174.911
18	X	17204.081	57	17198.239	17193.722	96	17181.870	17174.300
19	X	17203.928	58	17197.933	17193.339	97	17181.332	17173.682
20	X	X	59	17197.623	17192.949	98	17180.786	17173.059
21	X	17203.608	60	17197.304	17192.552	99	17180.234	17172.431
22	X	17203.440	61	17196.980	17192.147	100	17179.680	17171.796
23	X	17203.263	62	17196.649	17191.739	101	17179.114	17171.154
24	17204.998	17203.081	63	X	17191.326	102	17178.545	17170.507
25	17204.892	17202.891	64	17195.970	17190.905	103	17177.971	17169.853
26	17204.776	17202.700	65	17195.623	17190.478	104	17177.390	17169.195
27	17204.654	17202.501	66	17195.267	17190.046	105	17176.803	17168.530
28	17204.527	17202.292	67	17194.909	17189.606	106	17176.206	17167.858
29	17204.394	17202.083	68	17194.539	17189.163	107	17175.609	17167.182
30	17204.254	17201.861	69	17194.167	17188.716	108	17175.005	X
31	17204.109	17201.636	70	17193.789	X	109	17174.395	X
32	17203.957	17201.409	71	17193.405	17187.797	110	17173.778	X
33	X	17201.172	72	17193.018	17187.323	111	17173.157	17164.414
34	17203.640	17200.925	73	17192.621	17186.856	112	17172.525	17163.705
35	17203.473	X	74	17192.218	17186.377	113	17171.891	X
36	17203.296	17200.425	75	X	17185.885	114	17171.251	17162.273
37	17203.117	17200.168	76	17191.397	17185.394	115	17170.605	17161.550
38	X	17199.901	77	17190.978	17184.896	116	17169.952	X
39	17202.733	X	78	17190.553	17184.394	117	17169.294	17160.084
40	17202.535	17199.350	79	17190.120	17183.881	118	17168.629	X
41	17202.331	17199.068	80	17189.684	17183.367	119	17167.959	17158.590
42	17202.122	17198.779	81	17189.241	17182.843	120	X	17157.837
43	17201.903	17198.484	82	17188.791	17182.316	121	17166.600	17157.075
44	17201.680	17198.183	83	17188.336	17181.781	122	17165.906	X
45	17201.451	17197.876	84	17187.876	17181.243	123	X	X
46	17201.217	17197.562	85	17187.404	17180.699	124	X	17154.758
47	17200.976	17197.245	86	17186.938	17180.144	125	17163.807	X
48	X	17196.919	87	17186.456	17179.588	126	17163.096	X
49	17200.474	17196.587	88	17185.967	17179.026	127	17162.375	17152.388
50	17200.216	17196.249	89	17185.476	17178.453	128	X	17151.585
51	17199.952	17195.909	90	17184.979	17177.879	129	17160.924	17150.777

Table B.2 Continued. Observed rotational line positions for $v'' = 3 \rightarrow v' = 0$

J	R(J)	P(J)
130	17160.187	X
131	17159.442	17149.144
132	X	17148.316
133	17157.939	17147.482
134	17157.181	17146.646
135	17156.413	17145.800
136	17155.641	17144.950
137	17154.861	X
138	17154.077	17143.232
139	17153.285	17142.363
140	17152.493	17141.488
141	17151.688	17140.607
142	17150.879	17139.722
143	X	17138.829
144	17149.245	17137.936
145	17148.420	X
146	17147.586	X
147	X	X
148	17145.903	X
149	17145.054	X
150	X	X
151	17143.332	X
152	X	X
153	17141.588	X
154	17140.709	X
155	17139.823	X
156	17138.930	X
157	17138.038	X

Table B.3
Observed rotational line positions for $v'' = 3 \rightarrow v' = 1$

J	R(J)	P(J)	J	R(J)	P(J)	J	R(J)	P(J)
104	X	17300.405	143	17280.761	17269.554	182	17243.661	17229.446
105	X	17299.732	144	X	17268.642	183	17242.588	17228.293
106	X	17299.050	145	17279.084	17267.725	184	17241.508	17227.134
107	X	17298.367	146	17278.238	17266.797	185	17240.419	X
108	X	17297.674	147	17277.383	17265.868	186	17239.329	17224.803
109	X	17296.973	148	17276.526	17264.931	187	17238.231	17223.630
110	X	17296.268	149	17275.662	17263.988	188	17237.126	17222.448
111	X	17295.554	150	17274.784	17263.038	189	17236.017	17221.259
112	X	17294.835	151	17273.906	17262.083	190	17234.901	17220.065
113	X	17294.111	152	17273.022	17261.122	191	17233.778	X
114	X	17293.380	153	X	17260.154	192	17232.648	17217.661
115	X	17292.643	154	17271.237	17259.181	193	X	X
116	X	17291.898	155	X	17258.202	194	17230.374	X
117	17300.332	17291.153	156	17269.427	17257.218	195	17229.226	17214.013
118	17299.659	17290.399	157	17268.510	17256.226	196	17228.074	17212.776
119	17298.976	17289.638	158	17267.590	17255.227	197	X	17211.544
120	17298.291	17288.871	159	17266.663	17254.224	198	17225.747	17210.305
121	17297.597	17288.097	160	17265.733	17253.214	199	17224.576	X
122	X	17287.317	161	X	17252.195	200	17223.399	X
123	17296.188	17286.535	162	17263.852	17251.171	201	17222.215	X
124	17295.472	17285.743	163	17262.897	17250.139	202	17221.023	X
125	17294.753	17284.946	164	17261.940	17249.104	203	17219.826	X
126	X	17284.143	165	17260.978	17248.067	204	17218.629	X
127	17293.295	17283.333	166	17260.004	17247.022	205	X	X
128	17292.557	17282.519	167	17259.029	17245.969	206	17216.205	X
129	17291.813	17281.697	168	X	17244.909	207	17214.985	X
130	17291.065	X	169	17257.059	17243.844	208	17213.758	X
131	17290.308	17280.035	170	17256.066	X	209	17212.521	X
132	X	17279.196	171	17255.065	17241.698	210	X	X
133	17288.784	17278.350	172	17254.059	17240.614	211	17210.037	X
134	17288.003	X	173	17253.047	X			
135	X	17276.640	174	17252.029	17238.427			
136	X	17275.778	175	17251.006	17237.327			
137	X	X	176	17249.970	17236.218			
138	X	17274.026	177	17248.933	17235.104			
139	X	17273.145	178	17247.894	17233.986			
140	17283.231	17272.258	179	17246.844	17232.857			
141	17282.414	17271.361	180	17245.789	17231.727			
142	17281.591	17270.463	181	17244.730	X			

Table B.4
Observed rotational line positions for $v'' = 3 \rightarrow v' = 3$

J	R(J)	P(J)	J	R(J)	P(J)	J	R(J)	P(J)
6	X	17598.861	45	17594.537	17590.991	84	17580.165	17573.590
7	X	17598.778	46	17594.289	17590.664	85	17579.674	X
8	X	X	47	X	17590.331	86	17579.175	17572.441
9	X	17598.595	48	X	17589.992	87	17578.667	17571.857
10	X	17598.492	49	X	17589.646	88	17578.156	17571.267
11	X	17598.384	50	17593.230	X	89	17577.639	17570.670
12	X	17598.272	51	17592.947	17588.935	90	17577.111	17570.068
13	17599.202	17598.150	52	17592.661	17588.574	91	17576.582	17569.461
14	17599.153	17598.023	53	17592.367	17588.202	92	17576.042	17568.843
15	17599.097	17597.892	54	17592.068	17587.824	93	17575.499	17568.215
16	X	17597.751	55	17591.763	17587.441	94	17574.950	17567.588
17	17598.972	17597.608	56	17591.451	17587.047	95	17574.391	17566.955
18	17598.897	17597.456	57	17591.133	17586.649	96	17573.827	17566.315
19	17598.816	17597.298	58	17590.809	17586.249	97	17573.258	17565.668
20	17598.730	17597.132	59	17590.478	17585.840	98	17572.682	17565.015
21	17598.640	17596.963	60	17590.141	17585.426	99	X	X
22	17598.538	17596.785	61	17589.798	17585.005	100	17571.513	X
23	X	17596.604	62	17589.448	17584.579	101	17570.918	17563.024
24	17598.326	17596.413	63	17589.092	17584.145	102	17570.318	17562.346
25	17598.205	17596.218	64	17588.730	17583.704	103	X	17561.661
26	17598.080	17596.015	65	17588.361	17583.260	104	17569.098	17560.970
27	X	17595.807	66	17587.989	17582.806	105	17568.476	17560.273
28	17597.814	17595.595	67	17587.607	17582.347	106	17567.846	17559.569
29	17597.671	17595.372	68	17587.216	X	107	17567.216	X
30	17597.523	17595.146	69	17586.822	17581.411	108	17566.578	17558.137
31	17597.368	17594.913	70	17586.423	17580.934	109	17565.933	17557.416
32	X	X	71	17586.018	17580.450	110	17565.283	17556.689
33	17597.038	17594.427	72	17585.608	17579.962	111	X	X
34	17596.864	17594.177	73	17585.188	17579.463	112	X	17555.214
35	17596.685	X	74	17584.762	17578.963	113	X	17554.466
36	X	X	75	17584.331	17578.452	114	17562.615	17553.712
37	17596.307	17593.382	76	X	17577.938	115	17561.940	17552.955
38	17596.106	17593.106	77	17583.450	17577.415	116	17561.250	17552.188
39	17595.901	17592.822	78	17583.001	17576.889	117	17560.555	17551.414
40	17595.689	17592.534	79	17582.545	17576.354	118	17559.854	17550.634
41	17595.471	17592.240	80	17582.082	17575.815	119	X	17549.851
42	17595.248	X	81	17581.616	17575.270	120	17558.426	17549.057
43	X	X	82	17581.138	17574.714	121	17557.707	17548.259
44	17594.780	17591.311	83	X	17574.156	122	X	17547.457

Table B.4 Continued. Observed rotational line positions for $v'' = 3 \rightarrow v' = 3$

J	R(J)	P(J)
123	17556.249	17546.646
124	17555.510	17545.832
125	17554.764	17545.007
126	17554.011	17544.180
127	17553.257	17543.344
128	17552.491	17542.503
129	17551.720	X
130	17550.945	17540.800
131	17550.161	17539.940
132	17549.367	17539.073
133	17548.570	17538.201
134	17547.771	17537.320
135	17546.962	X
136	17546.148	17535.540
137	17545.326	17534.643
138	17544.500	X
139	17543.666	17532.831
140	17542.828	17531.915
141	17541.978	17530.990
142	17541.128	17530.061
143	17540.267	17529.126
144	X	17528.182
145	17538.532	17527.234
146	17537.655	17526.276
147	17536.766	17525.315
148	17535.877	X
149	17534.982	X
150	17534.077	X
151	17533.171	X
152	17532.258	X
153	17531.336	X
154	17530.405	X
155	X	X
156	17528.528	X
157	17527.582	X
158	17526.627	X
159	17525.668	X
160	17524.704	X

Table B.5
Observed rotational line positions for $v'' = 3 \rightarrow v' = 4$

J	R(J)	P(J)	J	R(J)	P(J)	J	R(J)	P(J)
7	X	17728.682	46	17724.077	17720.467	85	17709.194	X
8	X	17728.598	47	X	17720.125	86	17708.683	17701.968
9	X	17728.497	48	17723.550	17719.781	87	X	17701.375
10	X	17728.392	49	17723.276	17719.430	88	17707.646	X
11	X	X	50	17722.997	17719.072	89	17707.119	17700.172
12	X	17728.173	51	17722.712	17718.709	90	17706.584	17699.561
13	X	17728.048	52	17722.417	17718.340	91	17706.042	17698.942
14	X	17727.917	53	17722.121	17717.962	92	X	17698.314
15	X	17727.784	54	17721.816	X	93	17704.946	17697.685
16	17728.924	17727.644	55	17721.505	X	94	17704.383	17697.047
17	X	17727.500	56	17721.187	17716.795	95	17703.815	X
18	17728.783	17727.344	57	17720.865	17716.394	96	17703.245	17695.748
19	17728.700	17727.182	58	17720.533	17715.984	97	17702.663	17695.095
20	17728.610	X	59	17720.196	17715.569	98	17702.077	17694.432
21	17728.514	17726.839	60	17719.852	17715.148	99	17701.484	17693.761
22	17728.416	17726.665	61	17719.503	17714.723	100	17700.887	17693.085
23	X	17726.484	62	17719.147	17714.289	101	X	17692.408
24	17728.194	17726.288	63	17718.783	17713.849	102	17699.670	X
25	17728.075	17726.089	64	X	X	103	17699.052	X
26	17727.946	17725.886	65	17718.039	X	104	17698.428	X
27	17727.813	17725.678	66	17717.659	17712.490	105	X	X
28	17727.675	17725.459	67	17717.273	17712.028	106	17697.160	X
29	17727.530	17725.234	68	17716.875	17711.547	107	17696.518	X
30	17727.378	17725.005	69	17716.475	17711.077	108	17695.866	X
31	17727.217	17724.770	70	17716.068	X	109	17695.210	X
32	17727.055	17724.528	71	17715.653	X	110	17694.549	X
33	17726.881	17724.277	72	17715.233	17709.604	111	17693.879	X
34	17726.703	17724.024	73	17714.807	X	112	17693.205	X
35	17726.520	17723.762	74	17714.377	17708.589	113	17692.522	X
36	17726.329	17723.491	75	17713.936	17708.070	114	17691.836	X
37	17726.135	17723.221	76	17713.489	17707.548			
38	17725.929	17722.942	77	17713.040	17707.017			
39	17725.722	17722.652	78	17712.578	17706.482			
40	17725.507	17722.356	79	17712.115	17705.942			
41	17725.282	17722.059	80	17711.648	17705.393			
42	17725.054	17721.752	81	17711.169	X			
43	17724.820	17721.440	82	X	17704.279			
44	X	17721.120	83	17710.192	X			
45	17724.330	17720.797	84	17709.696	17703.136			

Table B.6
Observed rotational line positions for $v'' = 4 \rightarrow v' = 0$

J	R(J)	P(J)	J	R(J)	P(J)	J	R(J)	P(J)
3	X	17035.657	42	17032.213	17028.874	81	17019.592	17013.196
4	X	17035.593	43	17032.003	17028.586	82	17019.151	17012.675
5	X	17035.523	44	17031.782	17028.289	83	17018.706	17012.153
6	X	17035.448	45	17031.558	17027.987	84	17018.253	17011.624
7	X	17035.367	46	17031.329	17027.679	85	17017.796	17011.086
8	X	X	47	17031.092	17027.364	86	17017.330	17010.543
9	X	17035.190	48	17030.850	17027.045	87	17016.862	17009.993
10	X	17035.091	49	17030.604	17026.716	88	17016.384	17009.439
11	X	17034.989	50	17030.352	17026.385	89	17015.903	17008.880
12	X	17034.878	51	17030.091	17026.048	90	17015.417	17008.315
13	17035.824	17034.762	52	17029.831	17025.704	91	17014.921	17007.743
14	17035.781	17034.644	53	17029.555	17025.354	92	17014.423	17007.166
15	17035.734	17034.515	54	17029.279	17024.999	93	17013.917	17006.580
16	17035.680	17034.380	55	17028.998	17024.637	94	17013.403	17005.991
17	17035.621	17034.242	56	17028.711	17024.270	95	17012.888	17005.394
18	17035.553	17034.099	57	17028.412	17023.898	96	17012.366	17004.793
19	17035.481	17033.950	58	17028.114	17023.519	97	17011.837	17004.189
20	17035.404	17033.792	59	17027.808	17023.139	98	17011.302	17003.576
21	17035.324	17033.632	60	17027.497	17022.746	99	17010.762	17002.957
22	17035.231	17033.462	61	17027.178	17022.348	100	17010.216	17002.331
23	17035.134	17033.289	62	17026.855	17021.946	101	17009.662	17001.702
24	17035.032	17033.111	63	17026.523	17021.538	102	17009.104	17001.066
25	17034.927	17032.925	64	17026.186	17021.127	103	17008.541	17000.424
26	17034.813	17032.732	65	17025.847	17020.705	104	17007.973	16999.775
27	17034.693	17032.535	66	17025.500	17020.280	105	17007.396	16999.122
28	17034.571	17032.334	67	17025.146	17019.847	106	17006.812	16998.463
29	17034.439	17032.123	68	17024.791	17019.412	107	17006.226	16997.796
30	17034.306	17031.909	69	17024.426	17018.969	108	17005.633	16997.126
31	17034.162	17031.692	70	17024.055	17018.517	109	17005.034	16996.449
32	17034.017	17031.461	71	17023.678	17018.067	110	17004.429	16995.766
33	17033.860	17031.229	72	17023.296	17017.604	111	17003.816	16995.073
34	17033.699	17030.992	73	17022.908	17017.139	112	17003.201	16994.381
35	17033.535	17030.746	74	17022.513	17016.666	113	17002.579	16993.680
36	17033.362	17030.497	75	17022.115	17016.187	114	17001.953	16992.972
37	17033.186	17030.241	76	17021.709	17015.705	115	17001.318	X
38	17033.006	X	77	17021.297	17015.213	116	17000.676	X
39	17032.815	17029.707	78	17020.880	17014.720	117	17000.029	16990.823
40	17032.622	17029.438	79	17020.459	17014.217	118	16999.376	X
41	17032.422	17029.159	80	17020.028	17013.708	119	16998.717	16989.353

Table B.6 Continued. Observed rotational line positions for $v'' = 4 \rightarrow v' = 0$

J	R(J)	P(J)	J	R(J)	P(J)
120	16998.054	16988.611	159	X	X
121	16997.386	16987.863	160	16966.677	X
122	16996.709	16987.108	161	16965.773	16953.142
123	16996.028	16986.352	162	16964.862	16952.154
124	16995.342	16985.589	163	16963.947	16951.159
125	16994.652	16984.814	164	16963.023	16950.160
126	X	16984.037	165	16962.095	16949.154
127	16993.245	X	166	16961.158	16948.142
128	X	16982.467	167	16960.219	16947.124
129	16991.813	16981.672	168	X	X
130	16991.094	16980.871	169	X	X
131	16990.366	16980.063	170	16957.360	16944.034
132	16989.630	X	171	16956.396	16942.993
133	16988.890	X	172	16955.428	16941.946
134	16988.144	16977.611	173	16954.450	16940.893
135	16987.395	X	174	16953.469	16939.836
136	16986.636	X	175	16952.483	16938.771
137	16985.872	16975.103	176	16951.490	X
138	16985.100	16974.255	177	16950.490	16936.621
139	16984.325	16973.402	178	16949.485	16935.538
140	16983.546	X	179	16948.473	16934.451
141	16982.756	16971.676	180	16947.457	16933.356
142	X	16970.806	181	16946.433	16932.255
143	16981.164	X	182	X	X
144	16980.357	16969.046	183	16944.369	X
145	16979.549	X	184	16943.325	X
146	X	16967.265	185	16942.281	X
147	X	X	186	16941.229	X
148	X	16965.457	187	X	X
149	X	16964.546	188	16939.107	X
150	X	X	189	16938.035	X
151	16974.559	16962.704	190	16936.958	X
152	16973.707	16961.776	191	16935.875	X
153	16972.848	16960.837	192	16934.788	X
154	X	16959.897	X	X	X
155	16971.115	16958.950	X	X	X
156	16970.241	16957.998	X	X	X
157	X	16957.037	X	X	X
158	16968.470	16956.072	X	X	X

Table B.7
Observed rotational line positions for $v'' = 4 \rightarrow v' = 1$

J	R(J)	P(J)	J	R(J)	P(J)	J	R(J)	P(J)
11	X	17166.746	50	17161.978	17158.023	89	17147.249	17140.241
12	X	17166.635	51	17161.715	17157.681	90	17146.750	17139.667
13	X	17166.516	52	17161.445	17157.332	91	17146.248	17139.086
14	X	X	53	17161.167	17156.977	92	17145.739	X
15	X	17166.267	54	17160.885	17156.618	93	17145.225	17137.912
16	X	17166.135	55	17160.597	17156.250	94	17144.703	17137.313
17	X	17165.992	56	17160.302	17155.878	95	17144.178	17136.708
18	X	17165.844	57	17160.002	17155.502	96	17143.645	17136.093
19	X	17165.694	58	17159.696	17155.116	97	17143.105	17135.476
20	X	17165.535	59	17159.384	17154.726	98	17142.561	17134.853
21	X	17165.371	60	17159.067	17154.329	99	17142.010	17134.225
22	17166.963	X	61	17158.742	17153.926	100	17141.451	17133.590
23	17166.866	17165.025	62	17158.412	17153.520	101	17140.885	17132.949
24	17166.763	17164.842	63	17158.077	17153.104	102	X	17132.305
25	17166.652	17164.656	64	17157.735	17152.683	103	17139.743	17131.652
26	17166.536	17164.463	65	17157.387	17152.258	104	17139.164	17130.991
27	17166.417	17164.261	66	17157.033	17151.827	105	17138.577	17130.326
28	17166.288	17164.056	67	17156.674	17151.388	106	X	17129.657
29	17166.158	17163.844	68	17156.308	17150.943	107	17137.392	17128.980
30	17166.015	17163.627	69	17155.936	17150.496	108	17136.785	17128.297
31	17165.869	17163.404	70	17155.557	17150.038	109	17136.173	17127.609
32	17165.720	17163.173	71	X	17149.576	110	17135.557	17126.918
33	17165.562	17162.937	72	17154.785	17149.108	111	17134.933	17126.217
34	17165.400	17162.696	73	17154.390	17148.635	112	17134.306	17125.514
35	17165.229	X	74	17153.985	17148.153	113	17133.672	X
36	17165.055	17162.194	75	17153.579	17147.666	114	17133.032	17124.078
37	17164.872	17161.936	76	17153.168	17147.177	115	17132.387	17123.355
38	17164.687	17161.671	77	17152.747	17146.679	116	17131.734	17122.626
39	X	17161.400	78	17152.322	17146.176	117	17131.074	17121.893
40	17164.294	17161.124	79	17151.891	17145.664	118	17130.410	17121.147
41	17164.091	17160.839	80	17151.454	17145.151	119	17129.739	17120.399
42	17163.879	17160.551	81	17151.009	17144.632	120	17129.063	17119.647
43	17163.662	17160.255	82	17150.558	17144.101	121	17128.381	X
44	17163.441	17159.953	83	17150.105	17143.570	122	17127.692	17118.118
45	17163.211	17159.647	84	17149.644	17143.030	123	17127.001	17117.346
46	17162.977	17159.335	85	17149.178	17142.484	124	17126.301	17116.570
47	17162.736	17159.016	86	17148.704	17141.930	125	17125.595	17115.785
48	17162.491	17158.692	87	17148.223	17141.373	126	17124.883	X
49	17162.236	17158.360	88	17147.738	17140.812	127	17124.161	17114.200

Table B.7 Continued. Observed rotational line positions for $v'' = 4 \rightarrow v' = 1$

J	R(J)	P(J)
128	X	17113.400
129	X	17112.591
130	17121.978	17111.776
131	17121.234	17110.958
132	17120.483	17110.133
133	X	17109.301
134	17118.970	17108.462
135	17118.205	17107.620
136	17117.427	17106.768
137	X	17105.914
138	17115.869	17105.051
139	X	17104.187
140	X	X
141	17113.483	17102.432
142	17112.674	17101.551
143	17111.860	17100.653
144	X	X
145	17110.214	17098.855
146	X	17097.945
147	17108.545	17097.030
148	17107.701	17096.108
149	17106.850	17095.181
150	17105.994	17094.246
151	17105.134	X
152	17104.264	X
153	17103.390	X
154	17102.514	X
155	17101.625	X
156	17100.732	X
157	17099.834	X
158	17098.932	X
159	17098.025	X
160	17097.107	X
161	17096.182	X
162	X	X
163	17094.320	X

Table B.8
Observed rotational line positions for $v'' = 4 \rightarrow v' = 2$

J	R(J)	P(J)	J	R(J)	P(J)	J	R(J)	P(J)
23	X	17296.142	62	17289.346	17284.464	101	17271.490	17263.576
24	X	17295.954	63	17289.004	X	102	17270.911	17262.915
25	X	17295.764	64	17288.659	17283.616	103	X	17262.252
26	X	X	65	17288.304	17283.185	104	17269.735	17261.583
27	X	17295.365	66	17287.944	17282.746	105	17269.134	17260.909
28	X	17295.157	67	17287.574	17282.303	106	17268.532	17260.227
29	X	17294.942	68	X	17281.850	107	17267.923	17259.540
30	X	17294.722	69	17286.821	17281.392	108	17267.308	17258.847
31	X	17294.494	70	X	17280.932	109	17266.686	17258.146
32	X	17294.263	71	17286.044	17280.461	110	17266.060	17257.441
33	X	X	72	X	17279.985	111	17265.426	17256.729
34	17296.480	17293.780	73	17285.246	17279.505	112	X	17256.012
35	17296.306	17293.526	74	X	17279.018	113	17264.143	17255.288
36	17296.126	17293.271	75	17284.420	17278.526	114	17263.491	17254.561
37	17295.938	17293.008	76	17283.998	17278.026	115	17262.828	17253.823
38	17295.748	17292.740	77	17283.573	17277.520	116	17262.163	17253.081
39	X	17292.466	78	17283.138	17277.009	117	17261.494	17252.333
40	17295.347	17292.183	79	17282.698	17276.492	118	17260.818	17251.578
41	17295.139	X	80	17282.253	17275.971	119	X	17250.819
42	17294.923	17291.602	81	17281.801	17275.439	120	17259.446	17250.047
43	17294.701	17291.303	82	17281.342	X	121	17258.754	17249.276
44	17294.471	17290.997	83	X	17274.358	122	X	17248.501
45	17294.240	17290.687	84	17280.409	17273.810	123	17257.343	17247.717
46	17294.000	17290.369	85	X	17273.257	124	17256.630	17246.927
47	17293.756	17290.046	86	17279.451	17272.697	125	17255.912	17246.130
48	17293.502	17289.716	87	17278.965	X	126	17255.188	17245.328
49	17293.246	17289.380	88	17278.469	17271.560	127	17254.456	17244.519
50	17292.982	17289.039	89	17277.969	17270.978	128	17253.718	17243.705
51	17292.713	17288.695	90	17277.462	X	129	17252.975	17242.884
52	17292.439	17288.334	91	17276.952	17269.805	130	17252.226	17242.059
53	17292.155	17287.975	92	17276.432	17269.209	131	17251.469	17241.224
54	17291.867	17287.609	93	17275.909	17268.608	132	17250.708	X
55	17291.573	X	94	17275.377	17268.000	133	17249.937	17239.537
56	17291.273	17286.860	95	X	17267.386	134	17249.162	17238.688
57	17290.967	17286.476	96	17274.296	17266.766	135	17248.385	17237.829
58	17290.655	17286.084	97	17273.745	17266.137	136	17247.601	17236.968
59	17290.337	17285.689	98	17273.191	17265.505	137	17246.808	17236.097
60	17290.013	17285.287	99	17272.631	17264.872	138	17246.011	17235.223
61	17289.683	17284.879	100	17272.062	17264.228	139	17245.205	17234.342

Table B.8 Continued. Observed rotational line positions for $v'' = 4 \rightarrow v' = 2$

J	R(J)	P(J)
140	17244.397	17233.452
141	17243.580	17232.558
142	17242.759	17231.659
143	17241.928	17230.754
144	17241.091	17229.840
145	17240.253	17228.922
146	17239.405	17227.999
147	17238.551	17227.066
148	17237.694	17226.131
149	17236.827	17225.188
150	17235.957	17224.240
151	17235.079	17223.286
152	17234.195	17222.326
153	17233.305	17221.354
154	17232.411	17220.382
155	X	17219.406
156	X	X
157	17229.686	X
158	17228.768	17216.435
159	17227.840	17215.430
160	X	17214.420
161	X	X
162	17225.024	17212.381
163	17224.072	X
164	17223.116	17210.323
165	17222.154	X
166	17221.183	X
167	17220.208	X
168	17219.228	X
169	17218.244	X
170	17217.250	X
171	17216.248	X
172	X	X
173	X	X
174	X	X
175	X	X
176	17211.159	X
177	17210.123	X

Table B.9
Observed rotational line positions for $v'' = 5 \rightarrow v' = 1$

J	R(J)	P(J)	J	R(J)	P(J)	J	R(J)	P(J)
2	X	16998.239	41	16994.947	16991.697	80	16982.566	16976.261
3	X	16998.183	42	16994.742	16991.412	81	16982.130	16975.750
4	X	16998.120	43	16994.530	16991.123	82	16981.689	16975.230
5	X	X	44	16994.310	X	83	16981.244	16974.708
6	X	16997.977	45	X	16990.523	84	16980.790	16974.179
7	X	16997.896	46	16993.857	16990.215	85	X	16973.641
8	X	X	47	16993.622	16989.900	86	16979.869	16973.097
9	X	16997.721	48	16993.380	16989.581	87	X	16972.549
10	X	16997.621	49	16993.134	16989.255	88	X	16971.993
11	X	16997.517	50	16992.881	16988.925	89	16978.439	16971.437
12	X	16997.409	51	X	16988.587	90	16977.952	16970.872
13	X	X	52	16992.356	16988.244	91	16977.461	X
14	16998.308	16997.172	53	16992.086	16987.895	92	16976.961	16969.723
15	16998.259	16997.046	54	X	16987.540	93	X	16969.140
16	16998.206	16996.912	55	X	16987.179	94	16975.944	16968.551
17	16998.148	X	56	16991.241	16986.813	95	16975.430	16967.959
18	16998.079	16996.630	57	16990.945	16986.441	96	16974.906	16967.356
19	16998.008	X	58	16990.645	16986.061	97	X	16966.749
20	16997.930	16996.325	59	16990.340	16985.678	98	16973.843	16966.138
21	X	16996.161	60	16990.028	16985.288	99	X	16965.520
22	16997.760	X	61	16989.711	16984.895	100	16972.756	16964.896
23	16997.662	X	62	16989.387	16984.492	101	16972.206	16964.266
24	16997.560	16995.641	63	16989.059	16984.084	102	16971.649	16963.631
25	X	16995.456	64	16988.723	16983.670	103	16971.085	16962.992
26	16997.341	16995.264	65	16988.382	X	104	16970.515	X
27	16997.223	X	66	16988.034	16982.828	105	16969.939	16961.689
28	16997.099	16994.866	67	16987.682	16982.396	106	16969.358	16961.029
29	16996.967	X	68	16987.324	16981.960	107	16968.772	16960.365
30	16996.829	16994.442	69	16986.960	16981.517	108	16968.179	16959.694
31	X	16994.223	70	16986.589	16981.067	109	X	16959.018
32	X	16993.995	71	16986.216	16980.616	110	16966.977	16958.334
33	16996.389	16993.763	72	16985.833	16980.154	111	16966.367	16957.647
34	X	16993.526	73	16985.444	16979.687	112	16965.749	16956.952
35	16996.064	16993.281	74	16985.050	X	113	16965.128	16956.252
36	16995.893	16993.031	75	16984.648	16978.737	114	16964.498	16955.546
37	16995.716	16992.777	76	16984.245	X	115	16963.865	16954.834
38	16995.532	X	77	16983.834	16977.765	116	16963.226	16954.119
39	X	X	78	16983.416	16977.270	117	16962.579	16953.391
40	16995.148	X	79	16982.992	16976.772	118	16961.928	16952.662

Table B.9 Continued. Observed rotational line positions for $v'' = 5 \rightarrow v' = 1$

J	R(J)	P(J)
119	16961.269	16951.929
120	16960.607	16951.187
121	16959.938	16950.441
122	16959.264	16949.687
123	16958.581	16948.929
124	16957.895	16948.164
125	16957.202	16947.395
126	16956.503	16946.619
127	16955.799	X
128	16955.091	16945.048
129	16954.370	16944.253
130	16953.649	16943.455
131	16952.923	16942.648
132	16952.188	16941.839
133	16951.449	16941.021
134	16950.703	16940.196
135	16949.952	16939.369
136	16949.196	16938.534
137	16948.432	16937.693
138	16947.664	16936.845
139	16946.890	16935.992
140	X	16935.136
141	X	16934.271
142	16944.525	16933.402
143	16943.729	16932.525
144	16942.925	16931.644
145	16942.115	X
146	16941.299	X
147	16940.477	X
148	16939.649	X
149	16938.818	X
150	16937.975	X
151	16937.130	X
152	16936.277	X
153	16935.423	X
154	16934.558	X
155	16933.691	X

Appendix C. Spectral Fitting Function for CW LIF Spectra

In the vibrational transfer experiments, a single $\text{Bi}_2(\text{A})$ state vibrational level is initially populated. Mainly through collisions with the buffer gas, this population is redistributed throughout the A state vibrational manifold. In order to determine the relative populations of the different A state vibrational levels, the intensity of every radiative event must be accounted for. The density of the Bi_2 spectrum makes this an impossible task to accomplish if one is trying to look at each specific rotational transition. To this end, a mathematical expression has been found that accurately models emission from a thermalized vibration level in the A state to a single vibrational level in the X state. Emission from multiple upper state levels to multiple lower state levels can be modeled by use of this functional form on each vibrational transition of interest. The task of finding the relative populations is thus reduced to integrating the area under the curve associated with the function. The development and justification for using this mathematical expression will be discussed in the next several paragraphs.

C.1 Synthetic Spectra

The equation for fluorescence intensity was given by Equation 2.6. By substituting the expression $I = nh\nu$, an expression for the photon count of a single rotational transition can be found (9). This expression is

$$n_{v',v''}(J',J'') = Cq_{v',v''}\nu^3S(J',J'')N(v')f(J') \quad (\text{C.1})$$

where

$n_{v',v''}(J',J'')$ = photon flux (photons/s) of the $(v',J') \rightarrow (v'',J'')$ transition

C = arbitrary constant

$q_{v',v''}$ = Franck-Condon factor

$\nu = (v', J') \rightarrow (v'', J'')$ transition frequency

$S(J', J'')$ = Rotational linestrength factor

$N(v')$ = total population density in vibrational level v'

$f(J') = N(v', J')/N(v')$.

$N(v')$ is a constant value for a given vibrational transition. The rotational distribution, $f(J'')$, allows the prediction of the relative intensity of each rovibrational transition within the vibrational band. $N(v')$ is a scaling factor on the size of all these transitions. Figure C.1 shows a "stick spectrum" representing the relative intensity of a single vibrational band's rotational transition located at the transition emission wavelength. This "stick spectrum" is indicative of emission observed under infinite resolution (9).

The convolution of individual emission intensities of a single vibrational band under a finite resolution can be computed by Equation C.2.

$$n(\lambda_j) = \sum_{J'} \frac{n_{v',v''}(J', J'')}{\sqrt{2\pi} R} \exp \left[-\frac{1}{2} \left(\frac{\lambda_{J',J''} - \lambda_{j'}}{R} \right)^2 \right] \quad (\text{C.2})$$

This equation is simply a convolution of Gaussians associated with each rotational transition. The solid curve in Figure C.1 represents this convolution with a resolution element of 0.12 nm at a temperature of 400 K. This curve is the predicted spectrum under the given resolution.

C.2 Fitting Function

The following equation was found to be an acceptable model of the synthetically generated vibrational band:

$$I = \frac{ab}{c-b} [\exp(-b(\lambda - d)) - \exp(-c(\lambda - d))]. \quad (\text{C.3})$$

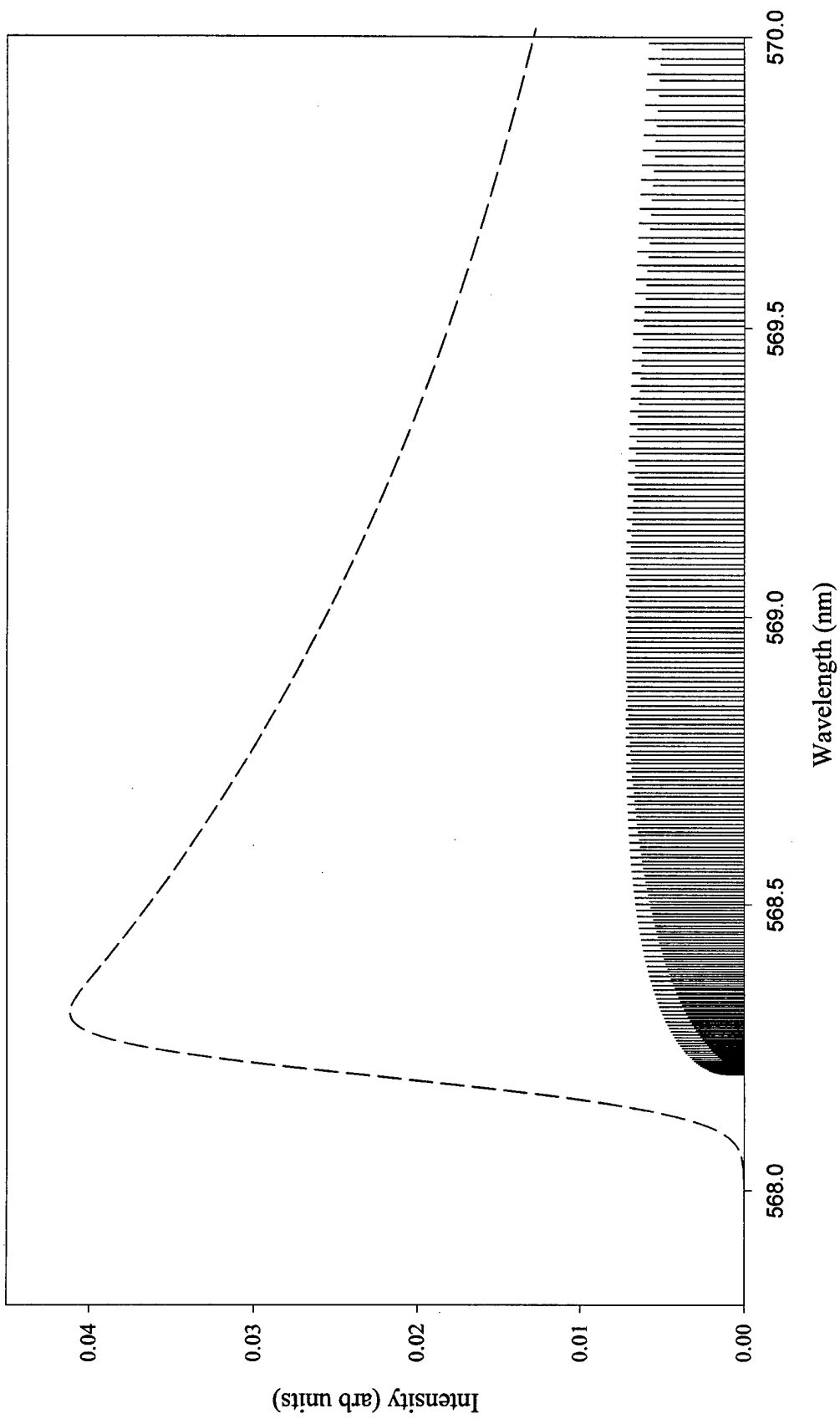


Figure C.1 Comparison of vibrational band "stick spectrum" with the synthetic CW LIF spectrum

This is simply a parametric fit. There was no attempt to mathematically derive Equation C.3. As can be seen in Figure C.2, there is good agreement between the generated synthetic spectrum and the predicted fit using the spectral fitting function. The number of data points generated from the fitting function has been reduced to allow better visualization of its behavior. This fitting function, when expressed in a slightly different manner, is a commonly used expression in chemical kinetics to model the time-dependent concentration behavior of the reaction intermediate in the two-step first order reaction: $A \rightarrow B \rightarrow C$ (51).

Several other asymmetric peak functions were found that also did a reasonable job of modeling the synthetic spectrum. However, Equation C.3 demonstrated the best fitting behavior at high rotational levels. This criteria was the main reason for selecting Equation C.3 over the other candidate functions.

The general features of emission of a single vibrational band are represented quite well. A few deficiencies need to be noted. At the abrupt start of the vibrational bandhead, the fitting function is a little slow to start its rise. This can be seen by the data point located just inside the synthetic spectrum line. At the peak intensity of the bandhead, the fitting function rolls over a little too rapidly and underestimates the intensity. However, the true benefit of this equation is seen in the behavior at high rotational levels where there is near coincidence of synthetic spectrum with the points predicted by the fitting function.

As was stated earlier, the method for determining population in a vibrational band is to measure the area under the curve of the spectrally resolved fluorescence. Thus, in order to use this fitting function, it must accurately predict this area. For the synthetic spectrum predicted in Figure C.2, the numerical value of the area, found by summing the area of the individual Gaussians that were convolved together, was 0.065349. The area under the curve of the fitting function is simply expressed as:

$$Area = \frac{a}{c}, \quad (C.4)$$

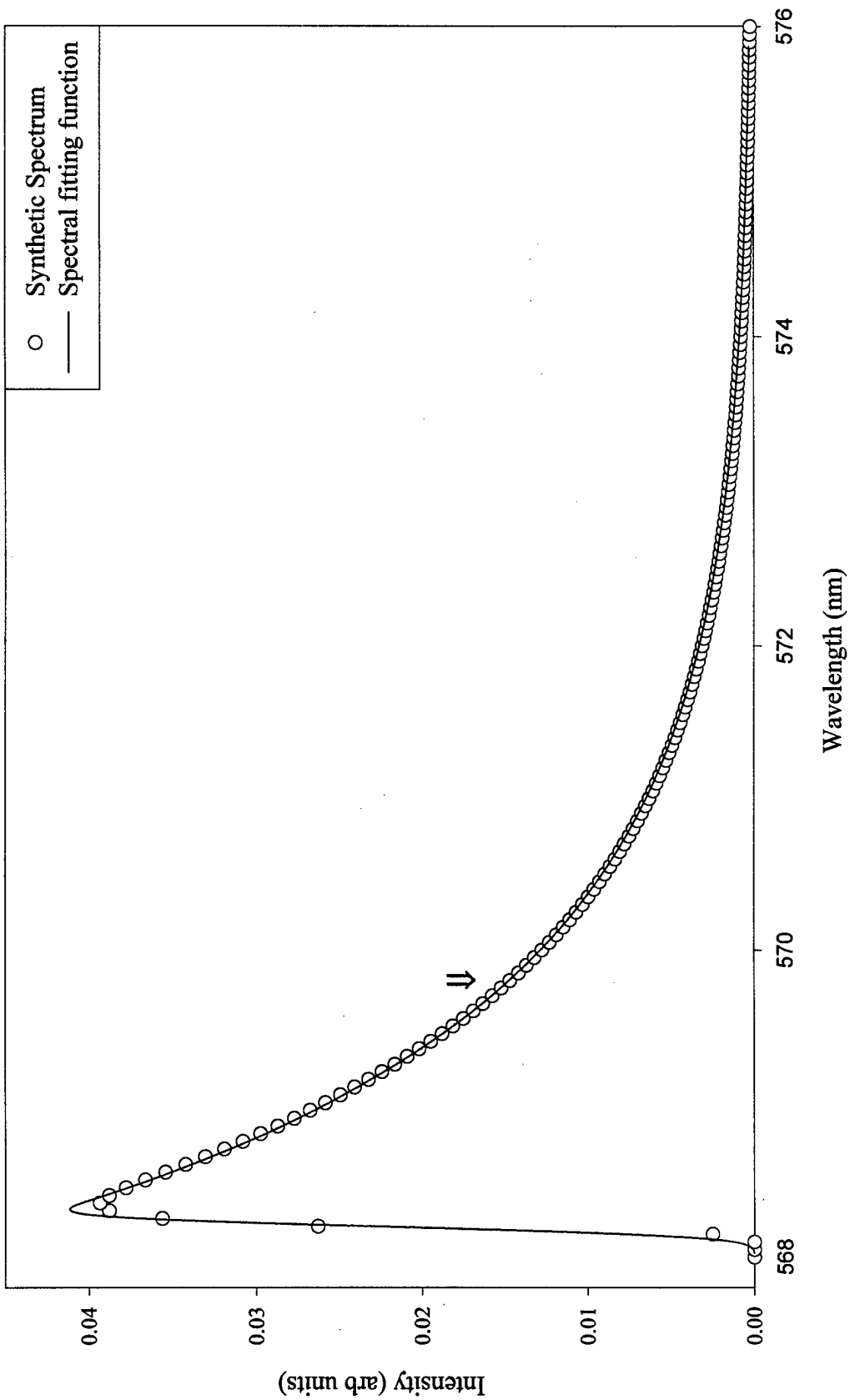


Figure C.2 Comparison of synthetic CW LIF spectrum with a spectral fitting function. The arrow on the graph indicates the relative position of the next vibrational band.

and for the example fit in Figure C.2 the predicted area is 0.06402. The ratio between these two different measures is 0.98. Thus, the fitting function does an extremely good job of predicting the population of a vibrational band.

As was stated earlier, this fitting function was found simply as a parametric fit to the synthetic spectrum. As such, there is no direct relation between the fit parameters and physically realizable quantities. However, the terms still have meaning. The a parameter can be seen as the band intensity as it is the term that controls how high the fitting function rises. Coupled with this rise is the d parameter, which defines the location of the rise, or in other words, the vibrational bandhead. The b and c parameters are essentially interchangeable. For a better explanation of this, see the reference by Steinfeld (51). The smaller of these two terms controls the high J behavior of the fitting function while the larger controls the slope of the rise at the bandhead. For the purpose of this research, c was kept the smaller of the two terms. An interesting behavior of c is noted if its value is plotted as a function of temperature. As seen in Figure C.3, there is a definite functional relation between these two values. This is not surprising as temperature has great influence on the rotational distribution of a molecule. A parametric fit to this relation yields the equation

$$c = \alpha + \beta T^{-\xi} \quad (\text{C.5})$$

where $\alpha = 0.0493 \pm 0.007$, $\beta = 601.1 \pm 38.2$ and $\xi = 1.14 \pm 0.01$. Even with the large error bound on these terms, the value of c can provide some insight to the rotational temperature of spectrally resolved fluorescence where the resolution is not fine enough to rotationally resolve the emissions.

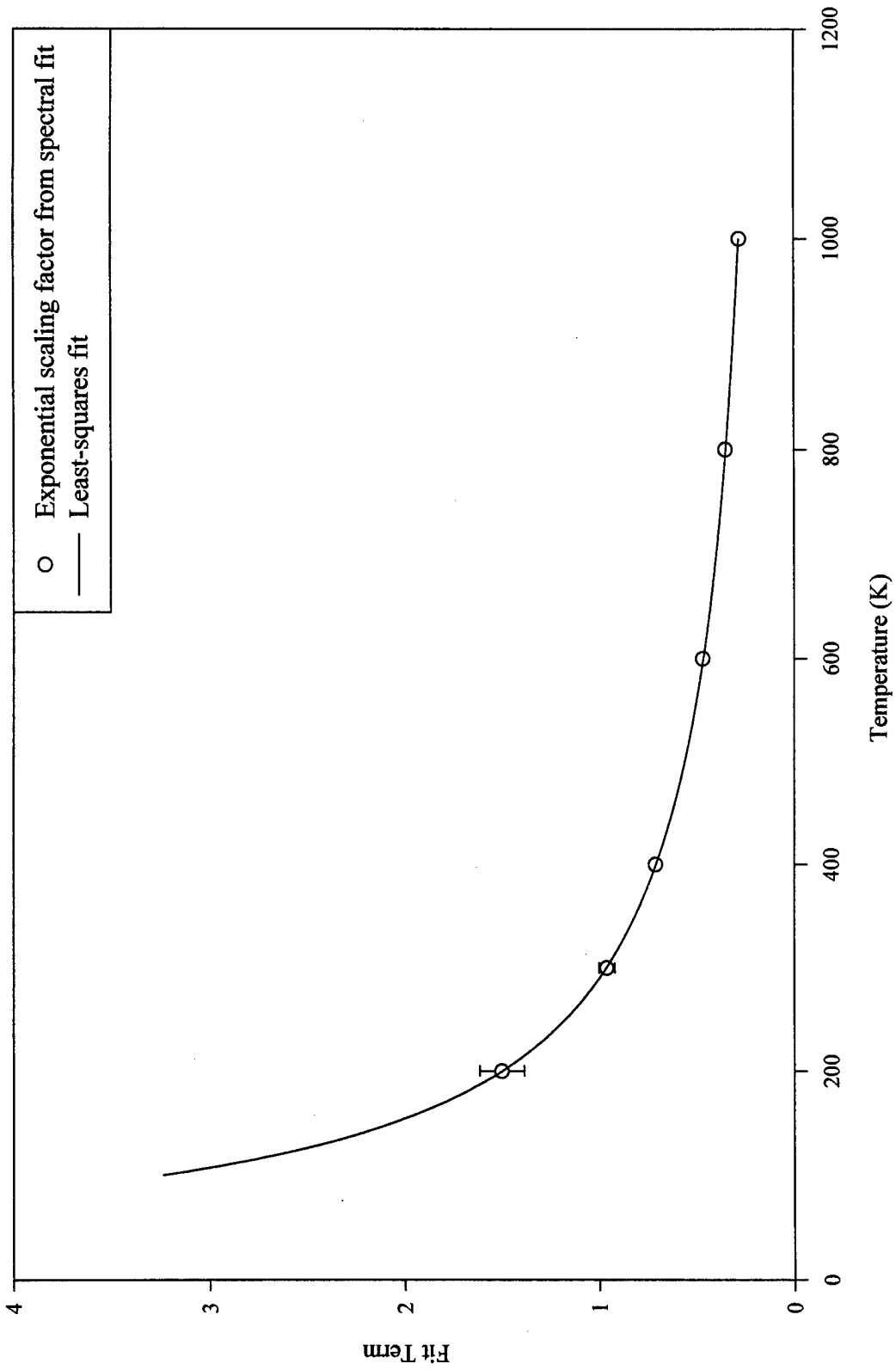


Figure C.3 Scaling of the spectral fitting function c parameter with temperature. The solid line is a least-squares parametric fit.

Appendix D. Rotational Transfer Fit Parameters

The rate coefficient for collisional transfer to a satellite level can be derived from the equation

$$\frac{N(J_f)}{N(J_0)} = \frac{aX}{1 + bX} \quad (\text{D.1})$$

where $N(J)$ is the population of the specific rotational state, X is the bath gas pressure and a and b are fit parameters. This equation effectively models the evolution of satellite rotation level populations plotted as a function of buffer gas pressure. For collisional energy transfer directly from the parent state to the observed satellite state, the transfer rate coefficient is derived from the a parameter through the relation

$$k_R(J_0 \rightarrow J_f) = a\Gamma(J_f)p \quad (\text{D.2})$$

where $\Gamma(J)$ is the lifetime of state J and p is a constant used to convert units of pressure to population density. In this study, $p = 2.8289 \times 10^{-17}$ cm³-torr/molec. As 590 ns is the only reported lifetime for any $v' = 1$ rotational level (23), this is the lifetime used in all conversion calculations.

The following table list the a and b parameters derived from a least-squares fits of the above equation to observed satellite population ratios plotted as a function of bath gas pressure. These tables also include the amount of angular momentum gained or lost in the collision as well as the corresponding rate transfer coefficient derived from the above relation in a . The errors listed for the a and b parameters are the standard errors derived from the least-squares fit to the data. The errors on the rotational transfer coefficients are derived from summing and differencing the a coefficient with its standard error.

Table D.1 Fit parameters and rotational transfer coefficients for $\text{Bi}_2(A, v'_0 = 1, J'_0 = 171)$ collisions with Helium.

ΔJ	a torr ⁻¹	b torr ⁻¹	$k_R(J'_0 \rightarrow J'_f)$ 10 ⁻¹¹ cm ³ /molec-sec
-2	2.711 ± 0.154	6.304 ± 0.486	13.052 ± 0.741
-4	1.467 ± 0.100	3.618 ± 0.037	7.065 ± 0.482
-6	0.945 ± 0.056	2.352 ± 0.235	4.549 ± 0.268
-8	0.713 ± 0.044	1.815 ± 0.204	3.435 ± 0.211
-10	0.639 ± 0.061	1.576 ± 0.286	3.078 ± 0.294
-12	0.552 ± 0.025	1.223 ± 0.124	2.660 ± 0.119
-14	0.409 ± 0.038	1.038 ± 0.232	1.969 ± 0.182
-16	0.378 ± 0.028	0.748 ± 0.161	1.819 ± 0.134
-18	0.364 ± 0.037	0.861 ± 0.237	1.751 ± 0.180
-20	0.288 ± 0.026	0.604 ± 0.177	1.385 ± 0.126
-22	0.349 ± 0.042	0.484 ± 0.287	1.682 ± 0.202
-24	0.265 ± 0.036	0.461 ± 0.233	1.277 ± 0.172
-26	0.231 ± 0.034	0.358 ± 0.235	1.111 ± 0.165
-28	0.223 ± 0.029	0.534 ± 0.242	1.071 ± 0.139
-30	0.205 ± 0.041	0.385 ± 0.333	0.985 ± 0.199
-32	0.194 ± 0.039	0.436 ± 0.356	0.935 ± 0.189
-34	0.149 ± 0.042	0.173 ± 0.390	0.719 ± 0.202
-36	0.174 ± 0.062	0.353 ± 0.564	0.839 ± 0.299
-38	0.149 ± 0.052	0.352 ± 0.551	0.716 ± 0.248
-40	0.184 ± 0.054	0.837 ± 0.595	0.886 ± 0.261
-42	0.133 ± 0.046	0.287 ± 0.534	0.638 ± 0.222
-44	0.109 ± 0.036	0.089 ± 0.430	0.526 ± 0.171
-46	0.088 ± 0.006	0.068 ± 0.084	0.422 ± 0.029
2	2.020 ± 0.142	5.089 ± 0.507	9.727 ± 0.682
4	1.080 ± 0.080	2.897 ± 0.350	5.201 ± 0.384
6	0.675 ± 0.052	1.732 ± 0.256	3.248 ± 0.251
8	0.531 ± 0.059	1.391 ± 0.324	2.555 ± 0.285
10	0.505 ± 0.058	1.606 ± 0.362	2.430 ± 0.281
12	0.319 ± 0.026	0.563 ± 0.154	1.535 ± 0.127
14	0.356 ± 0.037	1.025 ± 0.256	1.716 ± 0.180
16	0.269 ± 0.028	0.669 ± 0.208	1.294 ± 0.135
18	0.310 ± 0.046	1.428 ± 0.425	1.494 ± 0.219
20	0.248 ± 0.049	1.105 ± 0.495	1.193 ± 0.235
22	0.239 ± 0.024	0.734 ± 0.348	1.149 ± 0.113
24	0.217 ± 0.024	1.015 ± 0.257	1.043 ± 0.114

Table D.1 Continued. Fit parameters and rotational transfer coefficients for $\text{Bi}_2(A, v'_0 = 1, J'_0 = 171)$ collisions with Helium.

ΔJ	a torr ⁻¹	b torr ⁻¹	$k_R(J'_0 \rightarrow J'_f)$ 10 ⁻¹¹ cm ³ /molec-sec
26	0.165 ± 0.043	0.772 ± 0.530	0.793 ± 0.206
28	0.142 ± 0.025	0.331 ± 0.269	0.685 ± 0.120
30	0.138 ± 0.029	0.751 ± 0.426	0.663 ± 0.140
32	0.161 ± 0.022	1.433 ± 0.383	0.774 ± 0.106
34	0.097 ± 0.031	0.604 ± 0.564	0.467 ± 0.149
36	0.107 ± 0.048	0.903 ± 0.948	0.515 ± 0.232

Table D.2 Fit parameters and rotational transfer coefficients for $\text{Bi}_2(A, v'_0 = 1, J'_0 = 171)$ collisions with Helium.

ΔJ	a torr ⁻¹	b torr ⁻¹	$k_R(J'_0 \rightarrow J'_f)$ 10 ⁻¹¹ cm ³ /molec-sec
-2	1.985 ± 0.108	4.734 ± 0.366	9.558 ± 0.520
-4	1.200 ± 0.059	3.084 ± 0.232	5.778 ± 0.286
-6	0.840 ± 0.087	1.986 ± 0.352	4.045 ± 0.419
-8	0.661 ± 0.039	1.592 ± 0.169	3.181 ± 0.186
-10	0.515 ± 0.050	1.135 ± 0.229	2.479 ± 0.240
-12	0.432 ± 0.046	0.867 ± 0.199	2.082 ± 0.220
-14	0.420 ± 0.028	0.985 ± 0.133	2.023 ± 0.133
-16	0.303 ± 0.039	0.512 ± 0.204	1.457 ± 0.188
-18	0.310 ± 0.029	0.595 ± 0.158	1.491 ± 0.138
-20	0.238 ± 0.024	0.273 ± 0.131	1.146 ± 0.116
-22	0.299 ± 0.050	0.713 ± 0.305	1.438 ± 0.243
-24	0.249 ± 0.026	0.506 ± 0.166	1.198 ± 0.124
-26	0.216 ± 0.033	0.412 ± 0.225	1.041 ± 0.158
-28	0.205 ± 0.021	0.477 ± 0.159	0.987 ± 0.102
-30	0.160 ± 0.017	0.274 ± 0.133	0.771 ± 0.081
-32	0.151 ± 0.016	0.208 ± 0.128	0.725 ± 0.077
-34	0.183 ± 0.024	0.492 ± 0.204	0.883 ± 0.117
-36	0.132 ± 0.022	0.172 ± 0.197	0.636 ± 0.106
-38	0.139 ± 0.017	0.164 ± 0.138	0.671 ± 0.083
-40	0.154 ± 0.022	0.366 ± 0.200	0.740 ± 0.105
-44	0.093 ± 0.020	0.097 ± 0.238	0.448 ± 0.098
-46	0.090 ± 0.025	0.120 ± 0.294	0.435 ± 0.121
-48	0.095 ± 0.021	0.159 ± 0.265	0.458 ± 0.103
-54	0.071 ± 0.029	0.272 ± 0.490	0.342 ± 0.140
2	1.766 ± 0.076	4.334 ± 0.276	8.504 ± 0.365
4	0.926 ± 0.079	2.510 ± 0.365	4.461 ± 0.380
6	0.716 ± 0.058	2.371 ± 0.334	3.447 ± 0.281
8	0.514 ± 0.056	1.618 ± 0.294	2.473 ± 0.269
10	0.372 ± 0.043	0.920 ± 0.267	1.790 ± 0.205
12	0.419 ± 0.032	1.623 ± 0.240	2.015 ± 0.153
14	0.313 ± 0.048	1.163 ± 0.400	1.505 ± 0.231
16	0.173 ± 0.037	0.281 ± 0.314	0.832 ± 0.180
18	0.169 ± 0.025	0.398 ± 0.233	0.813 ± 0.119
20	0.209 ± 0.037	0.929 ± 0.392	1.006 ± 0.178
22	0.156 ± 0.043	0.644 ± 0.536	0.751 ± 0.207

Table D.2 Continued. Fit parameters and rotational transfer coefficients for $\text{Bi}_2(A, v'_0 = 1, J'_0 = 171)$ collisions with Helium.

ΔJ	a torr ⁻¹	b torr ⁻¹	$k_R(J'_0 \rightarrow J'_f)$ 10 ⁻¹¹ cm ³ /molec-sec
24	0.160 ± 0.018	0.641 ± 0.206	0.769 ± 0.084
26	0.151 ± 0.016	0.620 ± 0.197	0.729 ± 0.076
28	0.115 ± 0.016	0.448 ± 0.231	0.553 ± 0.075
30	0.104 ± 0.021	0.543 ± 0.388	0.500 ± 0.102
32	0.091 ± 0.033	0.475 ± 0.607	0.437 ± 0.158
36	0.083 ± 0.020	0.619 ± 0.437	0.397 ± 0.098
38	0.081 ± 0.051	0.531 ± 1.090	0.390 ± 0.247
40	0.082 ± 0.009	0.672 ± 0.206	0.396 ± 0.043
42	0.080 ± 0.016	0.616 ± 0.339	0.384 ± 0.076
44	0.061 ± 0.012	0.182 ± 0.245	0.293 ± 0.058

Table D.3 Fit parameters and rotational transfer coefficients for $\text{Bi}_2(A, v'_0 = 1, J'_0 = 231)$ collisions with Helium.

ΔJ	a torr ⁻¹	b torr ⁻¹	$k_R(J'_0 \rightarrow J'_f)$ 10 ⁻¹¹ cm ³ /molec-sec
-2	1.958 ± 0.334	4.429 ± 1.102	9.426 ± 1.608
-4	1.208 ± 0.175	2.576 ± 0.626	5.818 ± 0.841
-6	0.862 ± 0.220	2.504 ± 1.080	4.151 ± 1.057
-8	0.671 ± 0.126	1.396 ± 0.547	3.229 ± 0.606
-10	0.489 ± 0.056	0.976 ± 0.282	2.357 ± 0.270
-12	0.620 ± 0.117	1.667 ± 0.607	2.986 ± 0.563
-14	0.358 ± 0.066	0.679 ± 0.366	1.723 ± 0.319
-16	0.351 ± 0.048	0.281 ± 0.221	1.690 ± 0.230
-22	0.256 ± 0.112	0.469 ± 0.725	1.234 ± 0.539
-24	0.249 ± 0.064	0.501 ± 0.433	1.198 ± 0.306
-30	0.163 ± 0.032	0.007 ± 0.225	0.785 ± 0.152
2	1.901 ± 0.312	4.477 ± 1.029	9.152 ± 1.502
4	0.992 ± 0.251	2.753 ± 1.102	4.774 ± 1.207
6	0.932 ± 0.233	2.795 ± 1.120	4.487 ± 1.124
8	0.538 ± 0.088	1.189 ± 0.419	2.590 ± 0.421
12	0.453 ± 0.090	1.935 ± 0.687	2.180 ± 0.432
14	0.358 ± 0.079	1.475 ± 0.645	1.722 ± 0.378
16	0.531 ± 0.172	2.938 ± 1.481	2.557 ± 0.830
18	0.308 ± 0.223	1.223 ± 1.929	1.485 ± 1.076
22	0.186 ± 0.044	0.471 ± 0.410	0.898 ± 0.211
24	0.214 ± 0.069	0.142 ± 0.443	1.032 ± 0.334
26	0.207 ± 0.032	1.115 ± 0.390	0.998 ± 0.152
28	0.154 ± 0.049	0.486 ± 0.575	0.740 ± 0.236

Table D.4 Fit parameters and rotational transfer coefficients for $\text{Bi}_2(A, v'_0 = 1, J'_0 = 201)$ collisions with Neon.

ΔJ	a torr ⁻¹	b torr ⁻¹	$k_R(J'_0 \rightarrow J'_f)$ 10 ⁻¹¹ cm ³ /molec-sec
-2	1.645 ± 0.315	5.205 ± 1.325	7.920 ± 1.516
-4	0.990 ± 0.120	4.488 ± 0.744	4.766 ± 0.576
-6	0.603 ± 0.126	3.093 ± 0.952	2.902 ± 0.608
-8	0.572 ± 0.113	3.259 ± 0.934	2.755 ± 0.544
-10	0.405 ± 0.095	1.800 ± 0.725	1.952 ± 0.458
-12	0.287 ± 0.054	1.114 ± 0.428	1.380 ± 0.258
-14	0.271 ± 0.025	0.864 ± 0.187	1.303 ± 0.122
-16	0.226 ± 0.034	0.712 ± 0.271	1.086 ± 0.164
-18	0.228 ± 0.065	0.873 ± 0.568	1.099 ± 0.314
-20	0.202 ± 0.086	0.812 ± 0.817	0.972 ± 0.415
-22	0.157 ± 0.027	0.250 ± 0.217	0.754 ± 0.129
-24	0.164 ± 0.018	0.366 ± 0.149	0.790 ± 0.086
-26	0.205 ± 0.033	0.922 ± 0.336	0.985 ± 0.158
-28	0.168 ± 0.045	0.596 ± 0.456	0.807 ± 0.216
-30	0.282 ± 0.037	1.573 ± 0.373	1.357 ± 0.180
-32	0.163 ± 0.051	0.513 ± 0.485	0.786 ± 0.245
-34	0.132 ± 0.030	0.538 ± 0.366	0.636 ± 0.144
-36	0.129 ± 0.027	0.544 ± 0.342	0.620 ± 0.132
-38	0.159 ± 0.042	0.694 ± 0.476	0.767 ± 0.202
-40	0.142 ± 0.022	0.546 ± 0.246	0.682 ± 0.105
-42	0.157 ± 0.024	0.568 ± 0.249	0.756 ± 0.115
-44	0.147 ± 0.043	0.738 ± 0.557	0.705 ± 0.208
-46	0.157 ± 0.024	0.639 ± 0.256	0.756 ± 0.114
-48	0.143 ± 0.036	0.793 ± 0.478	0.687 ± 0.174
-52	0.117 ± 0.025	0.469 ± 0.320	0.565 ± 0.122
-54	0.118 ± 0.043	0.485 ± 0.555	0.568 ± 0.207
-56	0.120 ± 0.028	0.417 ± 0.339	0.576 ± 0.135
-58	0.112 ± 0.033	0.449 ± 0.419	0.537 ± 0.157
2	1.632 ± 0.241	5.798 ± 1.162	7.859 ± 1.159
4	0.652 ± 0.151	2.670 ± 1.005	3.138 ± 0.729
6	0.455 ± 0.066	2.173 ± 0.531	2.189 ± 0.316
8	0.176 ± 0.042	0.319 ± 0.325	0.848 ± 0.201
10	0.158 ± 0.045	0.486 ± 0.452	0.759 ± 0.216
12	0.294 ± 0.050	1.375 ± 0.461	1.416 ± 0.242
14	0.201 ± 0.049	1.170 ± 0.567	0.967 ± 0.234

Table D.4 Continued. Fit parameters and rotational transfer coefficients for $\text{Bi}_2(A, v'_0 = 1, J'_0 = 171)$ collisions with Neon.

ΔJ	a torr ⁻¹	b torr ⁻¹	$k_R(J'_0 \rightarrow J'_f)$ 10 ⁻¹¹ cm ³ /molec-sec
16	0.115 ± 0.019	0.334 ± 0.210	0.555 ± 0.090
18	0.189 ± 0.046	1.566 ± 0.683	0.911 ± 0.223
20	0.157 ± 0.026	0.904 ± 0.333	0.756 ± 0.124
22	0.177 ± 0.031	1.238 ± 0.401	0.851 ± 0.147
24	0.165 ± 0.064	1.766 ± 1.137	0.792 ± 0.309
26	0.105 ± 0.024	0.456 ± 0.335	0.505 ± 0.113
28	0.098 ± 0.022	0.495 ± 0.343	0.471 ± 0.107
32	0.083 ± 0.033	0.574 ± 0.664	0.399 ± 0.161
36	0.068 ± 0.011	0.289 ± 0.209	0.326 ± 0.055

Table D.5 Fit parameters and rotational transfer coefficients for $\text{Bi}_2(A, v'_0 = 1, J'_0 = 201)$ collisions with Argon.

ΔJ	a torr ⁻¹	b torr ⁻¹	$k_R(J'_0 \rightarrow J'_f)$ 10 ⁻¹¹ cm ³ /molec-sec
-2	1.695 ± 0.196	6.250 ± 0.983	8.162 ± 0.943
-4	0.880 ± 0.232	4.237 ± 1.667	4.235 ± 1.116
-6	0.905 ± 0.181	5.488 ± 1.535	4.359 ± 0.871
-10	0.492 ± 0.107	2.578 ± 0.983	2.367 ± 0.515
-12	0.284 ± 0.049	0.973 ± 0.447	1.367 ± 0.234
-14	0.233 ± 0.049	1.118 ± 0.576	1.123 ± 0.234
-16	0.203 ± 0.013	0.434 ± 0.124	0.978 ± 0.063
-18	0.278 ± 0.045	1.813 ± 0.587	1.340 ± 0.218
-20	0.166 ± 0.013	0.056 ± 0.112	0.800 ± 0.062
-22	0.278 ± 0.081	1.518 ± 0.918	1.338 ± 0.388
-24	0.209 ± 0.043	0.759 ± 0.475	1.007 ± 0.206
-26	0.213 ± 0.041	0.759 ± 0.439	1.027 ± 0.196
-28	0.210 ± 0.035	0.877 ± 0.407	1.009 ± 0.167
-30	0.173 ± 0.021	0.563 ± 0.243	0.832 ± 0.100
-32	0.237 ± 0.046	1.563 ± 0.622	1.139 ± 0.220
-34	0.241 ± 0.026	1.586 ± 0.353	1.161 ± 0.124
-36	0.181 ± 0.030	0.614 ± 0.342	0.869 ± 0.146
-38	0.199 ± 0.035	0.843 ± 0.427	0.957 ± 0.167
-40	0.336 ± 0.028	2.360 ± 0.333	1.617 ± 0.133
-42	0.204 ± 0.047	1.232 ± 0.664	0.980 ± 0.226
-44	0.187 ± 0.037	0.745 ± 0.450	0.902 ± 0.176
-46	0.173 ± 0.035	0.727 ± 0.433	0.833 ± 0.169
-48	0.229 ± 0.049	1.392 ± 0.653	1.104 ± 0.235
-50	0.156 ± 0.031	0.709 ± 0.433	0.751 ± 0.147
-52	0.209 ± 0.042	1.215 ± 0.561	1.006 ± 0.200
-54	0.218 ± 0.058	1.614 ± 0.876	1.052 ± 0.278
-56	0.177 ± 0.047	0.904 ± 0.639	0.850 ± 0.225
-60	0.161 ± 0.034	0.656 ± 0.461	0.775 ± 0.162
-62	0.181 ± 0.038	1.081 ± 0.537	0.870 ± 0.181
2	1.089 ± 0.125	3.900 ± 0.693	5.245 ± 0.602
4	0.700 ± 0.055	3.255 ± 0.421	3.369 ± 0.267
6	0.494 ± 0.121	2.653 ± 1.126	2.380 ± 0.582
8	0.390 ± 0.105	2.563 ± 1.214	1.876 ± 0.504
10	0.286 ± 0.022	1.790 ± 0.281	1.376 ± 0.107
12	0.244 ± 0.050	1.831 ± 0.741	1.176 ± 0.242

Table D.5 Continued. Fit parameters and rotational transfer coefficients for $\text{Bi}_2(A, v'_0 = 1, J'_0 = 201)$ collisions with Argon.

ΔJ	a torr ⁻¹	b torr ⁻¹	$k_R(J'_0 \rightarrow J'_f)$ 10 ⁻¹¹ cm ³ /molec-sec
14	0.229 ± 0.052	1.693 ± 0.788	1.101 ± 0.250
16	0.203 ± 0.060	1.443 ± 0.934	0.977 ± 0.289
28	0.132 ± 0.033	0.814 ± 0.588	0.637 ± 0.157
30	0.139 ± 0.036	1.432 ± 0.771	0.671 ± 0.171
34	0.095 ± 0.034	0.364 ± 0.656	0.458 ± 0.164

Appendix E. Error Analysis

The quoted errors for the molecular constants in Chapter III are the standard deviation to the least-squares fit of the appropriate two term Dunham polynomial. The number of digits used to express these terms are needed to accurately reproduce the reported term values.

The error associated with the experimentally determined Franck-Condon factors stems mainly from errors associated with the detector response function. The response function was first determined from a quartz calibration lamp. This function allowed a calibrated blackbody spectral response to be reproduced to within 10-12%. Thus, the error associated with the experimental Franck-Condon factors is estimated at $\pm 10\%$.

CW LIF experiments inherently have many sources of systematic errors which affect the accuracy of the predicted rate constants. These errors arise from uncertainty in the variables used to relate intensity to number density. These errors come from the following four primary sources: (a) uncertainty in Franck-Condon factors; (b) Uncertainty in radiative lifetimes; (c) errors in determining spectral response; and (d) uncertainty in the calculation of population ratios. The uncertainties associated with the spectral response and the Franck-Condon factors have already been discussed.

A single radiative lifetime of 590 ns was used for all kinetic calculations in this research. This was the reported lifetime of the $v' = 1, J' = 10$ rovibrational level. An error bound of $\pm 5\%$ is reported for this level. However, it is unclear whether or not this value is valid for all rovibrational levels studied. If one assumed there was a possible 100 ns error in this value, an error bound of 17% would be present in the reported lifetime. This large error bound should reasonably cover possible deviations in actual lifetimes of the rovibrational levels studied in this research.

The error bars on the population ratios presented in Chapters IV were determined as follows. Since the area under the spectral response function is determined by the ratio a/c (see Appendix C), the maximum area under the curve of a single vibrational band was found by dividing the maximum value of a by the minimum value of c . The maximum and minimum values of a particular parameter were found by adding and subtracting the parameters standard deviation to the least-squares fitted value of that parameter. The standard deviation was an output value from the TableCurve software. The minimum area under the curve was found in a similar manner by dividing a_{min} by c_{max} . The area of the Gaussians used for the P-R doublet is given by $\sqrt{2\pi}AR$ where A and R are as defined by Equation 4.3. The maximum and minimum areas of the Gaussians were found from appropriate maximum and minimum values of the A and R parameters. From these maximum and minimum areas, the maximum population ratio was calculated by dividing the maximum area of the satellite band by the minimum area associated with the parent band and vice versa. Typical uncertainty in the spectral ratio calculations was approximately 10%.

In Chapter V, the area of the Gaussian-Lorentzian sum used to model the rotational energy transfer along with its standard deviation were both output parameters from PeakFit. These two parameters were able to define the upper and lower limits of the area under the curve of the different rotational states. With these limits calculated, an analogous calculation to the previous paragraph allowed for the calculation of the limits on the population ratios. Population ratio uncertainties ranged from $\pm 10\%$ for low ΔJ levels to approximately 35% for high ΔJ .

If the estimated uncertainties are added in quadrature, as discussed by Bevington (54), and there is no assumed correlation between the uncertainties, the accuracy in vibrational transfer rate coefficients was estimated at $\pm 25\%$. The error for the rotational transfer rate coefficients is estimated at $\pm 25\%$ for the low ΔJ rates to $\pm 40\%$ for the high ΔJ rate coefficients.

Bibliography

1. N.Bloembergen and C.K.N., Co-chairs, APS Study Group Patel. *Rev. Mod. Phys.*, 59:S1, 1987.
2. T.A. Cool and R.R. Stephens. *Appl. Phys. Lett.*, 16:55, 1970.
3. W.E. McDermott, N.R. Pchelkin, D.J. Bernard, and R.R. Bousek. *Appl. Phys. Lett.*, 32:469, 1978.
4. G.P. Perram. Approximate Analytic Solution for the Dissociation of Molecular Iodine in the Presence of Singlet Oxygen. *International Journal of Chemical Kinetics*, 27:817-828, 1995.
5. G.P. Perram. Visible Chemical Lasers. *Proceedings of the International Conference on LASERS '89*, 1989.
6. G.P. Perram. The Challenges of Inexpensive Laser Demonstrations. *Proceedings of the International Conference on LASERS '92*, 1992.
7. C.D. Holmberg. *Spectroscopic and Vibrational Energy Transfer Studies in Molecular Bromine*. PhD thesis, Air Force Institute of Technology (AU), 1993.
8. Capt. D.W. Melton. *Collisional Dynamics of the B $^3\Pi(0_u^+)$ State of BrF*. PhD thesis, Air Force Institute of Technology (AU), 1991.
9. Capt. G.P. Perram. *Collisional Dynamics of the B State of Bromine Monochloride*. PhD thesis, Air Force Institute of Technology (AU), 1986.
10. Capt. G.S. Williams. *Vibrational Energy Transfer Within the B $^3\Pi(0_u^+)$ State of $^{79}\text{Br}_2$ upon collision with N₂, O₂, NO, and SF₆*. Master's thesis, Air Force Institute of Technology (AU), 1993.
11. Capt. P. Wolf. *Collisional Dynamics in the B $^3\Pi(0_u^+)$ State of Iodine Monofluoride*. PhD thesis, Air Force Institute of Technology (AU), 1986.
12. C.D. Holmberg, G.S. Williams, and G.P. Perram. Quantum-resolved Vibrational Energy Transfer in $^{79}\text{Br}_2$ B $^3\Pi(0_u^+)$, $v' \leq 3$. *J. Chem. Phys.*, 102:6481-6486, 1995.
13. G.P. Perram and S.J. Davis. Collisional Dynamics of the BrCl B $^3\Pi(0^+)$ state. II. Vibrational and Rotational Energy Transfer. *J. Chem. Phys.*, 98:373-382, 1993.
14. D.J. Benard. Threshold Oscillation of an NF($a^1\Delta$)/BiF Visible Wavelength Chemical Laser. *J. Appl. Phys.*, 74:2900-2907, 1993.
15. J.M. Herbelin. Short-wavelength Chemical Laser Development. *Proceedings of the International Conference on Lasers '89*, pages 241-246, 1990.
16. R. Hultgren, R.L. Orr, P.D. Anderson, and K.K. Kelley. *Selected Values of Thermodynamic Properties of Metal and Alloys*. John Wiley and Sons, 1963.

17. W.P. West and H.P. Broida. Optically Pumped Vapor Phase Bi₂ Laser. *Chem. Phys. Lett.*, 56:283–285, 1978.
18. S. Drosch and G. Gerber. Optically Pumped CW Molecular Bismuth Laser. *J. Chem. Phys.*, 77:123–130, 1982.
19. C. Effantin, A. Topouzkhian, J. Figuet, J. d'Incan, R.F. Barrow, and J. Verges. Electronic States of Bi₂ Studied by Laser-Excited Fluorescence. *J. Phys. B: Atomic and Molecular Physics*, 15:3829–3840, 1982.
20. G. Ehret and G. Gerber. Polarization Labeling Spectroscopy of the A(0_u⁺) State of Bi₂ with Narrowband Pulsed Dye Lasers. *Optics Communications*, 51:145–150, 1984.
21. G. Gerber, H. Honninger, and J. Janes. Rotational Analysis of the A-X Band System of Bi₂. *Chem. Phys. Lett.*, 85:415–417, 1982.
22. J.M. Blondeau, G. Gandara, P. Cayette, and J. Messelyn. Lifetimes of the A(0_u⁻) State and Quenching Cross Sections of Bi₂. *Chem. Phys. Lett.*, 71(2):246–252, 1980.
23. G. Ehret and G. Gerber. Lifetimes and Transition Moment of the A-X Band System of Bi₂. *Chemical Physics*, 66:27–38, 1982.
24. J.I. Steinfeld. *Molecules and Radiation*. the MIT Press, 1985.
25. G. Herzberg. *Spectra of Diatomic Molecules*. Van Nostrand Rheinhold Company, 1950.
26. R.S. Mulliken. The Interpretation of Band Spectra. *Review of Modern Physics*, 4:1–88, 1932.
27. K.K. Das, H. Liebermann, R.J. Buenker, and G. Hirsch. Relativistic Configuration Interaction Study of the Low-lying States of Bi₂. *J. Chem. Phys.*, 102:4518–4530, 1995.
28. G.M. Almy and F.M. Sparks. The Absorption Spectrum of Diatomic Bismuth. *Physical Review*, 44:365–375, 1933.
29. G. Gerber and H.P. Broida. Electronic States and Molecular Constants of Bi₂^{*}. *J. Chem. Phys.*, 64(8):3423–3437, 1975.
30. G. Gerber, K. Sakurai, and H.P. Broida. Laser Photoluminescence of Bi₂^{*}. *J. Chem. Phys.*, 64(8):3410–3422, 1975.
31. Capt. D.A. Massman. Quenching and Rotational Energy Transfer in Molecular Bromine: Br₂ B ³Π(0_u⁺). Master's thesis, Air Force Institute of Technology (AU), 1991.
32. G.P. Perram, D.W. Melton, T.L. Thompson, and W.B. Roh. Collisional Dynamics of the BrF B ³Π(0_u⁺) state. II. Vibrational Energy Transfer. *J. Chem. Phys.*, 97(5):3258–3264, 1991.

33. V. L. Landau and E. Teller. *Phys Z. Sowj Un*, 10:35, 1936.
34. R.N. Schwartz, Z.I. Slawsky, and K.F. Herzfeld. Calculation of Vibrational Relaxation Times in Gases. *J. Chem. Phys.*, 20:1591, 1951.
35. G.P. Perram, D.A. Massman, and S.J. Davis. Quantum Resolved Rotational Energy Transfer in the B $^3\Pi(0_u^+)$ state of Br₂. *J. Chem. Phys.*, 99:6634-6641, 1993.
36. J.C. Polanyi and K.B. Woodall. *J. Chem. Phys.*, 56:1563, 1972.
37. T.A. Brunner, N. Smith A.W. Dapr, and D.E. Pritchard. Rotational Energy Transfer in Na₂^{*} ($A\Sigma$) colliding with Xe, Kr, Ar, Ne, He, H₂, CH₄, and N₂: Experimental and Fitting Laws. *J. Chem. Phys.*, 74:3324, 1981.
38. D.E. Pritchard, N. Smith, R.D. Driver, and T.A. Brunner. *J. Chem. Phys.*, 70:2135, 1979.
39. N. Aslund, R.F. Barrow, W.G. Richards, and D.N. Travis. Rotational Analysis of Bands of the B-X System of Cu₂ and of the A-X system of Bi₂. *Arkiv For Fyzik*, 30:171, 1965.
40. G.Fabre, J.P. Bacci, C. Athenour, and R. Stringat. Laser Induced Fluorescence of the 0-6, 1-6, and 0-5 Bands of the Transition A(0_u^+)-X(0_g^+) of Bi₂. *Canadian Journal of Physics*, 60:73, 1982.
41. S. Gerstenkorn and P. Luc. *Atlas Du Spectre D'Absorption De La Moleé cule D'Iode*. Publications Scientifiques et litteraies, 1979.
42. S. Gerstenkorn and P. Luc. Absolute Iodine (I₂) Standards Measured by the Means of Fourier Transform Spectroscopy. *Revue de Physique Appliquee*, 14:791-794, 1979.
43. M. Heaven. FORTRAN computer code obtained from author.
44. R.B. Kurzel and J.I. Steinfeld. Energy-transfer Processes in Monochromatically Excited Iodine Molecules. III. Quenching and Multiquantum Transfer from $v' = 13$. *J. Chem. Phys.*, 53:3293, 1970.
45. Jandell Scientific. *TableCurve 2D, Automated Curve Fitting Software, Version 2.0*, 1994.
46. J.T. Yardley. *Introduction to Molecular Energy Transfer*. Academic Press, New York, 1980.
47. J.O. Hirschfelder, C.F. Curtis, and R.B. Byrd. *Molecular Theory of Gases and Liquids*. John Wiley and Sons, Inc., New York, 1954.
48. M.J. Sienko and R.A. Plane. *Chemical Principles and Properties, 2nd ed.* McGraw-Hill, Inc., USA, 1974.
49. S.J. Davis and K.W. Holtzclaw. Rotational Energy Transfer in Excited States of Halogen Molecules. I. Transfer from $v' = 6, J' = 72$ in IF B $^3\Pi(0_u^+)$. *J. Chem. Phys.*, 92:1661, 1990.

50. K. Bergmann and W. Demtroder. *Z. Phys.*, 243:1, 1971.
51. J.I. Steinfeld, J.S. Francisco, and W.L. Hase. *Chemical Kinetics and Dynamics*. Prentice Hall, New Jersey, 1989.
52. J.A. Barnes, M. Keil, R.E. Kutina, and J.C. Polanyi. *J. Chem. Phys.*, 76:913, 1982.
53. T.A. Brunner, R.D. Driver, N. Smith, and D.E. Pritchard. Simple Scaling Law for Rotational-energy Transfer in Na_2^* -Xe Collisions. *Phys. Rev. Lett.*, 41(13):856, 1978.
54. P.R. Bevington. *Data Reduction and Error Analysis for the Physical Sciences*. McGraw-Hill, Inc., New York, 1969.
55. J.I. Steinfeld and W. Klemperer. Energy Transfer Processes in Monochromatically Excited Iodine Molecules. I. Experimental Results. *J. Chem. Phys.*, 42:3475, 1965.
56. C.W. McCurdy and W.H. Miller. *J. Chem. Phys.*, 67:463, 1977.

Vita

Captain Robert E. Franklin was born on [REDACTED] in [REDACTED]. He graduated from Midway High School in Waco, Texas in 1982 and entered basic cadet training at the United States Air Force Academy in June of that year. He graduated from the Academy with a bachelors degree in Physics in 1986 and accepted a commission as a 2nd Lieutenant. His first assignment in the Air Force was to undergraduate navigator training (UNT) at Mather AFB, California, where he earned his wings in May of 1987. After UNT, he served as a weapons system officer (WSO) in the 12th Tactical Reconnaissance Squadron located at Bergstrom AFB, Texas. While at Bergstrom, Captain Franklin was upgraded to both an instructor WSO and a wing supervisor of flying (SOF). He also accumulated over 1000 hours of flight time in the McDonnell Douglas RF-4C Phantom II aircraft including approximately 100 hours of combat time on thirty-two combat sorties during the Persian Gulf War. With the phasing out of the venerable F-4 aircraft from the Air Force inventory, his next assignment was to attend graduate school in residence at the Air Force Institute of Technology (AFIT). He earned a Master of Science degree in Applied Physics in December of 1993 and was immediately accepted into the PhD program at AFIT. Rob married [REDACTED] of [REDACTED] in 1990. They have one son, [REDACTED], who was born in [REDACTED]. Rob was admitted to candidacy in 1995. His follow on assignment after AFIT is to the Phillips Laboratory at Kirtland AFB, NM where he he will work on infrared countermeasure (IRCM) development.

Permanent address: [REDACTED]
[REDACTED]